UNIVERSITÀ DEGLI STUDI DI PADOVA

UNIVERSITÀ DEGLI STUDI DI PADOVA
Dipartimento di Ingegneria Industriale DII
Corso di Laurea Magistrale in Ingegneria Aerospaziale

IMPLEMENTATION OF A SPANWISE MIXING MODEL FOR THROUGHFLOW CALCULATIONS IN AXIAL-FLOW COMPRESSORS

Relatore: Chiar. mo Prof. ERNESTO BENINI

Laureando: DAVIDE DURANTI
MATRICOLA 1069068

Anno Accademico 2015/2016

Ai miei cari.

Abstract

Throughflow calculations on the hub to casing surface are still the backbone of the modern compressor and turbine design process, and remain the most important tool for the designer in the preliminary phase of design. They are fast to implement and give reliable, even if approximate, results as a first insight of the global component functioning, relying on the assumption of inviscid axisymmetric compressible flow. This assumption, even simplifying throughflow calculations, can often lead to serious errors, since neglects the effect on the flow due to spanwise mixing. In this context, mixing refers to exchange of mass, momentum, and energy between stream sheets, thus implying either convection from secondary flows or turbulent diffusion, as well as the existence of shear stresses. The important influence of spanwise mixing on the flow through multistage axial-flow compressors has been investigated by incorporating the effect into a subroutine for a specific streamline curvature throughflow program. The mixing was modelled as a diffusion process including the influence of both secondary flows and turbulence. Two different analyses, comparing the results obtained including the mixing action to those from a streamline curvature model developed in Cranfield University and a well-validated CFD numerical model, were carried out for two operating points of NASA Rotor 67. The applicability of the implemented spanwise mixing model and its congruity with the actual flow behaviour have been investigated and discussed.

Contents

Nomenclature

Acronyms

S_1	Streamsurface of the first kind
S_2	Streamsurface of the second kind
S_3	Streamsurface of the third kind
0-D	Zero-dimensional
1-D	One-dimensional
2-D	Two-dimensional
3-D	Three-dimensional
A&S	Adkins and Smith
ATM	Automatic Topology and Meshing tool
CFD	Computational Fluid Dynamics
DCC	Dynamic Convergence Control
DD	Domain Duct
G&C	Gallimore and Cumpsty
LSRC	Low-Speed Research Compressor
M-C	MIXING-CFD
NC	Near Choke
NPE	Near Peak Efficiency

QO Quasi-orthogonal

R67 NASA Rotor 67

RE Radial Equilibrium

RMS Root mean square

S-M-C SOCRATES-MIXING-CFD

SLC Streamline Curvature

SOCRATES Synthesis Of Correlations for the Rapid Analysis of Turbomachine Engine Systems

SRE Simple Radial Equilibrium

Greek Symbols

α Stagger angle; Absolute flow angle

β Adkins and Smith mixing coefficient; Relative flow angle

δ Boundary layer thickness; Deflection

ϵ Angle of lean; Gallimore and Cumpsty mixing coefficient

Γ Blade circulation

γ Sweep angle

λ Secondary flow kinetic energy

μ_t Eddy viscosity

ν Kinematic eddy viscosity

Ω Angular velocity

ω Loss coefficient

Φ Dissipation function

ϕ Pitch angle; Flow coefficient

ψ Streamfunction

ρ Density

σ Stress

Θ Generic flow property

θ Circumferential coordinate

ζ Vorticity

Roman Symbols

$\hat{\mathrm{e}}$ Unit vector

$\dot{m}$ Mass flow rate

$\overline{u'}, \overline{v'}, \overline{w'}$ Turbulent velocity components

a Acceleration of a fluid particle; Cross-section width

c_p Specific heat at constant pressure

k_t Eddy thermal conductivity

r_c Radius of curvature

B Blockage factor

C, c Absolute velocity

E Shear body force density

F Blade body force density

GA Grid aspect ratio

H Height of the annulus

h Specific enthalpy

I Rothalpy

k Factor

L Length

l Typical length scale of turbulent eddies

Ma Mach number

N Number of blades

Pr Prandtl number

p Pressure

Q Heat per unit volume

q Velocity scale

Re Reynolds number

R Optimum relaxation factor

r Radial coordinate

Sc Schmidt number

s Specific entropy

T Temperature

t Time

U, u Tangential velocity component

V Velocity

W, w Relative velocity component

W Specific work input

w Streamsurface thickness

z Axial coordinate

Superscripts

$*$ Rotary

r Relative

Subscripts

$\perp$ component perpendicular to relative velocity

θ Circumferential component

$q-3D$ Quasi$-$3-D

S_3 On the transverse surface S_3

0 At the blade trailing edge; Total

1 Stator inlet

2 Stator exit

3 Rotor exit

A, a Actual

abs Absolute

casing At casing

ewbl Endwall boundary layer

e Direction obtained by rotating $\hat{\mathrm{e}}_q$ by angle ϵ counterclockwise; Empirical

hub	At hub
inv	Inviscid
is	Isentropic
i	Ideal
l	Loss
m	Meridional component
n	Distance normal to axisymmetric streamsurfaces of the main flowfield; Normal component
pbl	Profile boundary layer
p	Direction normal to q on the $m - q$ plane
q	Quasi-orthogonal component
r	Radial component
sf	Secondary flow
s	Spanwise component; Stage
t	Direction normal to q on the $m - q$ plane; Turbulent
visc	Viscous
z	Axial component

List of Figures

List of Tables

CHAPTER 1

Introduction

Throughflow calculations on the hub to casing surface are still the backbone of the modern compressor and turbine design process, and remain the most important tool for the designer in the preliminary phase of design. They find their origin in the General Theory produced by Wu, in which a three dimensional flow in a turbomachine environment could be analysed in two separated two-dimensional surfaces, namely the meridional plane and the blade-to-blade surface.

In particular, there are several throughflow methods for calculating the flow on the meridional plane: among the others, the most famous and used throughflow method is the Streamline Curvature method. Streamline curvature throughflow calculations can provide several information on the flow in compressors: for instance, they can determine blade inlet and exit angles and velocity variation from a specified spanwise work distribution, the total temperature or angular momentum and the total pressure being prescribed, or , when blade angles and the machine geometry are specified, they can predict flow angles, work, velocity distributions, and machine performance.

Streamline curvature throughflow methods are fast to implement and give reliable, even if approximate, results as a first insight of the global component functioning. Even so, as they are the logical evolution of Wu's General Theory, they rely on the same initial assumption of inviscid axisymmetric compressible flow. This assumption, even simplifying throughflow calculations, can often lead to serious errors, since neglects the effect on the flow due to spanwise mixing.

In this context, mixing refers to exchange of mass, momentum, and energy between stream sheets, thus implying either convection from secondary flows or turbulent diffusion, as well as the existence of shear stresses. In the literature, there are several models for spanwise mixing: the most important are that proposed by Adkins and Smith, and that formulated by Gallimore and Cumpsty. The first model, developed by Adkins and Smith, attributed the physical mechanism of spanwise mixing to a convective effect due to spanwise velocities set up by secondary flows, while Gallimore

and Cumpsty, in their formulation, concluded that turbulent diffusion was the primary physical mechanism generating the spanwise mixing effect.

The fact that two totally different concepts for estimating the mixing coefficient, that is Adkins and Smith's model based on convective effects due to secondary flows and Gallimore and Cumpsty's approach based on turbulent diffusion, would lead to similar results aroused considerable interest and controversy, giving birth to a debate. The first concrete step toward a resolution to the debate was a numerical three-dimensional Navier-Stokes analyses performed by Leylek and Wisler, who showed conclusively that spanwise mixing is caused by a combination of secondary flow and turbulent diffusion, and this was acknowledged by the most part of the authors included in the debate.

In this dissertation, the principal objective is to verify the applicability of a spanwise mixing model for throughflow calculations in axial-flow compressors, and to investigate its congruity with the actual physical behaviour of the flow in such environment. The important influence of spanwise mixing on the flow through multistage axial-flow compressor has been investigated by incorporating the effect into a subroutine for a specific streamline curvature throughflow program developed in Cranfield University, UK, by Pachidis et al., known as SOCRATES.

The spanwise mixing model implemented is that proposed by Adkins and Smith in their mixing analysis. In the present study, the mixing is modelled as a diffusion process including the influence of both secondary flows and turbulence.Two different analyses, comparing the results obtained including the mixing action to those from a SOCRATES streamline curvature model and a well-validated CFD numerical model, are carried out for two operating points of NASA Rotor 67 transonic compressor, which has been chosen as main test case.

Two kinds of analysis for two operating points of NASA Rotor 67, namely near choke and near peak efficiency operating points, will be performed: in the first, which will be referred to as S-M-C analysis, the spanwise mixing model implemented, indicated as MIXING, compares its predictions to those obtained from SOCRATES and CFD models. A comparison of the flow property distributions obtained from SOCRATES, MIXING, and CFD calculations, along with an analysis of errors, is carried out in order to study the applicability of the implemented spanwise mixing model as a tool for improving throughflow inviscid solutions, and to highlight the limits of the approach.

In M-C analysis, the spanwise mixing model implemented propagates flow property distributions directly obtained from CFD computations, which already take into account mixing effects by means of Navier-Stokes equations. MIXING relevance is to be investigated to verify its congruity with flow actual behaviour in axial-flow compressors.

The applicability of the implemented spanwise mixing model and its congruity with the actual flow behaviour are to be investigated and discussed in the following chapters. In particular, Chapter 2 reports a detailed literature review on transonic compressors and throughflow analysis method evolution. The problem of formulating and integrating spanwise mixing into throughflow calculations is addressed, and several

spanwise mixing model are presented.

In Chapter 3, the methodology used in S-M-C and M-C analyses is described in detail, reporting information on SOCRATES, CFD, and MIXING models characterisation and set-up.

Chapter 4 illustrates the results of the two mixing analyses, showing the flow property distribution evolution along the streamwise direction in NASA Rotor 67, and an analysis of errors is carried out and explained.

Finally, Chapter 5 summarises the most important outcomes of this study, suggesting further improvements for future works.

CHAPTER 2

Literature Review

2.1 Transonic compressors

2.1.1 Introduction

Nowadays transonic axial-flow compressors are widely used in aircraft engines since they can achieve high pressure ratios per single-stage. As a consequence, engine weight and size are reduced, decreasing investment, design, manufacture, and operational costs. According to Biollo and Benini [8], if properly designed, transonic compressor stages can guarantee:

- acceptable values of isentropic efficiency, around 83 - 90%, which can result in huge savings in fuel costs;
- high total pressure ratios, around 1.7 - 1.8, while subsonic compressor pressure ratios are around 1.3, thus reducing the number of compressor stages needed.

The total pressure ratio is increased giving the rotor a higher tip speed. Hence, in a transonic compressor stage there is a distribution of supersonic flow at the outer span of the rotor and a subsonic flow field at the inner span.

Despite the supersonic flow is only limited to a small portion at the compressor first-stage rotor blade tip, with a typical commercial-aircraft inlet relative flow Mach number around 1.3, and the relative flow in the rest of the first-stage rotor blade inlet, first-stage rotor blade outlet, and in the subsequent downstream stages is subsonic, the full compressor is known as transonic.

The axial velocity component of the flow is definitely subsonic at the blade inlet so, as stated by Cumpsty [19], the tangential component of velocity is high and the blades, in a supersonic compressor, must be highly staggered.

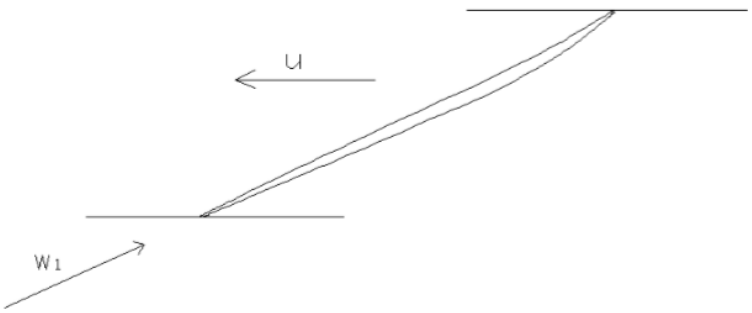

Figure 2.1: Supersonic blade profile (obtained from Benini, 2005). w_1 is the relative velocity component, u is the tangential velocity component.

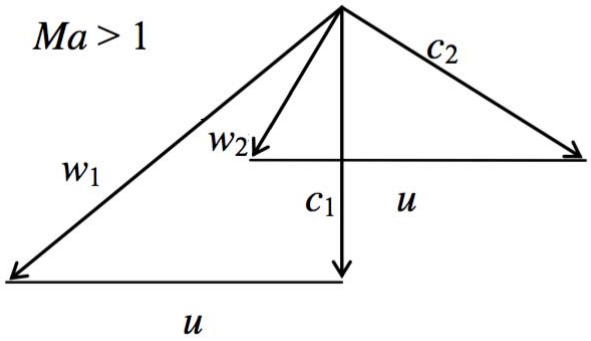

Figure 2.2: Velocity triangle in a transonic compressor (obtained and modified from Benini, 2014).

The conversion of the passing-flow dynamic pressure into static pressure is obtained by the formation of shock waves within the blade passages or upstream of the blades. Therefore supersonic blades are very thin at inlet (maximum thickness to chord ratio around 0.04), having a very small camber, centered after 50% of chord from leading edge, and a very low thickness, with a maximum thickness point located after half chord, Fig 2.1.

Since the pressure increase is realized through the shock wave configuration, and the relative velocity passes from supersonic to subsonic values, it is not possible to maintain constant the axial velocity component of the velocity triangle through the stage, as depicted in Fig 2.2. Supersonic compressors, as some transonic fans used in turbojet engines, have generally a single stage, so the absolute velocity is designed to be completely in the axial direction at the blade outlet and the shock is realized within the rotor passage.

The shock pattern is not only affected by the geometry of the blade but it is strongly influenced also by the inlet Mach number, the inlet flow direction and the back pressure behind the blade row.

Even though shock waves contribute to the deceleration of the relative velocity in

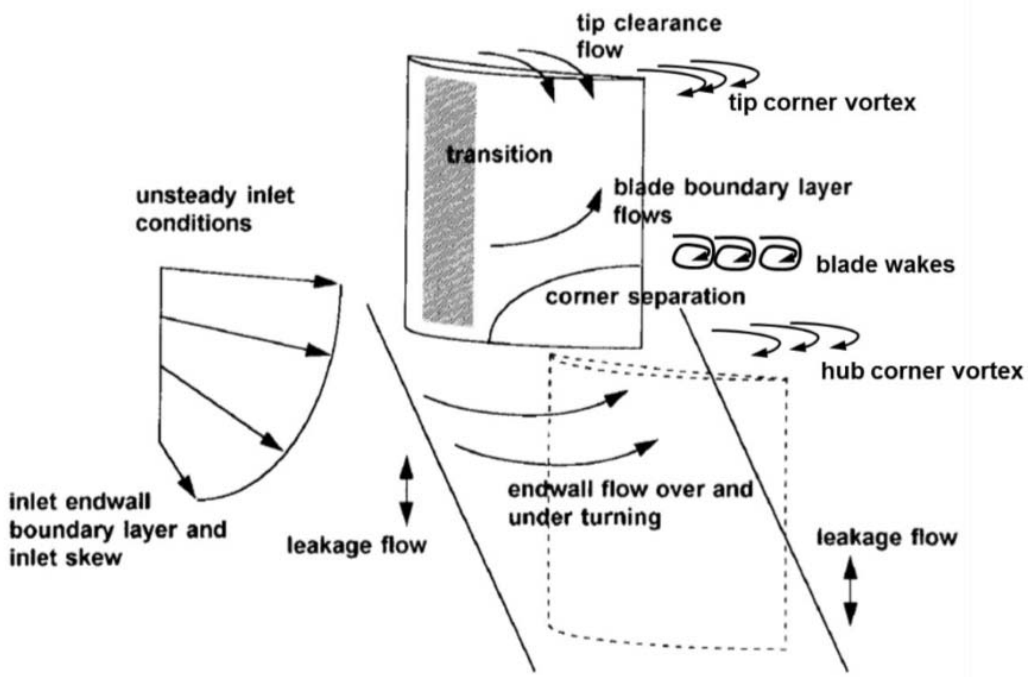

Figure 2.3: Flow features in a subsonic compressor (obtained from Gallimore, 1999).

the blade passage, leading to higher polytropic efficiencies, they generate a stagnation pressure loss that shortens the operation range. Conversely, when there is subsonic flow in a rotor, efficiencies increase and a wider operation range is obtained. Therefore, the combination of a wide operation range with high efficiencies from subsonic flow and the high pressure ratio that can be obtained due to shock wave compression in supersonic flow represents the trade-off to enhance the engine performance by means of transonic compressors.

2.1.2 Flow field viscosity effects

The flow field across a transonic axial-flow compressor is complex to analyse and its nature is yet to be fully understood. Some flow features are not still completely comprehended and consequently the aerodynamic design of transonic compressor rotors remains hard, since there aren't many empirical correlations as for the case of subsonic blade rows.

According to Biollo and Benini [8], a deeper understanding of the loss mechanisms of supersonic relative flow in compressors was possible thanks to the progress made in optical measurement techniques and computational methods, which led to new developments and designs.

The flow in compressors is inherently three-dimensional, viscous and unsteady. The main flow features in a subsonic axial-flow compressor, represented in Fig 2.3, consist of:

- profile losses, generated from blade boundary layer flows and wakes;

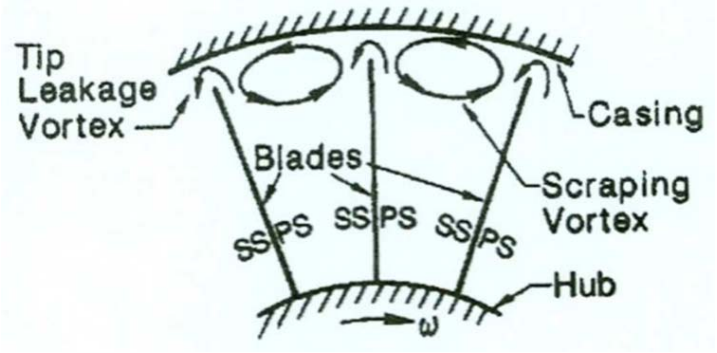

Figure 2.4: Tip clearance losses (obtained from Benini, 2014).

- secondary losses, due to leakage flow at the leading and trailing edge, tip clearance flow, and corner separation, where the latter two yield to tip corner vortex and hub corner vortex, respectively;
- endwall losses, arising from the endwall flow over and under turning.

These features can be further disturbed by unsteady inlet conditions or inlet endwall boundary layer conditions, such as initial boundary layer thickness or skew.

In a transonic axial-flow compressor there are additional losses due to shock waves and their interactions with the flow itself and the boundary layer, which dominate the tip flow field. This interaction between shock waves and boundary layer results in a higher boundary layer thickness increase that can eventually generate a reverse flow, with the formation a separation bubble and contributing to aerodynamic losses.

The most detrimental region is the tip endwall region, where intense secondary flows are developed due to the pressure difference between the suction side and the pressure side. The fluid is driven through the blade tip gap and propagates into the main flow, giving rise to a vortex, known as tip-clearance or tip-leakage vortex, which generally starts at the leading edge and develops within the passage, as shown in Fig 2.4.

From the interaction between these tip clearance flows, the casing boundary layer and the passage shock a complex flow structure arise, generating several effects on the overall rotor performance. As the operating point moves towards surge condition, the flow becomes stronger and unsteady, increasing the blade loading and inducing a tip-clearance vortex breakdown, producing a blockage near the blade tip and flow oscillation that causes shock-induced flow separations to vary in time, generating a rotor instability.

In addition to the aforementioned flow features, in a transonic compressor a spanwise flow migration occurs at the blade suction side, downstream of the passage shock, as illustrated in Fig 2.5. This radial flow causes the formation of a low-momentum region at the blade trailing edge, contributing to a boundary layer thickening and hence, building up for wake development, leading to an unfavourable stability by shortening the engine working range.

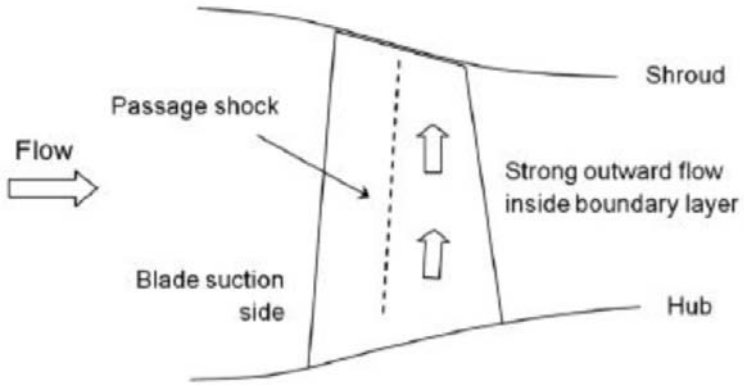

Figure 2.5: Spanwise flow migration downstream of the shock on the blade suction surface (obtained from Biollo and Benini, 2013).

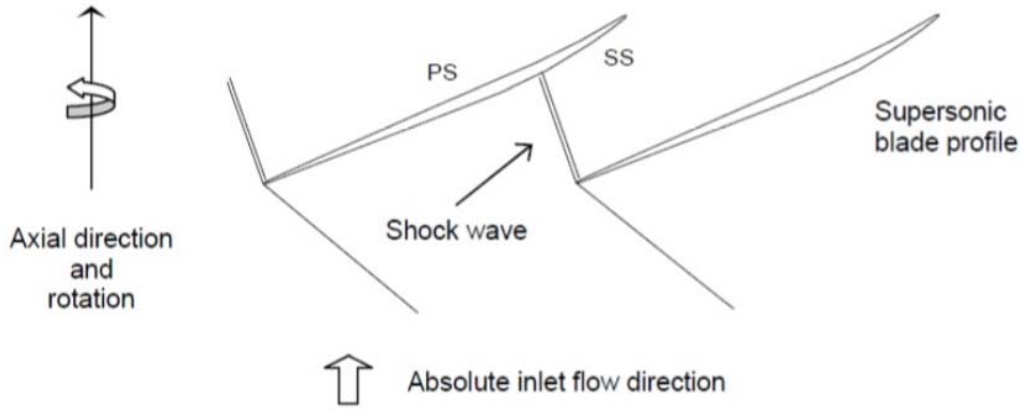

Figure 2.6: Shock wave in a transonic compressor (obtained and modified from Benini, 2014).

2.1.3 Shock structure

As stated by Benini [7], at the outer span of a transonic compressor blade, the relative flow is supersonic and the deflection imposed by the blade pressure side wall gives rise to a shock wave, which starts from the blade leading edge and propagates within the blade passage.

The supersonic flow, present only in transonic or supersonic compressors, generates intense shock waves, as represented in Fig 2.6, and in consequence shock losses, that provide a considerable increase of static pressure.

The shock is an irreversible process, inducing entropy generation, that involves a complex three-dimensional flow field physics triggering negative effects as shock waves, shock wave and boundary layer interaction, radial flow migration, shock wave interaction and tip clearance secondary flow interaction, blockage, corner stall and upstream wake destabilization, resulting in shock losses that cause an energy loss and hence efficiency reduction.

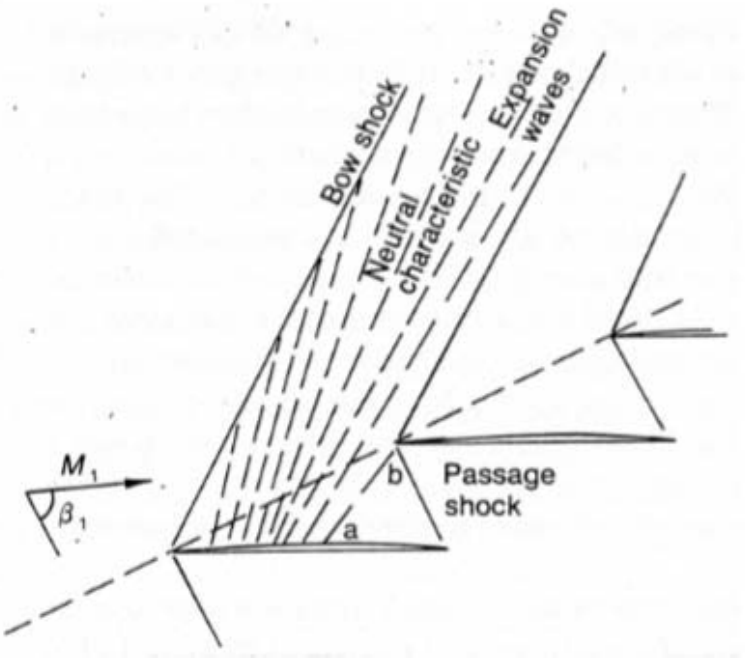

Figure 2.7: Idealized shock and expansion wave pattern in a supersonic rotor row at the unique incidence condition (obtained from Cumpsty, 1989).

The shock structure depends on the blade geometry and operating condition. Shock waves, in set with alternating expansion waves and weak shock waves, move along the blade passage and form starting from the blade pressure side to the leading edge of the other adjacent blade, as illustrated in Fig 2.7, representing an idealized choked flow configuration with a subsonic axial velocity. When such configuration is realized, the flow is known to be in the unique incidence condition, and the shock waves are attached to the blade leading edge. The bow shock is caused by the leading edge thickness and by the expansion waves due to the blade suction surface curvature. The expansion waves interact with the shocks upstream of the blades. In Fig 2.7 one expansion wave ab passes from the suction surface of one blade to the leading edge of the next: the flow is therefore supersonic in the region between the ab wave and the passage shock. As stated by Cumpsty [19], any curvature of the blade suction surface in the forward region, where the flow is supersonic, must bring about a Prandtl-Meyer acceleration of the flow leading to a higher Mach number across the section ab, and therefore a lower mass flow. For this reason, it is usual to make the forward region of the blades as flat as possible.

In general, shock waves are oblique, tending to shift upstream and become more normal to the incoming flow as the operating point moves towards surge condition, namely, as mass flow is reduced, causing a higher flow incidence.

Figs 2.8 and 2.9 show the blade-to-blade shock configuration inside a generic transonic compressor rotor, obtained varying the blade row incidence with constant inlet Mach number.

In Figs 2.8 and 2.9 a) the blade row is particularly loaded and the pressure ratio

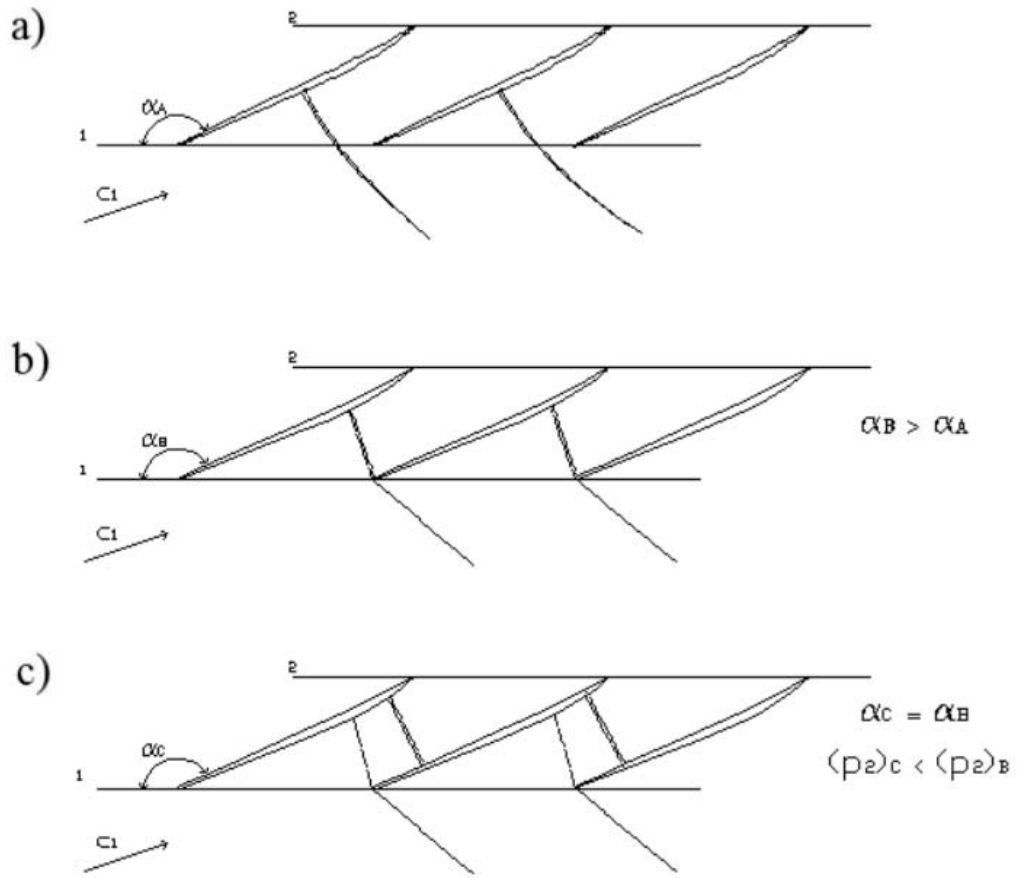

Figure 2.8: General shock configuration in a transonic compressor (obtained from Benini, 2014). a) Near-stall condition, b) Near-peak-efficiency condition, c) Choking condition.

p_2/p_1 rather high. The shock waves are completely detached from the blade leading edge and the shock within the blade passage is quasi-normal. This configuration is realized in a real transonic rotor in a near-stall condition. In this condition, any downstream adverse pressure perturbation can move upstream of blade leading edge, making the upstream pressure, the absolute subsonic velocity c_1, and hence the mass flow rate, vary. Increasing the incidence angle, shock losses rise due to a pre-shock Mach number increase caused by a supersonic turning ahead of the shock in set with higher upstream-running wave strength.

With a higher stagger angle α, the shock is attached to the leading edge showing a single system as depicted in Figs 2.8 and 2.9 b). This is possible since the deflection δ imposed on the flow by the pressure side blade wall is now lower than the maximum deflection δ_{max}, which is only function of the inlet Mach number Ma_1. As the back pressure is reduced, the mass flow starts to raise until peak-efficiency condition is reached. In this point, shock losses increase and profile losses decrease with respect to choking condition, so that total losses remain essentially the same.

Reducing the static pressure p_2 from the previous configuration, crossing the choking threshold, the flow is accelerated downstream of the first shock wave, which is

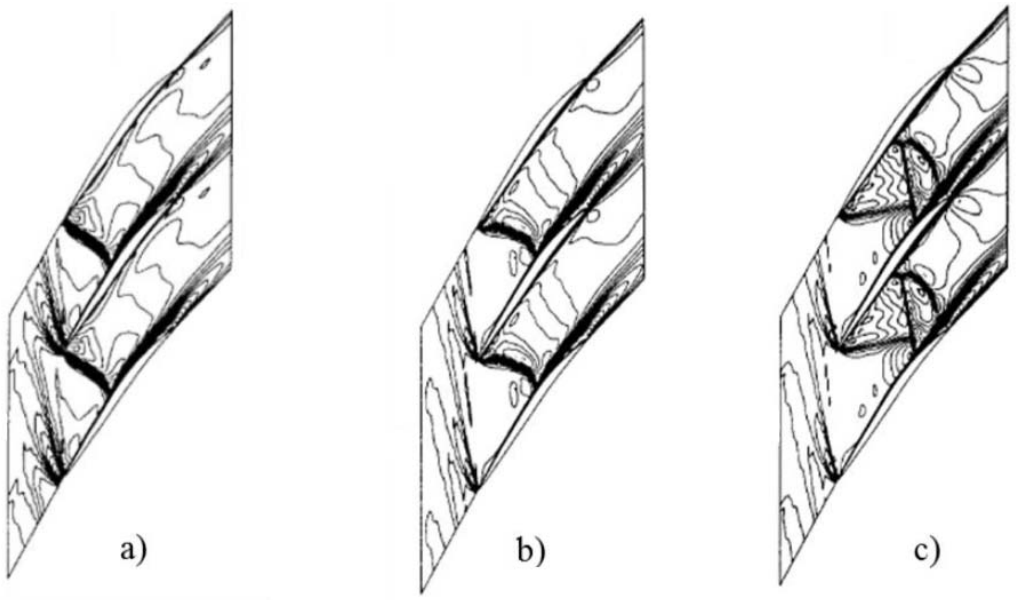

Figure 2.9: Shock structure in a blade-to-blade plane (obtained and modified from Calvert and Ginder, 1999). a) Near-stall condition, b) Near-peak-efficiency condition, c) Choking condition.

now weak, and a normal shock wave is generated within the blade passage. The inlet mass flow rate and the unique incidence angle remain constant, while the pressure ratio p_2/p_1 decreases. The normal shock wave at the leading edge develops highly-oblique shock waves on both surfaces as it can be observed in Figs 2.8 and 2.9 c). The upstream-running shock drives the inlet flow angle to satisfy the unique incidence condition whereas the downstream-running shock penetrates into the passage, interacting with the suction-surface boundary layer, inducing boundary layer separation and limiting diffusion. Although the downstream-running shock within the passage joins to the passage shock, the shock wave and boundary layer interaction generated is not significant as the boundary layer is reattached downstream. Near the maximum Mach number on the suction surface, the shock shows a lambda-foot structure that reduces the shock losses, however, the profile losses are increased and the loading is reduced due to a boundary layer blockage. While inside of the choking region, the back pressure can be further reduced, however the unique incidence angle and the inlet mass flow rate remain constant. For this reason, compressor performance maps show a vertical curve in the choking region when plotting for instance, pressure ratio, temperature ratio or isentropic efficiency, against mass flow, as illustrated in Fig 2.10.

The flow field behaviour, and therefore the compressor performance, are significantly determined by the blade geometry. Different solutions to diminish the flow negative impact can be found in the literature as blade profile geometry design, 3-D blade-shaping, casing treatments, and air injection or bleeding. As consequence, the stall limit increases leading to a wider operation range.

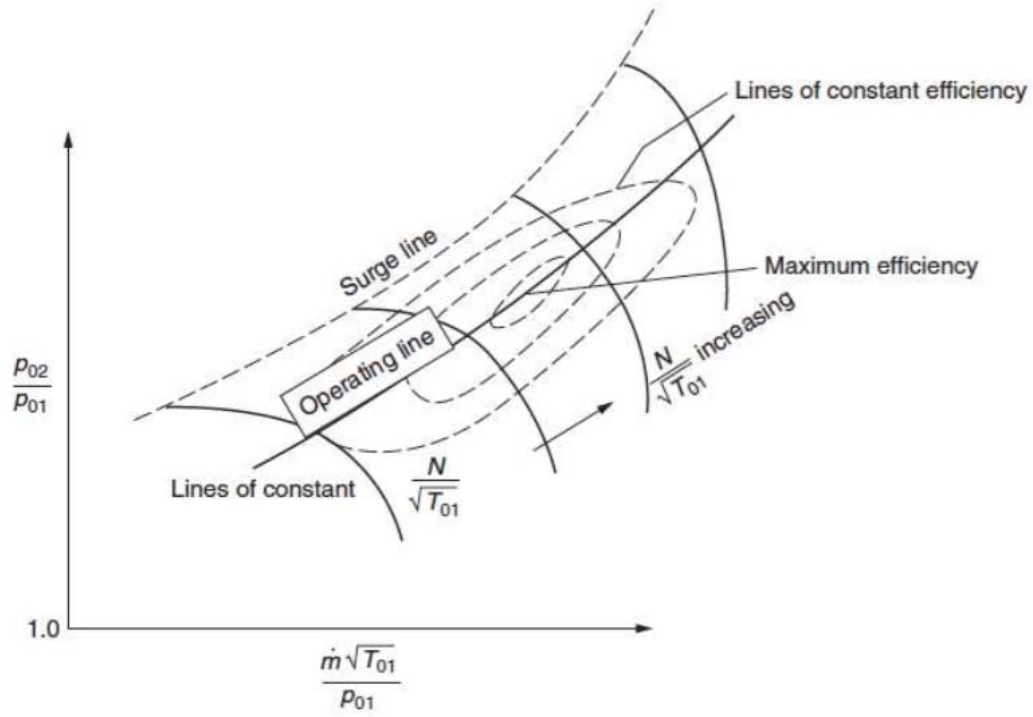

Figure 2.10: General compressor map (obtained from Benini, 2014).

2.2 Throughflow on the hub-casing surface

2.2.1 Introduction

Until the latest decades of the 20^{th} century, when the computing power started to handle three-dimensional flows in tubomachines properly, the typical approach for design was to conduct analyses in two separate but interrelated two-dimensional surfaces, namely, the blade-to-blade surface and the hub to casing surface. The latter surface is usually a meridional plane and is conventionally referred to as throughflow.

According to Cumpsty [19], the throughflow analysis in axial-flow compressor is meant to connect the blade-to-blade flow in the spanwise direction, verifying the compatibility of the flow at the various sections, which must satisfy the momentum equation in the radial direction: the blade performance is hence determined by the compressor as a whole. This is very important for the design of multistage compressors with low hub to casing ratio, $r_{hub} << r_{casing}$, since the flow is three-dimensional with strong spanwise gradients and the geometry must be compatible with the constraints imposed on the flow.

Throughflow calculation methods were the most used of all the calculation procedures, and they are nowadays still used in the preliminary phase of design, specifying the target aerodynamic performance to be achieved by the blading, since they are fast to implement and give reliable, even if approximate, results as a first insight of the global component functioning. Every major modification occurring later during the blade design process will be reevaluated on the throughflow model basis. Fig 2.11

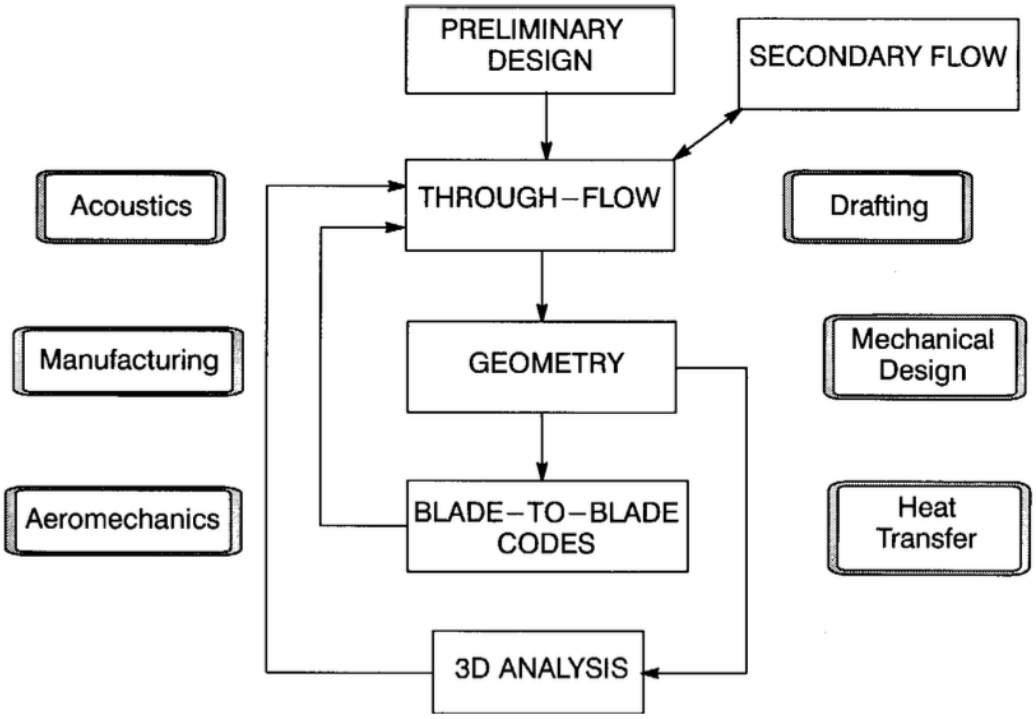

Figure 2.11: Turbomachinery aerodynamic design process (obtained from Jennions, 1994).

shows a typical design process for turbomachinery. The throughflow solver provides a preliminary blade shape, continually refined through solutions from higher-order and secondary flow models.

As mentioned by Boyer [11], throughflow calculations can be applied in several different ways. They can be used either in design, i. e. inverse mode, in order to determine blade inlet and exit angles and velocity variation from a specified spanwise work distribution, the total temperature or angular momentum and the total pressure being prescribed, or in analysis, i. e. direct, mode when blade angles and the machine geometry are specified and flow angles, work, velocity distributions, and machine performance in general are predicted. Finding the local performance of blades is essential for axial-flow compressor in order to provide compatibility along the entire span.

Another very important use of throughflow models is the interpretation of experimental data: the throughflow analysis recomputes the aerodynamic flow field inside the whole machine from experiments. Finally, the throughflow model is also used for coupling single blade row calculations in order to compute the flow field inside a multistage machine. The throughflow gives the boundary conditions to the 3-D single row calculations and the single row calculations give the flow angles and loss coefficients to the throughflow.

The level of approximation of throughflow depends on the application, but these methods are usually inviscid and carried out on a plane which is not a streamsurface, thus neglecting some terms in the equations. This represents both the convenience

and the limit of throughflow analyses. Nevertheless, these calculations are often incorporated in schemes which allow for their deficiencies, such as approximate input data or inaccuracies due to endwall boundary layer blockage, with the introduction of corrective terms. Indeed, only a few aerodynamic quantities are usually known from experiments and only at a limited number of locations. For example, only the stagnation pressures and temperatures at blade leading and trailing edges and the static pressures at annulus endwalls are known.

The main drawback of the throughflow models is that they heavily rely on empirical inputs, such as 2-D profile losses correlations or the aerodynamic blockage. The empirical calibrations included in a throughflow model allow them to accurately predict the flow field inside a whole machine and to provide credible designs, but this is only possible if the design parameters of that machine are close to the design parameters of the reference machine that has been used to calibrate the throughflow model.

In recent years, with the advent of CFD, it has become possible to calculate three-dimensional flows numerically, solving the Navier-Stokes equations. These calculations has a wider applicability than throughflow analyses, being able to detect almost entirely the flow features, viscosity effects included, making it possible to understand the basic physics and decide on good or bad features of the flow even when their effects cannot be quantified, but they are not always appropriate in the first stages of design, especially when the turbomachine geometry is still under evaluation.

The place of the through-flow progressively moved from the nearly sole design tool to one of the numerous tools used in a modern design tool chain for turbomachines. Nonetheless, it is still the backbone of the modern compressor and turbine design process, as stated by Horlock and Denton [41], and remains the most important tool for the designer, as noted by Denton and Dawes [23], and Adamczyk [3].

2.2.2 Historical background

The meridional flow theory in the frame of axial turbomachinery finds its first developments in the early part of the twentieth century. According to Denton [22], in the period 1900 - 1940, attention was directed mainly at steam turbines. The design was based on the Mean Line method, developed by Howell for compressors and Ainley and Mathieson for turbines, in that the meridional surface is collapsed onto a mean line through the machine, as stated by Frost [30]. The flow velocity triangles are only calculated in the duct regions between adjacent blade rows on the mean line, as represented in Fig 2.12, while providing some experimental corrections from cascade testing. The free vortex design was introduced in late 1920s but was not generally accepted until Whittle used it for the realisation of the first british turbojet model in late 1930s.

In the period 1940 - 1950 there was an intensive development of the jet engine: much of the basic science came from NGTE, Pyestock, where cascade testing was conducted. These experimental activity led to correlations, such as Howell's, Carter's, and Ainley & Mathieson's, part of which is still in use nowadays, that formed the basis of design.

In the late 1950s the Simple Radial Equilibrium theory, neglecting the streamlines

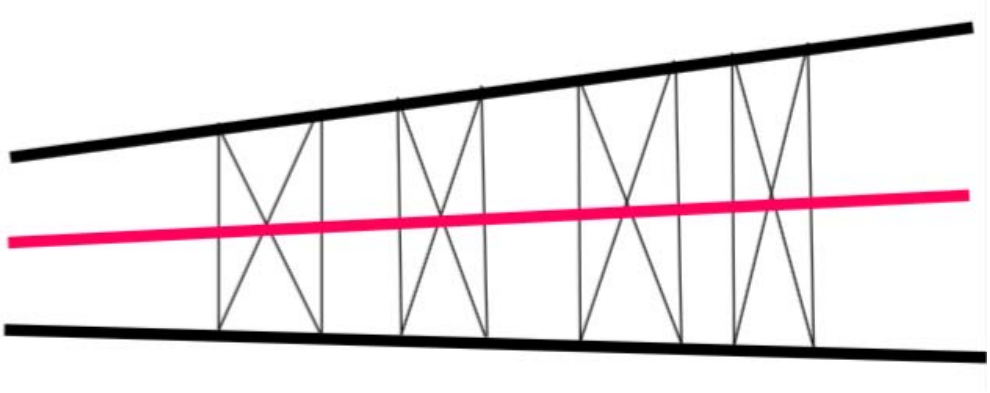

Figure 2.12: Mean Line method for turbines, developed in the early 20^{th} century (obtained from Denton, 2009).

curvature, coupled with prescribed free or forced vortex circumferential velocity distributions was in use. As mentioned by Cumpsty [19], for most axial compressors and turbines the dominant effect in the radial equation of momentum is the centripetal acceleration V_θ^2/r, which is set up by the swirl velocity, the other accelerations being negligible when the flow path is not highly curved in the meridional plane. The Simple Radial Equilibrium can demonstrate the connection of most axial stages in the spanwise direction, predicting the spanwise variation in velocity and the trends with changes in blade geometry or flow coefficient from the original design point.

There were two main issues to be addressed in the design procedure: first, the specification of work input along the blade span from hub to casing, in order to produce the required outlet conditions; second, the configuration arranged by the flow in the radial direction in response to the constraints imposed by the blades. Consider, for example, the case of an axial compressor stage in a parallel annulus. If the radial distance of the streamtube from the rotational axis is almost equal at inlet and outlet to the rotor, $r_1 = r_2$, the work input across the rotor for a steady flow along a mean streamtube is given by

$$W = h_{02} - h_{01} = U_2 V_{\theta 2} - U_1 V_{\theta 1} = \Omega(r_2 V_{\theta 2} - r_1 V_{\theta 1}) = U(V_{\theta 2} - V_{\theta 1})$$

and, if the work input is to be uniform in the radial direction then, since the blade speed is proportional to the radius, $U = \Omega r$, it is essential that the difference $(V_{\theta 2} - V_{\theta 1})$ is inversely proportional to radius, describing a free vortex condition. Normally, it is stagnation pressure rise, not work input, which is required to be radially uniform, allowing the work input to vary in order to compensate the predicted radial distribution in loss, hence describing a forced vortex condition.

Assuming that there is no variation in the circumferential θ direction, the radial momentum equation for an inviscid flow *F*Force is

$$V_z \frac{\partial V_r}{\partial z} + V_r \frac{\partial V_r}{\partial r} - \frac{V_\theta^2}{r} = -\frac{1}{\rho}\frac{\partial p}{\partial r} + F_r$$

where F_r is the radial force exerted by the blades on the gas. For most axial compressors F_r is negligible, and so are the radial velocities in a parallel annulus with the

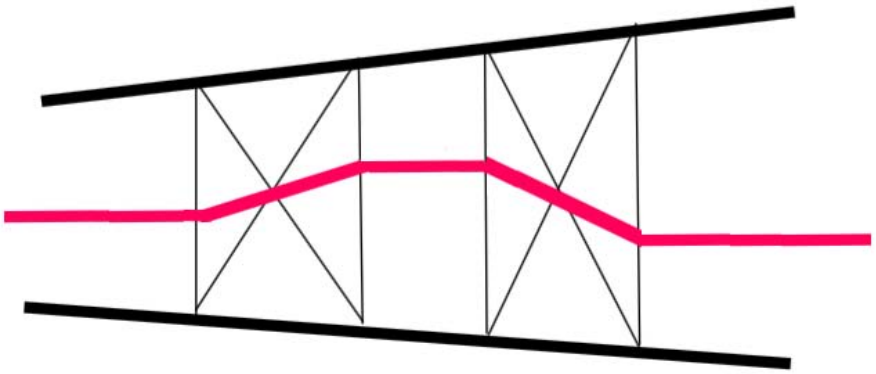

Figure 2.13: Simple Radial Equilibrium streamline pattern (obtained and modified from Denton, 2009).

blades operating near design. The equation then simplifies into the so-called Simple Radial Equilibrium (SRE) equation

$$\frac{\partial p}{\partial r} = \rho \frac{V_\theta^2}{r} \tag{2.1}$$

This equation can be deduced from the equilibrium of radial force and acceleration, and shows that the whirl velocity generates a radial pressure gradient.

Under the hypotheses of uniform total enthalpy h_0 and entropy in the radial direction, it also follows that the stagnation pressure will also be independent of radius

$$\frac{\partial p_0}{\partial r} = \frac{\partial p}{\partial r} + \frac{1}{2}\rho \frac{\partial}{\partial r}(V_z^2 + V_r^2 + V_\theta^2) = 0$$

and, being V_r much smaller than both axial and tangential velocities, and introducing equation 2.1, it yields

$$V_z \frac{\partial V_z}{\partial r} + \frac{V_\theta}{r}\frac{\partial}{\partial r}(rV_\theta) = 0$$

which shows that, if the whirl velocity is inversely proportional to radius for the free vortex condition, then the moment of momentum per unit mass rV_θ, crucial quantity for the determination of flow behaviour, is independent of radius and hence the axial velocity V_z is also uniform in the radial direction, which is a preference for the design of axial turbomachinery.

Fig 2.13 illustrates the implications of the Simple Radial Equilibrium approach. In this case the flow behaviour inside the blade row is not considered and all the streamline shift and the gas properties changes are assumed to occur within the blade rows, while in the actual flow the streamlines are not straight and change radius as they pass through the blade passage. Outside the blade row the streamlines have no radial velocity and the only acceleration is that due to the centripetal effect V_θ^2/r.

To achieve uniform stagnation pressure p_0 in the radial direction it was necessary to assume uniform entropy, but in practice the losses are greater near the inner and outer walls of the annulus and they increase when the relative Mach number is supersonic.

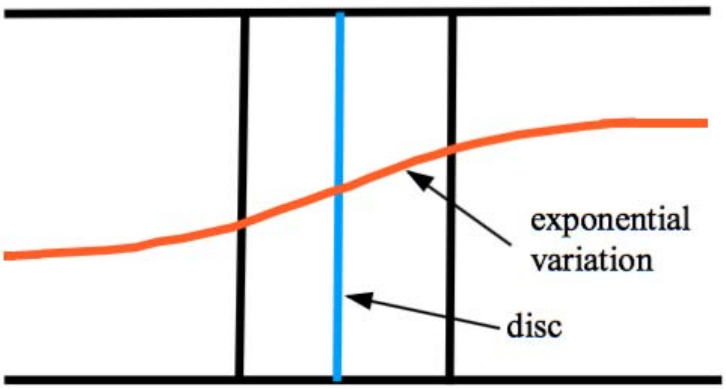

Figure 2.14: Schematic meridional streamline shape for actuator disc model (obtained and modified from Denton, 2009).

For this reason, to achieve uniform total pressure it is necessary to put more work into these regions and uniform moment of momentum per unity mass rV_θ is no longer adequate, the blades doing more or less turning in the endwall regions. This led to the development of twisted blading.

The Simple Radial Equilibrium method can determine the axial velocity distribution for prescribed distributions of whirl velocity or blade outlet flow direction, from which the blade angles are computed. According to Denton [22], The Avon and Olympus engines were almost certainly designed in this way, using standard blade sections such as C4, DCA, and T6.

Until the 1960s the Simple Radial Equilibrium was a major tool in the design of axial compressors and turbines, when it was left in place of other numerically based methods that relaxed the assumptions, providing generally more accurate results.

To make progress, the blades were approximated by one or more surfaces of discontinuity, known as actuator discs, placed across the annulus at a constant axial position, as represented in Fig 2.14. Across the actuator disc, which is equivalent to a blade row with an infinite number of blades of zero chord, the axial and radial velocities are continuous but the tangential velocity changes discontinuously.

This mathematical model was particularly attractive, since the solution could be performed in a blade-free region for which the differential equations are homogeneous. Marble showed that the axial velocity at stations upstream and downstream of the actuator disc changes exponentially so that

$$V_z(z,r) = V_z(z=0,r) \pm \frac{1}{2}[V_z(-\infty,r) - V_z(+\infty,r)][1 - e^{\pm\frac{\pi z}{H}}]$$

where H is the height of the annulus. This treatment involves Bessel functions for the case of axisymmetric geometries. The theory was shown to be capable of predicting the radial variation in axial velocity, but it could not handle the variation produced by the boundary layer in the endwall regions, which made the predictions look unsatisfactory for some flow features. The actuator disc method had then very little effect on compressor design and left place to other approaches based on numerical schemes.

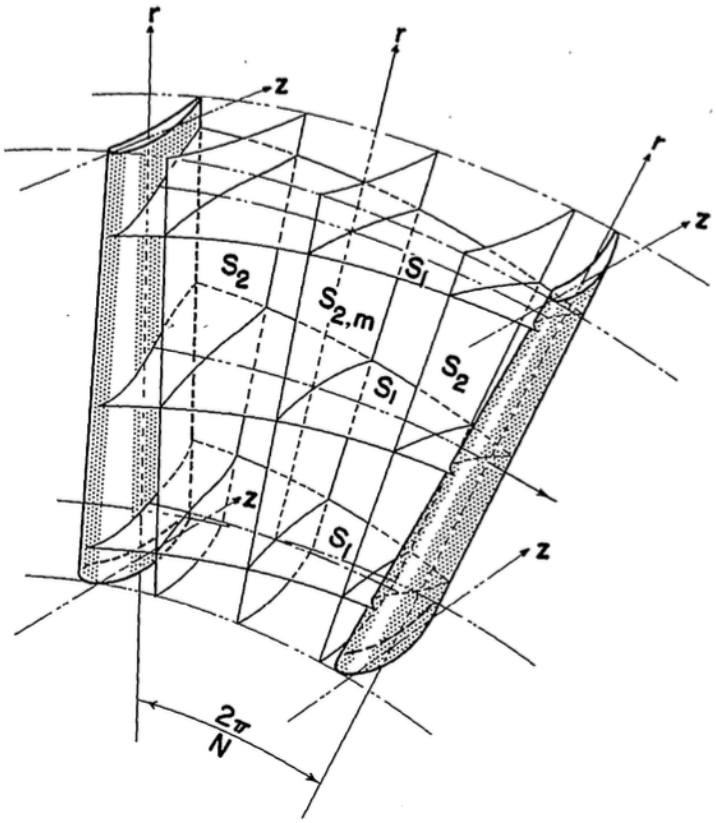

Figure 2.15: Intersecting S_1 and S_2 streamsurfaces in a blade row (obtained from Wu, 1952).

These schemes find their origin in the General Theory produced by Wu in 1952, which stipulated the concept of S_1 and S_2 streamsurfaces shown in Fig 2.15.

As reported in Wu [90], on the left side of Fig 2.16 a streamsurface of the first kind S_1 is illustrated. This streamsurface is formed by fluid particles lying on a circular arc ab of radius oa upstream of the blade row. This surface is allowed to take whatever shape it should have in order to satisfy all the equations governing the three-dimensional flow, and it actually twists and warps as it passes through the blade row. Nevertheless, it is usually assumed in ordinary two-dimensional treatments that S_1 streamsurfaces are formed as surfaces of revolution, the deviation from this condition being not very large if the rotationality of the inlet absolute flow is not high, either the blade is not designed for a velocity diagram quite different from the free-vortex type, or the blade length is not long in the direction of the through flow.

A streamsurface of the second kind S_2 is shown on the right side of Fig 2.16. This surface forms a meridional $z - r$ plane upstream of the blades extending from hub to casing, but it twists and warps too as it passes through the blade. The most important surface of S_2 family, designated the mean streamsurface $S_{2,m}$, is the one about midway between two blades dividing the mass flow in the channel into two approximately equal parts. For blades with radial elements, if the twist of the surface is expected not to be large, it is convenient to consider a mean streamsurface formed by fluid particles

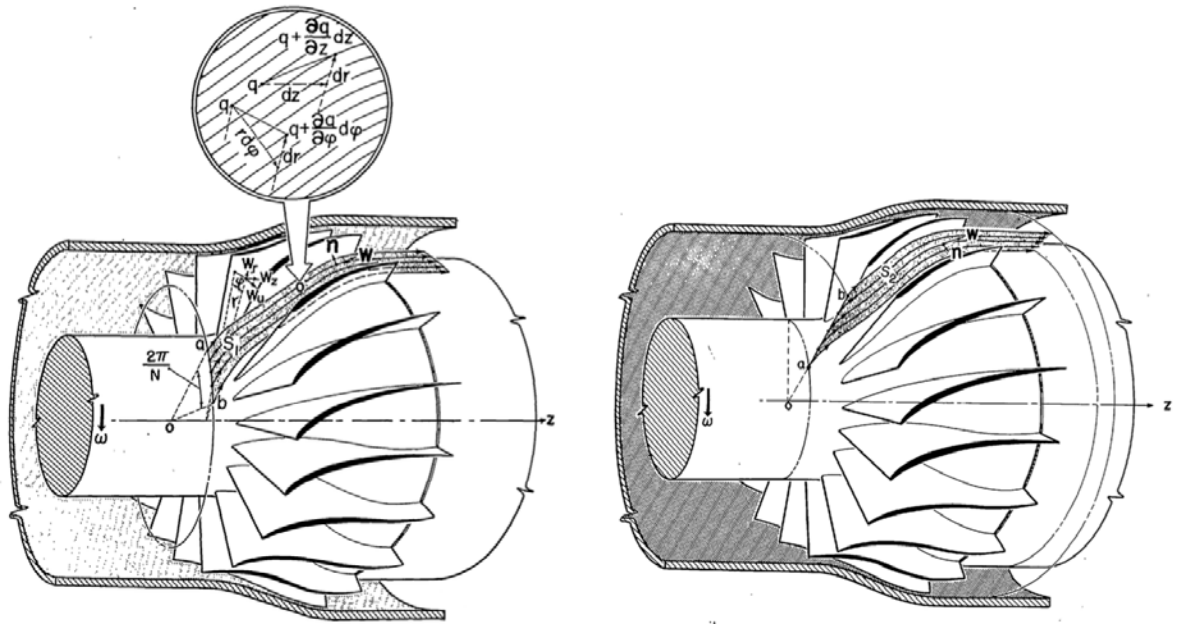

Figure 2.16: Relative streamsurfaces of first and second kind, S_1 and S_2 (obtained from Wu, 1952).

originally lying on a radial line ab upstream of the blade row, otherwise the radial line is chosen about midway in the passage with the fluid particles originally starting out from a curved line upstream of the blade row.

Wu's approach provides the solution for the inviscid three-dimensional flow as two analyses of the interrelated two-dimensional flow on the intersecting S_1 and S_2 surfaces. Both these two kinds of streamsurfaces are employed and the correct analysis on the first surface often requires some data obtainable from the second, and, consequently, successive solutions between these two are involved. This lends itself to a possible exact solution, iterating with the streamsurface shape changing with each iteration, but in practice this procedure has rarely been attempted, being far ahead of its time when no methods or computers were available to solve the resulting equations. Moreover, as stated by Cumpsty [19], there was an overwhelming source of inaccuracy in the method, due to the uncertainties associated with the endwall boundary layer and the prediction of such quantities as deviation, so that the errors introduced by simpler schemes were not as serious as these.

For this reason, the more common method of analysing the flow in two intersecting two-dimensional surfaces is to consider several untwisted S_1 surfaces and a single axisymmetric S_2 surface as represented in Fig 2.17. The flow is analysed on cylindrical blade-to-blade surfaces at several spanwise positions and on meridional planes, usually on only one average or mid-pitch meridional plane. These surfaces are not generally streamsurfaces but, since the importance of S_1 and S_2 in Wu's General Theory, they are still referred to as S_1 and S_2 surfaces.

According to Denton [22], the S2 solution, also known as hub to tip or throughflow, has become the backbone of turbomachinery design. Starting from the end of the 1960s, the throughflow methods began to replace the Simple Radial Equilibrium

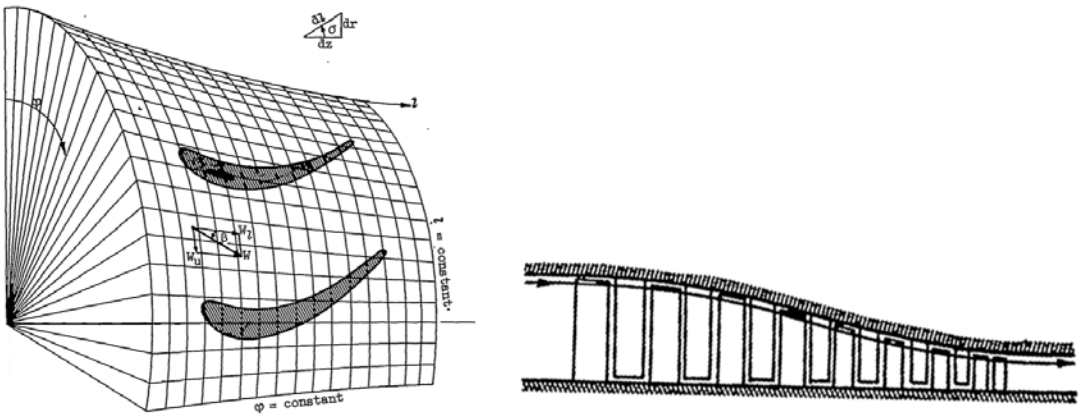

Figure 2.17: Conventional description of flow in compressors on blade-to-blade surface of revolution and on meridional plane (obtained and modified from Wu, 1952).

calculations. The throughflow methods used at that time consisted of the Streamline Curvature method and the Stream Function method. This age represents also the beginning of the use of the Computational Fluid Dynamics in the turbomachinery design.

2.2.3 Throughflow on the meridional plane

As pointed out by Marsh [60], there are several methods for predicting the flow through a turbomachine and the throughflow analysis can provide information about the overall flow pattern without including the effects of viscosity or time-dependent flows. The theory is based on the earlier work of Wu [90] and the throughflow analysis can be regarded as a simplified form of the General Theory for the flow through an arbitrary turbomachine. In the General Theory, the equations of fluid motion are satisfied on two intersecting families of streamsurfaces, S_1 and S_2, the complete solution for the three-dimensional flow field being obtained Iterating between the flows on the two sets of surfaces. In all of the analysis, the flow relative to each blade row is assumed to be steady, even if the flow and gas state at exit from a blade row vary circumferentially and the following blade row is then subject to a time-dependent inlet flow. The general method of analysis is therefore only applicable to the flow through an isolated blade row, or impeller channel, and even for these simple cases, the flow within the blade passage can only be estimated after specifying either the flow direction far downstream, or details of the flow at the trailing edge of the blades. The theory is general in the mathematical sense that it is a general method for estimating a steady three-dimensional flow by calculating the flow on the two sets of streamsurfaces. In order to apply the General Theory to estimate the flow through a multi-stage turbomachine, it would be necessary to remove the time dependence by circumferentially averaging the flow and the gas state between each pair of blade rows.

The throughflow theory is similar to the General Theory, but the equations of fluid motion are only solved for the steady inviscid flow on a mean streamsurface, and the blade thickness is still taken account of in that it affects the thickness of this surface. The flow and gas state on this surface may be regarded as average values for the flow

within the blade passage, a reasonable approximation when there are many blades. For a multi-stage turbomachine, the time dependence of the flow is removed by treating the throughflow solution as an axisymmetric flow for the duct region between each pair of blade rows.

The throughflow analysis for an isolated blade row does not require an assumption of axial symmetry. However, if axial symmetry is assumed, then the predicted flow pattern is the same as that which is obtained from the throughflow analysis for the flow on the mean streamsurface. The advantage in not assuming axial symmetry is that the throughflow analysis can then be seen to be the first stage in the General Theory and for an isolated blade row, or impeller, it is possible to continue the calculation to obtain the full three-dimensional flow field predicted by the General Theory.

There is, however, an important difference between the throughflow and axially symmetric solutions. As stated by Wu [90], if axial symmetry is assumed and a body force introduced, then differentiating and combining the velocity components does not give the true vorticity. A close examination of the assumption of axial symmetry shows that this is equivalent to replacing the blade row by an actuator duct where there are no blades, but the fluid is made to follow a certain surface by the application of a distributed body force. For a conducting fluid, this body force could be obtained by a magnetic field acting on a current flowing in the fluid. The assumption of axial symmetry is equivalent to forming an actuator duct model for the blade row and the inconsistency in calculating the vorticity arises from the use of the actuator duct model to represent the flow within the blade row. According to Marsh [60], the throughflow analysis avoids this inconsistency by solving for the flow on the mean streamsurface and by not assuming axial symmetry. However, the same flow pattern is obtained by assuming axial symmetry, or by solving for the flow on the mean streamsurface and then treating this as an axisymmetric solution. The same solution is obtained irrespective of whether the assumption of axial symmetry is made before or after the equations are solved. The throughflow analysis only estimates the flow on the mean streamsurface and the inconsistency in the calculation of vorticity is introduced by interpreting the solution as if it were axisymmetric.

As noted by Frost [30], the aim in the hub-to-tip problem is to solve for the flow only on a meridional surface S_2 of the turbomachine. There is normally a single surface extending from the hub to the casing, but there can be more. In the former case, the surface can be a streamsurface so that in a given blade passage half the flow is on one side of it and half on the other, as did Novak and Hearsey [62], or it can be a circumferential averaged surface, as in the model of Horlock and Marsh [42]. The errors involved in using these assumptions are acceptably small if compared to those attributable to viscous effects. Outside the blades, however, the loss-free flow would rapidly return to the axisymmetric condition and the different methods of averaging the flow all become equivalent.

According to Cumpsty [19], the model generally adopted is that the flow is uniform in the circumferential direction, i. e. for any generic fluid property Θ is $\partial\Theta/\partial\theta = 0$. Since blade forces in the tangential direction must be allowed, requiring thus tangential pressure gradients, putting $\partial p/\partial\theta = 0$ is equivalent to assuming an infinite number of blades, so that over the infinitesimal thickness oh the hub-casing surface the variation

with θ across the blade pitch is averaged out. The result is a mean streamsurface from hub to casing on which, at a given axial and radial position, the velocity components are all equal to their circumferential average. The solution is obtained after projecting the velocities onto the meridional plane $z - r$, which includes the axial and radial coordinates and is normal to the circumferential direction.

As noted by Denton [22], loss and deviation correlations remain an essential part of any throughflow method, in fact the method may be thought of as a means of applying the correlations to a non-uniform flow. The accuracy of the results is determined more by the accuracy of the correlations than by that of the numerical method. In the 1980s new correlations were developed by Craig & Cox, Dunham & Came, Howell & Calvert, and, despite these improvements correlations remain of very limited accuracy when applied to machines significantly different from those from which they were developed, preliminary design methods are still based on such correlations.

There are several methods for calculating the flow on the meridional surface, such as the Streamline Curvature method, developed in the United States of America by Novak and Smith and in the United Kingdom by Silvester and Hetherington of Rolls Royce and the National Gas Turbine Establishment (NGTE), which is surely the most widely used, and the Matrix-Streamfunction method.

According to Frost [30], the Streamline Curvature method, aimed at calculating the flow on a meridional plane right across the annulus, initially provided a solution which was still restricted to the duct regions. However, Marsh, in his Matrix-Streamfunction method [60], was able to extend the calculations within the blade rows by means of the specification of a meridional stream surface. This method employs a finite-difference technique rather than a streamline curvature approach for solving the equations and is restricted to subsonic relative flow within the blade rows. This is because, as stated by Denton [21], fir any streamfunction distribution there exist two possible velocity fields, and there is no a priori way of deciding which solution should be chosen. In the same way, it is possible to adapt the Streamline Curvature method so as to be able to calculate the flow within blade rows, by introducing the concept of a meridional stream surface. Since the two throughflow methods solve the same equations and make the same assumptions, the results obtained from them should be the same, but the Streamline Curvature Throughflow method is, in theory, capable of obtaining supersonic solutions with the restriction that the meridional Mach number should not exceed unity anywhere in the turbomachine. Also, the Streamline Curvature method requires far less computer storage than does the Matrix-Streamfunction method.

Therefore, though the initial rivalry between these two approaches, the Streamline Curvature method has become dominant in the 1970s, mainly through its relative simplicity and its superior ability to deal with supersonic flows.

Streamline Curvature method

The basic theory of Streamline Curvature (SLC) throughflow calculations has been described by many authors, particularly by Novak and Hearsey [62]. The basis of all throughflow methods is to obtain a solution for an axisymmetric flow and this may be regarded as being obtained by circumferentially averaging all flow properties or by solving for the flow on a mean blade-to-blade streamsurface whose thickness and inclinations are determined by the geometry of the blade rows, the same set of equations being achieved in both ways, as reported by Denton [21].

From the assumption of axial symmetry it is possible to define a series of meridional streamsurfaces as surfaces of revolution along which the fluid particles are assumed to move through the machine. The principle of Streamline Curvature method is to write the equations of motion along lines, known as quasi-orthogonals QOs, that are roughly perpendicular to these streamsurfaces, in term of the curvature of the surfaces in the meridional plane.

What is required is an equation for pressure or any equivalent property gradients in the spanwise direction. This may be obtained from the equations of motion as described by Korpela [50]. The approach adopted here is that given by Denton [21], which emphasizes the physical basis, showing a wide range of applicability for several geometries.

The acceleration of a fluid particle is given by

$$\vec{a} = \frac{\partial \vec{V}}{\partial t} + \vec{V} \cdot \nabla \vec{V}$$

in which the partial derivative term vanishes in steady flow, while the second term represents the spatial acceleration of the flow. In cylindrical coordinates the gradient operator for a generic flow property Θ can be written as

$$\nabla \Theta = \hat{\mathrm{e}}_z \, \frac{\partial \Theta}{\partial z} + \frac{\hat{\mathrm{e}}_\theta}{r} \, \frac{\partial \Theta}{\partial \theta} + \hat{\mathrm{e}}_r \, \frac{\partial \Theta}{\partial r}$$

The meridional velocity component is defined as

$$\vec{V}_m = V_m \, \hat{\mathrm{e}}_m = V_z \, \hat{\mathrm{e}}_z + V_r \, \hat{\mathrm{e}}_r$$

and the velocity vector can hence be written also as

$$\vec{V} = V_z \, \hat{\mathrm{e}}_z + V_\theta \, \hat{\mathrm{e}}_\theta + V_r \, \hat{\mathrm{e}}_r = V_m \, \hat{\mathrm{e}}_m + V_\theta \, \hat{\mathrm{e}}_\theta$$

The scalar product of the unit vector in the meridional direction on the meridional plane and the gradient operator gives the directional derivative in the direction of the unit vector

$$\hat{\mathrm{e}}_m \cdot \nabla \Theta = \frac{\partial \Theta}{\partial m} = (\hat{\mathrm{e}}_m \cdot \hat{\mathrm{e}}_z) \, \frac{\partial \Theta}{\partial z} + (\hat{\mathrm{e}}_m \cdot \hat{\mathrm{e}}_r) \, \frac{\partial \Theta}{\partial r}$$

the term in the tangential direction being dropped out because the unit vector $\hat{\mathrm{e}}_m$ is orthogonal to $\hat{\mathrm{e}}_\theta$.

The angle between the directions of $\hat{\mathrm{e}}_m$ and $\hat{\mathrm{e}}_z$, known as meridional pitch angle, is denoted by ϕ, and the partial derivatives in terms of this angle are given by

$$\frac{\partial \Theta}{\partial m} = \cos\phi \, \frac{\partial \Theta}{\partial z} + \sin\phi \, \frac{\partial \Theta}{\partial r}$$

and the gradient operator is

$$\nabla\Theta = \hat{\mathrm{e}}_m \, \frac{\partial \Theta}{\partial m} + \frac{\hat{\mathrm{e}}_\theta}{r} \, \frac{\partial \Theta}{\partial \theta}$$

The acceleration of a fluid particle can now be expressed as

$$\vec{a} = (V_m \, \hat{\mathrm{e}}_m + V_\theta \, \hat{\mathrm{e}}_\theta) \cdot \left(\hat{\mathrm{e}}_m \, \frac{\partial}{\partial m} + \frac{\hat{\mathrm{e}}_\theta}{r} \, \frac{\partial}{\partial \theta} \right) (V_m \, \hat{\mathrm{e}}_m + V_\theta \, \hat{\mathrm{e}}_\theta)$$

which leads to

$$\vec{a} = V_m \, \frac{\partial}{\partial m} \, (V_m \, \hat{\mathrm{e}}_m + V_\theta \, \hat{\mathrm{e}}_\theta) + \frac{V_\theta}{r} \, \frac{\partial}{\partial \theta} (V_m \, \hat{\mathrm{e}}_m + V_\theta \, \hat{\mathrm{e}}_\theta)$$

and after rearrangements

$$\vec{a} = \hat{\mathrm{e}}_m \, V_m \, \frac{\partial V_m}{\partial m} - \hat{\mathrm{e}}_n \, \frac{V_m^2}{r_c} + \hat{\mathrm{e}}_\theta \, V_m \, \frac{\partial V_\theta}{\partial m} - \hat{\mathrm{e}}_r \, \frac{V_\theta^2}{r}$$

where

$$\frac{\partial \hat{\mathrm{e}}_m}{\partial m} = -\frac{\hat{\mathrm{e}}_n}{r_c} \qquad \frac{\partial \hat{\mathrm{e}}_m}{\partial \theta} = 0 \qquad \frac{\partial \hat{\mathrm{e}}_\theta}{\partial m} = 0 \qquad \frac{\partial \hat{\mathrm{e}}_\theta}{\partial \theta} = -\hat{\mathrm{e}}_r$$

$r_c = \partial m / \partial \phi$ is the radius of curvature of a streamline on the meridional plane and it is taken as positive when the streamline is concave away from the z axis. The direction of the unit vector $\hat{\mathrm{e}}_n$, which lies in the mean hub-casing streamsurface inclined to the radial at an angle ϵ, known as angle of lean, is perpendicular to the direction of vector $\hat{\mathrm{e}}_m$ on the meridional plane in such a way that $(\hat{\mathrm{e}}_n, \, \hat{\mathrm{e}}_\theta, \, \hat{\mathrm{e}}_m)$ form a right-handed triple. This was obtained by rotation by the angle ϕ about the axis of $\hat{\mathrm{e}}_\theta$, hence the n direction coincides with the radial direction and the m direction coincides with the axial direction when $\phi = 0$, as shown in Figs 2.18 and 2.19.

In the view of the meridional plane, as reported in Fig 2.18, a streamline can be seen as projection of a streamsurface on the meridional plane itself. The local tangent is given by the unit vector $\hat{\mathrm{e}}_m$ and the normal to the streamline in the meridional surface is given by $\hat{\mathrm{e}}_n$, as illustrated in Fig 2.19. The angle of lean ϵ, with the flow taken as uniform in the θ direction, will be the local inclination of the blade camber line to the radial, and will not normally be constant with radius although it will be generally small.

Since attempts to work with the true normal to the streamlines get into difficulties because the directions are not known in advance, changing as the calculation progresses, consider next a direction specified by the unit vector $\hat{\mathrm{e}}_q$, lying on the meridional plane. This represents the so-called quasi-orthogonal, whose direction is chosen in advance roughly perpendicular to the streamlines and does not change during the

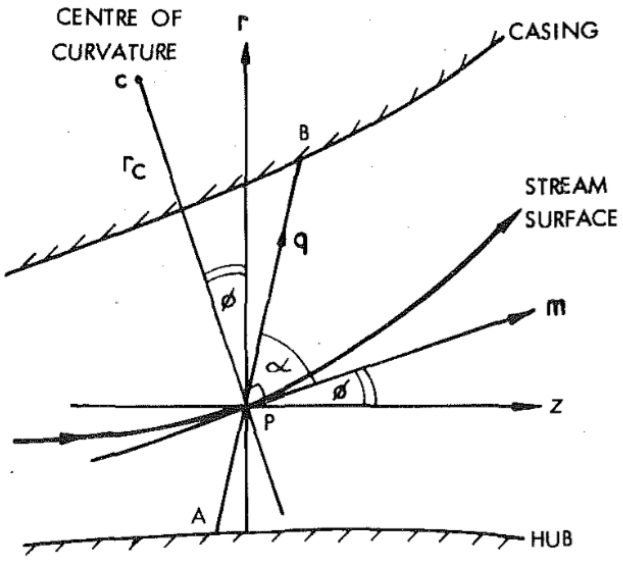

Figure 2.18: Streamline Curvature method coordinate system (obtained and modified from Denton, 1978).

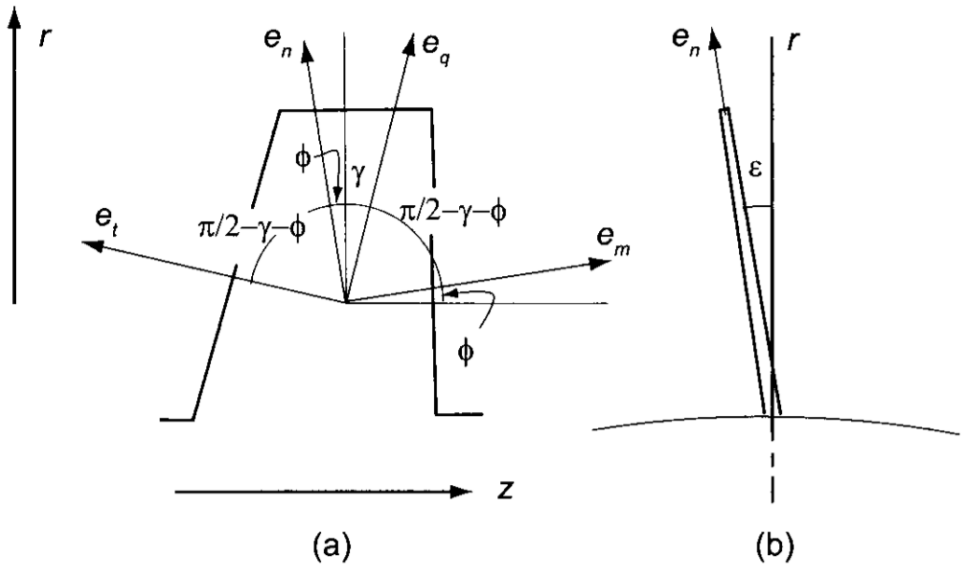

Figure 2.19: Geometry on a quasi-orthogonal (obtained from Korpela, 2011). (a) Unit vectors on meridional plane, (b) Angle of lean in a view along the axis.

calculation. $\hat{\mathrm{e}}_q$ is inclined to the radial direction by the angle γ, which is the sweep angle of the blade at its leading edge and is considered positive for a sweep toward the positive axial direction, so that for axial machines γ will be nearly zero. The angle between $\hat{\mathrm{e}}_q$ and the m direction is $\pi/2 - (\gamma + \phi)$, then the acceleration component in the $\hat{\mathrm{e}}_q$ direction is given by

$$a_q = (\hat{\mathrm{e}}_q \cdot \hat{\mathrm{e}}_m)\, V_m \frac{\partial V_m}{\partial m} - (\hat{\mathrm{e}}_q \cdot \hat{\mathrm{e}}_n)\, \frac{V_m^2}{r_c} + (\hat{\mathrm{e}}_q \cdot \hat{\mathrm{e}}_\theta)\, V_m \frac{\partial V_\theta}{\partial m} - (\hat{\mathrm{e}}_q \cdot \hat{\mathrm{e}}_r)\, \frac{V_\theta^2}{r}$$

that becomes

$$a_q = \sin(\gamma + \phi)\, V_m \frac{\partial V_m}{\partial m} - \cos(\gamma + \phi)\, \frac{V_m^2}{r_c} - \frac{V_\theta^2}{r}\, \cos\gamma \tag{2.2}$$

The acceleration of a fluid particle at point P of Fig 2.18 if formed of $V_m\, \partial V_m/\partial m$ in the m direction, which is the substantive acceleration in the direction of the flow; V_m^2/r_c in the n direction, being the centripetal acceleration generated from the flow following a path with radius of curvature r_c in the meridional plane; and $-V_\theta^2/r$ in the radial direction, which represents the centripetal acceleration due to the absolute swirl velocity included in the Simple Radial Equilibrium.

With the flow assumed to be axisymmetric, the differentials in the meridional plane are equal to those in the hub-casing surface, as noted by Cumpsty [19], but in more general calculation schemes this approximation could not be applied.

With respect to the magnitude of the terms of a_q, since the quasi-orthogonal direction is chosen approximately perpendicular to the meridional streamlines, the angle $(\gamma + \phi)$ will generally be small and, considering that turbomachine designers usually aim to keep the meridional velocity nearly constant, the first term of equation 2.2 can be neglected. The second term represents the component of acceleration in the q direction due to the curvature of the meridional streamline: the cosine will be near to unity and V_m will be of the same order of V_θ, but, nevertheless, in axial machines the radius of curvature r_c will generally be large, and the second term of a_q will be small, except for the front stages of low hub-casing ratio machines. For most axial compressors γ is very small and the last term of equation 2.2 can give a significant acceleration in the quasi-orthogonal direction. The magnitude of V_θ depends on the loading and the position in the machine, and is always larger downstream of rotors than stators. This third term is usually dominant for axial machines and represents the basis of the aforementioned Simple Radial Equilibrium method.

Next, let the unit vector $\hat{\mathrm{e}}_t$ denote a direction normal to $\hat{\mathrm{e}}_q$ on the meridional plane: the component of acceleration in this direction is

$$a_t = (\hat{\mathrm{e}}_t \cdot \hat{\mathrm{e}}_m)\, V_m \frac{\partial V_m}{\partial m} - (\hat{\mathrm{e}}_t \cdot \hat{\mathrm{e}}_n)\, \frac{V_m^2}{r_c} + (\hat{\mathrm{e}}_t \cdot \hat{\mathrm{e}}_\theta)\, V_m \frac{\partial V_\theta}{\partial m} - (\hat{\mathrm{e}}_t \cdot \hat{\mathrm{e}}_r)\, \frac{V_\theta^2}{r}$$

resulting in

$$a_t = \cos(\gamma + \phi)\, V_m \frac{\partial V_m}{\partial m} + \sin(\gamma + \phi)\, \frac{V_m^2}{r_c} - \frac{V_\theta^2}{r}\, \sin\gamma$$

Finally, the acceleration component in the tangential direction is given by

$$a_\theta = V_m \frac{\partial V_\theta}{\partial m}$$

If the blades lean at an angle ϵ from the meridional plane, in the direction opposite to θ, the acceleration components a_q and a_θ can be used to form new components that lie on the plane containing a blade with this lean angle. In order to attempt this, it is necessary a rotation of the surface about the axis containing the unit vector $\hat{\mathrm{e}}_t$. Let $\hat{\mathrm{e}}_e$ denote the unit vector obtained by rotating $\hat{\mathrm{e}}_q$ by angle ϵ counterclockwise: the acceleration component in the direction of $\hat{\mathrm{e}}_e$ is given by

$$a_e = (\hat{\mathrm{e}}_e \cdot \hat{\mathrm{e}}_q)\, a_q + (\hat{\mathrm{e}}_e \cdot \hat{\mathrm{e}}_\theta)\, a_\theta + (\hat{\mathrm{e}}_e \cdot \hat{\mathrm{e}}_t)\, a_t$$

which reduces to

$$a_e = a_q \, \cos\epsilon - a_\theta \, \sin\epsilon$$

The Euler vectorial equation for an inviscid flow is

$$\vec{a} = -\frac{1}{\rho} \nabla p + \frac{\vec{F}}{\rho}$$

and the components of acceleration in the directions $\hat{\mathrm{e}}_q$ and $\hat{\mathrm{e}}_e$ are respectively

$$a_q = -\frac{1}{\rho} \frac{\partial p}{\partial q} + \frac{F_q}{\rho} \qquad a_e = -\frac{1}{\rho} \frac{\partial p}{\partial e} + \frac{F_e}{\rho}$$

where the momentum equation applied in the streamsurface in the direction of $\hat{\mathrm{e}}_e$ is

$$-\frac{1}{\rho} \frac{\partial p}{\partial e} = a_q \, \cos\epsilon + a_\theta \, \sin\epsilon$$

so that, with $dq = de \, \cos\epsilon$, it results

$$-\frac{1}{\rho} \frac{\partial p}{\partial q} = a_q + a_\theta \, \tan\epsilon$$

The static pressure gradient is usually removed and replaced with gradients of enthalpy or entropy from the Second Law of Thermodynamics in the q direction

$$T \frac{\partial s}{\partial q} = \frac{\partial h}{\partial q} - \frac{1}{\rho} \frac{\partial p}{\partial q}$$

where the partial derivative of stagnation enthalpy

$$h_0 = h + \frac{1}{2} (V_m^2 + V_\theta^2)$$

in the q direction is

$$\frac{\partial h}{\partial q} = \frac{\partial h_0}{\partial q} - V_m \frac{\partial V_m}{\partial q} - V_\theta \frac{\partial V_\theta}{\partial q}$$

Using this expression for the pressure gradient results in

$$-\frac{1}{\rho}\frac{\partial p}{\partial q} = T\,\frac{\partial s}{\partial q} - \frac{\partial h_0}{\partial q} + V_m\,\frac{\partial V_m}{\partial q} + V_\theta\,\frac{\partial V_\theta}{\partial q}$$

that substituted into the equation for a_q gives

$$\sin(\gamma+\phi)\;V_m\,\frac{\partial V_m}{\partial m} - \cos(\gamma+\phi)\,\frac{V_m^2}{r_c} - V_m\,\frac{\partial V_m}{\partial q} =$$

$$T\,\frac{\partial s}{\partial q} - \frac{\partial h_0}{\partial q} + \frac{V_\theta^2}{r}\;\cos\gamma + V_\theta\,\frac{\partial V_\theta}{\partial q} + \frac{V_m}{r}\,\frac{\partial (rV_\theta)}{\partial m}\;\tan\epsilon$$

With $q = r/\cos\gamma$, the equation in its conventional form for gradients in the direction of the quasi-orthogonal in the meridional surface is therefore

$$\frac{1}{2}\,\frac{\partial V_m^2}{\partial q} = \frac{\partial h_0}{\partial q} - T\,\frac{\partial s}{\partial q} + \sin(\gamma+\phi)\;V_m\,\frac{\partial V_m}{\partial m} + \cos(\gamma+\phi)\,\frac{V_m^2}{r_c} + \tag{2.3}$$

$$-\frac{1}{2r^2}\,\frac{\partial (r^2V_\theta^2)}{\partial q} + \frac{V_m}{r}\,\frac{\partial (rV_\theta)}{\partial m}\;\tan\epsilon$$

This equation is called the Radial Equilibrium (RE) equation and represents the basis of all Streamline Curvature calculation methods, which take their name from the fourth term on the right hand side containing V_m^2/r_c.

The Radial Equilibrium equation, containing the term $V_m\,\partial V_m/\partial m$, must be solved in conjunction with the continuity equation along a streamtube:

$$\int_{hub}^{casing} \rho\,V_m\;\cos(\gamma+\phi)\;w\;dq = \frac{\dot{m}}{N} \tag{2.4}$$

where $\dot{m}$ is the total mass flow rate, N the number of blades and $w = 2\pi rB/N$ the streamsurface thickness, with B a measure of the blockage that would be equal to unity in an ideal flow. B is strongly affected by the boundary layer displacement on the annulus walls and blades, and is also reduced if the flow is not uniform in the circumferential direction θ.

According to Denton [21], in duct regions the distributions of total enthalpy, entropy, and angular momentum along the quasi-orthogonals is obtained from the conservation of these quantities along streamsurfaces. Within blade rows V_θ can be obtained from V_m, from the imposed flow directions and blade rotation, and from the blade geometry using correlations or blade-to-blade calculations. In stationary blade passages or outside blade rows the stagnation enthalpy h_0 is conserved along streamlines and can be calculated from the Euler equation, in moving blades it is the rothalpy $I = h + W^2/2 + U^2/2$ which is conserved. Entropy changes can be obtained from empirical loss correlations. The fluid density, needed when applying equation 2.4, may be obtained from the equation of state of the fluid once the enthalpy and entropy have been determined.

The Streamline Curvature method is an iterative approach for the flow field, starting from an initial guess of streamsurface shape. This guess estimates the streamline curvature terms in equation 2.3, $\sin(\gamma+\phi)\;V_m\,\partial V_m/\partial m$ and $\cos(\gamma+\phi)\;V_m^2/r_c$. Starting

at the first quasi-orthogonal, equations 2.3 and 2.4 are solved to give a new distribution of V_m and hence, by interpolation, new points of intersection of the streamsurfaces with the quasi-orthogonal. This procedure is repeated at each quasi-orthogonal in turn until a new streamsurface pattern is obtained for the whole machine. The streamline curvature terms of equation 2.3, $\sin(\gamma + \phi)\ V_m\ \partial V_m/\partial m$ and $\cos(\gamma + \phi)\ V_m^2/r_c$, can then be updated together with the meridional pitch angle ϕ, and the next iteration commenced using these updated values.

The procedure is algebraically quite involved and it is also usual, as did Novak and Hearsey [62], to express the cosine term of the Radial Equilibrium equation in terms of the rate of divergence of the streamsurfaces and the local meridional Mach number, introducing considerable additional complexity into the equation and producing a singularity when $Ma_m \rightarrow 1$. It is not obviously more accurate than the much simpler process of evaluating $\partial V_m/\partial m$ from the previous iteration and using it directly; moreover this procedure also avoids the singularity.

A further departure from convention comes from using equation 2.3 in unchanged form within blade rows, resulting in simpler equations and programming: it is more usual to recast the equation using the fact that within a blade row V_θ is determined by V_m and the blade angles. Moreover, there are stability constraints and the streamline shape must only be adapted by a small fraction of its predicted change for each iteration: the changes in the curvature terms and in ϕ must be damped by a relaxation factor which gets smaller as the Mach number rises and as the distance between quasi-orthogonals is reduced in relation to the distance between hub and casing. Wilkinson [88] proved that the optimum relaxation factor is given by

$$R = \frac{1}{1 + k\ GA^2\ (1 - Ma_m^2)}$$

where k is about 0.2 and GA denotes the grid aspect ratio, defined as the distance between hub and casing divided by the distance between quasi-orthogonals.

The method of solving the Streamline Curvature equation is rather specialized and here an example is illustrated, as reported by Cumpsty [19].

The Streamline Curvature method in analysis mode is applied to the meridional plane with information given about the blade angles, the starting point being a view of the meridional plane. The sequence is as follows:

1. choose quasi-orthogonals positions;

2. guess streamlines shape in meridional plane and evaluate the streamline curvature and streamtube contraction at intersections with quasi-orthogonals;

3. guess meridional velocity V_m at each intersection of quasi-orthogonal and streamline, and guess flow properties along the first quasi-orthogonal;

4. use blade-to-blade calculation or correlation with specified geometry and flow properties estimates to calculate flow outlet direction and loss, then calculate V_θ and p_0 along the quasi-orthogonal;

5. evaluate terms on the right hand side of Streamline Curvature equation 2.3 starting from the first quasi-orthogonal, using current estimate for shape of meridional streamlines;

6. integrate $\partial V_m^2/\partial q$ along the quasi-orthogonal to get V_m with an arbitrary or guessed constant

7. calculate overall mass flow rate from continuity equation 2.4 and adjust constant in predicted V_m distribution to get prescribed overall mass flow, then return to 6 unless no adjustment needed, in which case go to 8;

8. integrate V_m to find new locations of meridional streamlines along the quasi-orthogonal for correct mass flow between them and store this information;

9. move to next quasi-orthogonal and repeat steps 4 to 8, then after last quasi-orthogonal go to 10;

10. allow intersection of streamlines with quasi-orthogonals to move towards new position stored in step 8 but use relaxation factor to ensure stability, obtaining new streamline shape and curvature;

11. go to 5 unless movement required of streamlines is less than a convergence threshold, i. e. meridional solution is converged, in which case go to 12;

12. print out results.

As an alternative, from step 11 the calculation could return to step 4 and recalculate the blade-to-blade flow with the improved estimate for the meridional flow.

The method is extremely sensitive to the shape of hub and casing, whose surfaces used in the calculation should be smoothly curved in the meridional plane, even if the actual compressor fas significant discontinuities of radius or curvature. There then can be problems when the meridional curvature of the endwalls is large.

Alternative throughflow methods

Another method for the solution of an inviscid flow on the meridional plane involves the so-called streamfunctions. A streamfunction ψ is defined by

$$\frac{\partial \psi}{\partial p} = -r\ \rho\ B\ V_q \qquad \frac{\partial \psi}{\partial q} = r\ \rho\ B\ V_p \tag{2.5}$$

where p is the normal to the quasi-orthogonal in the direction of the flow and B is the aforementioned blockage factor.

The pressure gradient in the direction of the quasi-orthogonal is still given by

$$-\frac{1}{\rho}\frac{\partial p}{\partial q} = a_q + a_\theta\ \tan\epsilon$$

and the acceleration components in the q and θ direction are now conveniently written as

$$a_q = V_q \frac{\partial V_q}{\partial q} + V_p \frac{\partial V_q}{\partial p} - \frac{V_\theta^2}{r} \cos\gamma$$

$$a_\theta = \frac{V_m}{r} \frac{\partial (r V_\theta)}{\partial m}$$

Substituting the static pressure with the stagnation enthalpy and entropy, and using the streamfunction defined in equation 2.5 results

$$\frac{\partial^2 \psi}{\partial p^2} + \frac{\partial^2 \psi}{\partial q^2} = \frac{\partial \psi}{\partial p} \frac{\partial \ln(\rho\, r B)}{\partial p} + \frac{\partial \psi}{\partial q} \frac{\partial \ln(\rho\, r B)}{\partial q} + \tag{2.6}$$

$$+ \frac{\rho\, r B}{V_p} \left\{ \frac{\partial h_0}{\partial q} - T \frac{\partial s}{\partial q} - \frac{V_\theta}{r} \frac{\partial (r V_\theta)}{\partial q} + a_\theta \tan\epsilon \right\}$$

This is the Streamfunction equation and represents the basis of the Matrix-Streamfunction method. Equation 2.6 is usually solved in an iterative way, with the right hand side terms evaluated from an initial guess or the previous estimate. Marsh [60] solved the Streamfunction equation by a matrix inversion, and this is the reason why this flow calculation approach is referred to as Matrix-Streamfunction method.

As stated by Cumpsty [19], there appears to be little relative advantage and indeed no fluid mechanical difference between the Streamline Curvature and the Matrix-Streamline throughflow methods. The Streamline Curvature method resulted the most popular since its intuitive meaning of the terms in the equations, and its capability to deal with supersonic flows. The Matrix-Streamfunction method is inherently less satisfactory when the resultant Mach number is close to unity because because, the Mach number being two-valued for a particular streamfunction, there is no an a priori way to decide which Mach number value is to be chosen, either the one less than unity or the other greater; the Matrix-Streamfunction method therefore fails when the flow becomes even locally supersonic. In duct regions, i. e. outside the blade rows, the meridional Mach number normally remains below unity, but inside the blade passages the local relative Mach number often exceeds unity for axial-flow compressors. The Streamline Curvature method, considering continuity across the whole annulus, allows small patches of supersonic flow fairly easily.

Alternative methods for the calculations of the flow on the hub-casing surface have been developed in the late 1970s. One example is the Finite Element solution to the streamfunction developed by Hirsch and Warzee [40].

Another approach, representing a more significant departure from usual calculation strategies, is Spurr's Time-Marching method [75]. This last technique allows calculations in flow with regions of subsonic and supersonic flow without the customary restrictions. According to Denton [22], Time-Marching solutions were initially much slower but also able to cope with high Mach numbers and to capture shock waves, becoming then the dominant method. This type of approach was used to develop controlled diffusion blading for axial compressors, giving significant improvements in performance: although transonic compressors were initially designed without any

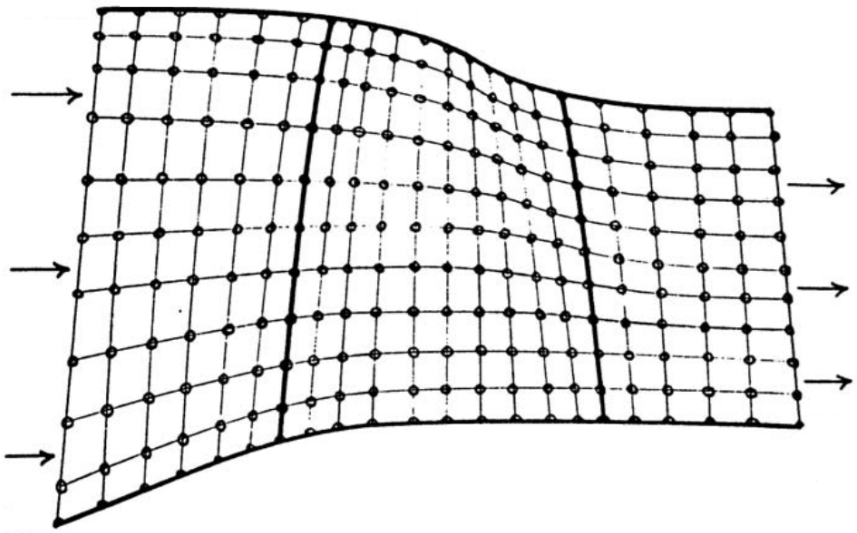

Figure 2.20: A typical coarse grid for early 3-D calculations (obtained and modified from Denton, 2009).

flow calculation methods, the Time-Marching method allowed their design to be put on a much more sound footing, especially when the solution had been extended to fully 3-D flow. Initially the available computers only allowed coarse grid solutions, typically 4000 (10 x 40 x 10) grid points, as represented in Fig 2.20: even though this seriously limited their accuracy, the 3-D methods soon led to improved physical understanding of 3-D effects, such as blade sweep and blade lean. In particular it was discovered that blade lean could have an extremely significant effect on the flow, which was neglected by previous methods.

As noted by Cumpsty [19], throughflow calculations have been routine tools for the design and analysis of axial-flow compressor for quite some time. These methods usually rely on the assumption of axial symmetry, developing as a useful tool, though its intrinsic approximations. If the approximations are unsatisfactory there are now more precise numerical approaches, analysing the flow using three-dimensional viscous procedure such as CFD. Throughflow assumptions and methods represent a good deal between calculation time and computational costs compared to the full three-dimensional solution strategies, a reason why Streamline Curvature methods, combined with blade-to-blade calculations, continued to receive refinements. The refinements offer some significant corrections for turbomachines with strong curvature in the meridional plane and large deflection near the hub, while the annulus boundary layer has a sufficiently small effect that it does not represent the major source of inaccuracies. In most cases it appears evident that the largest inaccuracies in describing the flow with a surface of revolution for the blade-to-blade flow and a meridional plane for the throughflow are not generated from errors in the averaging method, which takes account of variations

in the circumferential direction, or by neglecting the streamsurface distortion: it is errors in the prediction of flow turning by the blades, the presence of regions of high loss and low velocities near the solid surfaces, that is boundary layers, and spanwise mixing which are of most concern. Spanwise mixing, in particular, will be the main argument of section 2.3.

2.2.4 Recent developments

The most widespread throughflow method is certainly the Streamline Curvature method, which is based on the normal equilibrium and gets its name from the inclusion of the flow curvature effect in the meridional plane. The traditional Streamline Curvature formulation for the governing momentum equations is a first-order velocity gradient representation, one in the radial and one in the tangential direction.

It is generally accepted that any Streamline Curvature solution technique will yield satisfactory flow solutions as long as the deviation, losses, and blockage are accurately predicted. Accurate prediction of the deviation angle δ is essential to predict the correct flow turning and resulting blade work distribution. Clearly, blockage can change the distribution of flow through a blade row, some accounting for its effect being needed. In addition to the profile loss and the effects of other loss sources must be included for accurate performance estimation. Excellent reviews of loss mechanisms in turbomachines and their representation are provided by Bloch and by Denton in [5].

Denton and Dawes [23] reviewed the Streamline Curvature approach, suggesting that little has changed since the review of Hirsch and Denton in 1981 [39] because of the focus on and success of full CFD methods made possible by advancements in computational power. However, they pointed out the need of reliable correlations, in order to predict the general trend regarding the influence of parameters of interest, in particular the Mach number, especially for off-design conditions. Cetin et al. [17] reviewed loss and deviation correlations relative to transonic axial compressors, but there was still the need for a consistent endwall boundary layer and secondary loss calculation method, and spanwise loss mixing procedures for more accurate predictions.

Throughflow calculations still rely heavily on empirical estimates of loss, deviation, and blockage in compressor endwall regions. To compute these explicitly Dunham [29] developed an analytically based endwall model using both annulus wall boundary layer theory and secondary flow theory, and incorporated the model into a Streamline Curvature program, applying it to low-speed and high-speed multistage compressors to predict overall performance and radial distributions for both on and off-design conditions. He attributed the performance differences with measurements to excessively thick predicted casing boundary layers in the 3^{rd} and 4^{th} stages, which gave rise to exaggerated deviation estimates in the throughflow and hence an enthalpy rise that was too low. Further, Dunham's model could not handle endwall corner stall, whose the prediction remained elusive.

Bloch et al. in [5] developed a physics-based shock loss model, including influence of operating conditions, estimation of choking incidence, detached bow shock model, for supersonic compressor cascades of arbitrary shape over the entire operating range, showing that shock loss is much more sensitive to inlet Mach number than is profile

loss. Further, they concluded that the dramatic increase in overall loss with increasing flow angle results from increasing shock loss, much of this due to a detached bow shock.

Perhaps one of the most sophisticated development of throughflow methods is the approach presented by Gallimore [33], who extended the previous axisymmetric viscous model presented in [43] by including a novel approach using tangential blade forces to calculate the extra loss and deviation associated with tip clearance and endwall flows. Gallimore combined this with the standard approach of using 2-D blade performance predictions for loss and deviation away from the annulus walls, producing realistic results of accuracy comparable to those from viscous CFD calculations.

In 1980, Spurr [75] has proposed another approach to compute the meridional flow field based on the Euler equations. This approach has only started to retain attention at in the 1990s.

As an example of this novel use of a Streamline Curvature model, Hale et al. [38] developed a 3-D, unsteady, compressible numerical approximation which has been used to study inlet distortion effects on various compression systems. They used a fixed grid to solve the 3-D Euler equations throughout the computational domain, with turbomachinery source terms provided by application of a Streamline Curvature code across each blade row. In their work Hale et al. applied the computational grid into and through the blade row, and allowed time-dependent radial variation of the streamlines through the bladed region.

According to Simon [74], the methods based on the Euler equations present some interesting features and remove some of the drawbacks of the Streamline Curvature approach, such as the difficulty capturing shock. Euler equations are built so as to capture shock features, with the mass flow rate as a result of the computation, allowing to capture the choke mass flow. Furthermore, the generally adopted Time-Marching techniques to solve these equations bring a natural unsteady capability of the developed solvers.

A drawback of the throughflow model based on the Streamline Curvature method as well as of the Euler throughflow model is the treatment of the annulus endwalls which is inherently inviscid with a slip condition along the walls: this represents the major concern with throughflow models. As discussed above, it is common practice to introduce an aerodynamic blockage B, equivalent to the displacement thickness of the annulus endwalls boundary layers, as correction for the mass flow in order to obtain the right level of velocity in the core flow. The blockage factor is a very sensitive quantity relying on empiricism and, if the aerodynamic blockage level is mispredicted, the compressor will be mismatched, some stages not working at their design condition for the overall compressor design point. This can lead to reduce the efficiency, the stall margin, and hence compressor performance. Another solution is to include the effect of the viscous flow on the annulus endwall in an inviscid computation in conjunction to a separate boundary layer calculation. However, it is now recognised that the use of the boundary layer theory for computing the endwall flows inside a compressor is inappropriate, as pointed out by Cumpsty [19] and Horlock & Denton [41].

Simon [74] in his dissertation brought a third solution with a throughflow model

directly based on the Navier-Stokes equations, which is able to resolve the viscous flow on the annulus endwalls, computing the flow blockage in a direct way. Furthermore, this method is able to capture 2-D recirculations.

Simon moved toward a less empiricism dependent throughflow, using high order throughflow method based on Adamczyk's cascade averaging procedure [2]. There are several methods for obtaining an unsteady flow field at a lower cost than a 3-D unsteady simulation over full annulus including all blade passages, namely the domain scaling, the phase-lagged and the harmonic methods. Another approach, also based on the average-passage model devised by Adamczyk [2], can obtain a mean representation of the unsteady flow, resulting in a steady flow field which contains the averaged effect of the unsteadiness.

Adamczyk addresses the 3-D unsteady and turbulent flow field through several averaging operations. The first one is the well known Reynolds-averaging, which eliminates the effect of the turbulence, leaving a deterministic unsteady flow. The second one is a time-averaging procedure, removing the remaining effect of unsteadiness due to the rotation of the rotor blades against the stator blades. The last average eliminates the aperiodicity of the flow generated from the blade indexing, i. e. relative circumferential position of blade rows placed on the same shaft. The resulting flow field is steady and periodic but contains the mean effects of turbulence, unsteadiness and aperiodicity altogether.

The equations associated to this flow show the Reynolds stresses, the deterministic stresses, the passage-to-passage stresses and the blade forces, which are all unknowns bringing the aforementioned effects. These equations, which have been rigorously obtained, are the average-passage equations of Adamczyk and describe the steady flow field inside a blade row embedded in a multistage configuration. Simon improved the previous model by circumferentially averaging the average-passage equations in order to obtain an axisymmetric representation of the flow. The equations are also rigorously obtained and contain now the effect of non-axial symmetry of the flow through circumferential stresses and blade forces. This set of equations represents the ultimate throughflow model which is obtained with no other assumptions that the ones prevailing to the establishment of the Navier-Stokes equations.

2.3 Spanwise mixing

2.3.1 Introduction

According to Hah [36], flow mixing is an important aspect of compressor aerodynamic performance, which became a topic of increasing interest in the last decades of the 20^{th} century. In those years, conventional turbomachinery design techniques used for meridional flow normally idealized the flow as lying along surfaces of revolution in an axisymmetric frame of reference, that is a stream sheet. Moreover, the flow was considered as inviscid and non-conducting. Blade designs were formulated based on the presumed velocity distributions at the blade passage inlet and exit for each stream sheet. These assumptions often led to serious errors which were compensated for in

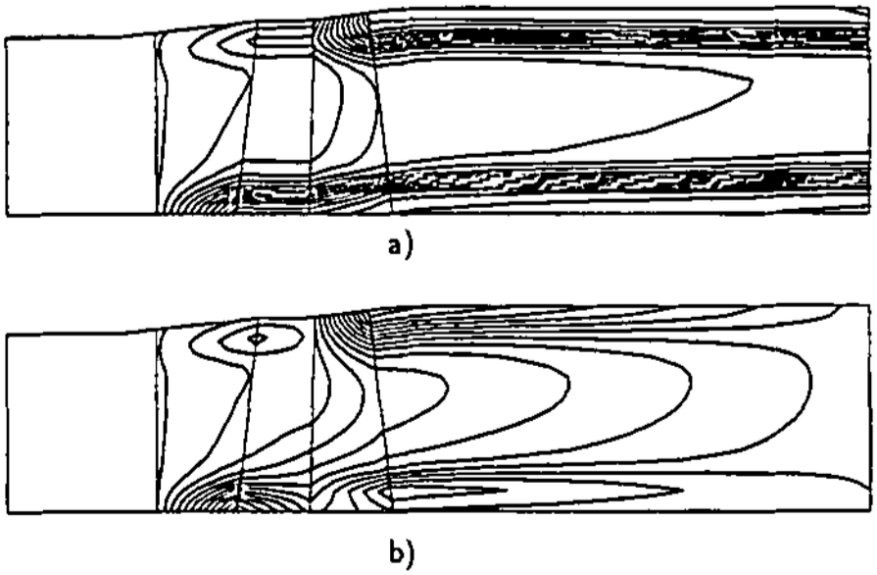

Figure 2.21: Entropy distribution in a single-stage turbine at design load (obtained from Petrovic & Riess, 1997). a) Calculation without spanwise mixing model, b) Calculation applying spanwise mixing model.

an approximate manner, but, unfortunately, the compensation to correct one variable generated inconsistencies in another.

As mentioned by Cumpsty [19], in order to get satisfactory predictions in multi-stage compressors using throughflow calculation methods, it was necessary to include loss estimates. Since little was known of loss mechanisms in three dimensions, an estimate had to be made for endwall losses, profile losses and corner losses so that the total loss adds up to a value to give reasonable agreement with the overall measured performance.

Endwall and corner losses, which contain many different mechanisms, make up most of the loss and could not be neglected, but, if a realistic radial distribution of the loss was adopted, the inviscid throughflow analysis would fail numerically if several stages were calculated. To avoid this problem, the loss were then spread out radially, pretending that the profile loss near mid-span was much higher than is realistic, and, consequently, that the loss was lower near the endwalls. With this expedient the stagnation pressure distribution might be reasonably well predicted, but stagnation temperature showed a quite erroneous trend.

On the other hand, it has been found that when stagnation pressure and stagnation temperature measurement were analysed using throughflow methods, the predicted loss near mid-span seemed unreasonably high, sometimes exceeding the loss near the endwalls, where the loss was occasionally even inferred to be negative from measurements.

A similar issue also appeared in the case of turbines. Throughflow calculations relating to realistic model of radial loss distribution showed unreal accumulations of entropy increases in endwall regions, as depicted in Fig 2.21.

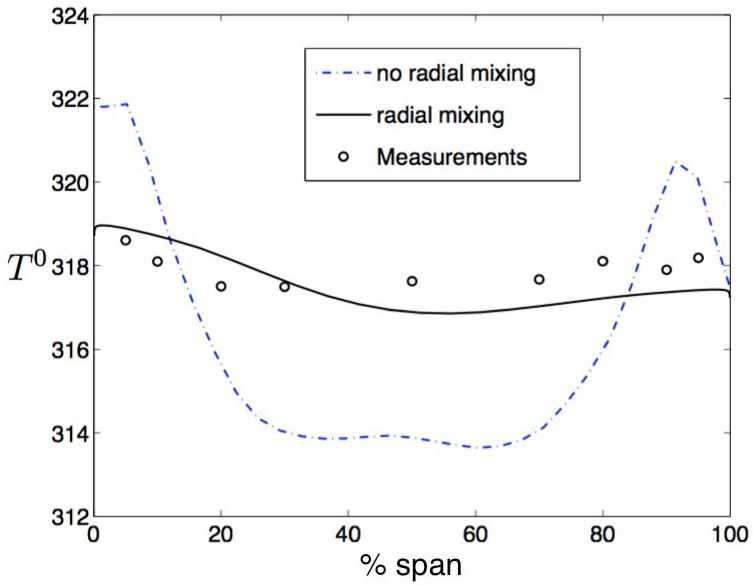

Figure 2.22: Radial distribution of total temperature at the outlet of a three-stage compressor: comparison of measured data with computations with and without a radial mixing model (obtained and modified from Simon, 2007).

It is quite evident that the loss creation was not being properly handled by the inviscid throughflow methods.

The stream sheet approach, by itself, ignores mixing between stream sheets, as it was originally considered a minor effect. In this context, mixing refers to exchange of mass, momentum, and energy between stream sheets, thus implying either convection from secondary flows or diffusion, as well as the existence of shear stresses.

Moreover, the existence of the repeating stage condition, one of the most surprising effect that has been observed in multistage machines, where velocity profiles entering and leaving a stage are very similar, suggests that some process redistributes the loss in the spanwise direction. Fig 2.22 illustrates this by comparing experimental measurements performed on a 3-stage compressor with the results of two computations, including or not a radial mixing model. The repeating stage condition, as reported by Gallimore [32], is highly beneficial, because velocity and flow angle variations deep in multistage machines do not continue to deteriorate, but as yet there is no reasonable explanation of how it is set up and maintained by the flow. Having found that radial mixing has a large influence on the radial distribution of flow properties in a compressor it is reasonable to suggest that spanwise mixing plays an important part in this process. The large amounts of loss generated on the endwalls are spread out across the annulus so that the radial gradient of loss is reduced, hence reducing the velocity profile gradient. This is analogous to the production of fully developed pipe flow where the endwall loss generation is balanced by the continuous spread of loss toward the center of the pipe. Spanwise mixing therefore plays an important part in allowing the rear stages of multistage compressors to perform adequately. Of course the mixing process is irreversible and so creates a certain amount of loss itself.

The trend in gas turbine compressor design towards higher stage loadings and lower aspect ratios enhanced the importance of mixing effects, which were also more easily detected in the flow behaviour, especially in the rear stages of multistage machines, where blade aspect ratios are typically very low. This mixing can substantially influence the spanwise distributions of thermodynamic flow properties. Therefore, the inclusion of spanwise mixing to simulate shear stresses and heat transfer processes can greatly improve the accuracy and validity of meridional calculation methods.

Adkins and Smith [4] addressed the essential issue, which is to find a mixing process in the spanwise direction which needs to be included in any method for predicting the flow and in interpreting measurements to deduce the loss, summarizing the spanwise mixing effect for turbomachinery blade rows and proposing a model to incorporate this phenomenon in the traditional design framework. They developed a method for estimating the spanwise mixing, whose physical mechanism was attributed to a convective effect due to spanwise velocities set up by secondary flows, which, according to Hah [36], had previously been assumed to be of little consequence for the most part.

Adkins and Smith constructed a method in which the secondary flow included the effects of main-stream non-free vortex flow, endwall boundary layers, blade end clearances, blade end shrouding, and blade boundary layer and wake centrifugation. The spanwise mixing phenomenon is modeled as a diffusion process, where the mixing coefficient β is related to the calculated spanwise secondary velocities. The crucial point of their model is that the radial mixing is supposed to be deterministic.

What followed the work of Adkins and Smith was a period of intense study to identify physical mechanisms associated with radial transport to permit development of more precise design models, thanks also to novel data acquisition techniques to evaluate mixing levels in complex flows, such as tracer-gas technique. Convincing arguments were subsequently published by Gallimore and Cumpsty [31], that concluded that turbulent diffusion was the primary physical mechanism generating the spanwise mixing effect. Gallimore [32] incorporated then the effect of radial mixing into an axisymmetric Streamline Curvature throughflow program, modelling the mixing as a turbulent diffusion process based on the experimental observations reported in [31]. The inclusion of the mixing was found to be crucial in accurately predicting spanwise variation of exit stagnation temperature in multistage compressors, and the effect of mixing on loss distributions inferred from measurements appeared significant, so that upstream loss sources could only be determined from downstream distributions when the effect of mixing was included.

The fact that two totally different concepts for estimating the mixing coefficient, that is Adkins and Smith's model based on convective effects due to secondary flows and Gallimore and Cumpsty's approach based on turbulent diffusion, would lead to similar results aroused considerable interest and controversy, giving birth to a debate. As reported by Wennerstrom [87], further experiments were conducted by Wisler et al. [89], using the ethylene tracer technique, hot-wire measurements and conventional methods, led to the conclusion that both mechanisms of transport and diffusion are important. However, the extensive discussion that followed that paper left the question somewhat unresolved.

As stated by Wennerstrom [87], in some respects, from the designer's point of view who simply wants a useful end result, the difference may be largely academic, supporting the remark made by Denton and Dawes [23] that any theoretical modelling of mixing is so oversimplified that it is preferable and simpler to include an empirical rate of exchange of mass, enthalpy, angular momentum and entropy between streamlines. L. H. Smith, Jr., in the discussion of the paper published by Wisler et al., pointed out: "The secondary flows calculated by Adkins and Smith, while not always correct in detail, do spring from phenomena that are bound to agitate the flow and cause turbulent mixing, and that these agitations should be more ore less proportional to the strengths of the secondary flows calculated. With this view, it doesn't really matter much how the mixing is divided between secondary flow convection and turbulent diffusion; the end result is the same, and that end result has been found to be a satisfactory representation of the circumferential average properties of the flow". Since both methods show a remarkable improvement relative to the unmixed case, the first doing about as well as the second, a designer can adopt the method thought to be easier to implement in the Streamline Curvature computational scheme in use, regardless of the mechanism.

The first concrete step toward a resolution to the debate was the numerical three-dimensional Navier-Stokes analyses of Leylek and Wisler [55]. The major area of disagreement of the controversy revolved around what importance, if any, convective secondary flow phenomena had in the overall context of mixing, there being a shared evidence in the role of turbulent diffusion. Leylek and Wisler showed conclusively that spanwise mixing is caused by a combination of secondary flow and turbulent diffusion, and this was acknowledged by the most part of the authors included in the debate. Moreover, it was found that, in regions of large secondary flows, diffusion models were fundamentally incorrect, under-predicting spanwise mixing near endwalls and in low aspect ratio machines, where secondary flows are substantial.

2.3.2 The debate

According to Wennerstrom [87], the fact that two totally different methods, namely that developed by Adkins and Smith [4] and that by Gallimore and Cumpsty [31], would lead to very similar results for estimating the mixing effects aroused considerable interest and controversy.

The first concrete attempt to resolve this was made by Wisler et al. [89] in which further experiments, investigating the relative importance of convection due to secondary flows and diffusion generated from turbulence as mechanisms responsible for mixing in multistage axial-flow compressors, were conducted using the ethylene tracer technique and hot-wire anemometry. The tests were performed at two loading levels in a low-speed four-stage compressor. The experimental results showed that considerable cross-passage and spanwise fluid motion can occur and that both secondary flow and turbulent diffusion can play important roles in the mixing process, depending upon location in the compressor and loading level. In particular, in the so-called freestream region turbulent diffusion appeared to be the dominant mixing mechanism; however, near the endwalls and along airfoil surfaces at both loading levels, the convective effects from secondary flow were of the same order of magnitude as, and in some cases

	Rotor	Stator
Solidity	1.11	1.32
Aspect Ratio	1.25	1.45
Chord, cm	9.12	7.90
Stagger, Deg.	49.05	20.27
Camber, Deg.	32.32	53.39
No. of Airfoils	54	74
Axial Spacing, cm	2.79	

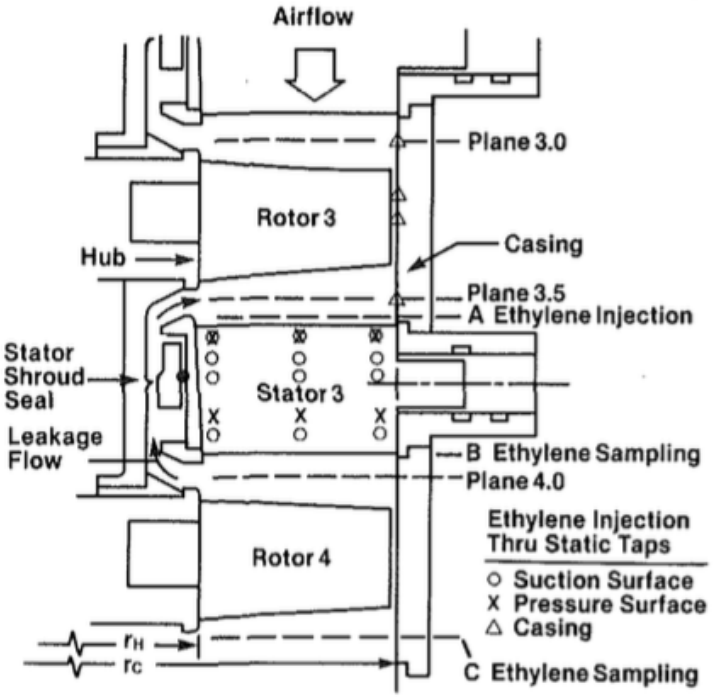

Figure 2.23: Cross section of LSRC test stage (obtained and modified from Wisler et al., 1987).

greater than, the diffusive effects from turbulence.

Wisler et al. set up a test program in the General Electric Low-Speed Research Compressor (LSRC), represented in Fig 2.23, to measure secondary flowfields and diffusion rates in an embedded stage of a multistage compressor. They used the ethylene tracer-gas technique and three-dimensional slanted-hot-wire anemometry to measure secondary flows, fluid migration, diffusion rates, velocities and turbulence intensities for two loading levels.

The LSRC basically duplicates the essential features of a small high-speed-compressor flowfield in a large low-speed machine where very detailed investigations of the flow can be made with good-quality blading, representative of current compressor design practice. The compressor was set up with four identical stages in order to simulate the repeating stage environment, and the third stage was chosen as test stage.

The tracer-gas technique involves the introduction of trace amounts of a non-reacting

gas at some point in the flow, then sensing spatially varying concentrations of the entrained contaminant in a downstream sample plane. Ethylene was used as the tracer because it has nearly the same molecular weight as air and is therefore neutrally buoyant. Ethylene was injected into the flow using a crooked L-shaped injection probe and through casing and vane-surface static pressure taps, with injection rates respectively of 80 cc/min and 60 cc/min. Downstream sampling was done with a small single-element total pressure probe, determining ethylene concentration by passing the sample through a flame ionization detector capable of sensing concentrations as low as 3-5 ppm. Injection Plane A and sampling Plane B are shown in Fig 2.23.

The ethylene tracer-gas results are therefore presented as lines of constant ethylene concentration. In particular, the principal elements of interest are the core migration and the contour shapes, where core migration refers to the movement of peak ethylene concentration region relative to its injection location, and the contours represent the isoconcentration lines surrounding the core. Core migrations are caused by pressure gradients due to the combined effects of primary and secondary flows. The contours shapes reveal the physical process the flow is locally subjected to: symmetric ethylene spreadings with respect to the core axis are primarily the result of isotropic turbulent diffusion; distorted or skewed ethylene contours with marked elongation in one or more directions can result from secondary flows or gradients in either velocity and/or turbulence intensity in the flow.

Fig 2.24 illustrates the results obtained from LSRC with ethylene tracer technique for two different operational points, namely design point, reported in Figs 2.24 a) - c), and increased loading point, represented in Figs 2.24 b) - d). The upstream injection locations are marked in the downstream Plane B with an X and the core positions of the contours are marked with an O. The upstream injection was along a radial line in Plane A, and its distortion in the downstream plane, found by connecting the core positions in Plane B, shows important cross passage and radial features of the flow, as can be seen on the left side of Fig 2.24. On the right side of Fig 2.24 the shapes and spacings of the contours exhibit the effects of secondary flows and turbulent diffusion in relation to their magnitudes in the whole stator passage.

Let us analyse Figs 2.24 a) - b): core migration at both loading levels reveals the existence of substantial secondary flow. In particular, as can be seen in Fig 2.24 a) for the design point, near the casing there is pronounced underturning as the cores are swept toward the pressure surface, exhibiting significant cross-passage flow, in addition to some radially outward flow toward the casing. In the midpassage region there is no radial motion, and only a small amount of overturning is present, since the core locations move slightly toward the suction surface. Near the hub the cores move toward the pressure surface, revealing underturning not as dramatic as near the casing, except for the region adjacent the hub, where there is a marked overturning. Core migration at increased loading is more noticeable, as depicted in Fig 2.24 b): substantial underturning is present in the endwall regions, while in the midstream there is an enhanced overturning.

Core migration experimental analysis points out the presence of cross-passage motion at both loading levels all along the span, but spanwise motion is relevant only near the endwalls and vane edges and is almost not present in the midstream.

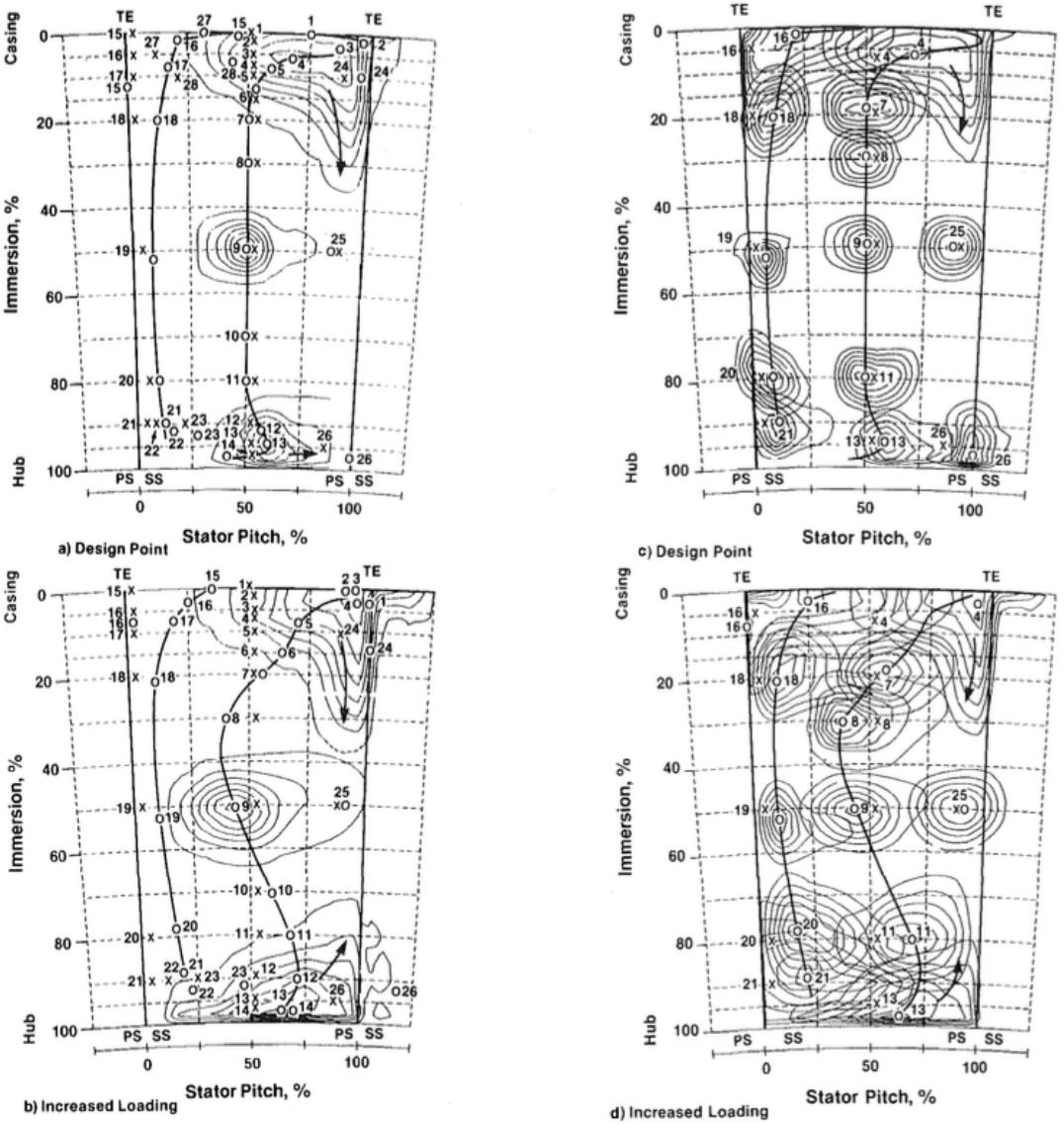

Figure 2.24: Ethylene tracer results on LSRC (obtained from Wisler et al., 1987). On the left side: ethylene core migration. On the right side: ethylene contour spreading. a) - c) Design point, b) - d) Increased loading.

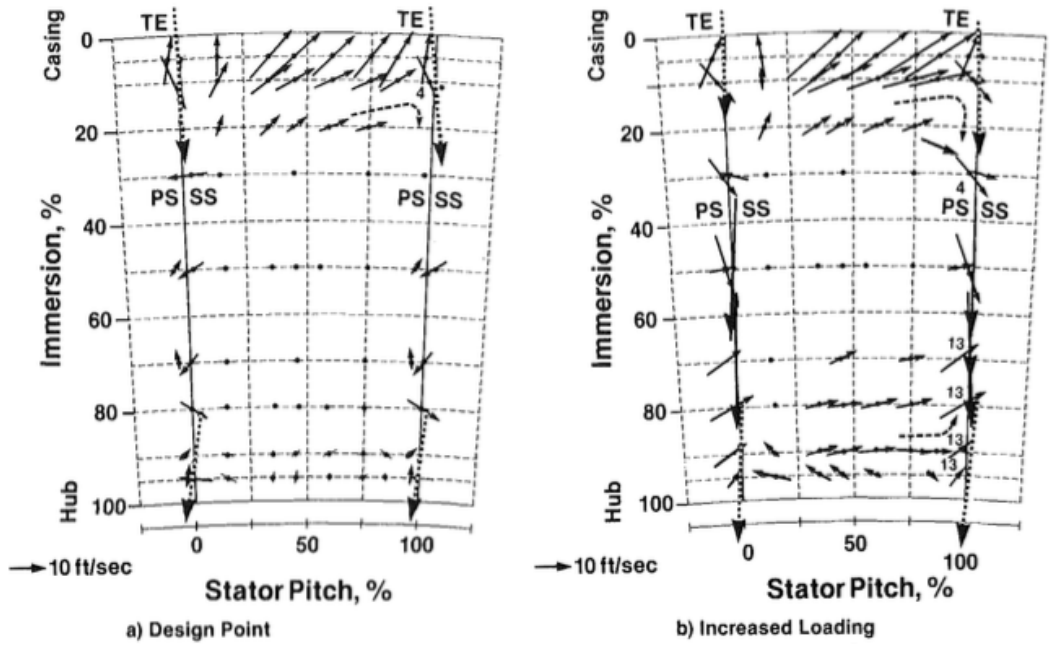

Figure 2.25: Hot-wire measurements results on LSRC at Stator 3 exit (obtained and modified from Wisler et al., 1987). a) Design point, b) Increased loading.

Figs 2.24 c) - d) illustrate the evidence for the existence of turbulent diffusion at both loading levels: in Fig 2.24 c), at the design point the spread of ethylene is nearly circular in the midpassage region; however, near the endwalls, although increased turbulent diffusion is present, there is significant distortion of the contour shapes, resulting from gradients in velocity due to secondary flow rather than from gradients in turbulence intensity. At increased loading in Fig 2.24 d), a marked increase in the level of turbulence diffusion occurs in the midstream, as well as an increase in distortion of contours is present in the endwalls, indicating the effect of secondary flow.

As mentioned above, Wisler et al. conducted also measurements of flow velocity and turbulence intensity at the inlet and exit of the third stator of LSRC using a 45 deg, slanted-hot-wire anemometer system, whose results, reported in Figs 2.25 and 2.26, substantially confirm the considerations from tracer-gas analysis. At the design point in Fig 2.25 a), cross-passage velocities toward the pressure surface and radial velocities toward the casing are present in the region near the casing, which is consistent with the core migration and underturning observed with the tracer gas. A very small amount of overturning is noticed at midspan, with no significant radial flow. At increased loading, the velocities due to secondary flows increase, causing higher cross-passage and radially outward velocities near the casing and large radially inward velocities in the vane wake, again underlining the consistency with core motions shown above.

Dealing with turbulence intensity measurements, at the design point in Figs 2.26 a) - b) a midstream region of lower turbulence intensity can be clearly distinguished from the endwall regions of higher intensities. At each immersion and circumferential location, the average unsteadiness velocities $\overline{u'}$, $\overline{v'}$, $\overline{w'}$ are nearly equal, indicating isotropic turbulence and explaining the circular shape of contours in Fig 2.24 c). This also

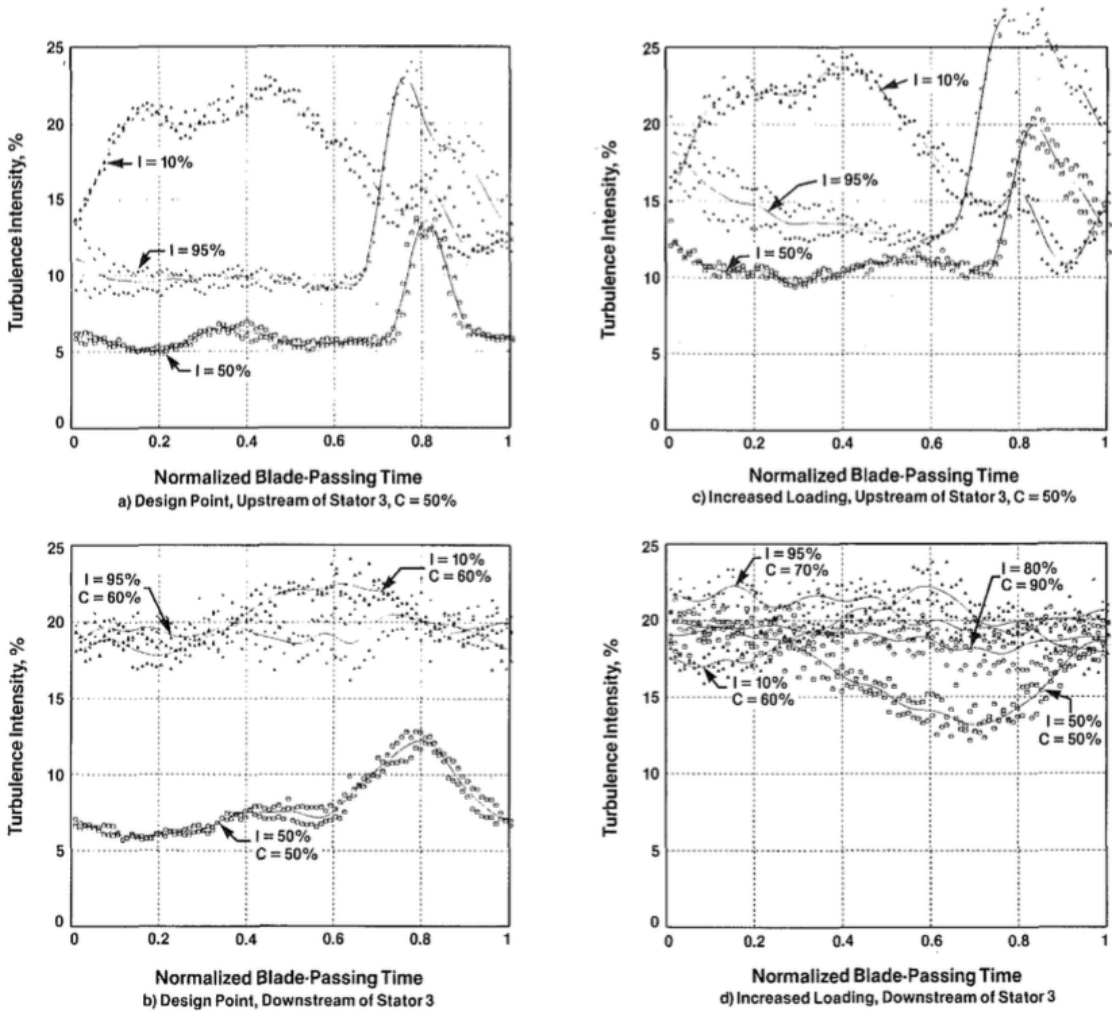

Figure 2.26: Turbulence intensity measurements for Stator 3 (obtained from Wisler et al., 1987). I is percent immersion, C is percent stator pitch. a) - b) Design point, c) - d) Increased loading.

supports the consideration that secondary flow, not turbulence diffusion, is primarily responsible for contour distortion near the endwalls. At increased loading, a more uniformly high level of turbulence across the whole span is observed in Figs 2.26 c) - d), and there is no distinction between midstream and endwall regions. This is consistent with the contour spreads shown above and indicate a behaviour of multistage axial-flow compressors similar to that described by Gallimore and Cumpsty [31].

The principal conclusions drawn from Wisler et al. are that both secondary flow and turbulence diffusion play important roles in the mixing process: near the endwalls and along airfoil surfaces, the convective mixing effects of secondary flow are of the same order of magnitude as, and in some cases greater than, the diffusive effects from turbulence; in the freestream region, turbulent diffusion appears the dominant mixing mechanism. The relative importance of the two mixing mechanisms is also configuration dependent.

These considerations were in contrast to the conclusions of Gallimore and Cumpsty [31] and Gallimore [32], in which the dominant mechanism causing spanwise mixing in multistage compressors was found to be a random, turbulent-type diffusion.

The Wisler et al. paper [89] was then followed by an extensive discussion including the original authors of the controversy, namely Gallimore and Cumpsty on one side and Adkins and Smith on the other side, which left the question somewhat unresolved.

Gallimore and Cumpsty proposed a different interpretation of the results presented by Wisler et al. based on looking at the core of the ethylene contours and at the shape of the contours. They drew attention to the shifts in the positions of the core of the ethylene contours: they noticed that there is little radial motion of the core of contours in the casing region, which implies that radial secondary flows are small, as can be seen for example about the core of contour 4 in Fig 2.24. On their evidence the radial secondary flow cannot be contributing significantly to the radial mixing. Furthermore, Gallimore and Cumpsty explained the contours for test 4 shown in Fig 2.24 a) in terms of the nearly isotropic mixing a small distance out from the solid surfaces and anisotropic mixing very close to the surfaces, while Wisler et al. attributed this feature to deterministic secondary flow near the pressure surface of the blade, even if there is little evidence of such motion from the ethylene tests with injection on the blade or from the measurements of secondary velocities where the radial component seems to be most pronounced on the suction surface. Gallimore and Cumpsty concluded then that spanwise secondary flows are small, being restricted to localized regions near the blade surface-endwall corners, and therefore do not contribute significantly to spanwise mixing, hence maintaining that the overwhelming contributor to radial mixing is turbulent diffusion.

As stated by Wennerstrom [87], in some respects, from the designer's point of view who simply wants a useful end result, the difference between the two mixing models, specifically the Adkins and Smith model based on convection by deterministic secondary flow and the Gallimore and Cumpsty approach based on turbulent diffusion, may be largely academic. Smith, in his discussion to the Wisler et al. paper, pointed out that the ethylene tracer-gas core location measurements indicate that the symmetric cellular flow pattern of Adkins and Smith linearized inviscid secondary flow model is very much distorted and the spanwise velocities are generally lower than calculated.

The measurements also showed that turbulent diffusion plays a major role in mixing, but the origin and magnitude of the turbulence then come into question: Smith suggested that the secondary flows calculated by Adkins and Smith, while not always correct in detail, do spring from phenomena that are bound to agitate the flow and cause turbulent mixing, and that these agitations should be more or less proportional to the strengths of the secondary flows calculated. With this view, continuing quoting Smith, it doesn't really matter much how the mixing is divided between secondary flow convection and turbulent diffusion: the end result is the same, and that end result has been found to be a satisfactory representation of the circumferential-average properties of the flow.

Since this topic was first given, there never had been any disagreement about the importance of turbulent diffusion in the mixing process; rather the debate revolved around what importance, if any, convective secondary flow had in the overall context of spanwise mixing. The major area of disagreement in this controversy was resolved by Leylek and Wisler [55], who showed conclusively that spanwise mixing is caused by a combination of secondary flow and turbulent diffusion.

Leylek and Wisler performed detailed three-dimensional Navier-Stokes numerical analyses, with high order turbulence modeling, for the flow through a compressor vane row at both design and increased loading, and compared these computations with detailed experimental data from Wisler et al. [89], showing excellent agreement at both loading levels. Investigating the three-dimensional development of flow in the spanwise and circumferential direction, Leylek and Wisler were able to explain important features of mixing in compressors: their numerical solutions in fact supported previous results and interpretations of experimental data obtained by Wisler et al. on the same blading using the ethylene tracer-gas technique and hot-wire anemometry, concluding that both secondary flow and turbulent diffusion are mechanisms responsible for both spanwise and circumferential mixing in axial-flow compressors and that the relative importance of the two mechanisms depends upon the configuration and loading levels.

A significant aspect of the Leylek and Wisler paper was the use of a three-dimensional viscous computational fluid dynamic (CFD) code to support the experimental observations. They used a validated 3-D Navier-Stokes system to compute the flowfield in the same high-pressure compressor Stator 3 as reported by Wisler et al. [89], without any special handling, tuning, or adjustments made to match experimental data in their study. A highly refined computational grid mesh, composed of 236 160 grid nodes with 40 tangential, 48 radial, and 123 axial nodes, was generated to make large-scale simulations of aerodynamic flowfields for two loading levels, as reported in Fig 2.27. Inlet and exit boundary conditions for both design point and increased loading cases were derived from actual LSRC measurements: they matched the time-averaged inlet vorticity and average turbulence kinetic energy at the inlet plane, imposing constant inlet total temperature plus the adiabatic wall boundary condition, and matched the measured static pressure near the hub endwall at the exit plane, imposing asymptotic conditions were imposed for all other variables. Overall mass flow rates were matched identically.

The computational model of Leylek and Wisler was found to be very close to its experimental counterpart at both design and increased loading, as can be seen in Fig 2.28,

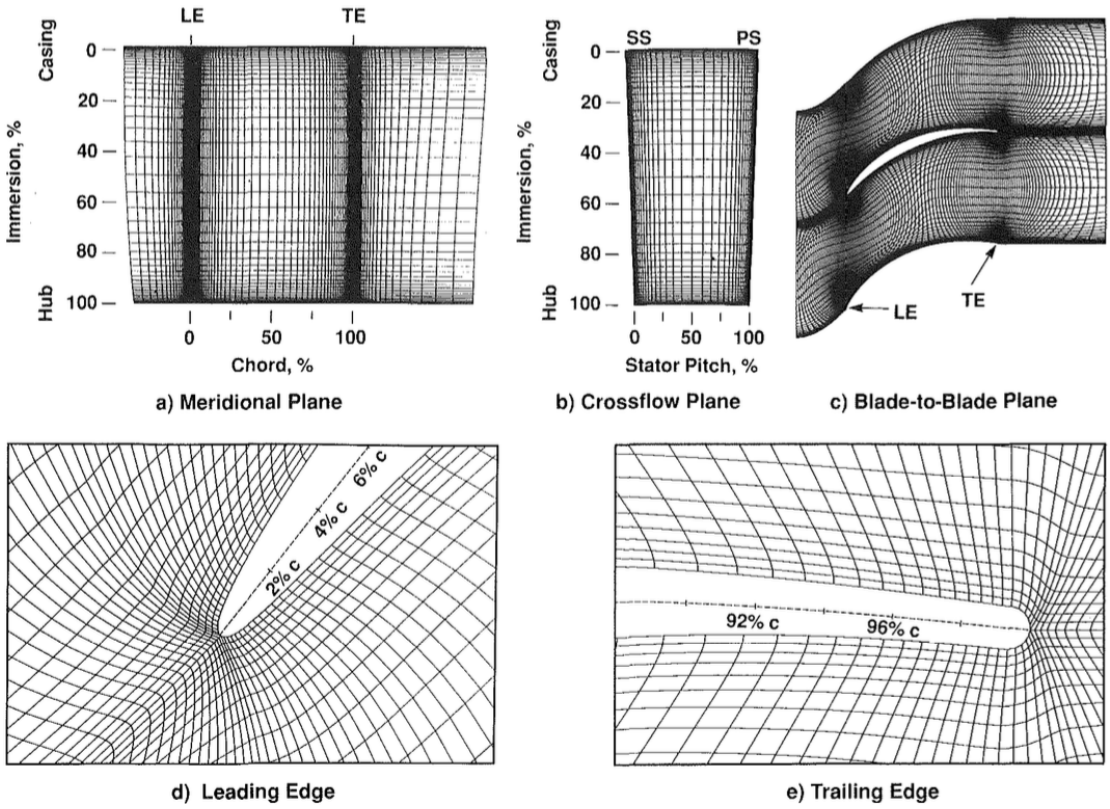

Figure 2.27: Computational grid for LSRC Stator 3 passage (obtained from Leylek and Wisler, 1991). a) Meridional Plane, b) Crossflow Plane, c) Blade-to-Blade Plane, d) Leading Edge, e) Trailing Edge.

which presents the excellent agreement between computed and measured data for total pressure, swirl angle, and loss coefficient at Stator 3 exit, and, consequently, meaningful comparisons could be made and conclusions drawn, especially about secondary flows, with considerable confidence.

The principal outcome of the Leylek and Wisler numerical analyses is that it can be conclusively recognized that both secondary flow and turbulent diffusion can contribute significantly to both spanwise and tangential mixing in an axial-flow compressor. Actually, mixing is composed of convective and diffusive fluxes interacting, in some areas augmenting each other and in other areas opposing each other.

The experimental and computational comparisons are illustrated in Fig 2.29. For the design point in Fig 2.29 a), comparing the computed contours of radial velocity to the experimental core motion along the midpitch radial injection line C-H, it is apparent that the tracer gas was injected all across the span into a midpitch region having no radial velocity, and that, therefore, even as the cores near the casing are transported circumferentially toward the pressure surface by the tangential secondary flow, they are transported into a region of little radial velocity as shown by the computations. Only those cores very near the casing that get transported circumferentially to a region near the pressure surface experience the outward radial flow in the corner and move accordingly, thus explaining why there is little radial core motion for these points. Near

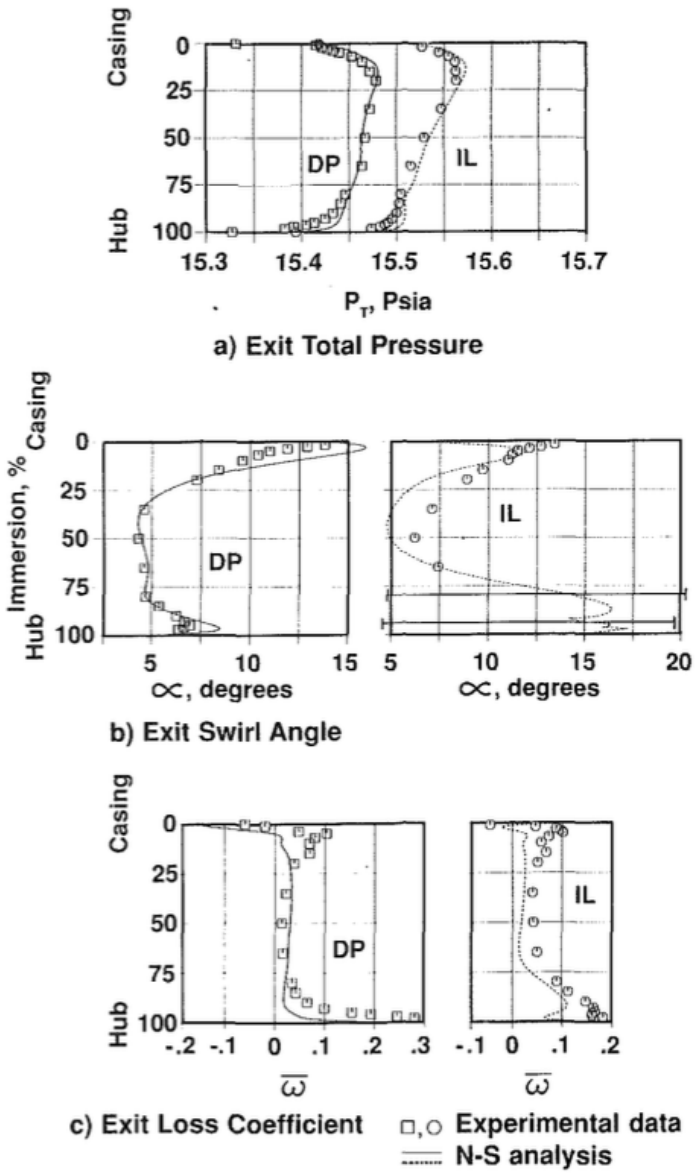

Figure 2.28: Comparison of the computed and measured flowfield at Stator 3 exit for design point (DP) and increased loading (IL) (obtained from Leylek and Wisler, 1991). Symbols are experimental, lines are three-dimensional computations. a) Total Pressure, b) Swirl Angle, c) Loss Coefficient.

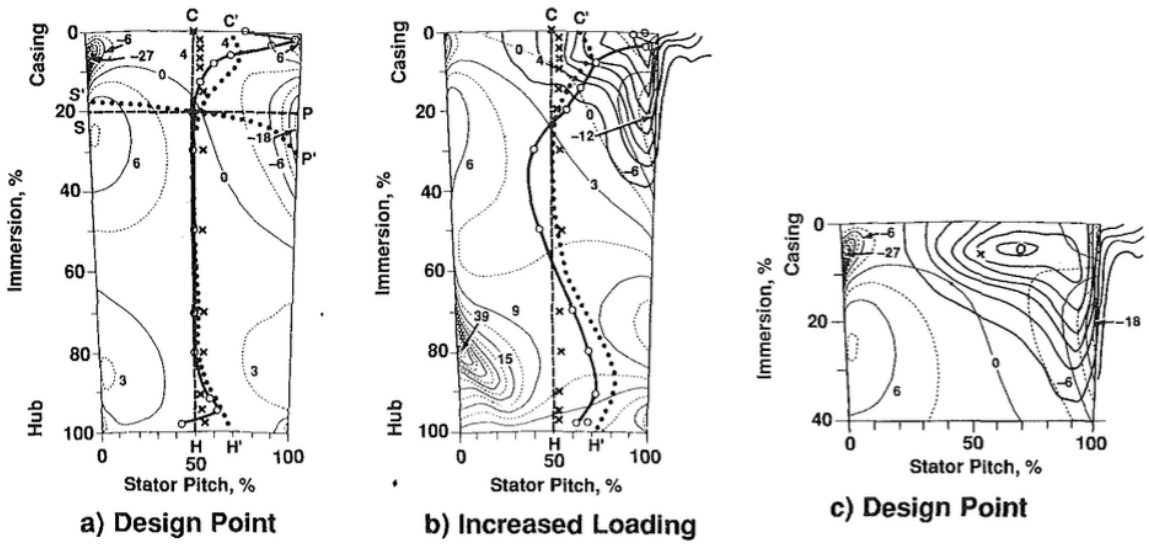

Figure 2.29: Comparisons of 3-D Navier-Stokes computations and experiment show the effects of spanwise and circumferential secondary flows as mechanisms for distorting tracer lines and contours (obtained from Leylek and Wisler, 1991). Experiment: X ethylene injection location at stator leading edge, O ethylene core location at stator trailing edge. Computation: C- - -H, S- - -P tracer line started at stator leading edge, C'$\cdots$H', S'$\cdots$P' shape of tracer line found at stator trailing edge. a) Design Point, b) Increased Loading, c) Particular at Design Point.

the hub, the cross-passage secondary flow from the boundary layer skew transports the cores a small amount toward the pressure surface, and, very near the hub, the stator shroud leakage transports that core toward the suction surface. Very near the casing the measured boundary layer skew effects are larger than computed. Distortion of line S-P to line S'-P' demonstrates that fluid particles near the pressure surface can be transported radially by secondary flow a distance equal to 10% span. This occurs well away from the airfoil/endwall corner regions and leads to an explanation of spanwise contour distortion.

In Figs 2.29 b) - c), tracer-gas Contour 4 is superimposed on the computations, showing clearly its motion: as the fluid near the casing diffuses about the circumferentially transported core, it becomes entrained in the pocket of secondary flow along the pressure surface, and the contours are pulled radially inward. Experimental Contour 4 shows radially inward distortion exactly where the computed, radially inward, secondary flow is located. The contribution of classical-type secondary flow to the distortion of Contour 4 near the pressure surface is confirmed, as well as turbulent diffusion contribution to the contour distortion even if this was not in doubt.

Leylek and Wisler supported their reasoning with further evidence, which is omitted for the sake of brevity. Their work eventually represented the resolution of the debate on the causes of spanwise mixing, which was then acknowledged to be generated from the contribution of both secondary flows and turbulent diffusion, whose relative importance of each of these two mechanisms is configuration and loading dependent. In particular, in the endwall regions and along airfoil surfaces secondary flow

was found to be of the same order of magnitude as turbulent diffusion, which is anyway an important mixing mechanism everywhere.

2.3.3 Spanwise mixing modelling for compressors

Adkins & Smith

Adkins and Smith [4] developed an approximate method for design throughflow calculations, that included effects on flow properties due to both spanwise mixing and endwall regions. The method is based on inviscid, small-perturbation secondary flow theory. Even though frictional effects are not directly included, secondary flows generated from annulus wall and blade boundary layers are included in an approximate way. The spanwise mixing phenomenon is modelled as a diffusion process where the mixing coefficient is related to the calculated spanwise secondary velocities. In order to account for the dissipation caused by secondary velocities and interactions with downstream blade rows, empirical adjustment are employed, so that, according to the assumption made in the construction of the model, the method results applicable only to near peak efficiency operating-points, where losses are relatively small and there are no significant regions of separated flow.

Secondary flows normally generate spanwise as well as cross-passage velocities, convecting the fluid from hub to tip or vice versa, and these can persist for some distance downstream of the blade row that causes them. Moreover, blade boundary layer tends to be centrifuged outward on rotor blades and moved inward on stator vanes by the prevailing static pressure field. The sweeping of blades can also cause boundary layer cross flows.

The importance of the effects due to spanwise flows on the overall flow process depends upon the machine configuration considered. Secondary flows usually increase in strength when aerodynamic loading is increased, and the depth of penetration into the main stream of endwall secondary flows is known to be proportional to blade circumferential spacing. Therefore, in machines with low passage aspect ratios, endwall flows affect the total flow for a larger fraction than usual. Also tip clearance and leakage, whose magnitudes are proportional to the size of the clearances involved, tend to show a three-dimensional nature.

To account for all these effects, Adkins and Smith included in their method models of

- main-stream non-free vortex flow,
- endwall boundary layers,
- blade end clearances,
- blade end shrouding,
- blade boundary layer and wake centrifugation,

which are believed to be the principal secondary flow mechanisms generating spanwise fluid movements.

The spanwise distributions of the losses that originate in each blade row have an important influence on the secondary flows that are generated and hence on the mixing process. Losses, specified at each blade row trailing edge, are made up of a profile loss that depends upon the usual cascade parameters and an end-wall loss that depends upon clearances, passage aspect ratios, and proximity to stall. The profile loss is usually relatively small and varies only slightly along the span, at least for subsonic cases. The endwall loss is concentrated in the endwall boundary layers, whose penetrations into the main stream are related to the blading staggered spacings. The loss determination and distribution methods employed do not incorporate consideration of all blading and endwall details that are known to affect losses. To account for the blockage effect of annulus wall boundary layers, the calculation domain extends across the full annulus from metal casing to metal hub, and an effective-area blockage coefficient is employed in the continuity equation. The velocity perturbations associated with the secondary flows that are calculated often contribute some endwall boundary layer features to the calculated flow pattern that imply a displacement thickness; these might have caused confusion if the other method had been elected. The large majority of the work done so far by the authors in developing this method has been associated with compressors. However, it is believed that the basic approach should also be applicable to axial-flow turbines, although the larger turning angles characteristic of turbines make some of the approximations employed much less suitable.

The spanwise component of secondary velocity V_s that creates the trailing edge vortex sheet, for any stator blade row or for a rotor blade row of the axial-flow type, is given by

$$V_s = \frac{1}{2}\left[W_1\,\zeta_{\perp 1}\,\frac{\Gamma_A}{W_\infty^2} - \frac{1}{2}\left(1+\frac{W_1^2}{W_\infty^2}\right)\frac{\Gamma_A}{c_p}\,\frac{ds}{dn_1} + \frac{d\Gamma_A}{dn_1}\right]\frac{dn_1}{dn_2}$$

where Γ_A is the actual blade circulation, including secondary flow effects, $\zeta_\perp$ is the flow vorticity component perpendicular to relative velocity, W is the velocity relative to the rotor, with $W_\infty = \frac{W_1+W_2}{2}$, and n is the distance normal to axisymmetric stream-surfaces of the main flowfield. Since this equation is not directly usable, for Γ_A is unknown at this point, it is necessary to calculate secondary vorticity and integrate it over a Trefftz-type surface to deduce secondary velocities. Employing Stokes law, it yields

$$\zeta_s\,a = \left[W_1\,\zeta_{\perp 1}\,\frac{\Gamma_A}{W_\infty^2} - \frac{1}{2}\left(1+\frac{W_1^2}{W_\infty^2}\right)\frac{\Gamma_A}{c_p}\,\frac{ds}{dn_1} + \frac{d\Gamma}{dn_1}\right]\frac{dn_1}{dn_2} \tag{2.7}$$

where the blade circulation in the last term has now been replaced with that of the primary flow only, and $a = \frac{2\pi r}{N}\cos\beta$ is the passage width at blade exit. Introducing the definition of primary flow blade circulation, substituting a form of the Radial Equilibrium equation, and employing thermodynamic relationships, the equation becomes

$$\zeta_s\,a = \left\{\left[\frac{1}{\rho_{01}}\,\frac{dp_{01}}{dn_1} - \frac{d(UC_\theta)_1}{dn_1} + \left(U_1\,C_{\theta 1} - \frac{U_1^2}{2}\right)\frac{ds}{c_p\,dn_1}\right]\frac{\Gamma_A}{W_\infty^2} - \frac{\Gamma_A}{2c_p}\,\frac{ds}{dn_1} + \frac{d\Gamma}{dn_1}\right\}\frac{dn_1}{dn_2}$$

The solution surface for the secondary flow calculation is a plane, approximated as a rectangle whose height in the r direction is the blade span and whose θ direction width

$\bar{a}$ is the average of the blade cross-passage staggered spacings at casing and hub. The secondary flow is considered to be a small perturbation on the primary flow, satisfying the Poisson equation

$$\nabla^2 \psi = \zeta_s$$

from which secondaries velocity are found, using the definition of velocity streamfunction.

Dealing with endwall boundary layer secondary flows, Adkins and Smith postulated that the velocity vector on an endwall at entrance to a blade row in the frame of reference of the upstream blade row is reduced in magnitude with unchanged direction by a fraction k_1, which establishes the strength of the endwall boundary layer, from that of the main flowfield solution. When the upstream blade row is moving relative to the blade row considered a skewing of the boundary layer is produced, generating significant effects on the flow. The inlet vorticity component perpendicular to the inlet relative velocity is

$$\zeta_{\perp 1} = \frac{k_1\, C_1}{\delta_1}\, cos(\alpha_1 - \beta_1)$$

Substituting this equation into the equation of secondary vorticity 2.7, with the assumption of no streamwise exit vorticity in the primary flow, the secondary vorticity associated with an endwall boundary layer becomes

$$\zeta_s\, a = \frac{k_1\, C_1}{\delta_1}\left\{ W_1\, \cos(\alpha_1 - \beta_1)\, \frac{\Gamma_A}{W_\infty^2} + \frac{2\pi}{N}\left[r_2\, \frac{W_1}{W_2}\, \cos(\alpha_1 - \beta_1)\, \sin\beta_2 - r_1\, \sin\alpha_1 \right] \right\} \frac{dn_1}{dn_2}$$

where δ_1 is the inlet boundary layer thickness. Similar expression can be written for the other three endwall elements, which are then solved for a semi-infinite strip of width a using the aforementioned Poisson equation.

For the calculation of tip clearances secondary flows an approximate method is used, in which the strength of the secondary flows is considered to be proportional to the shed vortex strength given by

$$\Gamma_{\textit{shed vortex}} = (1 - k_{casing})\, \Gamma_{\textit{primary flow}}$$

where $\Gamma_{\textit{primary flow}}$ is the circulation a blade would have in two-dimensional flow, and k_{casing} is determined empirically following the method proposed by Lakshiminarayana and Horlock [51]. In their paper Lakshiminarayana and Horlock found that, although $\Gamma_{\textit{shed vortex}}$ is in reality largely concentrated in a vortex core that lies roughly midway between the wakes of adjacent blades, a rather good representation of the induced pitchwise-average cross-passage secondary-flow angle distribution could be obtained by treating the vortex core as if its vorticity were uniform in the pitchwise direction and varied as the first half-cycle of a sine wave in the spanwise direction, and then using this vorticity distribution like secondary vorticity in a Trefftz plane integration to obtain secondary flow velocities.

Following a similar approach as with endwall boundary layer secondary flows, shrouded blade end leakage secondary flow vorticity is modelled as

$$\zeta_{\perp 1} = \frac{k_1\, C_1}{\delta_1}$$

that, substituted into equation 2.7, considering the case of a stator and hence replacing W with C, gives

$$\zeta_s \, a = \frac{k_1 \, C_1}{\delta_1} \left\{ C_1 \, \frac{\Gamma_A}{C_\infty^2} + \frac{2\pi}{N} \left[r_2 \, \frac{C_1}{C_2} \, \sin\alpha_2 - r_1 \, \sin\alpha_1 \right] \right\} \frac{dn_1}{dn_2}$$

Leakage flows enter the annulus with zero or very small meridional velocity, and they become entrained by the main flow, removing momentum from the main flow and generating an additional boundary layer on it that is more or less collateral in the frame of reference of the following annulus surface and blade row.

Neglecting viscous stresses, the spanwise acceleration of a representative small mass of fluid in the blade boundary layer is calculated at a representative point along the chord and assumed to act over the time it takes for the small mass to travel a representative distance. The resulting spanwise velocity is then compared with some available test data, which leads to the selection of the value of a constant in the model. Blade boundary layer crossflow is calculated from the equation of motion for flow in rotating coordinates

$$\frac{d\vec{w}}{dt} + 2\vec{\omega} \times \vec{w} = \omega^2 \vec{r} - \frac{\nabla p}{\rho}$$

that, differentiated following the fluid for free-stream fluid, after rearrangement, becomes

$$\frac{dw_r}{W_r} = \frac{1}{k_w} \left\{ \frac{dW_r}{W_z} - \frac{dz}{r} \left[\tan^2\beta_z \, (1 - k_w^2) + 2 \tan\beta_z \, \frac{\omega r}{W_z} \, (1 - k_w) \right] \right\}$$

This equation gives an inviscid approximation for the development of spanwise velocity in the boundary layer w on an axial-flow turbomachine blade in terms of mainstream properties and the depth in the boundary layer as measured by $k_w = w_z / W_z$.

The meridional plane solution and the secondary flow solution are mutually dependent, thus requiring an iterative procedure. Once spanwise velocities are calculated, the mixing analysis takes place. Adkins and Smith model the mixing process as an inviscid phenomenon resulting from the convection of fluid properties by the secondary velocity field previously calculated. This mixing analysis determines the behaviour of skew downstream a blade row: at locations after the blade trailing edge the distribution of a fluid property is determined by its original distribution at the blade row exit and by its movement due to secondary flowfield effects.

Let us assume that the flow between two adjacent blades moves downstream in a straight channel of rectangular cress-section having width a and spanwise height H, as depicted in Fig 2.30. Let Θ be a generic fluid property, then

$$\Theta(r, \theta, z) = \Theta(r_0, \theta_0)$$

where r_0 is the spanwise coordinate at the blade trailing edge and θ_0 is the circumferential coordinate at the blade trailing edge. The relation the coordinates at the blade trailing edge (r_0, θ_0) and the local coordinate (r, θ, z) is given by

$$r_0 = r - \frac{V_r}{V_z} \, z \qquad\qquad r\theta_0 = r\theta - \frac{V_\theta}{V_z} \, z$$

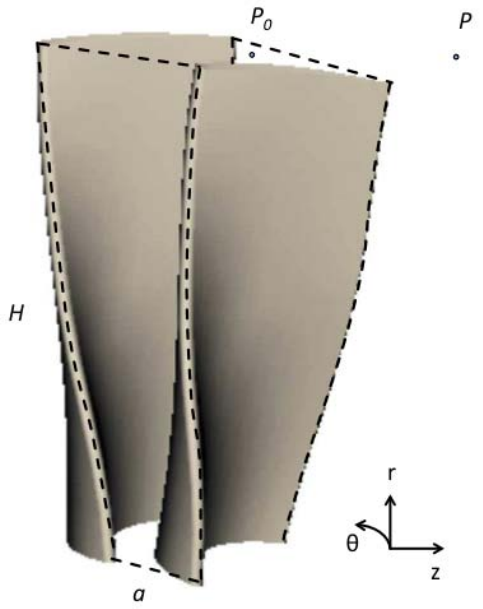

Figure 2.30: Schematic model for Adkins and Smith's mixing analysis (obtained and modified from Benini, 2014).

with V_r, V_θ, V_z respectively spanwise secondary velocity, circumferential secondary velocity, main stream axial velocity, and z axial distance from trailing edge plane. For each location θ_0, the function $\Theta(r_0, \theta_0)$ can be represented by the Taylor series

$$\Theta(r_0,\theta_0) = \Theta(\theta_0)\Big|_{r_0=0} + r_0 \left.\frac{\partial\Theta(\theta_0)}{\partial r}\right|_{r_0=0} + \frac{1}{2}\, r_0^2 \left.\frac{\partial^2\Theta(\theta_0)}{\partial r^2}\right|_{r_0=0} + \dots$$

that, rearranged with the expression of the coordinate at trailing edge, gives

$$\Theta(r,\theta,z) = \Theta(\theta_0)\Big|_{r_0=0} + \left(r - \frac{V_r}{V_z}\, z\right) \left.\frac{\partial\Theta(\theta_0)}{\partial r}\right|_{r_0=0} + \frac{1}{2}\left(r - \frac{V_r}{V_z}\, z\right)^2 \left.\frac{\partial^2\Theta(\theta_0)}{\partial r^2}\right|_{r_0=0} + \dots$$

The mixing analysis is normally applied to a circumferential-average meridional-plane calculation, in which the distribution of flow properties in the θ direction is not known. The circumferential averaged value of property Θ is

$$\overline{\Theta}(r,z) = \frac{1}{a} \int_{pitch} \Theta(r,\theta,z)\, r d\theta$$

The effect of mixing is to cause the property $\overline{\Theta}$ to change with z. If there is no variation of passage spacing with z, it results

$$\frac{\partial\overline{\Theta}(r,z)}{\partial z} = \frac{1}{a} \int_{pitch} \frac{\partial\Theta(r,\theta,z)}{\partial z}\, r d\theta$$

that, evaluated at the reference spanwise coordinate $r = 0$, yields

$$\frac{\partial\overline{\Theta}(r,z)}{\partial z} = -\frac{1}{a} \int_{pitch} \frac{V_r}{V_z} \left.\frac{\partial\Theta(\theta_0)}{\partial r}\right|_{r_0=0} r d\theta + \frac{z}{a} \int_{pitch} \left(\frac{V_r}{V_z}\right)^2 \left.\frac{\partial^2\Theta(\theta_0)}{\partial r^2}\right|_{r_0=0} r d\theta + \dots$$

If the first and second spanwise derivatives of Θ are assumed constant in the circumferential direction at the blade trailing edge and if the trailing edge second spanwise derivative is represented by its local value, and considering that the first term on the right hand side of the last equation disappears because the cross-passage average of the spanwise velocity must be zero to satisfy continuity, the resulting mixing equation results to be

$$\frac{\partial \overline{\Theta}}{\partial z} = \beta \, \frac{\partial^2 \overline{\Theta}}{\partial r^2} \tag{2.8}$$

where β, which has dimension of length, is the mixing coefficient, defined as

$$\beta = \frac{z}{a} \int_{pitch} \left(\frac{V_r}{V_z} \right)^2 r d\theta \tag{2.9}$$

The total spanwise secondary velocity V_r used in equation 2.9 is the sum of the passage secondary velocities and the blade boundary layer crossflow velocity, all assumed to occur at the trailing edge plane even though the blade boundary layer crossflow velocity was calibrated using data measured some distance downstream of the trailing edge, previously calculated. This formulation shows that β increases linearly in the downstream direction. Furthermore, the nature of the secondary flow field generally results in high values of β being concentrated near the endwalls with rather low values of e at mid-span locations. The analysis which led to equation 2.9, however, did not allow for viscous dissipation of the secondary flow field, nor did it allow for interactions with endwalls and succeeding blade rows.

It is recognized that the fluid properties in a real turbomachine do have circumferential variations and that the mixing process, proceeding downstream, may interact with endwalls and with succeeding blade rows as well as effects due to viscosity, so that equation 2.8 should be considered a simplification of the actual physical process. Adkins and Smith allowed their model to approach to this issue introducing empirical modification of the mixing coefficient β, in order to account for downstream interactions as follows

$$\beta(r,z) = \begin{cases} \left[z' \left(1 - \frac{z'}{\Delta z} \right) \right] \left[\left(1 - \frac{z''}{\Delta z} \right) \frac{1}{a} \int_{pitch} \left(\frac{V_{r_0}}{V_{z_0}} \right)^2 r d\theta + \right. & \\ \left. + \frac{z''}{\Delta z} \frac{1}{a} \overline{\int_{pitch} \left(\frac{V_{r_0}}{V_{z_0}} \right)^2 r d\theta} \right] \left[e^{-\frac{0.693 z'''}{b}} \right] \left(\frac{V_{z_0}}{V_z} \right)^2 & \text{if } 0 < z' < \Delta z \\ 0 & \text{if } z' > \Delta z \end{cases}$$

where z' is the axial distance downstream from mid-axial-chord location, z'' is the axial distance downstream from the trailing edge, z''' is the axial distance downstream from leading edge of the second downstream blade row, being zero for points upstream of leading edge of the second downstream blade row, Δz is the axial distance corresponding to five trailing edge annulus heights in the flow direction, b is the axial chord

projection of the next blade row, and the bar over the integral indicates the spanwise mass average value.

The linear increase of β with downstream distance has been decreased by a linear function of downstream distance, resulting in a parabolic function that initially increases at the proper rate but later peaks out and then decreases to zero at a downstream distance in the flow direction equal to Δz. The origin for z in equation 2.9 is not placed at the trailing edge but is located at mid-axial chord to recognize the fact that the mixing effectively starts ahead of the trailing edge. The integral part of β is a strong function of spanwise position that has been modified to linearly approach the spanwise average constant value with a downstream distance to reach full flattening taken to be again five times the annulus height. The chopping action of succeeding blade rows has been represented by an exponential decay of β which starts at the leading edge of the second downstream blade row and which proceeds at a rate that produces a 50% reduction by the trailing edge of that same second downstream blade row. Finally, the effect of changes in axial velocity has been accounted for by including the square of the ratio of the trailing edge axial velocity to the local axial velocity. The mixing coefficient then at any location is taken to be the sum of the contributions of all the upstream blade rows.

The mixing equation 2.8 together with the mixing coefficient empirical adjustments is applied between calculation stations during the main flowfield meridional plane solution. The flow properties that are mixed are stagnation pressure p_0, stagnation temperature T_0, and angular momentum rC_θ. Endwall boundary conditions applied to the mixing equation allow no flux of the mixed quantities out of the flow, thus providing a conservative system.

Fig 2.31 compares calculated and measured stagnation temperature and pressure distributions for two P&WA three-stage compressors with different aspect ratios. The results are referred to the exit survey plane, which was located several annulus heights downstream of the last stator trailing edge. Adkins and Smith performed also calculations for which the cross-passage secondary flow angle perturbations were maintained as previously calculated but for which mixing was not allowed to occur, i. e. $\beta = 0$, and compared the results. The dashed line represents the calculation results including mixing, the solid line the unmixed case and the circles the measurements. The effects of mixing are seen to be very strong for both configurations of low and high aspect ratio compressors, making it difficult to identify the locations where losses really do initiate. Agreement is reasonable, except near the walls where the lack of wall shear stress acting over the substantial distance from the last blade row to the measurement plane causes the discrepancy.

Furthermore, Adkins and Smith applied their calculation method to a high-speed 9-stage compressor, whose results for some interstage transverse data are reported in Fig 2.32. The substantial flattening of the stagnation temperature profile that occurs through stator 9 and the following diffuser must be caused, according to the authors, primarily by mixing and the analysis models most, but not all, of this flattening. As in the previous example, the analysis without mixing yields temperature profiles that are much too severe.

In the rear stages of multistage machines, mixing can then substantially influence

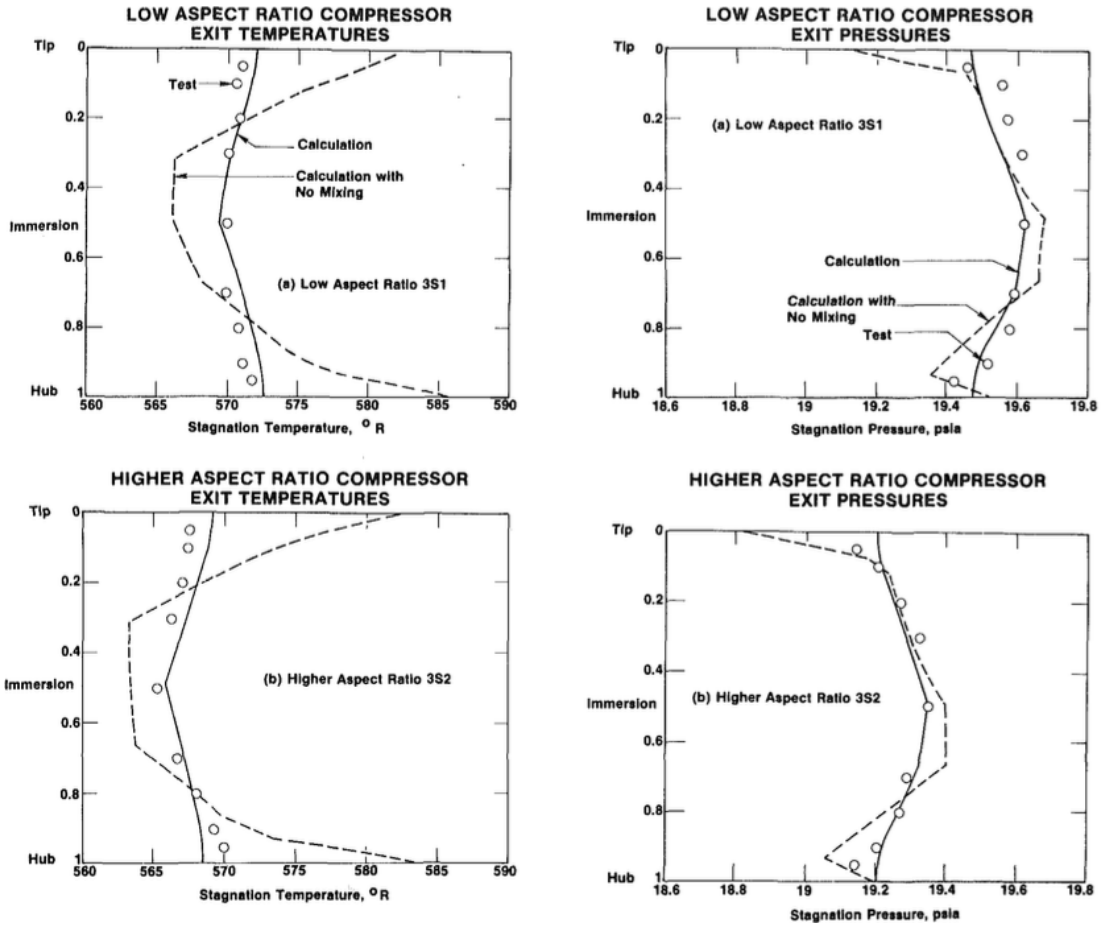

Figure 2.31: Distributions from 3-stage compressors having different aspect ratios (obtained from Adkins and Smith, 1982). On the left side: exit total temperature, on the right side: exit total pressure.

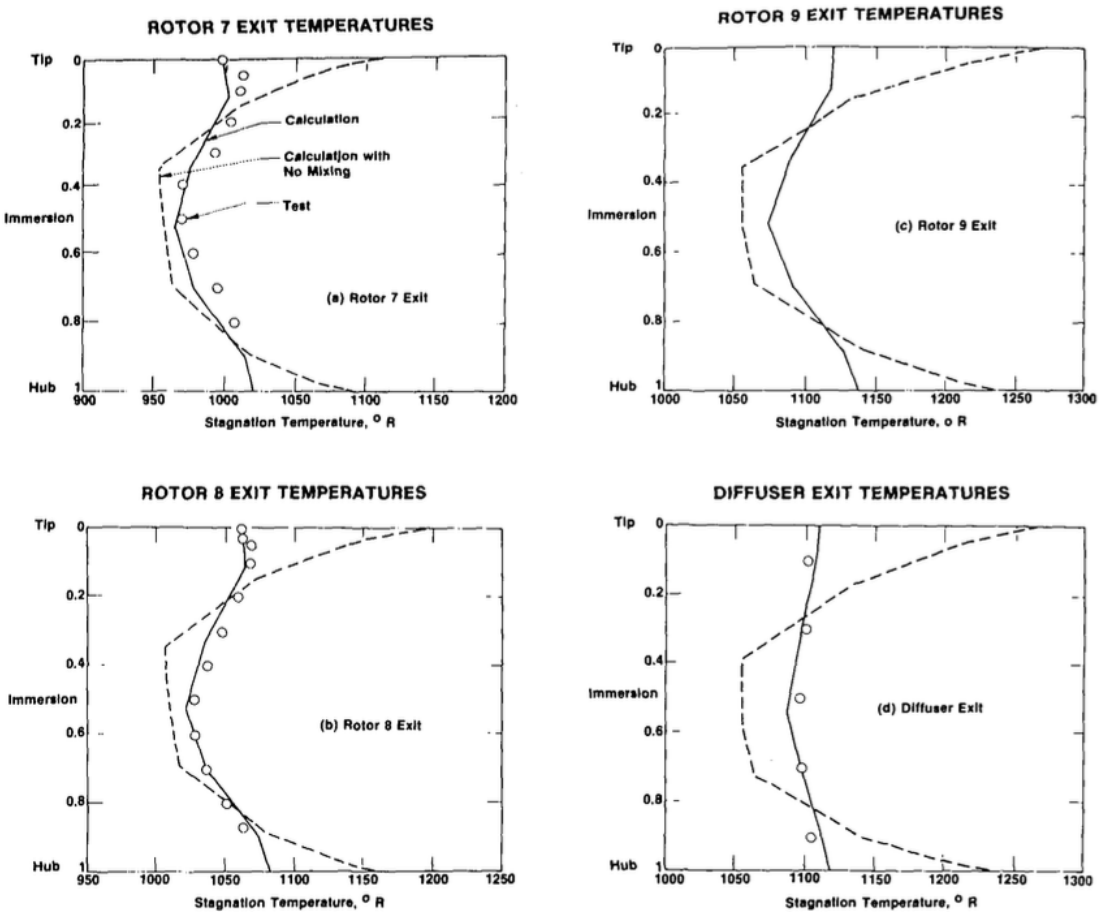

Figure 2.32: Total temperature distributions for the rear stages of a 9-stage compressor (obtained from Adkins and Smith, 1982).

the spanwise distributions of thermodynamic properties. This makes it difficult to pinpoint loss sources when measured data are being studied. The mixing process downstream of a blade row trailing edge is a complex process and the method developed by Adkins and Smith is rather crude and empirical, though capable of modelling it quite well.

Gallimore & Cumpsty

Gallimore [32] investigated the important influence of spanwise mixing on the flow through multistage axial compressors by incorporating the effect into an axisymmetric Streamline Curvature throughflow program. The mixing was modeled as a turbulent diffusion process based on the experimental observations reported by Gallimore and Cumpsty [31], recognizing that as the dominant physical mechanism. They found that the inclusion of the mixing was crucial in accurately predicting spanwise variations of exit total temperature in multistage machines. Moreover, the effect of mixing on loss distributions inferred from measurements was found to be significant so that upstream loss sources could only be determined from downstream distributions when the effect

of mixing was included.

The Streamline Curvature method adopted by Gallimore is substantially a modified version of the program described by Denton [21] in which the adiabatic and inviscid assumptions are no longer considered, allowing heat transfer in the radial direction and radial transfer of momentum, that implies the presence of axial and tangential shear stresses. The physical processes that are being represented by the mixing model are the radial mixing of momentum and heat by turbulent mixing, which are assumed to be represented by an eddy viscosity μ_t, and an eddy thermal conductivity k_t, which are related by the turbulent Prandtl number

$$Pr_t = \mu_t \frac{c_p}{k_t}$$

while the eddy viscosity is related to the mixing coefficient ϵ, which is also known as eddy diffusion and has dimension of squared length per time, by the turbulent Schmidt number

$$Sc_t = \frac{\mu_t}{\rho\epsilon}$$

The formulation for the mixing coefficient ϵ is the result of the experimental analyses conducted by Gallimore and Cumpsty [31] and is now presented. Let us consider a repeating stage in a multistage axial compressor where the flow velocities and turbulence levels at exit are identical to those at inlet to the stage. Turbulence is assumed to be homogeneous and isotropic through the whole machine. Within the stage turbulence is caused by shear stresses in the blade boundary layers and wakes and in the flow near the endwalls. These shear stresses create a drag force on the flow through the stage which, because the stage is repeating and there is therefore no momentum change across it, must be balanced by a static pressure loss Δp_l across the stage such that

$$\Delta p_a = \Delta p_i - \Delta p_l$$

where Δp_a is the actual static pressure rise across the stage, and Δp_i is the ideal static pressure rise. The amount of turbulence energy generated in the stage is give approximately by $\Delta p_l V_z a H$, where V_z is the mean axial velocity through the stage, a is the blade pitch, and H is the blade height. The turbulent kinetic energy per unit mass of gas is given by $3q^2/2$, with q as the velocity scale, defined such that

$$q = \sqrt{\frac{1}{3}\left(\overline{u'^2} + \overline{v'^2} + \overline{w'^2}\right)}$$

where $\overline{u'}$, $\overline{v'}$, $\overline{w'}$ are the turbulent velocity components. If the typical length scale of turbulent eddies is l, the rate of dissipation is given approximately by $3q^3/2l$, and, consequently, the rate at which turbulent kinetic energy decays within the stage is $3q^3\rho a H L_s/2l$, with L_s as the stage axial length. If the energy decay is balanced by the turbulence generation, it follows that

$$\Delta p_l V_z = \frac{3}{2}\frac{q^3 \rho L_s}{l}$$

The kinematic eddy viscosity $\nu = \mu_t/\rho$, and hence the mixing coefficient ϵ through the turbulent Schmidt number, can be related to the turbulence level such as

$$\nu = 0.4\, ql$$

The scale of turbulence l is assumed to be of the same magnitude of the blade thickness, so that $l = O(t)$. Rearranging the expression for the kinematic eddy viscosity, it yields

$$\nu^3 = \frac{2}{3}\,\frac{0.4^3 \Delta p_l V_z t^4}{\rho L_s}$$

The mean axial velocity through the stage is conveniently nondimensionalised by the mean blade speed U_m to give the flow coefficient ϕ, and the pressure loss Δp_l is also nondimensionalised by the quantity ρU_m^2 to give the loss coefficient ω.

In his analysis, Gallimore [32] assumed that $Pr_t = Sc_t = 1$, and that laminar or molecular effects, as well as effects of turbulent mixing in the streamwise direction, are negligible.

The expression for the eddy viscosity ν, and hence for the eddy diffusion ϵ, nondimensionalised by stage axial length and mean axial velocity is therefore

$$\frac{\epsilon}{L_s V_z} = 0.4 \left(\frac{t}{L_s}\right) \left[\frac{\omega\ (t/L_s)}{3\phi^2}\right]^{\frac{1}{3}} \tag{2.10}$$

This analysis, that led to the formulation of the mixing coefficient in equation 2.10, is very approximate, containing several assumptions, but Gallimore and Cumpsty [31] showed that, even if simple, the preceding approach gives sufficiently accurate results. The model results in specifying a certain level of mixing which is constant over the whole span and through the compressor. Furthermore, Gallimore and Cumpsty showed that the resulting flow field is relatively independent of the exact level of the mixing: a variation of an order of two or three in the level of mixing did not deteriorate significantly the quality of the solution, which is also the reason why Gallimore chose to ignore the spanwise variation of the mixing coefficient.

Gallimore modified Denton's Radial Equilibrium equation 2.3, reported below for simplicity, introducing a different formulation for entropy, tangential momentum, and stagnation enthalpy change along the streamline as follows.

$$\frac{1}{2}\,\frac{\partial V_m^2}{\partial q} = \frac{\partial h_0}{\partial q} - T\,\frac{\partial s}{\partial q} + \sin(\gamma+\phi)\,V_m\,\frac{\partial V_m}{\partial m} + \cos(\gamma+\phi)\,\frac{V_m^2}{r_c} +$$
$$-\frac{1}{2r^2}\,\frac{\partial (r^2 V_\theta^2)}{\partial q} + \frac{V_m}{r}\,\frac{\partial (r V_\theta)}{\partial m}\,\tan\epsilon \quad \text{(Denton's RE equation 2.3)}$$

Gallimore used the axial, radial, and tangential momentum equations and the energy equation to calculate these streamwise changes. The mixing model implied two effective shear stresses, acting on the radially inward and outward-facing surfaces of the fluid element illustrated in Fig 2.33. Assuming the flow axisymmetric, and that

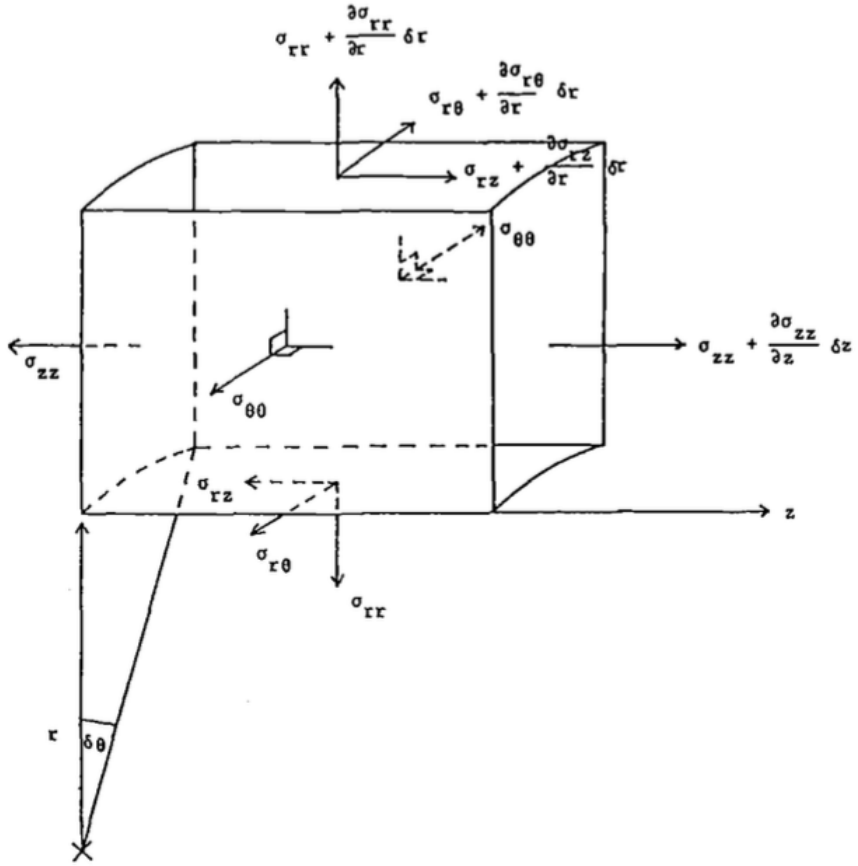

Figure 2.33: Stresses on an elemental fluid volume in a cylindrical coordinate system (obtained from Gallimore, 1986).

changes in V_r with position, as well as changes in the axial direction, are small, the shear stresses can be related to the velocity gradients by

$$\sigma_{r\theta} = \mu_t \left[\frac{\partial V_\theta}{\partial r} - \frac{V_\theta}{r} \right] \qquad \sigma_{rz} = \mu_t \left[\frac{\partial V_z}{\partial r} \right]$$

while the normal stresses are related only to the static pressure

$$\sigma_{rr} = \sigma_{\theta\theta} = \sigma_{zz} = -p$$

The momentum equation for a compressible fluid subjected to body force densities $\vec{F}$ can be written as

$$r\text{:} \qquad \rho\left(\frac{dV_r}{dt} - \frac{V_\theta^2}{r} \right) = F_r - \frac{\partial p}{\partial r}$$

$$\theta\text{:} \qquad \rho\left(\frac{dV_\theta}{dt} - \frac{V_r\, V_\theta^2}{r} \right) = F_\theta - E_\theta$$

$$z\text{:} \qquad \rho\left(\frac{dV_z}{dt} \right) = F_z - \frac{\partial p}{\partial z} + E_z$$

where

$$E_\theta = \frac{\partial}{\partial r}\left(\mu_t\left[\frac{\partial V_\theta}{\partial r} - \frac{V_\theta}{r}\right]\right) + \frac{2\mu_t}{r}\left[\frac{\partial V_\theta}{\partial r} - \frac{V_\theta}{r}\right] \qquad E_z = \frac{1}{r}\frac{\partial}{\partial r}\left[\mu_t r \frac{\partial V_z}{\partial r}\right]$$

The energy equation in terms of specific entropy is

$$\rho T \frac{ds}{dt} = \frac{dQ}{dt} + \Phi$$

where the heat added per unit volume is allowed to come only from radial transfer and is related to the radial temperature gradient by

$$\frac{dQ}{dt} = \frac{1}{r}\frac{\partial}{\partial r}\left(r k_t \frac{\partial T}{\partial r}\right)$$

and the dissipation function Φ is related to the velocity gradients by

$$\Phi = \mu_t\left[\left(\frac{\partial V_z}{\partial r}\right)^2 + \left(\frac{\partial V_\theta}{\partial r} - \frac{V_\theta}{r}\right)^2\right]$$

The entropy change along the streamline can then be calculated from the energy equation

$$\frac{\partial s}{\partial m} = \frac{1}{r\rho T V_m}\frac{\partial}{\partial r}\left(r k_t \frac{\partial T}{\partial r}\right) + \frac{\Phi}{\rho T V_m} + \frac{\partial s_e}{\partial m} \tag{2.11}$$

where s_e represents entropy due to any specified empirical loss coefficients.

The tangential momentum change along the streamline, rearranged by using the definitions for V_r, $d/dt = V_m \partial/\partial m$, and $\sin\phi = \partial r/\partial m$, is given by

$$\frac{1}{2r^2}\frac{\partial (r V_\theta)^2}{\partial m} = \frac{V_\theta}{V_m}\left(\frac{F_\theta + E_\theta}{\rho}\right) \tag{2.12}$$

where F_θ and E_θ are the tangential blade force and the tangential shear force respectively.

Finally the stagnation enthalpy change along the streamline is derived from the momentum equations in the radial and axial directions

$$\frac{\partial h_0}{\partial m} = T\frac{\partial s}{\partial m} + \frac{1}{2r^2}\frac{\partial (r V_\theta)^2}{\partial m} + \frac{F_m}{\rho} + \frac{E_z}{\rho}\cos\phi \tag{2.13}$$

Equations 2.11, 2.12, 2.13 are evaluated as follows. A second-order finite-difference scheme is used to calculate the radial derivatives of velocity and temperature required to evaluate the axial shear force E_z, the tangential shear force E_θ, the dissipation function Φ, and the heat transfer term dQ/dt, allowing then the energy equation 2.11 to be solved to give the total entropy change, including any entropy increases due to empirical loss coefficients. The momentum equation 2.12 is calculated in the same manner to give the change in tangential momentum, which is the result of two tangential forces: the blade force F_θ deduced from the specified relative flow angle in blade

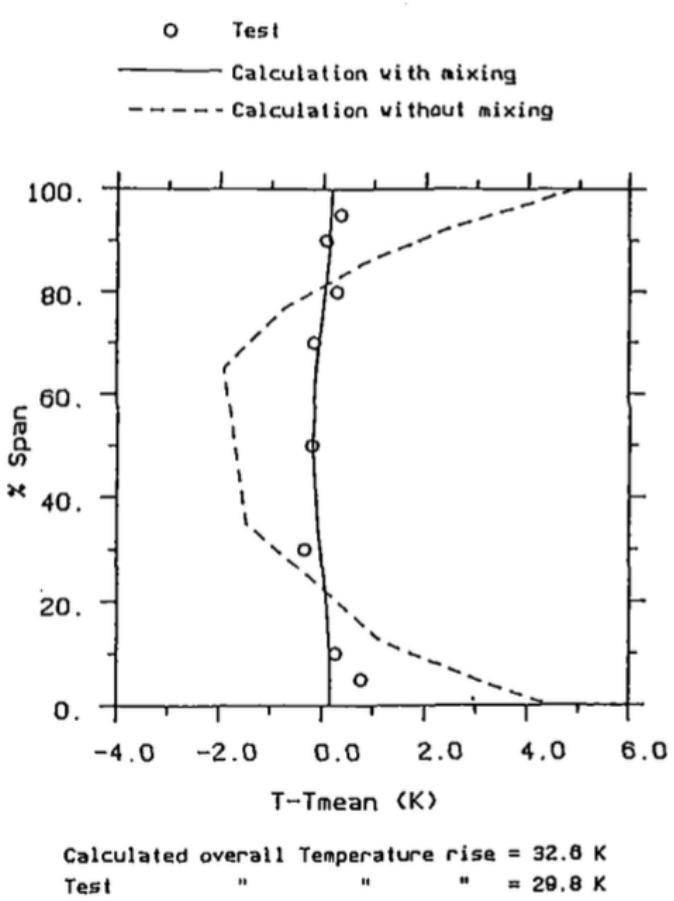

Figure 2.34: Exit total temperature distribution from lower aspect ratio compressor 3S1 (obtained from Gallimore, 1986).

rows, and an additional force E_θ caused by the tangential shear stress. The presence of shear stress will make the calculated flow angle differ slightly from that specified in blade rows, which now represents the flow angle that would be achieved if there were no mixing and consequently no shear stress. Equation 2.13 can then be solved, provided that a value for the meridional blade force F_m is known, to give the stagnation enthalpy change. The endwall conditions assume that the mixing level across the adiabatic solid boundaries and the shear stresses there are set to zero, which also implies that Φ is zero. This is clearly a simplification which has to be compensated for by a raised level of losses.

Gallimore verified his method including spanwise mixing phenomenon comparing the results with that obtained for the unmixed case and the measured data. Flow properties distributions for two P&W high-speed three-stage subsonic compressors are reported below. Provided that shock waves are absent, which is true for all except for perhaps the front few rotors of a high-speed machine, low-speed compressors are believed to model adequately the behaviour of high-speed multistage machines, and the mixing mechanism is believed to be substantially the same in both cases.

The calculated exit total temperature profiles are compared to test data in Figs 2.34

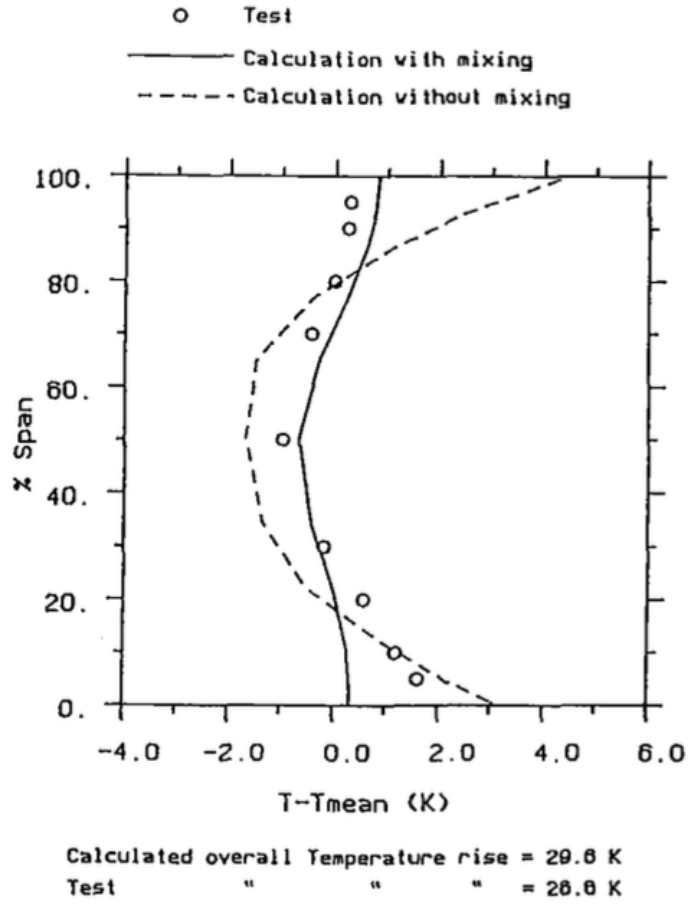

Figure 2.35: Exit total temperature distribution from higher aspect ratio compressor 3S2 (obtained from Gallimore, 1986).

and 2.35, where the circles represent the measured data, the solid line the calculation results including mixing and the dashed line the results for the unmixed case. The machine designated 3S1 had an average aspect ratio of 0.81 while compressor 3S2 had an aspect ratio of 1.22. The calculated temperature rises are some 10% greater than those measured and Gallimore attributed this discrepancy to the effect of blockage, which was not taken into account in the calculations. However, these differences in absolute levels are unimportant in this demonstration of the effect of radial mixing on the spanwise distribution of flow properties, where it is the shape of the distributions that is of interest. Consequently the results have been plotted as variations from the mean value of each distribution. The total temperature profiles calculated for the two compressors show the much improved agreement between the calculation and experiment when mixing is included; the overestimation of the total temperature rise at the end walls has been much reduced to realistic levels. Despite the specified loss coefficient profiles were comparatively flat, having been adjusted by the designers to give reasonable agreement with multistage data, the calculations without mixing have still overestimated the wall temperatures by a significant amount everywhere except near the hub of the 3S2 compressor.

De Ruyck, Hirsch and Segaert

De Ruyck et al. [24] developed a radial mixing computation method in the framework of a quasi−3-D turbomachinery flow calculation. The radial mixing computation is performed on the cross-sectional surface, taking into account both convective and diffusive mixing mechanisms. The convective mixing due to secondary flows is calculated explicitly, while the diffusive mixing due to random effects of turbulence is modelled by means of empirical coefficients. Similarly to Adkins and Smith [4], the flowfield is reconstructed from the knowledge of axial vorticity contributions for several flow regions, which contribute to a quasi-harmonic Poisson-type streamfunction equation. The axial vorticity components are calculated from vorticity equations for inviscid flow, combined with integral methods for 3-D endwall and profile boundary layers, and asymmetric wakes.

De Ruyck et al. predicted the redistribution of radial temperature profiles for three axial compressors, validating their secondary flow computation against experimental data.

The convective mixing is defined as the mixing generated from the flow pattern on the cross-sectional surface, thus it is considered as a correction to the quasi−3-D flowfield and does not represent the classical secondary flowfield. For this reason, De Ruyck et al. divided the absolute velocity $\vec{V}$ into two components, namely the quasi−3-D component $\vec{V}_{q-3D}$ and the transverse component $\vec{V}_{S_3}$

$$\vec{V} = \vec{V}_{q-3D} + \vec{V}_{S_3} \tag{2.14}$$

where S_3 is the cross-sectional or transverse surface in the $r - \theta$ plane, i. e. a streamsurface of the third kind, as a logical extension of Wu's S_1 and S_2 definitions. The quasi−3-D velocity component takes into account not only the traditional contributions from throughflow and blade-to-blade calculations, but also the two-dimensional effects due to viscosity, such as endwall and profile boundary layers, and wakes, and consequently the influence of blockage on the continuity equation. The transverse velocity component represents any deviation of the quasi−3-D flow from the real flow, containing the crossflow components of the viscous layers.

De Ruyck et al. used a density-weighted geometrical pitch-average of both velocity components, further subdividing them into an averaged axisymmetric component and a fluctuation component, that represents the deviation from axial symmetry due to flow deflections induced by the blades and due to flow patterns occurring in the S_3 streamsurface.

The diffusive mixing caused by the high levels of turbulence in multistage axial-flow compressors contributes to the radial redistribution of flow properties in a homogeneous uniformisation process. The influence of turbulence on the mixing process is modelled through the use of a turbulent mixing coefficient, likewise the approach followed by Gallimore [32].

Assuming that the flow is compressible and steady relative to a blade row, and that the flow on the S_3 streamsurface is two-dimensional, it is possible to introduce a

streamfunction $\psi(r,\theta)$, which satisfies the continuity equation, such as

$$\frac{\partial \psi}{\partial r} = \rho\, V_{\theta,S_3} \qquad\qquad \frac{\partial \psi}{\partial \theta} = -\rho\, r\, V_{r,S_3}$$

Taking into account that the streamfunction ψ is independent of the axial position z, the quasi-harmonic Poisson-type equation governing the streamfunction distribution on the S_3 streamsurface is given by

$$\nabla \cdot \left(\frac{1}{\rho}\, \nabla \psi \right) = \zeta_{z,S_3} \tag{2.15}$$

where ζ_{z,S_3} is the axial vorticity component of the total flowfield, which can be decomposed in an inviscid component and in a viscous component

$$\zeta_{z,S_3} = \zeta_{z,S_3,inv} + \zeta_{z,S_3,visc}$$

The axial vorticity component $\zeta_{z,S_3,inv}$ is associated to the S_3 flows induced by the inviscid core flow region and is defined over the whole computational domain, while the axial vorticity component $\zeta_{z,S_3,visc}$ is associated to the viscous regions, containing several contributions from endwall boundary layers, profile boundary layers and asymmetric wakes.

The general flow solution is obtained from a second-order linear ordinary differential equation, solved by using a second-order central finite difference scheme, following the superposition principle.

The equation of motion for the inviscid part of the flow, which contributes to the cross-sectional flowfield through the classical secondary flow mechanisms of deflection, is the Helmholtz vorticity equation, which is written relative to the blade row, neglecting the presence of volume forces and assuming the fluid to be a perfect gas. The vorticity involved in the equation is the absolute vorticity $\vec{\zeta}_{abs} = \vec{\zeta} + 2\vec{\Omega}$ and it is assumed that the axial vorticity contribution $\zeta_{z,S_3,inv}$ can be adequately approximated by its passage-averaged value $\overline{\zeta}_{z,S_3,inv}$. Standing these assumptions, the equation describing the evolution in the meridional direction of the axial component of the absolute total vorticity associated to the inviscid flow region becomes

$$\overline{V}_m\, \frac{\partial \overline{\zeta}_{abs,z}}{\partial m} = \overline{\zeta}_{abs,z} \left[\tan\phi\, \frac{\partial \overline{V}_z}{\partial r} - \frac{1}{r}\, \frac{\partial (r \overline{V}_r)}{\partial r} \right] +$$

$$-\frac{1}{aB} \left[(\tan\phi\ \tan\epsilon + \tan\beta')\overline{\zeta}_{abs,z}\ +\ \overline{\zeta}_{abs,\theta} \right] [V_z]_p^s$$

where ϕ is the pitch angle, ϵ the lean angle, B the blockage factor, a the pitch, β' the blade angle, and $[V_z]_p^s$ represents the variation in axial velocity from suction to pressure side.

In endwall boundary layer regions there is generation of radial flows from cross-flows due to a higher curvature of streamlines inside the endwall boundary layer, which is necessary to maintain equilibrium between the pressure gradient from suction to pressure side of the blade passage and the mainflow velocity decreasing from

its freestream value at the boundary layer to zero at the endwall. Furthermore, in this region there is the influence of tip clearances that cause leakage flows from pressure to suction side of the blade, resulting in a 2-D overall flow pattern in the transverse surface. The axial vorticity component associated to the endwall boundary layer contribution is given by

$$\zeta_{z,ewbl} = \frac{1}{r}\,\frac{\partial(r\overline{V}_{\theta,S_3,ewbl})}{\partial r} - \frac{1}{aB}\,\tan\epsilon\,[V_{\theta,S_3,ewbl}]_p^s - \frac{1}{aB}\,[V_{r,S_3,ewbl}]_p^s$$

where $V_{r,S_3,ewbl}$ and $V_{\theta,S_3,ewbl}$ are the axial velocity distributions inside endwall boundary layers.

Low-momentum profile boundary layers are three-dimensional and contribute to both radial convection and turbulent diffusion, being centrifuged by the rotary movement in rotors and moving then inward through pressure gradients in stators. In a similar manner to the formulation for the endwall boundary layer vorticity component, the axial vorticity component associated to the contribution of profile boundary layer flows is

$$\zeta_{z,pbl} = -\frac{1}{r}\,\frac{\partial V_{r,S_3,pbl}}{\partial\theta}$$

Wakes are the physical continuation of profile boundary layer regions and the convective mixing mechanism is likewise represented by the centrifugation of low-momentum fluid, causing strong radial flows especially in the near wake. The axial vorticity component due to wake contribution is given by

$$\zeta_{z,wake} = -\frac{1}{r}\,\frac{\partial V_{r,S_3,wake}}{\partial\theta}$$

Finally, also high turbulence levels contribute substantially to the radial mixing process in a turbomachinery flow. De Ruyck et al. made no attempt for an explicit computation of the turbulence field, relying someway on the formulation proposed by Gallimore and Cumpsty [31]. In particular, they introduced an empirical turbulent mixing coefficient ϵ_t in order to account for the effects of turbulence. Since the wake has an important effect on the radial mixing mechanism, De Ruyck et al. chose to correlate ϵ_t to the wake decay, which describes the magnitude of turbulent diffusion in the wake, leading to the following expression

$$\epsilon_t = k\delta B\overline{V}_z$$

where δ is the wake thickness and k is a factor depending on turbulence intensity.

De Ruyck et al. used a governing equation for the radial mixing process which is derived from the First Law of Thermodynamics for a compressible flow. Since energy is most often described by total temperature, they decided to perform the mixing analysis on this flow property. The convection-diffusion equation for stagnation temperature, using the aforementioned decomposition of velocities, is given by

$$V_{z,q-3D}\,\frac{\partial T_0^*}{\partial z} = -V_{r,S_3}\,\frac{\partial T_0^*}{\partial r} - \frac{V_{\theta,S_3}}{r}\,\frac{\partial T_0^*}{\partial\theta} + \epsilon_t\left[\frac{1}{r}\,\frac{\partial}{\partial r}\left(r\,\frac{\partial T_0^r}{\partial z}\right) + \frac{1}{r^2}\,\frac{\partial^2 T_0^r}{\partial\theta^2}\right] \quad (2.16)$$

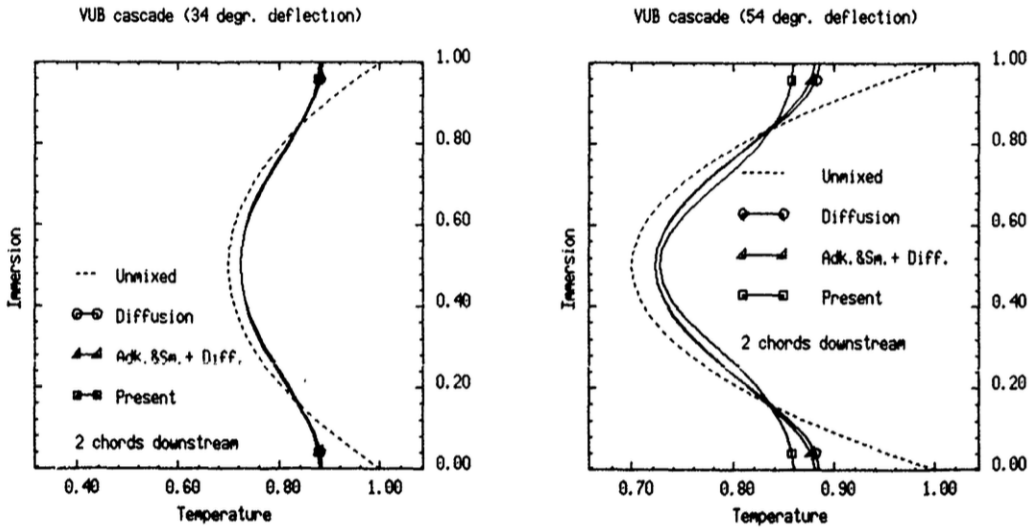

Figure 2.36: Radial temperature profiles for the VUB cascade with deflection $\delta_1 = 34°$ and $\delta_2 = 54°$ (obtained from De Ruyck et al., 1988).

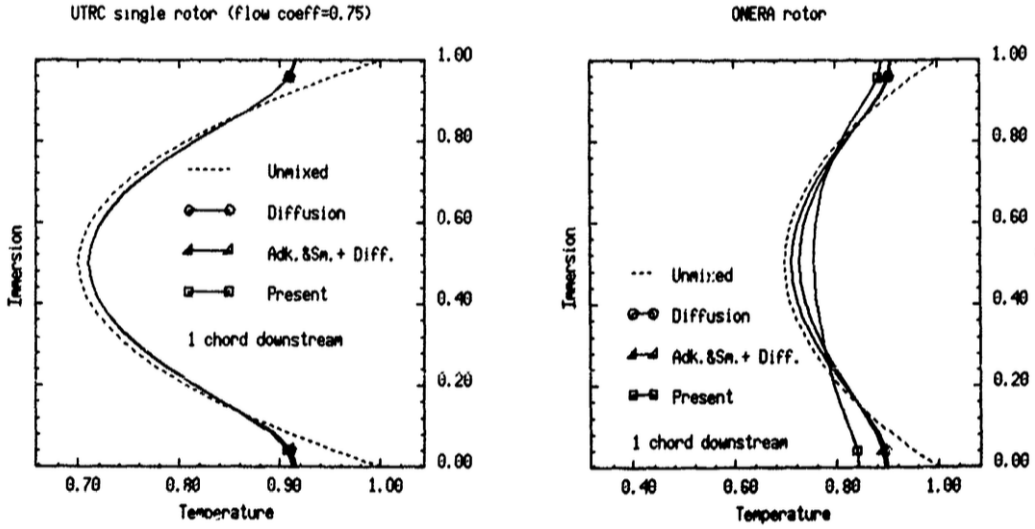

Figure 2.37: Radial temperature profiles for UTRC compressor rotor and ONERA compressor rotor (obtained from De Ruyck et al., 1988).

where $T_0^r = h^r/c_p$ is the relative total temperature and $T_0^* = I/c_p$ is the rotary total temperature. This transport equation is representative of the energy redistribution process through the whole machine and includes two different sources of energy redistribution, namely the convective mixing due to secondary flows, described by the first two terms on the right hand side of equation 2.16, and the diffusive mixing caused by turbulence, described by the last term of the governing equation. The boundary conditions for the mixing equation state that the machine operates adiabatically.

Equation 2.16 describes a two-dimensional mixing process on the cross-sectional

surface S_3 and, if the kinetic energy is small compared to static enthalpy h, may be reduced to a 2-D convection-diffusion equation for static temperature T instead of stagnation temperature T_0. Figs 2.36 and 2.37 illustrate the pitch-averaged radial temperature profiles resulting from the application of equation 2.16 to each test case. The mixing is performed on the static temperature, so that the kinetic energies involved are neglected with respect to the static temperature. Four different lines are drawn on the pitch-averaged temperature plots:

- dashed line: quadratic axisymmetric input temperature profile;
- solid line with circles: temperature profile obtained from a one dimensional diffusion process through Adkins and Smith mixing equation 2.8;
- solid line with triangles: temperature profile obtained from Adkins and Smith mixing equation 2.8, with the mixing coefficient replaced by the sum of Adkins and Smith mixing coefficient β and the mixing coefficient ϵ_t modelled by De Ruyck et al.;
- solid line with squares: temperature profile obtained from De Ruyck et al. mixing equation 2.16.

In this case, the results are passage-averaged values of the computed 2D temperature fields.

In the case of the VUB cascade with deflection $\delta = 34°$, where the turbulent mixing coefficient has been taken as $\epsilon_t/V_z L_s = 0.002$, the radial temperature profile tends to become more uniform and energy is hence transported from the endwall boundary layer regions to the mid-span region, either through convection of high-energy fluid from the endwalls towards mid-span and of low-energy fluid from mid-span towards the endwalls, either through the uniformisation due to turbulence. If deflection is increased to $\delta = 54°$, the secondary velocities also increase, resulting in a temperature distribution more severely distorted.

The case of the UTRC compressor rotor presents a very important difference with the cascade test case, that is the presence of centrifugation effects through the rotary movement, with a secondary velocity flowfield possessing a double-vortex structure. The turbulent mixing coefficient is again set to the typical value of 0.002, the convective mixing by the secondary flowfield being almost negligible. Although local radial velocities can be high, the amount of convected fluid is not large enough to induce significant convective mixing, leaving turbulent diffusion as the dominant mixing mechanism. As a result, all the radial temperature profiles coincide.

Finally, in the ONERA rotor test case, which has been designed to exhibit large secondary flows, the temperature distribution is strongly distorted by the secondary flowfield, and the convective mixing is the dominant mixing mechanism. Although this test case exhibits an extreme secondary flow behaviour, the continuing trend towards lower aspect ratios and higher blade loadings for axial turbomachinery tends lead to increased secondary flows, and thus, in these machines, the temperature distribution on the transverse surface can be severely distorted, causing convective mixing effects to become very important.

2.3.4 Spanwise mixing modelling for turbines

Lewis

Lewis [54] determined two scaling expressions to account for the influence of both turbulent diffusion and convective mechanisms, responsible for spanwise transport, which had been incorporated into a throughflow model in the framework of multistage turbines.

In [53], Lewis reported an experimental investigation conducted with the tracer gas technique into the flowfield of low aspect ratio low-speed multistage turbines, and observed that the time-mean flow adjusts through the machine as the spanwise gradients of entropy and total pressure develop until a repeating stage condition is reached. Including spanwise mixing allowed to explain the existence of this repeating stage condition, which was shown to occur typically after two stages in axial-flow turbines, suggesting that the rate of generation of endwall loss balances the flux of loss away from the endwall regions. Moreover, spanwise mixing modelling led to predict more realistic loss distributions and the attenuation of temperature profiles through such machines.

The tracer gas results showed that in a multistage environment both turbulent diffusion and classical secondary flow are responsible for spanwise redistribution. Subsequent to the debate between Adkins & Smith and Gallimore & Cumpsty, several throughflow models appeared, introducing either or both spanwise mixing mechanisms, but most researches were focused on their application to multistage compressors, giving little attention to the modelling of radial transport in turbines. Furthermore, most approaches relied on semi-empirical coefficients, tuned mainly for compressor flowfield predictions. Thus Lewis developed two formulations for both convective and random mixing and implemented them into a simple diffusive model, demonstrating the crucial influence of spanwise mixing on the radial variation of efficiency and total temperature.

In his work, Lewis preferred simplicity at the expense of sophistication and rigor. From the experimental results there appeared the evidence that spanwise transport could only be included within a throughflow model by the introduction of a diffusive term, since no mass, by definition, can be transferred across a streamtube boundary. Similarly to the model developed by Adkins and Smith [4], the spanwise transport of the generic flow property Θ is modelled by

$$V_m \frac{\partial \Theta}{\partial m} = \epsilon \frac{\partial^2 \Theta}{\partial r^2} \tag{2.17}$$

where m and r are respectively the meridional and radial directions, and ϵ is the diffusion coefficient. This mixing coefficient is an effective diffusion coefficient determined by contributions from both turbulent diffusion and spanwise convection

$$\epsilon = \epsilon_t + \epsilon_{sf} \tag{2.18}$$

where ϵ_{sf} is based on classical secondary flow theory.

Following the approach of Gallimore and Cumpsty [31], the turbulent diffusion mixing coefficient is determined considering that the production of turbulence is directly related to the generation of loss and therefore entropy. Assuming a repeating stage condition within a multistage turbine, the turbulence level at inlet to the stage is the same as at exit and, since loss is still generated within the stage, the rate of turbulence production must be balanced by the rate of turbulence decay. Turbulence is treated as homogeneous and isotropic, so that within the repeating stage each streamtube experiences the same increase in entropy and change in enthalpy, even if this does not mean that the rate of generation of entropy in each streamtube is necessarily the same. The flow is assumed to be two-dimensional and incompressible. Using the Second Law of Thermodynamics

$$T_3 \, \Delta s = \Delta h_0 - \frac{\Delta p_0}{\rho}$$

the definition of isentropic efficiency for turbines

$$\eta_{is} = \frac{\Delta h_0}{\Delta h_{0,is}} = \frac{\Delta h_0}{\Delta h_0 + T_3 \Delta s}$$

and the expression for Euler work

$$W = -\Delta h_0 = U V_z \left(\tan \alpha_3 - \tan \alpha_2\right) = U V_z \left(\tan \alpha_1 - \tan \alpha_2\right)$$

the entropy increase in each streamtube results

$$T_3 \, \Delta s = U V_z \left(\tan \alpha_1 - \tan \alpha_2\right) \frac{1 - \eta_{is}}{\eta_{is}}$$

where subscripts 1, 2, 3 refer respectively to stator inlet, stator exit, and rotor exit, and α is the absolute flow angle in the axial reference. The rate of entropy production is proportional to the production rate of turbulent kinetic energy, and hence, due to the repeating stage condition, to the dissipation rate of turbulent kinetic energy, which can therefore be written as

$$\Phi = \frac{A_t \, \dot{m} \, T_3 \, \Delta s}{\rho \, \Delta \mathit{Vol}}$$

where A_t is the proportionality constant and $\Delta \mathit{Vol}$ the volume of the stage. Given a typical length scale of turbulent eddies l, the kinematic eddy viscosity is

$$\nu = \Phi^{1/3} \, l^{4/3} = \left(\frac{A_t \, U \, V_z^2 \left(\tan \alpha_2 - \tan \alpha_1\right)(1 - \eta_{is})}{L_s \, \eta_{is}} \right)^{1/3} l^{4/3}$$

which, assuming a Schmidt number of unity and nondimensionalising, becomes

$$\frac{\epsilon_t}{V_z L_s} = \left(\frac{A_t \, U \left(\tan \alpha_2 - \tan \alpha_1\right)(1 - \eta_{is})}{V_z \, \eta_{is}} \right)^{1/3} \left(\frac{l}{L_s} \right)^{4/3} \tag{2.19}$$

Typical values for $\epsilon_t / V_z L_s$ are about 0.0007 - 0.0026.

For the formulation of the mixing coefficient due to secondary flow, Lewis assumed that the redistribution process attributable to secondary flow has a nature similar to

turbulent mixing, so that an eddy viscosity concept was used to define an effective viscosity coefficient due to secondary flow ν_{sf}, even though secondary flow is an inviscid mechanism. The application of the eddy viscosity approximation and a Schmidt number of unity allows ϵ_{sf} to be prescribed by a velocity scale, represented by the secondary flow kinetic energy λ, and a length scale l_{sf} as follows

$$\epsilon_{sf} = A_{sf}\ \sqrt{\lambda}\ l_{sf}$$

where A_{sf} is a constant. The secondary kinetic energy is determined by applying inviscid vortex theory to the uniform density flow through a rotating linear cascade. If the velocity profile at inlet to the cascade is assumed to consist of a linear gradient with boundary layer thickness δ_1, and a free-stream velocity of V_1, the mean secondary kinetic energy is

$$\lambda = \frac{V_1^2\ \Upsilon^2\ a'}{H}\ f\left(\frac{\delta_1}{a'}\right)$$

where a' is the projected blade pitch, Υ is the quantity

$$\Upsilon = -\frac{\sin(\alpha_1 - \beta_1)\ \cos\beta_1}{\cos\beta_2} + \frac{\cos(\alpha_1 - \beta_1)}{\cos\beta_1\ \cos\beta_2}\left(\frac{\sin 2\beta_2 - \sin 2\beta_1}{2} + \beta_2 - \beta_1\right)$$

and $f(\delta_1/a')$ is the series expansion given by

$$f\left(\frac{\delta_1}{a'}\right) = 8\left(\frac{a'}{\delta_1}\right)^2 \sum_{k=1,3,5}^{\infty} \frac{1}{(k\pi)^5}\left[\frac{k\pi\delta_1}{a'} - 1 + e^{-\frac{k\pi\delta_1}{a'}}\left(2 - \cosh\frac{k\pi\delta_1}{a'}\right)\right]$$

This expression for λ is based on a stationary wall being upstream of the rotating cascade. The maximum possible size of the secondary flow vortex will be determined by the throat of the cascade and can be approximated by a'. Thus substituting and nondimensionalising, the expression for the mixing coefficient due to secondary flow is

$$\frac{\epsilon_{sf}}{V_z L_s} = A_{sf}\left(\frac{\Upsilon^2\ a'\ f(\delta_1/a')}{H\ V_z\ \cos^2\alpha_1}\right)^{1/2}\ \frac{a'}{L_s} \tag{2.20}$$

Typical values for $\epsilon_{sf}/V_z L_s$ are about 0.0016 - 0.0056.

Lewis further modified equation 2.18, using a constant distribution of ϵ_t and a linear distribution of ϵ_{sf}, and allowing an axial variation of the total mixing coefficient, as the stages upstream of the repeating stage experience a reduced level of free-stream turbulence

$$\epsilon = (\epsilon_t + \epsilon_{sf})\ \tanh\left(\frac{2z}{3L_s}\right) \tag{2.21}$$

This modification is somewhat arbitrary, but Lewis justified it comparing to experimental data and finding an acceptable agreement for the turbine case considered in [53].

The spanwise transport model is written into a subroutine that is called by the throughflow model after the inviscid distributions of stagnation enthalpy, entropy, and angular momentum at each quasi-orthogonal have been calculated. The transport equation 2.17 is discretized using a finite difference scheme and solved for the same flow

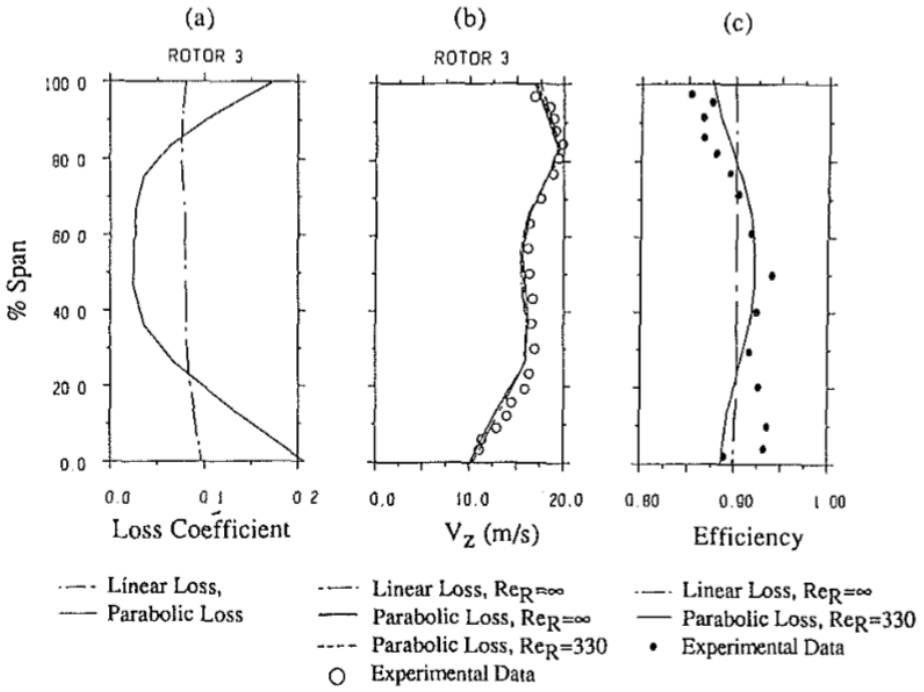

Figure 2.38: Spanwise distributions in LL turbine (obtained from Lewis, 1994). (a) Loss coefficient of rotor 3, (b) Axial velocity downstream rotor 3, (c) Efficiency of stage 3.

properties using the local meridional velocity V_m and value of ϵ defined by equations 2.19, 2.20, and 2.21. A zero gradient boundary condition is used in evaluating the diffusive terms at the endwalls.

Lewis performed an investigation into the importance of spanwise mixing in the redistribution of entropy across the span, using the LL turbine data described in [53]. The loss coefficient was distributed across the span using two different methods, namely a linear distribution of secondary loss superimposed on the local profile loss and a parabolic distribution from endwall to midspan of secondary loss superimposed on the local profile loss, as depicted in Fig 2.38 (a). The throughflow calculation was run with and without spanwise transport using the two distribution methods, obtaining different axial velocity profiles, which are reported in Fig 2.38 (b). Although the loss distributions are significantly different, the effect on the axial velocity distribution is negligible except in the endwall regions. The Reynolds number based on effective diffusion coefficient at rotor midspan, axial velocity, and stage length was $Re_R = V_z L_s/\epsilon = 330$. The spanwise distribution of efficiency, illustrated in Fig 2.38 (b), is strongly influenced by both loss distribution and spanwise transport.

Lewis applied the streamline curvature code to three other applications, which have strong gradients across the annulus of either a scalar or stagnation temperature at inlet. First, Lewis studied the attenuation of an axisymmetric concentration profile in a one and a half stage low-speed turbine, the profile at inlet simulating the spanwise temperature profile typically found at entry to a high-pressure turbine. The calculated concentration profiles are compared to the test data in Fig 2.39 downstream of stator 1,

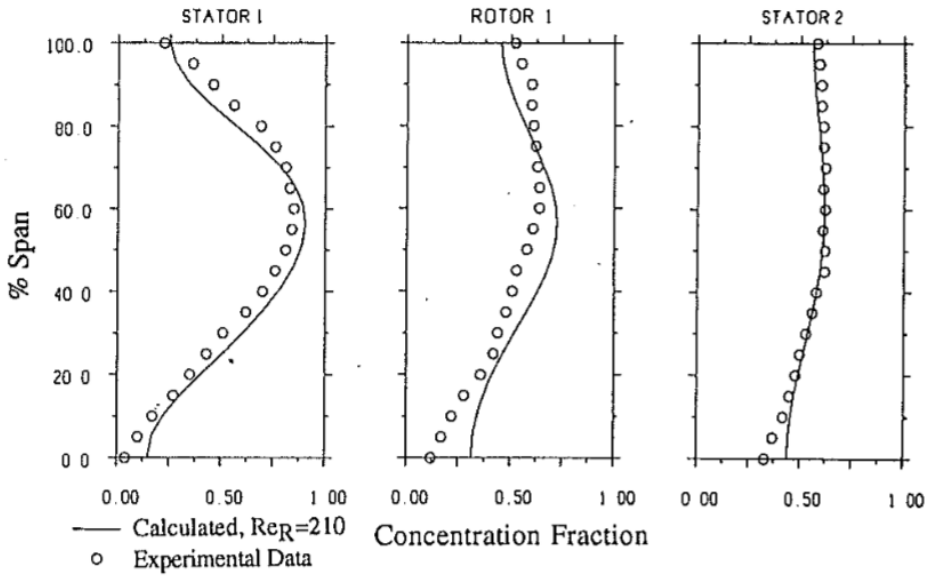

Figure 2.39: Attenuation of an axisymmetric concentration profile in a one and a half stage low-speed turbine (obtained from Lewis, 1994).

rotor 1, and stator 2, respectively, with a Reynolds number based on effective diffusion coefficient at rotor midspan $Re_R = 210$. The main area of discrepancy is downstream of the rotor, where the calculated profile suggests that the scaling models give transport coefficients that are too low.

Second, Lewis performed an experimental study of the flow through a single-stage turbine with a nonuniform radial temperature profile at inlet, comparing measured data to the mixing analysis with and without spanwise transport calculated at a traverse plane 0.76 m downstream of the rotor with a Reynolds number based on the effective diffusion coefficient at rotor exit $Re_R = 350$. The comparison is reported in Fig 2.40 (a). When spanwise mixing is included the temperature profile is well predicted, while, in the unmixed case with $Re_R = \infty$, the endwall temperatures are underpredicted by approximately 50 K and the midspan region overpredicted by 30 K.

Third, the final application is based on data obtained from a steam mixed-flow two-stage turbine. From the experimental data a significant temperature profile still exists at exit from the second stage, as seen in Fig 2.40 (b). The calculated temperature profile, with spanwise transport included with $Re_R = 420$, shows improved agreement between experiment and calculation, the difference not being substantial.

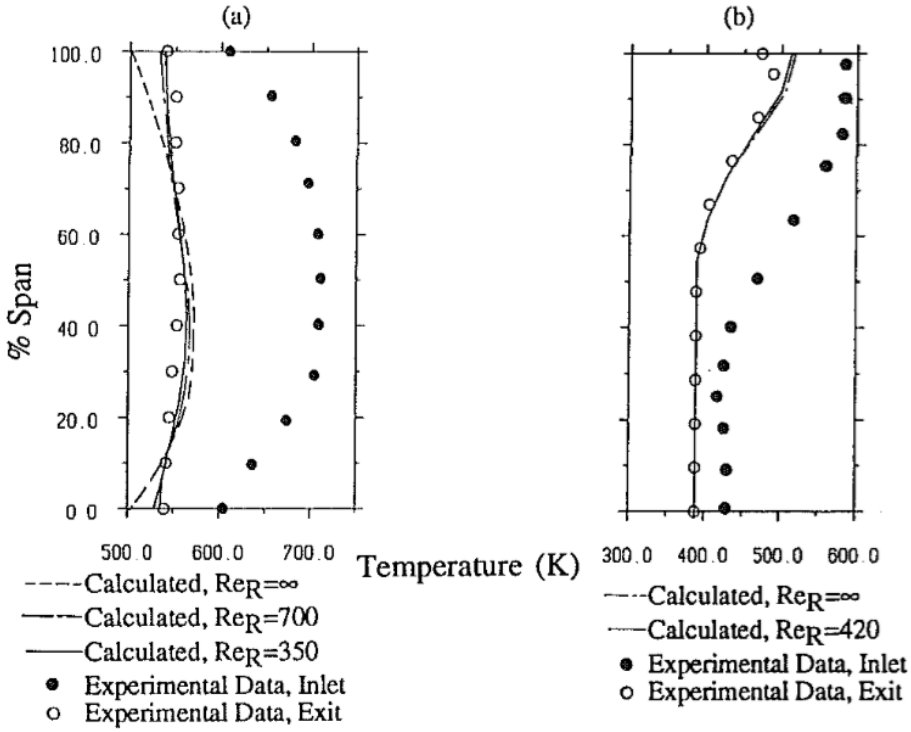

Figure 2.40: Temperature profile attenuation (obtained from Lewis, 1994). (a) Single-stage turbine, (b) Two-stage turbine.

Petrovic & Riess

Petrovic and Riess [69] developed a throughflow method for calculations in axial flow turbines which could handle local flow reversal and loss prediction at off-design operating conditions for both subsonic and transonic turbines.

In order to avoid unreal accumulations of entropy increases in end-wall regions, they included a simple mathematical model for mixing endwall and main flows which simulates the transfer of enthalpy, entropy and angular momentum between streamlines.

Mixing within the blade rows and mixing in axial ducts are handled separately: the spanwise mixing model of Petrovic and Riess assumes that mixing effects within the blade row are already included in the model for radial loss distribution, since it is developed on the basis of experimental data and gives loss distribution at the outlet of the blade row, while additional spanwise mixing occurs in axial ducts between the blade rows and turbine outlet diffuser.

The radial transport process is modelled as a redistribution of stagnation enthalpy h_0, entropy s, and angular momentum (rc_θ) in all nodes in ducts. During the flow calculation in an axial duct, in all nodes lying at the duct exit, values of h_0, s, and (rc_θ) are at first estimated as if there was no mixing: h_0^I, s^I, and $(rc_\theta)^I$ are the original unmixed distribution of stagnation enthalpy, entropy, and angular momentum respectively. Then, these values are approximated with a spline function, and new values are

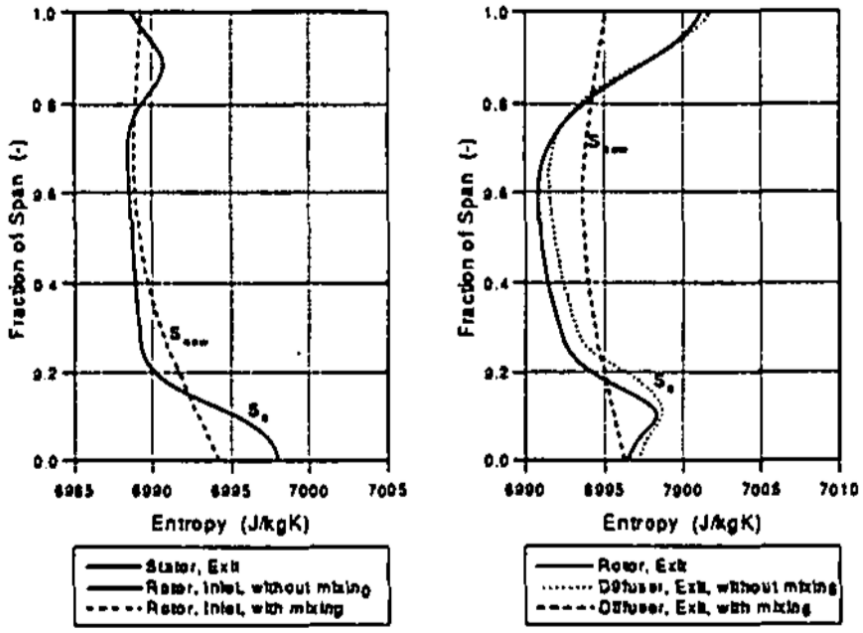

Figure 2.41: Effect of the spanwise mixing model of Petrovic and Riess on entropy distribution in a single-stage turbine at design load (obtained from Petrovic and Riess, 1997).

distributed in all calculated nodes at the duct exit: h_0^{II}, s^{II}, and $(rc_\theta)^{II}$ are the new distributions. The proportion factor of the selected spline polynomial is chosen in a way that the extreme values of original distribution curves of stagnation enthalpy, entropy, and angular momentum at exit of an axial duct are reduced by 50% compared to the linear approximation of the original distribution. The new distributions have the same integral values over the mass low as the original one

$$\int_0^1 h_0^I d\psi = \int_0^1 h_0^{II} d\psi \qquad \int_0^1 s^I d\psi = \int_0^1 s^{II} d\psi \qquad \int_0^1 (rc_\theta)^I d\psi = \int_0^1 (rc_\theta)^{II} d\psi$$

but have smaller gradients. The changes of values h_0, s, and (rc_θ) along a streamline from the duct inlet to the duct outlet are linearly distributed. The influence of this mixing model on flow parameters is controlled by comparing calculations with experimental data.

Fig 2.41 shows effect of the mixing model on the entropy distribution in axial duct between stator and rotor, and in outlet diffuser of an experimental single-stage turbine. The implementation of the spanwise mixing model in throughflow procedure resulted simple and the model appeared to be reliable, giving acceptable results for the flow calculations in low-pressure steam turbine with high Mach numbers.

CHAPTER 3

Methodology

3.1 Introduction

The principal objective of the present dissertation, as mentioned in the opening introduction, Chapter 1, is to investigate the applicability of a specific spanwise mixing model in the context of throughflow calculations for axial-flow compressors. The mixing is exclusively applied in duct regions after rotor blade rows so that flow properties profiles are allowed to mix and smooth under the dual action of turbulent diffusion and convective secondary flows. To accomplish this, two different kinds of analysis have been performed in order to compare the results from a 2-D SLC program without mixing with the predictions obtained including mixing. The basis of comparison toward a higher-fidelity SLC program was a well-validated CFD analysis reported in [1].

In particular, the first kind of analysis will be referred to as SOCRATES-MIXING-CFD analysis (S-M-C), after the three computations compared, namely SOCRATES, a 2-D SLC program developed in Cranfield University described below in Section 3.3, MIXING, the spanwise mixing model in study illustrated in Section 3.5, and CFD viscous model clarified in Section 3.4, which is taken as representative of the actual behaviour of the flow. In S-M-C analyses, the spanwise mixing model is thought as an improvement of the SLC program calculation, and hence MIXING elaborates the action of spanwise mixing starting from SOCRATES results. Both SOCRATES and MIXING results are compared to those obtained from a CFD analysis performed at the same operating points.

The second kind of analysis, which will be referred to as MIXING-CFD analysis (M-C), investigates closely if the spanwise mixing model implemented in MIXING has any relevance with the actual flow behaviour in a turbomachine environment. For this reason, MIXING now propagates its action using the initial input provided by CFD computations, and is directly compared against CFD results.

In either case, the reliability of the implemented spanwise mixing model has been evaluated for two operating points, specifically near-peak-efficiency point and near-choke point, for both SOCRATES and CFD.

The analysis test case chosen is NASA Rotor 67 (R67), which is a low-aspect-ratio transonic axial-flow fan rotor. This represents a further step forward in the study of spanwise mixing phenomenon. In fact, as Wennerstrom highlighted in his review of transport phenomena in axial-flow compressors [87], all the foregoing comparisons, those of Adkins and Smith [4], Gallimore and Cumpsty [31], Wisler et al. [89], and Leylek and Wisler [55], were made with relatively low-speed multistage compressors. Although Reynolds numbers and loading levels were fully simulated, in such machines operating near peak performance, the boundary layers are relatively unseparated. In transonic and supersonic stages, the situation may be very different, as described in Section 2.1. Here, the suction surface boundary layer on rotor blades frequently separates at the shock impingement line and it may or may not reattach. In a transonic compressor the rotor blade wakes downstream of the blade trailing edge have radial velocities that may be of the same order as the axial or tangential velocities, and, while these radial velocity components average nearly to zero in the peripheral mean, they can lead to very strong radial coupling in the flow because of radial disequilibrium caused by the difference between tangential velocities in the wake and in the inviscid flow. Also, this phenomenon is quite capable of being important in a single stage; it does not have to be the result of passage through several upstream stages.

Thus, accepting the fact that both turbulent diffusion and convective secondary flows play a significant role at low Mach numbers, at transonic and supersonic Mach numbers and possibly under some other circumstances convective secondary flows may achieve even greater importance. This is a reason why the choice for the model to be implemented eventually revolved around the mixing analysis proposed by Adkins and Smith [4]. MIXING is substantially the application of the Adkins and Smith mixing equation to the duct region of NASA Rotor 67 propagating after the rotor blade row. The mixing equation is basically a diffusion-type differential equation relating the flow property derivatives in the meridional and spanwise directions through a mixing coefficient. This mixing coefficient can be evaluated in different ways: MIXING includes three different definitions for the mixing coefficient, namely that proposed by Adkins and Smith [4] based on secondary flow magnitude, that formulated by Gallimore and Cumpsty [31] based on turbulence diffusion, and that obtained by summing the two former formulations, in order to take into account both the effects resulting in the mixing process.

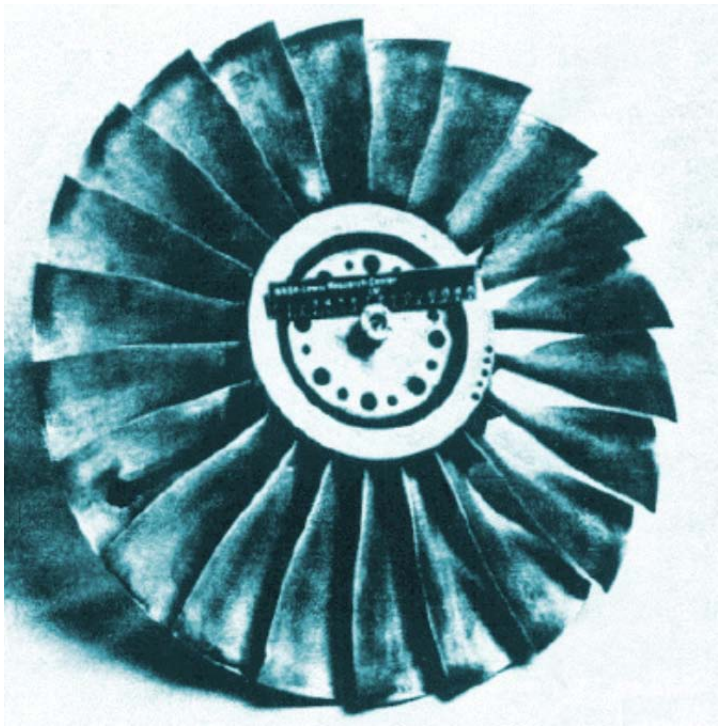

Figure 3.1: NASA Rotor 67 configuration (obtained from Strazisar et al., 1989).

3.2 NASA Rotor 67

The test case rotor, NASA Rotor 67, is shown in Fig 3.1. It is an undampered low-aspect-ratio design rotor and is the first-stage rotor of a two-stage fan. It is used since the late 80s to test computational algorithms, especially those which include viscous terms. Inlet and exit velocity vector diagrams are shown at the design condition at 10% span in Fig 3.2.

Fig 3.2 shows the diagrams of inlet and outlet velocity vectors at design condition at 10% span. The rotor design pressure ratio is 1.63 with a mass flow of 33.25 kg/s. The design rotational speed is 16 043 rpm, which yields a tip speed of 429 m/s and an inlet tip relative Mach number of 1.38. The rotor has 22 blades and an aspect ratio, based on average span/root axial chord, of 1.56. The rotor solidity varies from 3.11 at the hub to 1.29 at the tip. The inlet and exit tip diameters are respectively 51.4 and 48.5 cm, and the inlet and outlet hub/tip radius ratios are 0.375 and 0.478, respectively. The rotor geometry under design speed operating conditions is normally determined by applying deflections calculated by the NASTRAN finite-element computer code to the blade manufacturing coordinates. The geometry derived was also corrected with the laser measurements at the blade tip.

A complete description of the aerodynamic design of the full two-stage fan is given in references [20, 86].

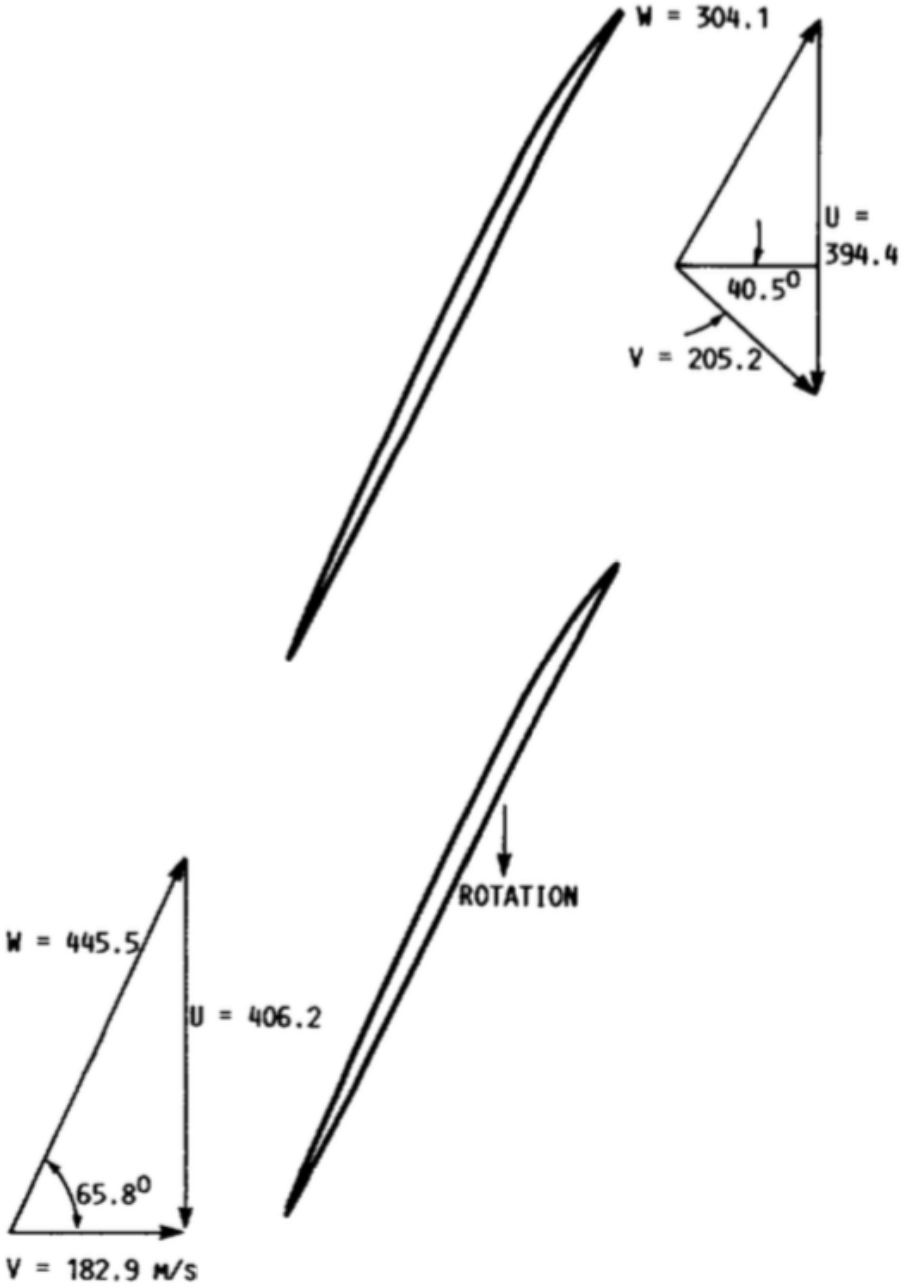

Figure 3.2: NASA Rotor 67 velocity diagrams at design conditions at 10% span from tip (obtained and modified from Strazisar et al., 1989). V, W, and U are respectively the absolute, relative, and tangential velocities.

3.3 SOCRATES

3.3.1 Historical background

As mentioned in the previous chapter, turbomachinery flow is in general complex, three-dimensional, highly viscous, and turbulent. For these reasons, the flow calculation is limited to be analysed in the hub-to-tip plane considering axisymmetric conditions so that the flow field solution is obtained in a meridional surface.

A validated method for calculating the flow on the meridional surface is the SLC method, which works under an iterative technique to calculate position, slope and curvature of the streamlines, under the assumptions for the flow to be compressible, axisymmetric, steady and inviscid. Flow field solution is mainly based on the fundamental laws of Thermofluids, namely Newton's Second Law or conservation of momentum. In fact, the conservation of momentum considers the continuity equation, resulting in the Euler equation of motion, which, in turn, considers the surface traction, and can be expressed in terms of the stress field σ_{ij}. As the flow is considered inviscid, the stress tensor becomes isotropic, resulting in the law of conservation of angular momentum or in the simplified version of the Navier-Stokes equation for a non-viscous fluid. Within this equation, blade forces are neglected whereas centripetal and Coriolis accelerations are considered.

After solving the system of equations in the three directions, radial, tangential and axial, the meridional velocity gradient is expressed by the full RE equation. The RE equation, in set with the conservation of mass equation, is iteratively solved based on a mesh constructed between the intersection of streamlines and the blade leading and trailing edge rows, where the streamlines initial position, slope and curvature are firstly assumed. At every intersection or node of every blade row, meridional velocities are calculated to obtain the mass flow of every streamtube across the total axial length and along the radial direction. Having every streamtube mass flow, compressor total mass flow is obtained, which is compared against the given actual mass flow: if different, a new iteration begins with a new inlet meridional velocity, and streamline location and shape, until an agreement is found between the calculated mass flow and the actual mass flow within a specified error tolerance.

Due to inviscid flow assumption, empirical correlations are included to compensate for viscosity, deviation and losses. First, a set of streamlines is assumed to begin an iterative process involving the RE equation, throughflow equations, and empirical models until the mass flow, rotational speed and boundary conditions are satisfied. To ensure accurate fidelity, in general, a SLC algorithm structure should include correlations of:

- minimum loss incidence angle,
- deviation angle,
- off-design calculations,
- stall and passage choking prediction,

- blade profile, secondary and shock losses.

Improvements in loss modelling, off-design calculations and stall prediction have been implemented in recent years in SLC methods. For instance, Howard and Gallimore [43] improved the SLC program from Jennions and Stow [48], which already included the spanwise mixing model developed by Gallimore [32] consisting in a turbulent diffusion model, by including endwall shear force calculations. This improvement came as a substitution of empirical blockage factors or endwall boundary layer calculations, to guarantee a more realistic prediction of velocity and flow angle distribution near the endwall.

Dunham [29] developed endwall loss models for a more realistic performance in SLC methods for axial-flow compressors and studied spanwise mixing in axial flow due to turbulent diffusion for SLC compressor analysis, which was further improved as turbulent convection due to secondary flow, spanwise surface boundary layer migration and spanwise convection between flow and blade wake were considered.

Boyer and O'Brien [12] enhanced the SLC computer code for transonic axial-flow compressors developed by Boyer [11], to obtain a more accurate pressure loss modelling at off-design conditions. This was achieved through the implementation of a physics-based shock loss model that considers shock-structure changes depending on the inlet relative Mach number, flow turning and blade profile section geometry.

Hu et al. [45] presented enhancements to the minimum loss incidence angle and total pressure loss model for SLC methods at design and off-design points. The minimum loss incidence was set up to be dependent on the inlet Mach number and blade profile geometry, as solidity, camber and thickness distribution. Total pressure losses was divided in minimum loss as a function of Mach number and Reynolds number, and in additional loss due to a difference between minimum loss incidence and the actual incidence angle. Later, Hu et al. implemented further improved models for incidence and losses in an existing SLC approach to analyse transonic axial-flow compressors.

In the present study a validated SLC model has been taken into consideration, namely the 2-D SLC compressor performance simulator known as SOCRATES (Synthesis Of Correlations for the Rapid Analysis of Turbomachine Engine Systems), a turbomachinery design and performance simulation tool developed by researchers at Cranfield University, UK [63–68, 80–82] (Fig 3.3).

The fidelity of such simulator is required to be improved through the development and implementation of new models and libraries to deal with the flow field typically encountered in modern transonic compressors. In particular, some of SOCRATES improvement strategies deal with:

1. implementation of a blade-element layout method to account for 3-D blading, namely, axial-sweep and tangential-lean,

2. optimization for design point of axial-sweep and tangential-lean to increase efficiency and surge margin, and validation performance against CFD analysis for the optimized model,

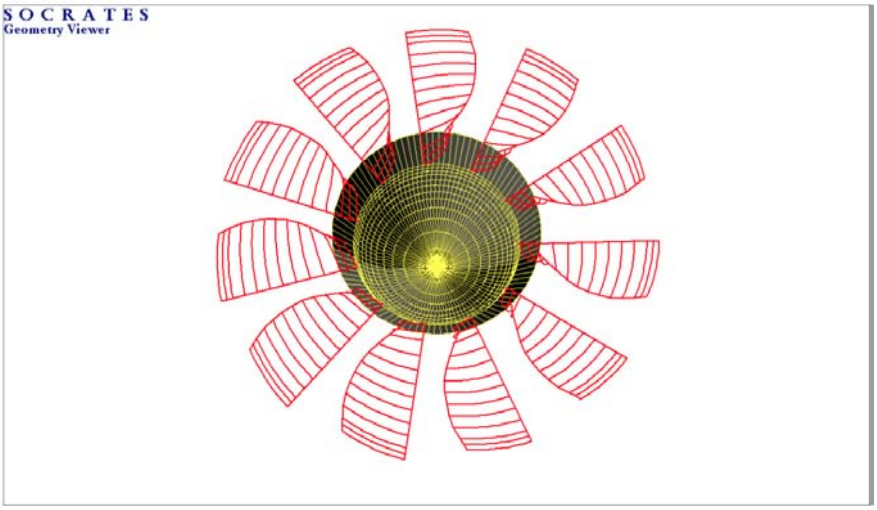

Figure 3.3: Example of turbomachinery design environment in SOCRATES (obtained from Pachidis et al., 2010). Single stage fan with cone.

3. implementation of a new shock loss model to increase fidelity and validation against CFD analysis,

4. implementation of a new spanwise flow mixing model to further increase the flow field fidelity and consider radial flow interactions due to the blade axial-sweep and tangential-lean influence,

5. implementation of a blockage factor prediction scheme, since the blade tip shock wave strength reduces and there is a radial flow towards the tip, which affect the annulus wall boundary layer modifying the blockage factors,

6. second optimization of blade axial-sweep and tangential-lean using an improved SOCRATES version that includes the shock and flow process models mentioned above that address for higher-fidelity, and validation against CFD analysis,

7. integration of SOCRATES 2-D SLC compressor module with a 0-D gas-turbine engine cycle solver, namely PYTHIA, to further optimize the 3-D blade shape at design point to maximize efficiency and enlarge operating range towards surge, and validation against CFD analysis for the optimized model,

8. multi-objective optimization of the 3-D compressor blading for off-design points, specifically near-surge, peak efficiency, and near-choking, having as objective functions the efficiency and stall margin increase, with a final validation against CFD analysis of the optimized model for the different off-design conditions for verification.

This dissertation is focused mainly on point 4 of the previous list, specifically the implementation of a spanwise mixing model for SLC calculations and the study of its applicability through validation against CFD analyses, which will be treated separately in Section 3.5.

Concerning the other strategies of improvement for a 2-D SLC program, as mentioned above, it is important to notice that deviation and loss models rely on statistics-based experimental curve approximations; however, they show large differences against actual performance. To compensate for this, Pachidis et al. [66] developed a strategy of adapting a blade profile loss model against performance experimental data through an iterative process.

Templalexis et al. [81] reported the deviation and loss models included in SOCRATES SLC code. Minimum loss incidence angle was calculated with model from Lieblein [59], while models from Carter [15], Lieblein [58] and Cetin et al. [17] were used to calculate deviation angle. Deviation angle at off-design was coded from Creveling and Carmody [18]. Blade row stall prediction was considered from Aungier [6], whereas blade passage choking was a critical Mach number-based approach. In terms of loss models, the following correlations were programmed and implemented in SOCRATES: profile loss were obtained from Swan [79], and Jansen and Moffatt [46], shock loss from Schwenk et al. [72], and secondary losses from Howell [44] and Griepentrog [35].

A recent study by Tiwari et al. [83] showed the improvement of a SLC solver to deal with subsonic and supersonic flow solution. The procedure was developed to identify supersonic flow, calculate the SLC gradient term to avoid singularities at supersonic meridional Mach numbers, and a method to handle choked flow. The SLC gradient term calculation is based from Denton [21] and Came [14]. This SLC enhancement led to substantially increase the solution accuracy, providing robustness for transonic flow analyses.

Not only flow correlations have been improved in SLC methods but also the internal algorithms that are behind it. Pachidis et al. [68] developed, implemented and tested a dynamic convergence control (DCC) algorithm for the solution of the REE in their SOCRATES 2-D SLC solver. The new DCC algorithm was introduced with the purpose of avoiding user intervention during the RE equation solution execution while keeping reasonable speed, accuracy and robustness. It was monitored that DCC scheme had more convergence difficulties at off-design conditions; however, convergence was achieved with good agreement against experimental results. In a separate study by Templalexis [82], the viscous force terms significance in the flow momentum equation and hence, in the RE equation in SOCRATES, was addressed. A better match of the SLC results against experimental plots was found, when the force terms were considered, leading to a higher fidelity simulation. Despite the increase in the RE equation complexity, more solutions were converged and fewer iterations were required to achieve convergence when the force terms were included. SLC methods have been adapted to satisfy the needs of the compression system structure, particularly for fans, where the flow is split into bypass and core channels. Shan [73] designed an approach for mass flow addition in SLC methods to treat inverse design in fans.

Furthermore, SLC methods have found application in analysing complex flow processes affecting the compressor and the engine. For instance, an integration by Pachidis et al. [65] of a low-fidelity 0-D gas-turbine performance simulator and a high-fidelity 2-D SLC compressor program (SOCRATES), was used to obtain the overall engine and compressor performance under compressor inlet flow radial pressure distortion. The

advantage of this integration technique is that the influence on engine performance due to physical phenomena arising in the compressor and analysed through SLC methods, can be represented. Equally, Doulgeris et al. [25] coupled a parallel compressor method to a SLC code to analyse fan inlet flow distortion and predict surge. The purpose of their paper was to move towards a quasi-3-D analysis so that parallel compressor theory provides with a circumferential solution while SLC with a solution in the meridional plane. The effect of having a duct upstream of the compressor and consequently, boundary layer ingestion and growth, was studied by Templalexis et al. [81] using SOCRATES 2-D SLC code. In this same study the lean angle variation was assessed to compensate the boundary-layer-ingestion-induced pressure ratio and efficiency reduction.

In short, SLC methods offer the advantage of analysing isolated gas-turbine engine components in detail, providing an accurate and inexpensive solution in terms of computational run-time against CFD. In terms of flexibility, SLC strategy allows to include empiricism in the form of all kind of deviation and loss models unlike CFD, where correlations are pre-defined and cannot be modified. Moreover, SLC analyses require less initial and boundary conditions in comparison with CFD. Even more, high-fidelity analyses from a 2-D SLC compressor performance simulator can be incorporated into a low-fidelity entire 0-D engine solver. Through this amalgamation strategy, the influence of other engine components is considered to obtain detailed performance results of the SLC-analysed independent component, which is known as component zooming. On the other hand, engine performance prediction is more accurate as internal physical phenomena and a geometry-based approach are contemplated to compute component boundary conditions. Thus, component SLC analyses offer a good trade-off between accuracy and low computational cost and time; if coupled with a low-fidelity engine performance cycle simulator, a more accurate and cost-effective engine performance estimation can be obtained.

3.3.2 Set-up

Fig 3.4 shows R67 compressor and rotor blade geometry on the meridional plane: the meridional plane is representative of the whole compressor, as a circumferentially averaged surface on which calculation is preformed. SOCRATES, as a 2-D SLC program, takes as input endwall and blade geometry information, compressor inlet flow total conditions and compressor outlet flow static conditions. Then SOCRATES analyses flow behaviour on the meridional plane solving the RE equation, along with continuity. The calculation proceeds starting at the first quasi-orthogonal (QO), verifying the congruity of radial equilibrium and conservation of mass at each QO through the whole machine. The discretization for R67 is represented in Fig 3.5, where it is possible to visualise the nodes each QO is subdivided into. Once the calculation is completed, SOCRATES gives as output flow properties at inlet and outlet of each domain duct (DD), illustrated in Fig 3.6.

SOCRATES computational grid is composed of 179 QOs, and each QO is discretized into 31 nodes, with a maximum and minimum spatial resolution in the axial direction of 0.5683 and 0.3712 cm in the region in front of and after the rotor respec-

Table 3.1: SOCRATES solver set-up.

SOCRATES solver set-up					
		INLET		**OUTLET**	
	$\dot{m}/\dot{m}_c$ [%]	P_0 [Pa]	T_0 [K]	P [Pa]	T [K]
NC	100	101128	288.2	100985	294.9
NPE	98.456	101128	288.2	110661	301.2

tively, and a maximum and minimum spatial resolution in the radial direction of 0.5581 and 0.3348 cm. The computational field is made up of 7 domain ducts, including the rotor, which is represented in Fig 3.6 as the fourth domain duct.

Two analyses for different operating points of R67 have been considered, specifically the first near peak efficiency (NPE) condition and the second near choke (NC) condition, whose information is reported in Table 3.1.

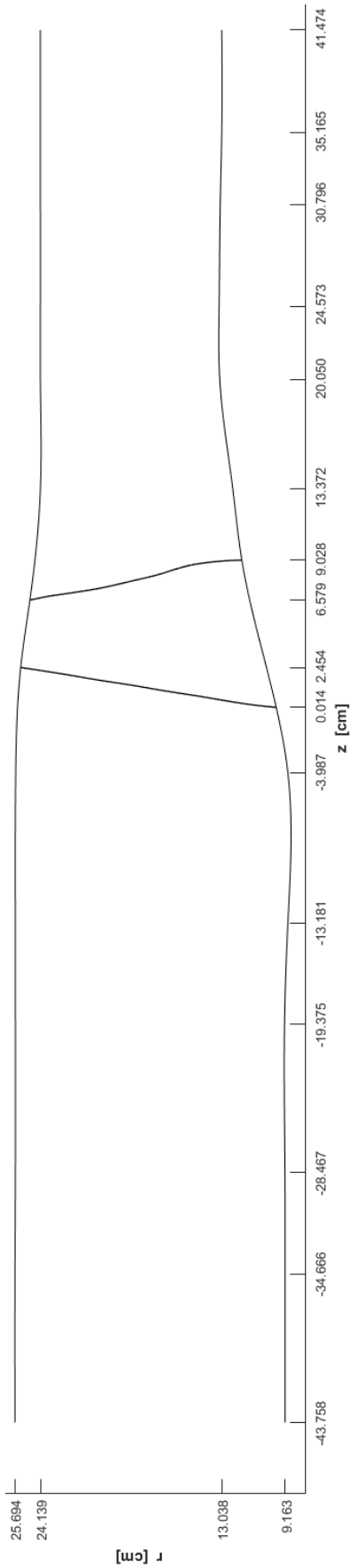

Figure 3.4: NASA Rotor 67 blade geometry input to SOCRATES.

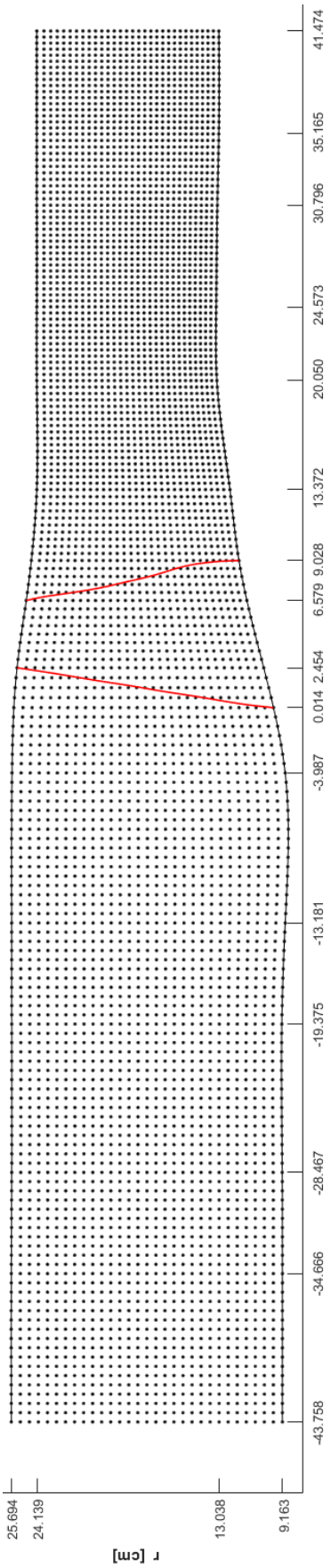

Figure 3.5: NASA Rotor 67 blade meridional plane quasi-orthogonals.

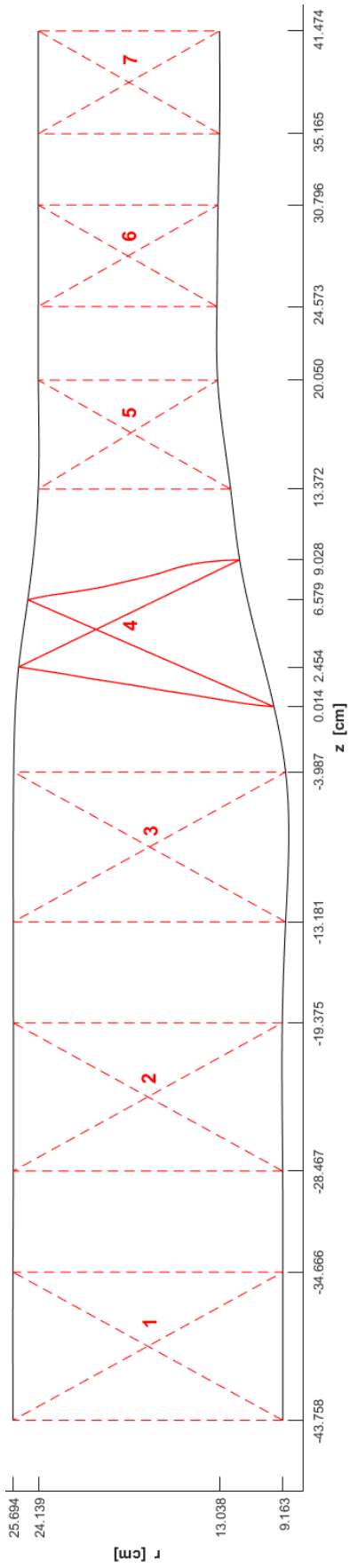

Figure 3.6: NASA Rotor 67 blade meridional plane domain ducts.

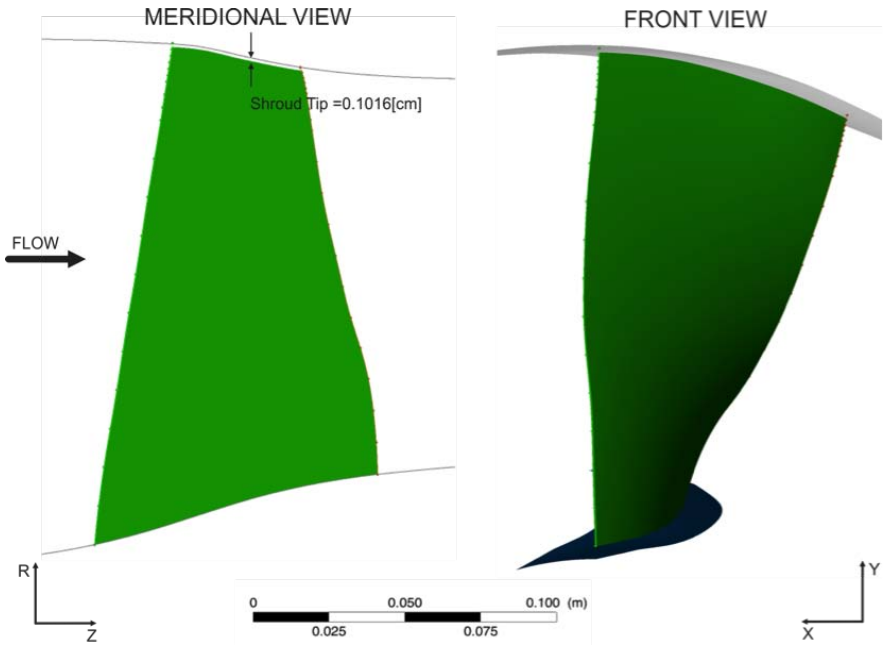

Figure 3.7: NASA Rotor 67 blade geometry (obtained from Abate, 2012).

3.4 CFD

3.4.1 Blade geometry

The geometry provided in NASA report [76] comprises 14 blade spanwise sections, which were formatted in a proper way to be given to ANSYS® TurboGrid in order to reconstruct the baseline geometry. The result of such operation is illustrated in Fig 3.7.

3.4.2 Flow solver and computational domain

In this section the numerical model set-up is described, which includes the computational grid and the CFD solver set-up.

Grid

As far as the numerical grid is concerned, the optimized Automatic Topology and Meshing tool (ATM) within ANSYS® TurboGrid v14.0 was used to generate a multi-block structured grid. As depicted in Fig 3.8, there are three blocks: inlet, passage and outlet.

The main grid parameters were deduced from those adopted in the validation analysis carried out in [1]. In particular, the structured grid of the passage block were created interpolating 10 spanwise layers, as those depicted in Fig 3.9. The topology is ATM based, which indeed does not match with any of the standard topologies. The target passage mesh size method with a target value of 1.7 M elements was prescribed.

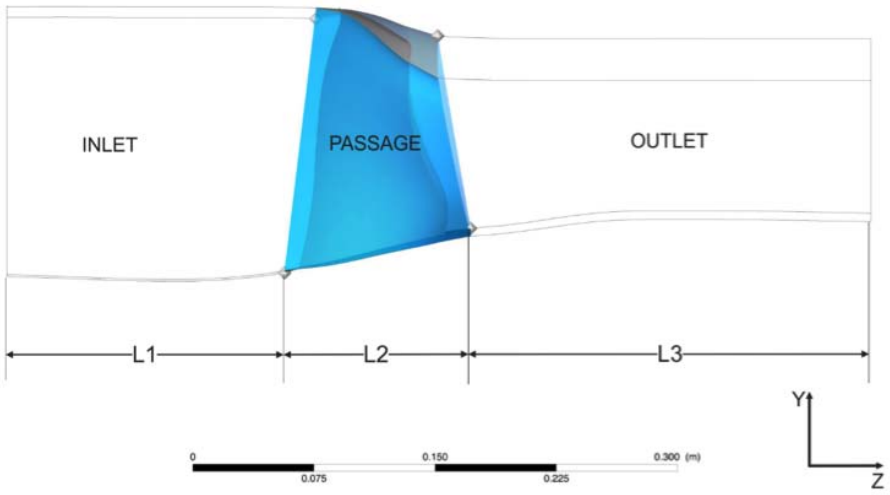

Figure 3.8: NASA rotor 67 computational domain (obtained from Abate, 2012).

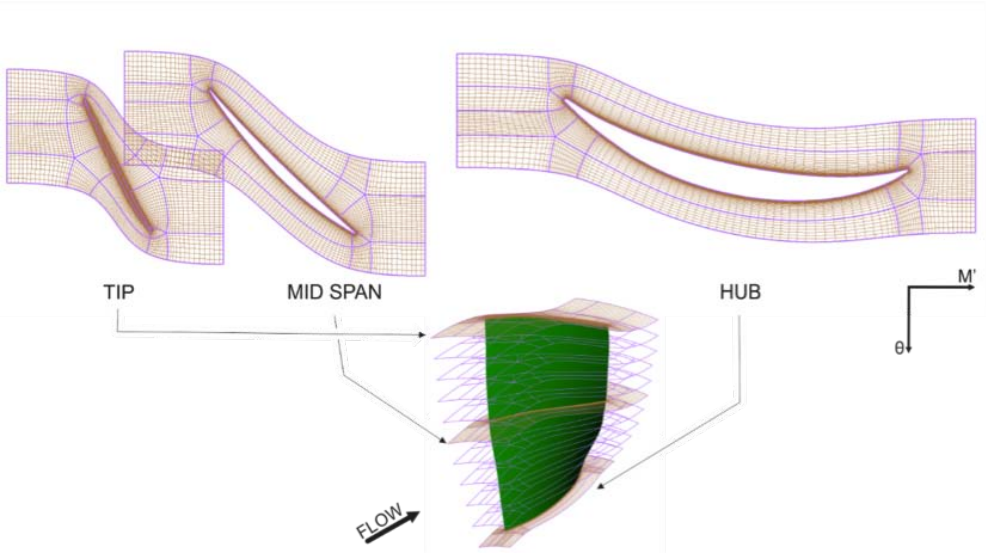

Figure 3.9: ANSYS® TurboGrid topology: layers of hub, midspan and tip section (obtained from Abate, 2012).

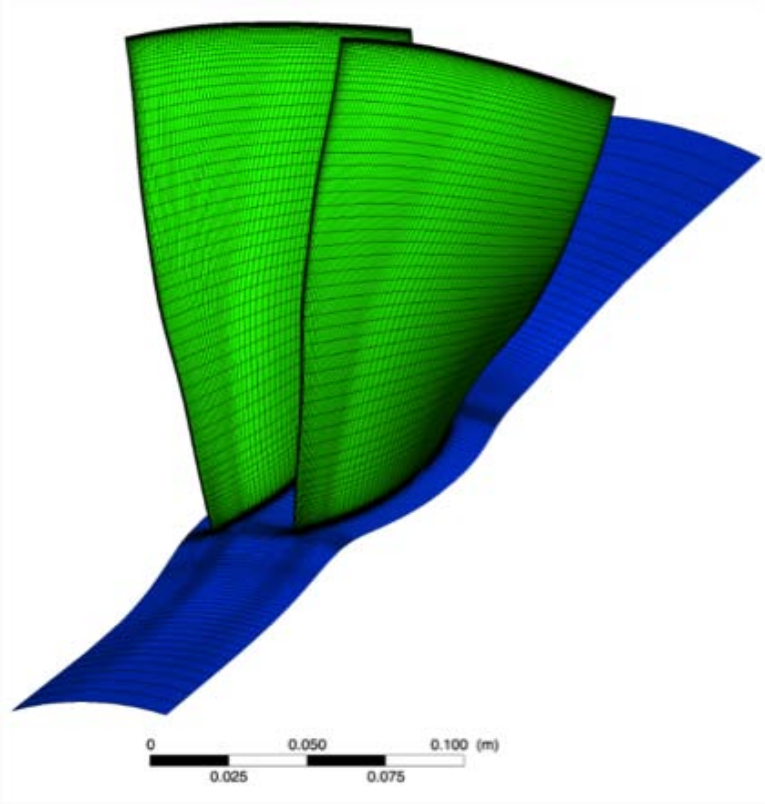

Figure 3.10: NASA rotor 67 computational grid (obtained from Abate, 2012).

The first layer height was selected in order to achieve a y+ lower than unity all over the wall surfaces imposing 2×10^6 as reference Reynolds number. In the spanwise direction 110 elements were adopted, in addition to 42 more nodes in the shroud tip region. As for the inlet and outlet blocks, H-grid topology with 28 and 34 streamwise elements respectively was selected. The resulting mesh was composed by 2.2 M elements, as illustrated in Fig 3.10, where the final computational grid is represented.

Flow solver set-up

The steady state 3-D flow field around the blade was computed by means of the commercial CFD code ANSYS® CFX v14.0, in which the Reynolds-averaged equations deduced form of the Navier-Stokes equations are solved using a finite-element based finite-volume method.

Computational analyses comprised one blade passage, and a periodic condition was applied on lateral passage surfaces. The flow was fully turbulent and the k-ω SST [61] turbulence model was adopted. All the computational domain rotated at Ω = -16073 [rpm] along the z axis. CFX-Pre set-up is summarized in Table 3.2: using this well-validated CFD model, described in detail in [1], two analyses for two different operating points, namely near-peak-efficiency point and near-choke point, were performed modifying the original boundary conditions of [1].

Table 3.2: ANSYS® CFX solver set-up.

ANSYS® CFX solver set-up		
Formulation	Steady State	
Domain	Material	Air Ideal Gas
	Domain Motion	-16073 @z-axis
	Reference Pressure	0 [atm]
	Heat Transfer	Total Energy
	Turbulence Model	k-ω SST + high speed
BC	Inlet	Inlet + frame stationary
		Subsonic
		Stationary Total Pressure 101128 [Pa]
		Direction normal to boundary
		Stationary Total Temperature 288.2 [K]
		Turbulence intensity 5%
	Outlet	Outlet + frame stationary
		Subsonic
		a) Average Static Pressure 104000 - 114000 [Pa]
		b) Mass Flow Rate
	Blade	Wall + no slip
		Adiabatic
	Periodic	Periodic
		Conservative Interface Flux
	Hub	Wall + no slip
		Rotating frame
		Adiabatic
	Shroud	Wall + no slip
		Rotating frame
		Counter Rotating wall
		Adiabatic
Solver Control	Advection Scheme	High resolution
	Turbulence Numerics	High resolution
	Timescale Control	Auto timescale

Since convergence was critical throughout all the calculation, a user function was implemented with the purpose of adapting the maximum timescale, which indeed is of utmost importance for calculation stability. In particular, at the beginning a value of 1×10^{-7} [s] was set, then it was increased up to 1×10^{-4} [s], for then return to lower values around 1×10^{-5} [s] before calculation was stopped.

The convergence was established when the RMS maximum residue was lower than 1×10^{-5} and the variables of interest had an asymptotic behaviour.

3.5 MIXING

As described in Section 2.2, throughflow methods, and hence SLC methods themselves, rely, among others, on the assumption of inviscid axisymmetric flow. Although this assumption significantly simplifies calculation leading to excellent even approximate results, it neglects the effect of exchange of mass, momentum, and energy between streamtubes, thus leading often to serious errors. This transport phenomenon is usually referred to as spanwise mixing, and its formulation and implementation in SLC programs is a problem which has been addressed to by researchers since the early 1980s.

Including spanwise mixing into a subroutine of an SLC method as SOCRATES should represent an improvement of flow behaviour predictions against experiments compared to the calculation without mixing. As described in the opening introduction, Chapter 1, this dissertation aims to study the applicability and congruity with numerical analyses of a spanwise mixing model, comparing its results with those obtained from unmixed calculations, specifically from SOCRATES, and from viscous 3-D CFD calculations.

The subroutine developed and investigated here will be referred to as MIXING. At this first stage, MIXING subroutine is intended to be called by the throughflow model after the inviscid distributions of flow properties at each QO have been calculated. MIXING requires, as input, flow properties profiles at the rotor blade trailing edge, obtained from the throughflow inviscid calculation, and then propagates these very distributions through the following duct region, giving as output the mixed flow properties profiles at each QO. MIXING does not operate within the rotor blade passage, since mixing effects are thought to be already taken into account in the blade action on the flow.

As mentioned above, many spanwise mixing models have been proposed by several authors, but the main important models are recognised to be that developed by Adkins and Smith [4] and that by Gallimore and Cumpsty [31]. The debate revolving around the relative importance of turbulent diffusion and secondary flow in the mixing phenomenon in multistage axial-flow compressors concluded that both turbulent diffusion and convective secondary flows play a significant role in the transport process, and that they should be then both considered in a mixing analysis. However, at transonic Mach numbers secondary flows may achieve even greater importance than turbulence. For this reason, the model chosen to be implemented in this dissertation, for the specific test case of NASA Rotor 67, is the mixing analysis proposed by Adkins and Smith [4].

MIXING is substantially the application of the Adkins and Smith mixing equation 2.8, reported here for simplicity,

$$\frac{\partial \Theta}{\partial z} = \beta \, \frac{\partial^2 \Theta}{\partial r^2} \tag{3.1}$$

to the duct region of R67 propagating after the rotor blade row. Mixing equation 3.1 is basically a diffusion-type differential equation relating the first and second derivatives, $\partial\Theta/\partial z$ and $\partial^2\Theta/\partial r^2$, of the generic flow property Θ in the meridional and spanwise directions through a mixing coefficient β.

As for the spanwise mixing models, there are several ways for evaluating the mixing coefficient, each of them based on a specific formulation. MIXING includes three different definitions for the mixing coefficient. First, the mixing coefficient formulation proposed by Adkins and Smith [4] based on secondary flows:

$$\beta_{sf} = \frac{z}{a} \int_{pitch} \left(\frac{V_r}{V_z} \right)^2 r d\theta \tag{3.2}$$

Second, that formulated by Gallimore and Cumpsty [31] based on turbulence diffusion:

$$\frac{\epsilon_t}{L_s V_z} = 0.4 \left(\frac{t}{L_s} \right) \left[\frac{\omega \, (t/L_s)}{3\phi^2} \right]^{\frac{1}{3}} \tag{3.3}$$

Third, the mixing coefficient obtained by summing the two former formulations, in order to take into account both the effects resulting in the mixing process:

$$\beta = \beta_{sf} + \beta_t \tag{3.4}$$

where β_t is given by

$$\beta_t = \frac{\epsilon_t}{V_z}$$

Regarding the calculation of the Gallimore and Cumpsty mixing coefficient, whose formulation involves the computation of the loss coefficient ω, defined by Gallimore and Cumpsty as

$$\omega = \frac{\Delta p_l}{\rho U_m^2}$$

with the loss in stage static pressure rise Δp_l given by

$$\Delta p_l = \Delta p_i - \Delta p_a$$

where Δp_i is the ideal stage static pressure rise and Δp_a is the actual stage static pressure rise, the ideal static pressure rise has been calculated in the hypothesis that the relative total pressure after the rotor blade passage is equal to the relative total pressure ahead of the rotor, $P_{0,w\,2} = P_{0,w\,1}$. In this manner, losses due to viscosity are somewhat neglected in the computation of Δp_i. Of course, in transonic compressors there are losses due to shock as well, but in the present analysis their contribution has been neglected.

In both S-M-C and M-C analyses, MIXING computes mixed flow properties distributions after R67 rotor blade trailing edge solving the transport equation 3.1 for the same quantities with values of the mixing coefficient defined by equations 3.2, 3.3, and 3.4, and compares the results with those obtained from SOCRATES and CFD.

From specific literature, it appears not very clear which flow properties are to be mixed: Adkins and Smith [4] in their analysis studied the effect of spanwise mixing on stagnation pressure P_0, stagnation temperature T_0, and angular momentum (rC_θ), while Gallimore and Cumpsty [31] mixed stagnation enthalpy h_0, entropy s, and angular momentum (rC_θ). In order to study spanwise mixing effects on flow properties and investigate Adkins and Smith mixing equation features, MIXING analyses the behaviour of total pressure P_0, total temperature T_0, static pressure P, static temperature T, and angular momentum (rC_θ), under the action of radial transport.

3.5.1 Finite difference method

To obtain the flow properties distribution including the effect of radial transport, MIXING solves the mixing equation 3.1 through a discretization of the computational field representing the duct region of R67, using the finite difference scheme described below.

MIXING is meant to be a subroutine to be called by SOCRATES after the inviscid computation is completed, so it is very important that its implementation does not affect the computational time negatively. For this reason, the transport equation is solved by means of a finite difference explicit method, which is faster than implicit methods. Using a forward difference for the axial coordinate z and a second-order central difference for the radial coordinate r, as depicted in Fig 3.11, equation 3.1

$$\frac{\partial \Theta}{\partial z} = \beta \, \frac{\partial^2 \Theta}{\partial r^2}$$

is discretized as follows.

The first derivative of flow property Θ along the axial direction z at the node (i, j), with i = i_{TE},..., $i_{R67,OUT}$ and j = j_{HUB}, ..., j_{CASING}, where i_{TE} and $i_{R67,OUT}$ are the axial position at the rotor blade trailing edge and at the compressor outlet respectively, and j_{HUB} and j_{CASING} are the radial position at hub and casing, is given by

$$\left(\frac{\partial \Theta}{\partial z}\right)_{i,j} = \frac{\Theta_{i,j} - \Theta_{i-1,j}}{z_{i,j} - z_{i-1,j}}$$

The second derivative along the radial direction r can be written as

$$\frac{\partial^2 \Theta}{\partial r^2} = \frac{\partial}{\partial r}\left(\frac{\partial \Theta}{\partial r}\right)$$

If the gradient of flow property Θ is constant then this term is zero and no spanwise mixing takes place, as the spanwise transfer due to diffusion of Θ from the streamline with the higher value is compensated by the spanwise transfer from the adjacent streamline with the lower value.

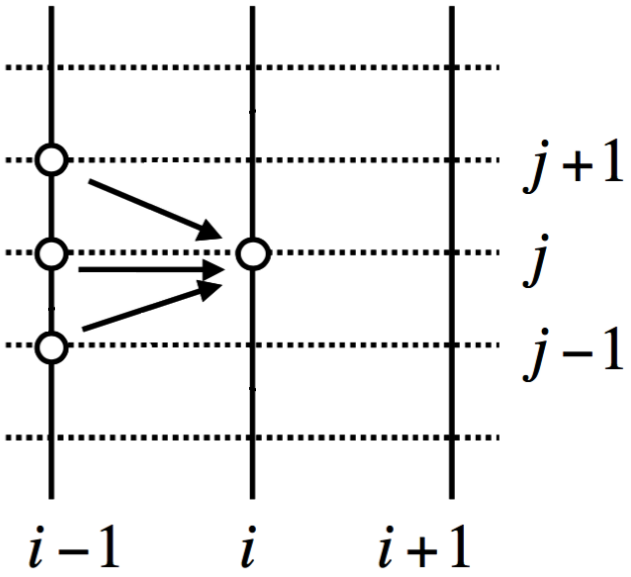

Figure 3.11: Finite difference scheme (obtained and modified from Casey and Robinson, 2008).

An approximate value of this second derivative at the node (i, j) is

$$\left(\frac{\partial^2\Theta}{\partial r^2}\right)_{i,j} = \frac{2}{r_{i,j+1} - r_{i,j-1}} \left(\frac{\Theta_{i-1,j+1} - \Theta_{i-1,j}}{r_{i,j+1} - r_{i,j}} - \frac{\Theta_{i-1,j} - \Theta_{i-1,j-1}}{r_{i,j} - r_{i,j-1}} \right)$$

so that the discretized mixing equation becomes

$$\frac{\Theta_{i,j} - \Theta_{i-1,j}}{z_{i,j} - z_{i-1,j}} = \frac{2\beta_{i,j}}{r_{i,j+1} - r_{i,j-1}} \left(\frac{\Theta_{i-1,j+1} - \Theta_{i-1,j}}{r_{i,j+1} - r_{i,j}} - \frac{\Theta_{i-1,j} - \Theta_{i-1,j-1}}{r_{i,j} - r_{i,j-1}} \right)$$

where it is possible to evaluate the local mixing coefficient $\beta_{i,j}$ at the node (i, j). This recurrence expression of the transport equation allows to obtain $\Theta_{i,j}$ from the other values this way:

$$\Theta_{i,j} = \Theta_{i-1,j} + 2\beta_{i,j} \frac{z_{i,j} - z_{i-1,j}}{r_{i,j+1} - r_{i,j-1}} \left(\frac{\Theta_{i-1,j+1} - \Theta_{i-1,j}}{r_{i,j+1} - r_{i,j}} - \frac{\Theta_{i-1,j} - \Theta_{i-1,j-1}}{r_{i,j} - r_{i,j-1}} \right) \quad (3.5)$$

Equation 3.5 is the final formulation of the Adkins and Smith mixing equation, and represents the heart of MIXING.

Hence, with this recurrence relation, and knowing the flow properties distributions at axial coordinate i-1, it is possible to obtain the corresponding distribution at axial coordinate i. The values of the flow property at the endwalls, $\Theta_{i,j_{HUB}}$ and $\Theta_{i,j_{CASING}}$, must be replaced by the boundary conditions, which is a zero gradient boundary condition given by

$$\frac{\partial\Theta}{\partial r} = 0$$

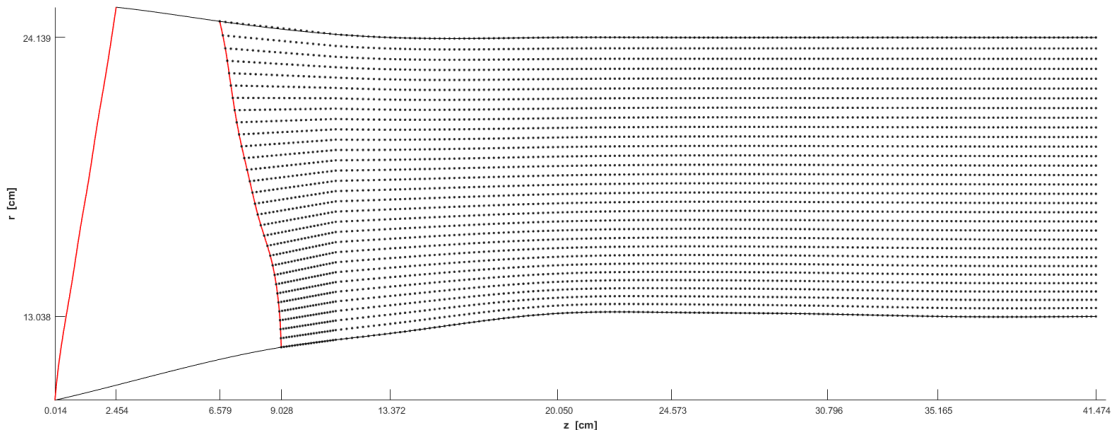

Figure 3.12: MIXING computational grid.

that, using a forward finite difference discretization for the hub and a backward finite difference discretization for the casing, becomes

$$\Theta_{i,j_{HUB}} = \frac{4\Theta_{i,j_{HUB}+1} - \Theta_{i,j_{HUB}+2}}{3} \qquad \Theta_{i,j_{CASING}} = \frac{4\Theta_{i,j_{CASING}-1} - \Theta_{i,j_{CASING}-2}}{3} \tag{3.6}$$

As can be seen in Fig 3.11, the value of flow property Θ at node (i, j) is the result of three contributions from the nodes of the upstream axial station, namely nodes (i-1, j+1), (i-1, j), and (i-1, j-1). For the endwalls, the value of the flow property Θ is given by the contribution of the two adjacent nodes at the same axial position.

This explicit method is known to be numerically stable and convergent whenever it is verified that

$$1 - 2\beta_{i,j} \frac{z_{i,j} - z_{i-1,j}}{(r_{i,j+1} - r_{i,j})(r_{i,j} - r_{i,j-1})} \geq 0$$

The numerical errors are proportional to the increment in the axial position and the square of the increment in the radial position, $\delta\Theta = O(\delta z) + O(\delta r^2)$.

3.5.2 Set-up

Fig 3.12 illustrates the computational grid used by MIXING for solving the transport equation in the duct region after R67 rotor blade row. The mesh is composed of 179 QOs, and each QO is subdivided into 31 nodes, with a maximum and minimum spatial resolution in the axial direction of 0.1856 and 0.1086 cm,and a maximum and minimum spatial resolution in the radial direction of 0.5581 and 0.3348 cm. The mesh is refined in the axial direction compared to that of SOCRATES, particularly in the hub region near the blade trailing edge. MIXING, being thought as a logical extension of SOCRATES SLC program, maintains its division in domain ducts.

In S-M-C analyses, MIXING propagates flow properties distributions throughout the considered duct region, solving the transport equation for total and static quantities, and angular momentum, with flow properties profiles at rotor blade trailing edge

obtained from SOCRATES as initial conditions, so that, at rotor blade row exit SOCRATES and MIXING have the very same values of quantities. The mixing coefficient is evaluated from values predicted by SOCRATES as well. The results obtained from the mixing analysis are compared to those from the unmixed solution from SOCRATES and those from the viscous CFD analysis, which contains itself the mixing phenomenon in the Navier-Stokes equations. In this context, CFD results are considered as representative of the actual behaviour of the flow through R67. The results of this analysis for two different operating points, namely NPE and NC, are presented in the next chapter at inlet and outlet of each domain duct belonging to the duct region, along with the analysis of the error.

Since further experimental data was not available, M-C analyses have been performed to study the congruity of the transport equation with physical reality. In this kind of analyses, MIXING operates similarly to S-M-C calculations, but it computes, for both NPE and NC operating points, the flow properties distributions using as initial conditions and as parameters for the evaluation of the mixing coefficient only data obtained from CFD.

CHAPTER 4

Results

4.1 Introduction

In this section the results obtained from the S-M-C and M-C analyses for both NC and NPE operating points of NASA Rotor 67 are presented.

First of all, it is important to notice that the following mixing analyses are premised on the results obtained from a 2-D Streamline Curvature throughflow program developed at Cranfield University, UK, known as SOCRATES [63–68, 80–82], and a well-validated CFD computation described in [1]. A comparison of the solution of these

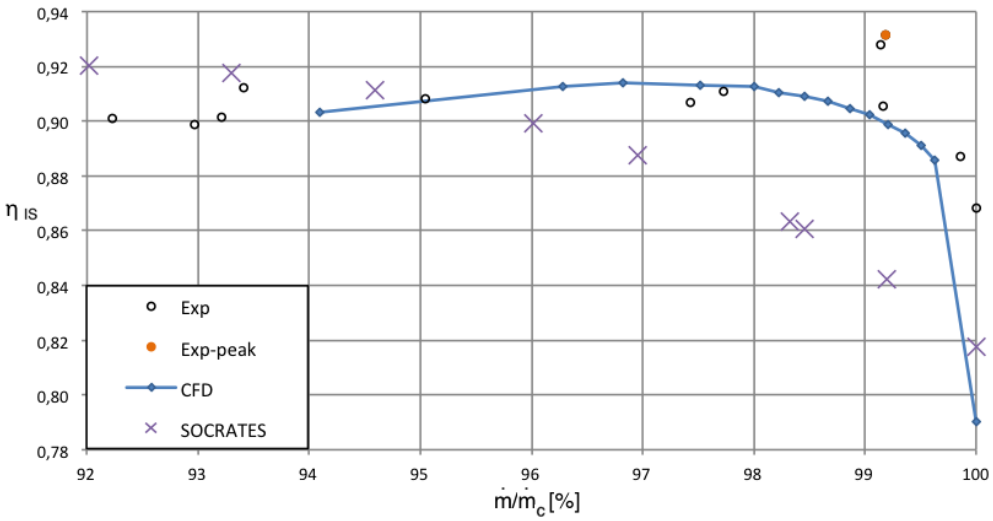

Figure 4.1: NASA Rotor 67 isentropic efficiency-mass flow ratio chart. Circles are experiment, solid line with squares is CFD, crosses are SOCRATES.

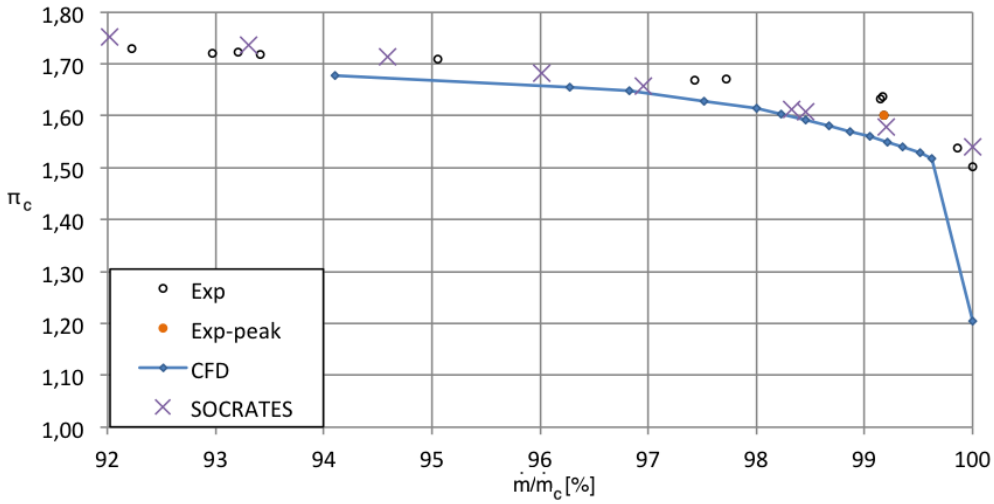

Figure 4.2: NASA Rotor 67 pressure ratio-mass flow ratio chart. Circles are experiment, solid line with squares is CFD, crosses are SOCRATES.

models will be made, in order to investigate the implemented spanwise mixing model, MIXING, validity and applicability.

Figs 4.1 and 4.2 illustrate NASA Rotor 67 isentropic efficiency-mass flow ratio and pressure ratio-mass flow ratio charts, where the mass flow ratio is relative to the mass flow rate at choke condition. In the same figures, experimental data from [76] are reported. It is apparent that some differences in the predictions of SOCRATES and CFD models with the measurements, and in the predictions of SOCRATES itself with CFD analysis. Although these discrepancies may appear relevant and quite concerning, for the purpose of the present study they will be somewhat neglected. It is nonetheless clear that, whenever the variance between SOCRATES and CFD is too large, MIXING subroutine cannot provide for the disagreement and it is improbable to a certain extent that MIXING, in this context, actually represents an improvement of the inviscid solution toward a better agreement with numerical results from viscous calculation.

If these conditions of initial disagreement between SOCRATES and CFD are not met, it is possible to compare the three predictions and derive some constructive assessments in the frame of spanwise mixing phenomenon in throughflow calculations for multistage axial-flow compressors.

As explained in Chapter 3, two different kinds of analysis have been performed. S-M-C analyses compare calculations obtained from SOCRATES, MIXING, and CFD, where MIXING takes as input data from SOCRATES. The objective of this kind of analysis is to verify if the spanwise mixing model implemented can effectively be considered an improvement of the unmixed prediction.

On the other hand, since further comparison baseline was not available, M-C analyses have been carried out, in order to investigate the applicability of the chosen spanwise mixing model and its congruity with the actual behaviour of the flow. In M-C analyses, MIXING takes as input data exclusively from CFD computations, propagat-

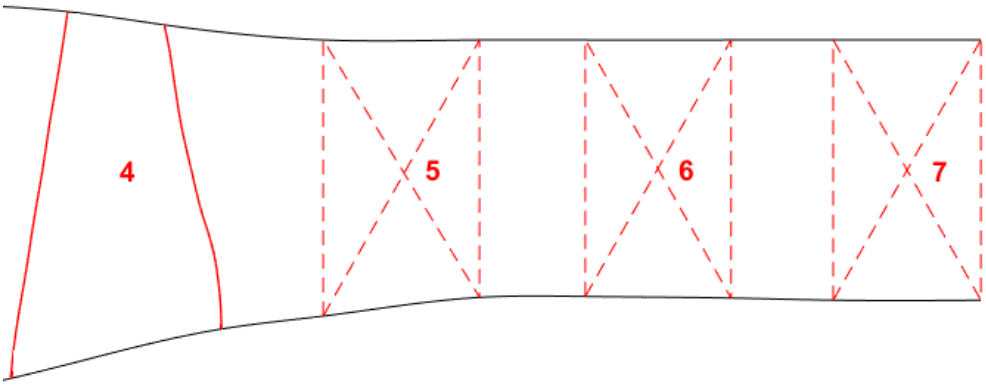

Figure 4.3: MIXING computational field and domain ducts.

ing CFD results from rotor blade trailing edge throughout the remaining duct region of the compressor.

For both S-M-C and M-C analyses, MIXING functioning has been investigated at two compressor operating conditions. Near choke operating point refers to a mass flow rate ratio $\dot{m}/\dot{m}_c$ = 100%, while near peak efficiency condition is denoted by a mass flow ratio of 98.456%. It is important to notice that from experimental data the peak efficiency condition, at a rotational speed Ω = 16073 rpm, occurs when $\dot{m}/\dot{m}_c$ = 99.184%, while, according to CFD computation, the peak efficiency condition occurs at a mass flow ratio of 97.518%.

MIXING results are presented as flow property profiles all along the span at a certain axial station, from rotor outlet to domain duct 7 inlet, which are represented in Fig 4.3. Domain duct 7 outlet has not been considered in analysis comparison, since CFD boundary conditions were applied there and could therefore affect the comparison itself. Flow properties distributions obtained from MIXING are represented in percentage to their average value at rotor blade trailing edge. In particular, in S-M-C analyses this average value is that obtained from SOCRATES, in M-C analyses the average value is referred to CFD.

In addition to the comparison of flow quantities distributions, MIXING predictions reliability is studied by means of the analysis of the mean absolute error, defined as the absolute value of the average difference between CFD result and that from the model considered. For example, for SOCRATES calculation, the mean absolute error is given by $|\delta\Theta_{SOCRATES}| = |\overline{\Theta_{CFD} - \Theta_{SOCRATES}}|$. The mean absolute error is normalised with respect to CFD average local value for all the analysis, and it is expressed in percentage.

Another important parameter is the local error, defined simply as the difference between CFD predictions and those from the other calculations. For instance, for MIXING computation using the Adkins and Smith mixing coefficient calculation, the local error is $\delta\Theta_{MIXING,A\&S} = \Theta_{CFD} - \Theta_{MIXING,A\&S}$. Information on the local error can be deduced from flow properties spanwise distribution graphs as well, while for the mean absolute error it is presented in histograms.

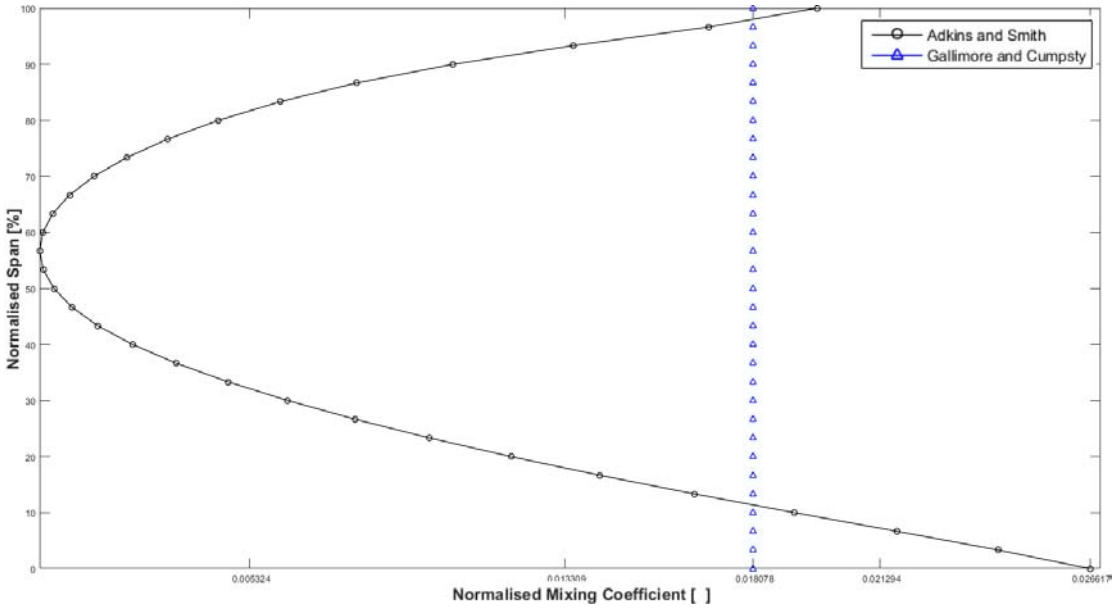

Figure 4.4: S-M-C near choke analysis normalised mixing coefficient. Solid black line with circles is Adkins and Smith formulation, solid blue line with triangles is Gallimore and Cumpsty formulation.

4.2 S-M-C analysis

As described above, in S-M-C analyses, MIXING propagates flow properties distributions through the whole duct region, solving the transport equation for total pressure, total temperature, static pressure, static temperature, and angular momentum.

The initial conditions are represented by flow properties profiles at rotor blade trailing edge obtained from SOCRATES: in this way, at rotor blade row exit SOCRATES and MIXING have the very same values of quantities, as can be seen in the following figures illustrating the comparison between SOCRATES, MIXING, and CFD at the inlet and outlet of each domain duct. For simplicity, these figures report results only at rotor outlet, domain duct 5 inlet, domain duct 6 inlet and domain duct 7 inlet. The mixing coefficient is evaluated from values predicted by SOCRATES as well.

The results obtained from the mixing analysis are compared, using different mixing coefficient formulations, to those from the unmixed solution from SOCRATES and those from the viscous CFD analysis, which contains itself the action of in the Navier-Stokes equations. As it has already been mentioned, CFD results are considered as representative of the actual behaviour of the flow through R67.

The results of this analysis for two different operating points, namely NPE and NC, are now presented in figures composed of three columns referring to MIXING calculations each involving a specific mixing coefficient formulation. In particular, the first column refers to the Adkins and Smith mixing coefficient, the second column refers to that by Gallimore and Cumpsty, and the third represent mixing calculations including both the previous mixing coefficient definitions.

In addition to this, the analysis of the error is carried out below. The flow properties distributions at each domain duct are reported in percentage with respect to SOCRATES average value at rotor blade trailing edge. Histograms dealing with the mean absolute error are presented in percentage to local CFD average value.

4.2.1 Near choke operating point

Fig 4.4 illustrates the normalised spanwise distribution of the mixing coefficient at near choke condition for both models by Adkins and Smith, and Gallimore and Cumpsty. It can be noticed that, as expected from the two different formulations, the normalised Gallimore and Cumpsty mixing factor is constant all along the span and in the axial direction as well, while that from Adkins and Smith model presents a spanwise distribution with a minimum in the core region, since secondary velocities there are very small compared to axial velocity.

From the mixing coefficient distributions, it is to be expected that, in the mixing analysis with the Adkins and Smith mixing coefficient, the flow property profiles will be mixed principally at the endwall regions, while in the core region the quantity distributions will slightly differ from their initial value at blade rotor trailing edge. In the mixing analysis involving the Gallimore and Cumpsty mixing coefficient, the effect of mixing is rather evident along the whole span, in particular in the core region. This is the logical consequence of mixing coefficient formulations, which are in agreement with the physical principle they are based on: the Adkins and Smith mixing coefficient is directly calculated from secondary and axial velocities, while the Gallimore and Cumpsty mixing coefficient relies on turbulence magnitude.

Fig 4.5 reports the results of MIXING about stagnation pressure. The solid black line with circles represents SOCRATES calculation, the dotted blue one with triangles is CFD outcome, and the dashed red line with stars is referred to MIXING. The importance of this kind of graphs relies on their mutual comparison, in order to make it possible to visualise the flow property distribution evolution proceeding in the streamwise direction. For this reason, it is not really important the unit of measurement these graphs are presented with, as long as they are reported using the same scale, so that flow properties evolution can be appreciated.

The actual value of distributions is taken into consideration in the analysis of the error, where it plays a significant role in determining whether the spanwise mixing model is able to provide a better prediction with respect to the unmixed case.

In Fig 4.5 the mixing analysis features mentioned above are present. In particular, at rotor blade trailing edge, SOCRATES and MIXING present the same total pressure profile, which is then propagated streamwise. For the mixing calculation involving the Adkins and Smith mixing coefficient (A&S), total pressure profile is almost equal to the initial distribution for what concerns the core region, where secondary velocities are small, while total pressure distribution evolution at endwall regions is driven from the zero-gradient boundary condition.

MIXING results obtained by using the Gallimore and Cumpsty mixing coefficient (G&C) show a development of total pressure profile also in the core region, even if its

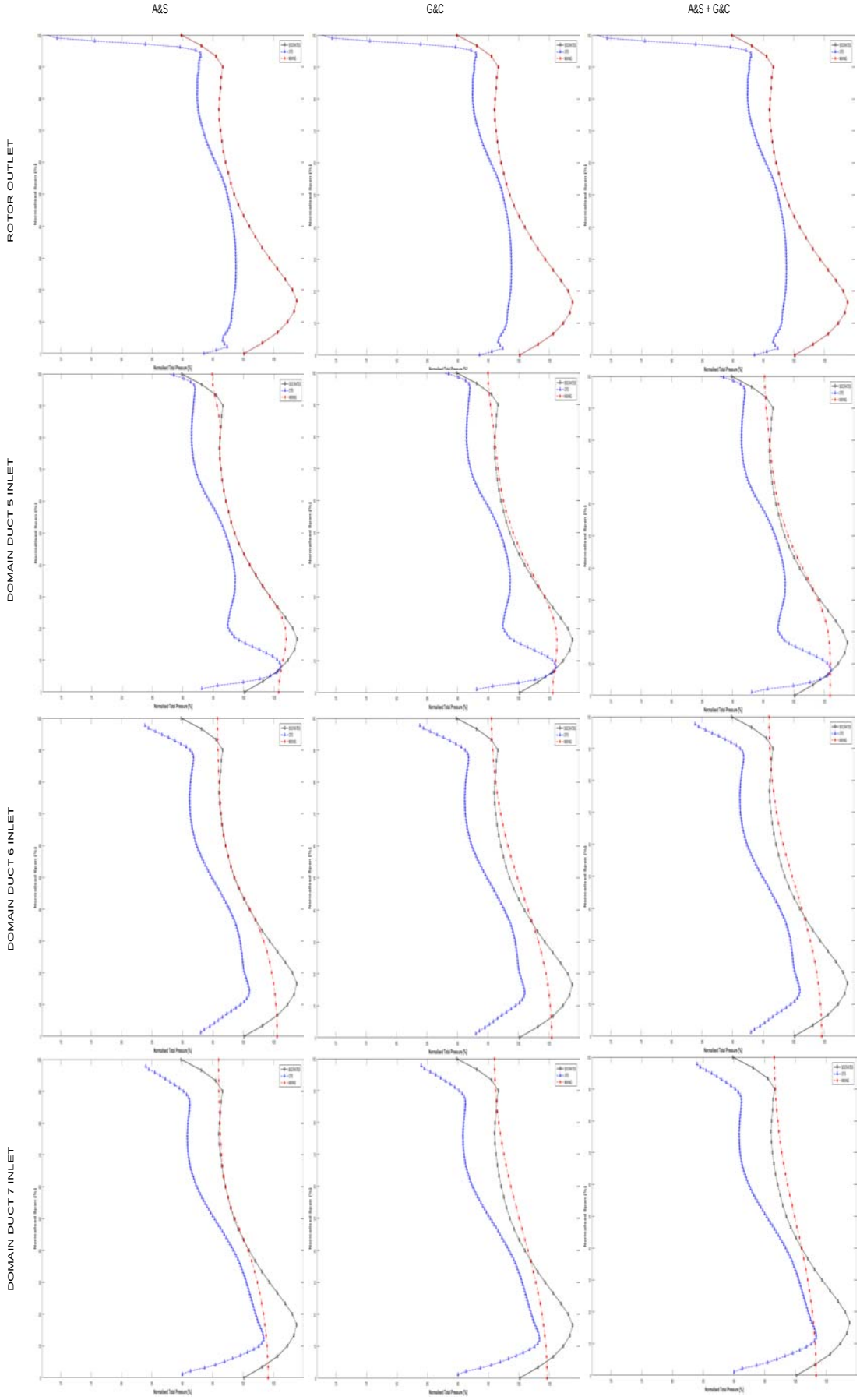

Figure 4.5: S-M-C near choke analysis results: total pressure. SOCRATES average value at rotor outlet is 147652 Pa. Solid black line with circles is SOCRATES, dotted blue line with triangles is CFD, dashed red line with stars is MIXING.

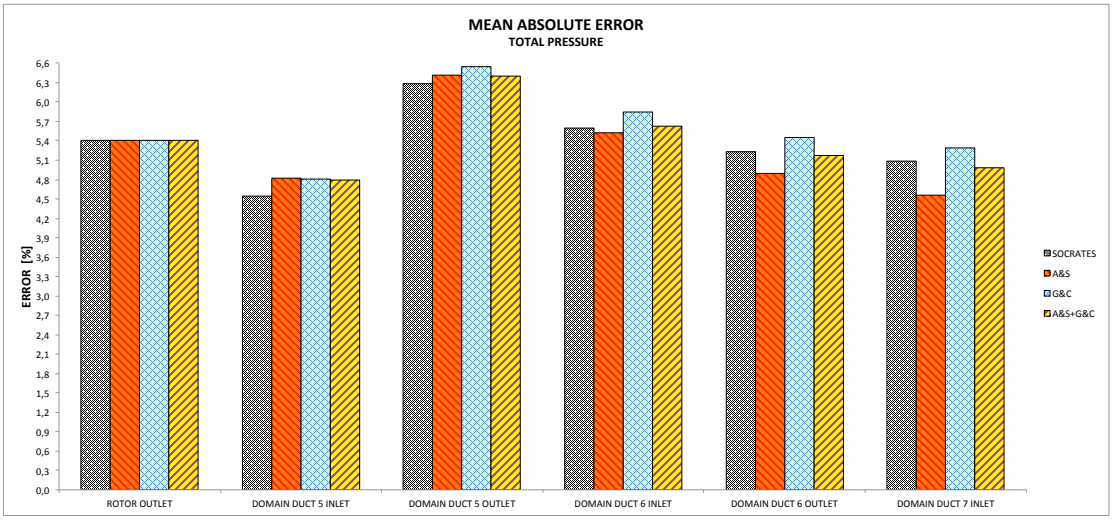

Figure 4.6: S-M-C near choke analysis mean absolute error: total pressure. Dotted black and white pattern is SOCRATES, orange pattern with descending red lines is MIXING A&S, green pattern with blue net is MIXING G&C, yellow pattern with ascending purple lines is MIXING A&S+G&C.

trend is almost the same as for the A&S mixing analysis. In either cases, total pressure profile exhibit an inflection point in the core region, which is reasonably caused by the endwall boundary condition. This consideration is not limited to total pressure distribution, but represents a recurring characteristic of MIXING results.

The third graph column of Fig 4.5 deals with MIXING calculation involving both A&S and G&C mixing coefficients summed together. Of course, using a higher value for the mixing coefficient brings to total pressure, and more generally flow property, distributions that are smoothed faster, being subjected to an increased mixing action.

Concerning the question whether, for the specific case of total pressure, MIXING effectively represents an improvement of SOCRATES inviscid prediction, the absolute mean error analysis provides a quantitative means of evaluation.

Fig 4.6 shows the mean absolute error in total pressure. First of all, it must be noticed that, since SOCRATES and MIXING have the very same stagnation pressure distribution at rotor blade trailing edge, they exhibit the same mean absolute error at rotor outlet. For this particular case, the mean absolute errors from SOCRATES and the three MIXING calculations are slightly distinct, with a difference lower than 0.5% with respect to CFD average local value. Even so, proceeding in the streamwise direction, A&S mixing analysis appears to get closer to CFD than SOCRATES prediction. This can be explained in regard to total pressure behaviour at endwalls, especially in the region near the hub, where the error $\delta P_{0,A\&S} = P_{0,CFD} - P_{0,A\&S}$ is lower than that resulting from SOCRATES. Nevertheless, it cannot be considered as a significant improvement of the unmixed analysis.

Fig 4.7 reports total temperature results from the mixing calculation. Also in this case, MIXING calculations exhibit the same behaviour described for total pressure results, but total temperature distribution at rotor blade trailing edge has a maximum-

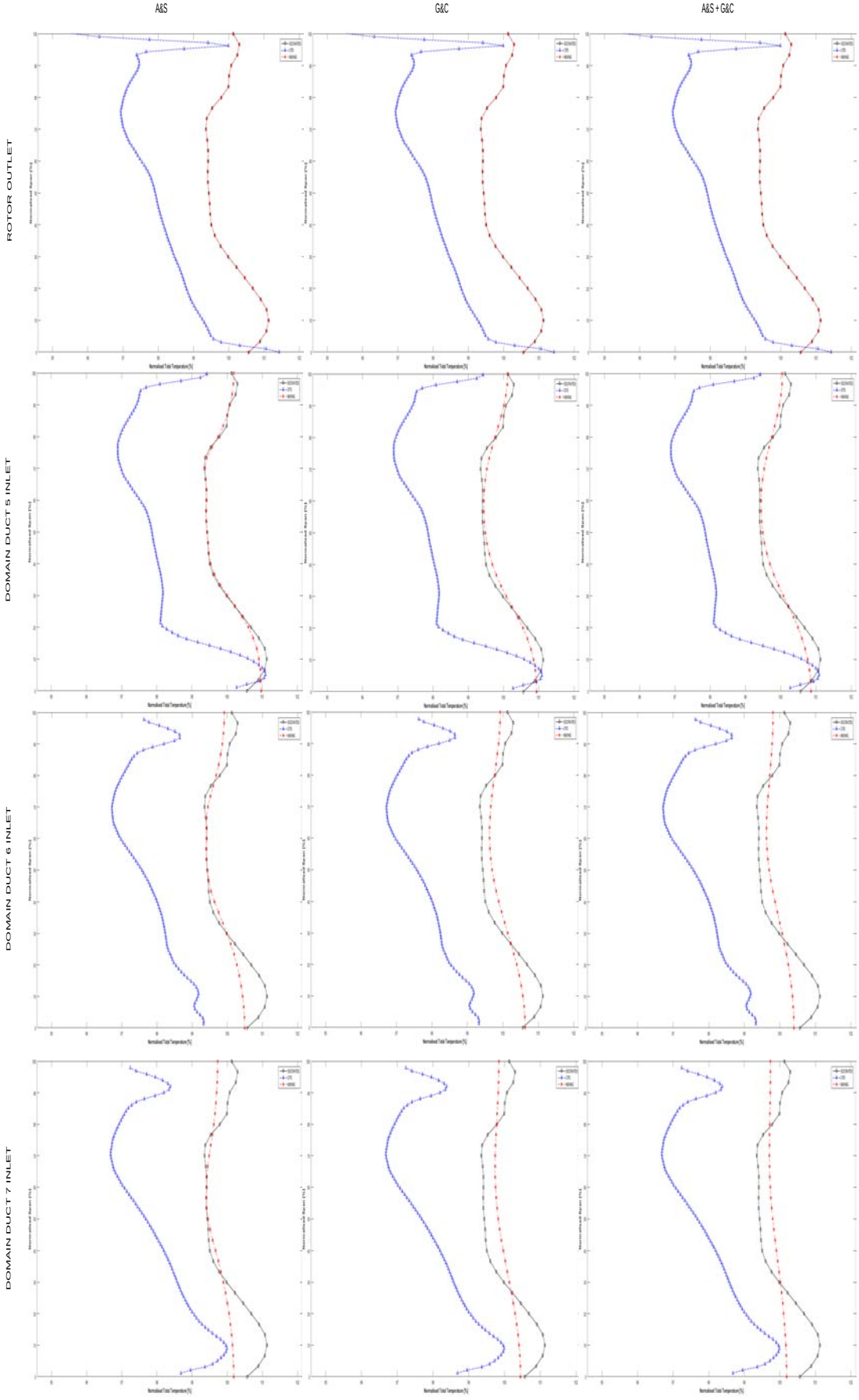

Figure 4.7: S-M-C near choke analysis results: total temperature. SOCRATES average value at rotor outlet is 327,3 K. Solid black line with circles is SOCRATES, dotted blue line with triangles is CFD, dashed red line with stars is MIXING.

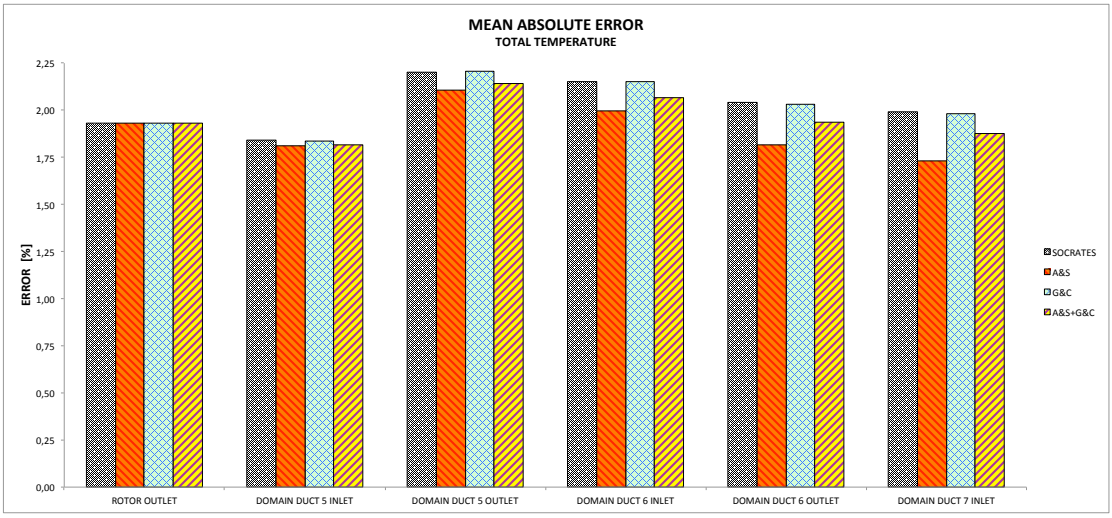

Figure 4.8: S-M-C near choke analysis mean absolute error: total temperature. Dotted black and white pattern is SOCRATES, orange pattern with descending red lines is MIXING A&S, green pattern with blue net is MIXING G&C, yellow pattern with ascending purple lines is MIXING A&S+G&C.

minimum variation lower than 2%, so that can be considered as almost mixed out. Mixing action drives total pressure profiles to become more uniform, especially in the A&S+G&C analysis, where the final total pressure distribution is practically a straight line.

The mean absolute error relative to total temperature is reported in Fig 4.8. Again, A&S computation seems that obtaining a better agreement with CFD results, but it is also apparent that for all the calculations the mean absolute error is very small. Therefore, there is no reason to consider, at this stage, the mixing analysis an improvement of the unmixed one.

It is important to notice that this last consideration is strictly connected to the error δT_0, which is negative for all the calculations. Since there are no intersection, at rotor blade trailing edge, between SOCRATES, and hence MIXING, and CFD profiles in the core region, the error is negative almost in the whole span, and the two initial profiles, namely SOCRATES and CFD profiles, are too separated to allow MIXING, which operates starting from SOCRATES, to propagate the flow property distribution toward a better agreement with CFD.

Even so, since SOCRATES is a SLC inviscid flow solver, its stagnation quantities profiles remain constant in duct regions, but this is not to be considered as representative of the actual behaviour of the flow, especially in a viscous environment with significant losses such as transonic compressors, as confirmed by CFD distributions in Figs 4.5 and 4.7. It is in this very context that a mixing analysis has to be performed.

A different situation appears concerning flow static quantities. Let us consider, for instance, Fig 4.9 reporting the mixing analysis results relative to static pressure. Now SOCRATES and CFD predictions are closer one another, even if there is a maximum-minimum variation of about 25% in profiles, which present at least one intersection in

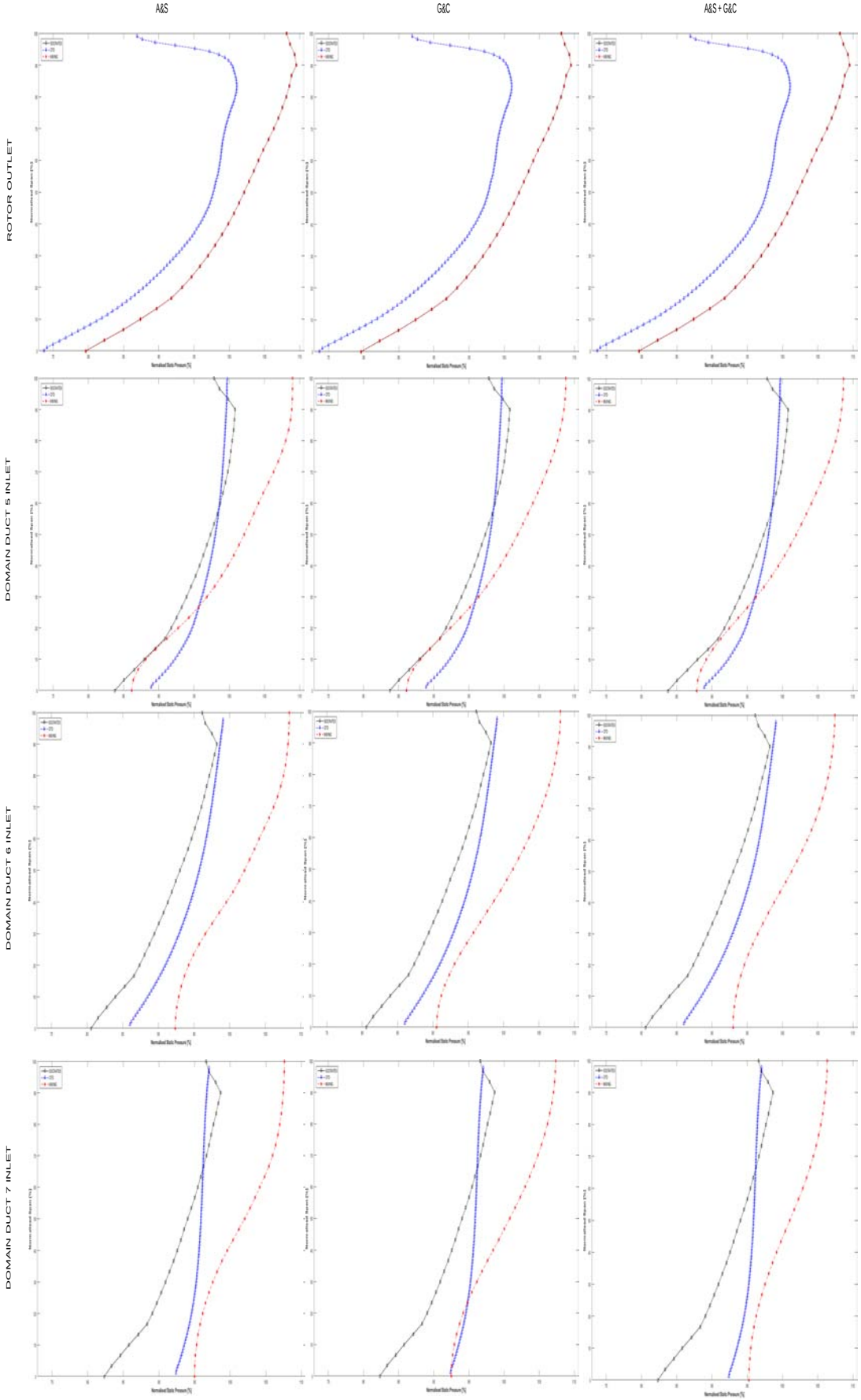

Figure 4.9: S-M-C near choke analysis results: static pressure. SOCRATES average value at rotor outlet is 101581 Pa. Solid black line with circles is SOCRATES, dotted blue line with triangles is CFD, dashed red line with stars is MIXING.

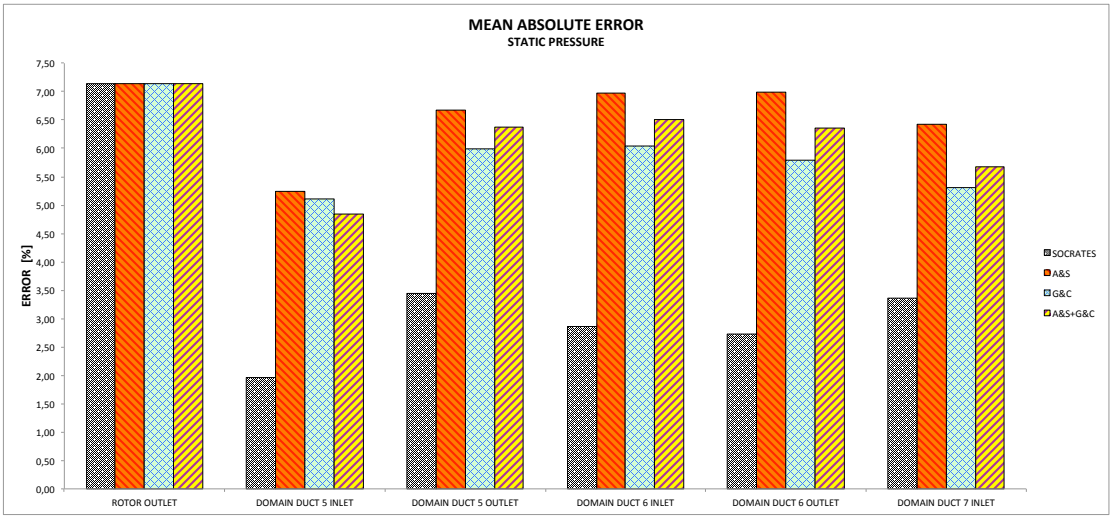

Figure 4.10: S-M-C near choke analysis mean absolute error: static pressure. Dotted black and white pattern is SOCRATES, orange pattern with descending red lines is MIXING A&S, green pattern with blue net is MIXING G&C, yellow pattern with ascending purple lines is MIXING A&S+G&C.

the core region along their evolution in the streamwise direction.

The effect of mixing, as well as the contribution due to the specific mixing coefficient formulation, can be investigated. In A&S mixing computation, static pressure distribution remains almost constant in the core region, evolving principally near the endwall under the action of the boundary condition. However, SOCRATES profile is no longer constant and moves in agreement with CFD results. In this case, A&S does not improve the inviscid solution, as can be seen from the absolute mean error in Fig 4.12.

Concerning with the other mixing computations on static pressure in Fig 4.9, turbulent mixing coefficient action allows the profiles to evolve in the core region with respect to their initial conformation, thus matching better CFD outcomes.

Globally the absolute mean errors are greater than that from SOCRATES, since they are almost double, but, with a local insight, it is evident that SOCRATES matches better CFD results in the region near the casing, while MIXING accords with CFD in the hub region. Therefore, it is thought that a solution obtained by considering the mutual interaction of SOCRATES and MIXING would improve best the agreement with CFD prediction with respect to the unmixed case.

The same considerations described for static pressure can be made concerning with static temperature. Fig 4.11 reports static temperature results of the mixing analysis. Again, there is at least one intersection between SOCRATES and CFD profiles, so that the error $\delta T_{SOCRATES}$ is not always negative. Unfortunately, this is not true for the distributions obtained from MIXING, whose error is negative through the whole span, except for the hub region.

There MIXING is in accordance with CFD, but it is the boundary condition action,

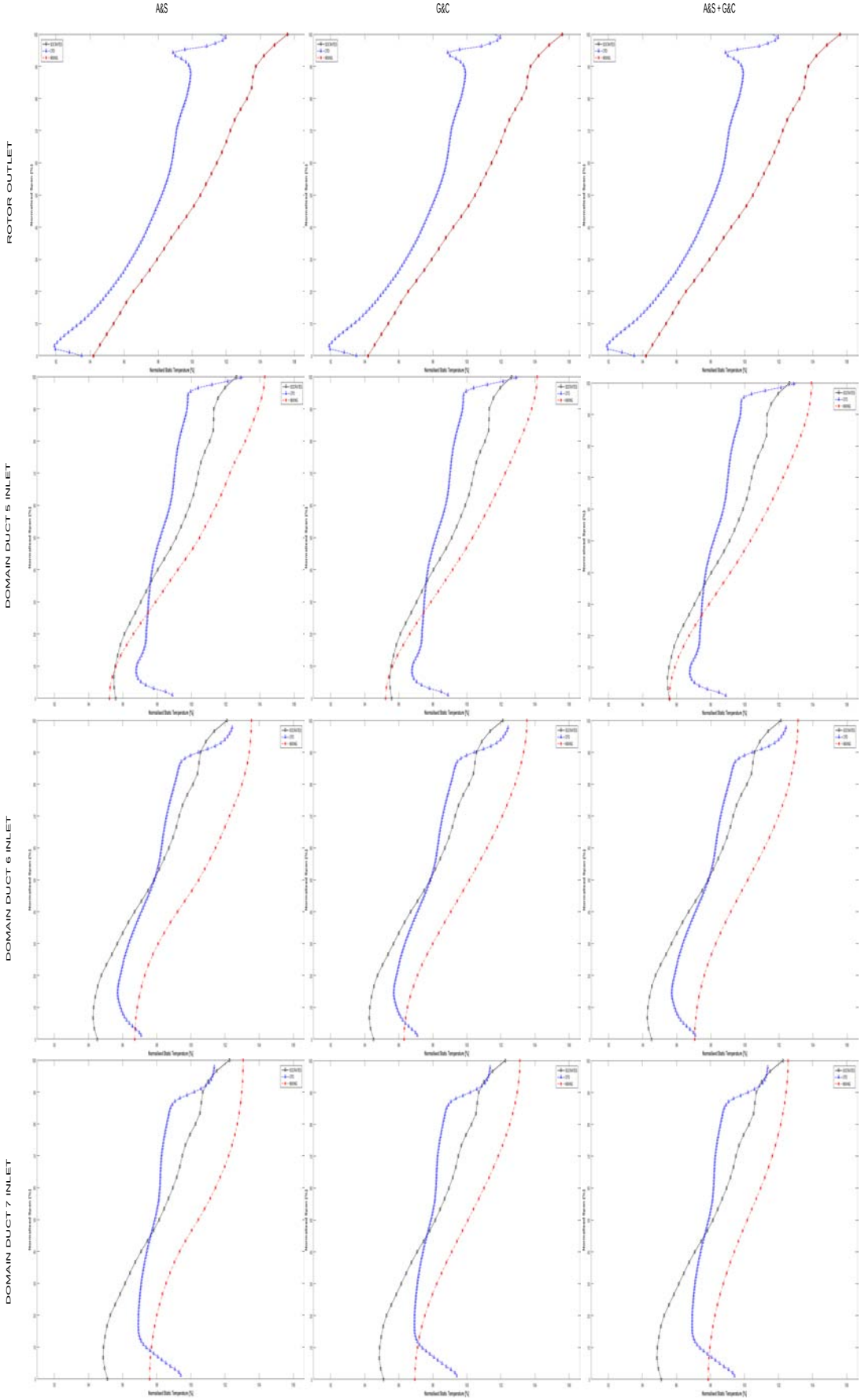

Figure 4.11: S-M-C near choke analysis results: static temperature. SOCRATES average value at rotor outlet is 293,5 K. Solid black line with circles is SOCRATES, dotted blue line with triangles is CFD, dashed red line with stars is MIXING.

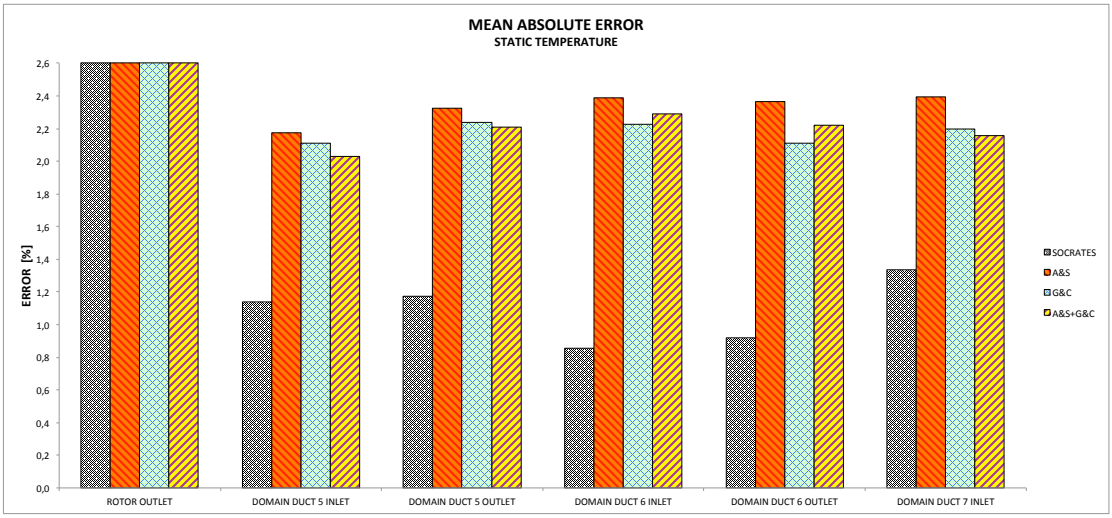

Figure 4.12: S-M-C near choke analysis mean absolute error: static temperature. Dotted black and white pattern is SOCRATES, orange pattern with descending red lines is MIXING A&S, green pattern with blue net is MIXING G&C, yellow pattern with ascending purple lines is MIXING A&S+G&C.

rather than that of the transport equation, that drives mixing analysis solution this way.

The absolute mean error histogram, represented in Fig 4.12, shows that the absolute mean errors from MIXING are almost double than those from SOCRATES, but it must be noticed that they are about 2.5%, while CFD maximum-minimum initial variation is about 8%. Therefore, for the specific case of static temperature, each calculation gives reasonable results, eve if it is still thought that the best agreement with CFD would result from an integration of SOCRATES and MIXING, operated in an iterative way.

The last flow quantity to be analysed is angular momentum. The relative mixing analysis results are illustrated in Fig 4.13. Similarly to the case of stagnation pressure and temperature, SOCRATES and CFD profiles are too separated starting from the rotor blade trailing edge, so that the error $\delta(rC_\theta)$ for both SOCRATES and MIXING is negative all along the span, and the mixing analysis cannot improve the inviscid solution, since it is operating referring to a too different initial average angular momentum value.

Here, the absolute mean error in Fig 4.14 is more significant, with values of about 20%, while CFD maximum-minimum variation at domain duct 7 inlet is of the same magnitude. Therefore, MIXING cannot be considered an improvement of SOCRATES solution, since SOCRATES prediction itself it very different in regard to CFD one.

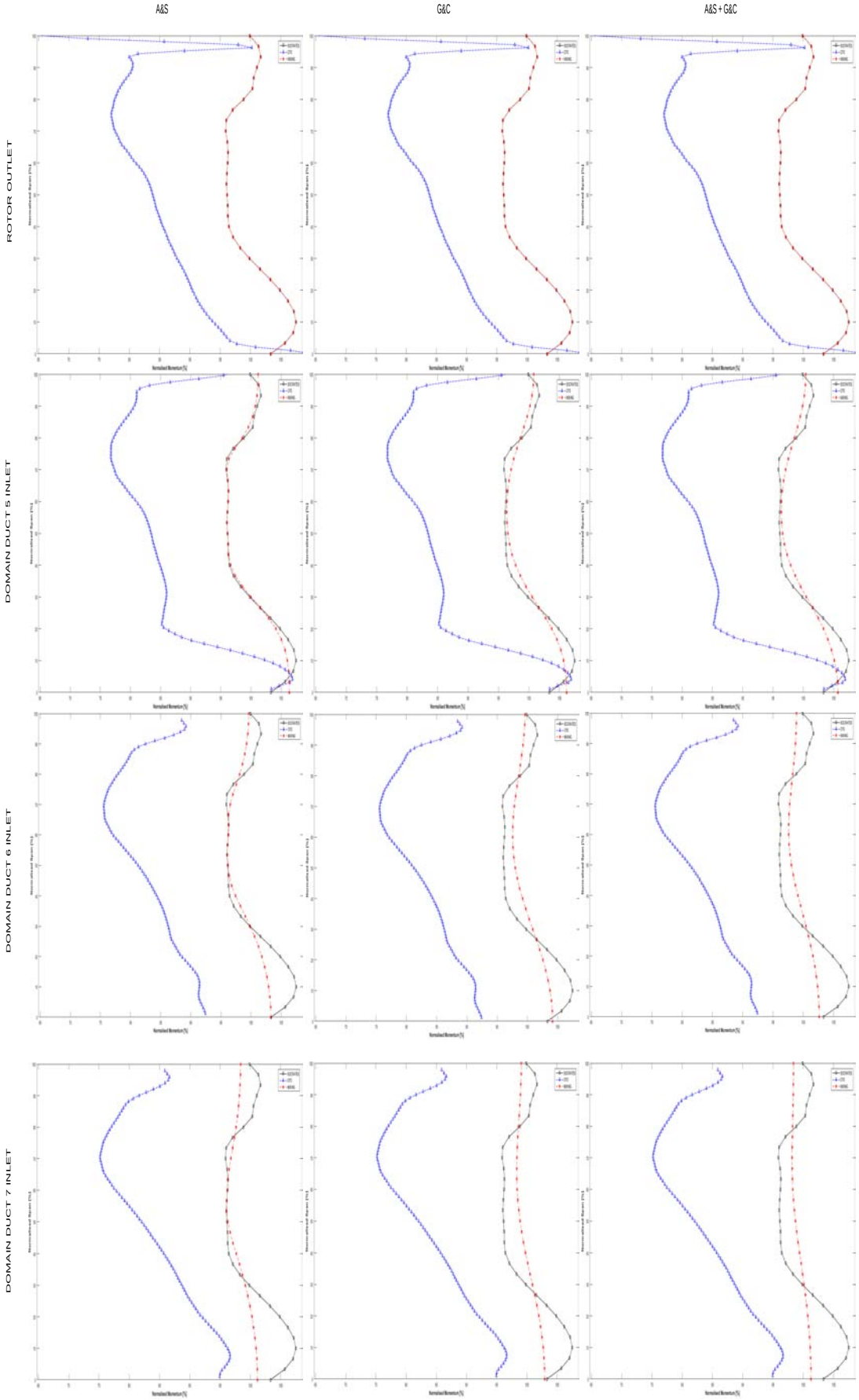

Figure 4.13: S-M-C near choke analysis results: angular momentum. SOCRATES average value at rotor outlet is 23.4 m^2/s. Solid black line with circles is SOCRATES, dotted blue line with triangles is CFD, dashed red line with stars is MIXING.

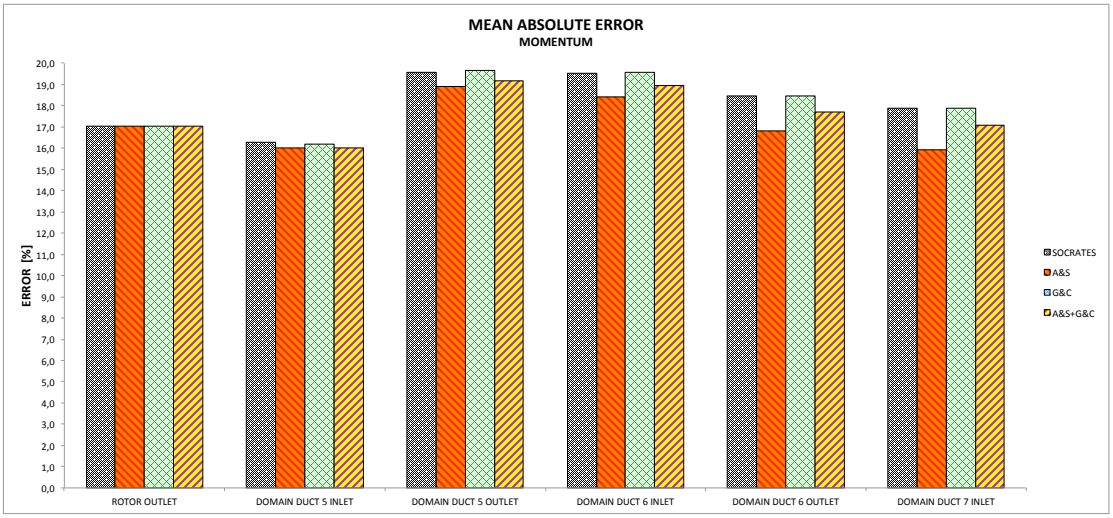

Figure 4.14: S-M-C near choke analysis mean absolute error: static temperature. Dotted black and white pattern is SOCRATES, orange pattern with descending red lines is MIXING A&S, green pattern with blue net is MIXING G&C, yellow pattern with ascending purple lines is MIXING A&S+G&C.

4.2.2 Near peak efficiency operating point

In this section the results of S-M-C analysis for NPE condition of NASA Rotor 67 are illustrated and discussed.

Fig 4.15 reports the distributions of the Adkins and Smith, and Gallimore and Cumpsty mixing coefficient. At the near peak efficiency operating point considered, G&C normalised mixing coefficient is slightly decreased with respect to its value at near choke, since shock configuration is changed. A&S normalised mixing coefficient distribution at NPE shows the same trend as for near choke condition, and the two values are very similar, the operating points being not very distant, so that secondary to axial velocity ratio, whose square value influences the mixing coefficient, is almost equal to that for NC.

Near peak efficiency mixing analysis features resemble those encountered in near choke analysis. In particular, for total quantities, namely stagnation pressure and temperature, as well as for angular momentum, there is no intersection between SOCRATES and CFD resulting profiles, and the generic error $\delta\Theta_{SOCRATES}$, and hence $\delta\Theta_{MIXING}$, is negative all along the span. When this condition is verified, the initial discrepancy between the unmixed solution and the viscous one does not allow MIXING to further improve the inviscid prediction significantly.

Concerning with static quantities, specifically static pressure and temperature, the generic error $\delta\Theta$ assumes both positive and negative values, and it is possible for MIXING to operate in order to improve SOCRATES outcomes. SOCRATES prediction matches CFD results excellently in the region near the casing, while MIXING agrees with the numerical viscous prediction in the region near the hub. Again, an iterative integration of SOCRATES and MIXING is believed to represent the best solution in

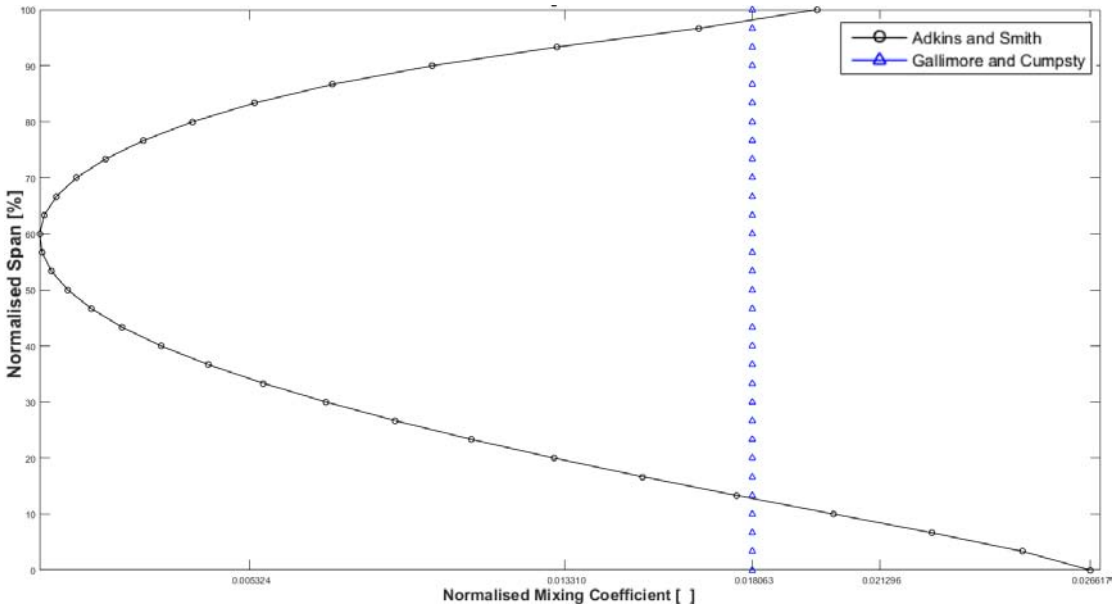

Figure 4.15: S-M-C near peak efficiency analysis normalised mixing coefficient. Solid black line with circles is Adkins and Smith formulation, solid blue line with triangles is Gallimore and Cumpsty formulation.

order to achieve a superior agreement with CFD.

As for what regards total temperature and static temperature predictions, the mean absolute error analysis concludes that both SOCRATES and MIXING calculations provide can be considered optimistically a good solution for the flow, since the absolute mean error for these quantities is very small, and so is CFD maximum-minimum initial variation in the core region.

MIXING near peak efficiency analysis results are presented in the following figures, along with mean absolute error histograms.

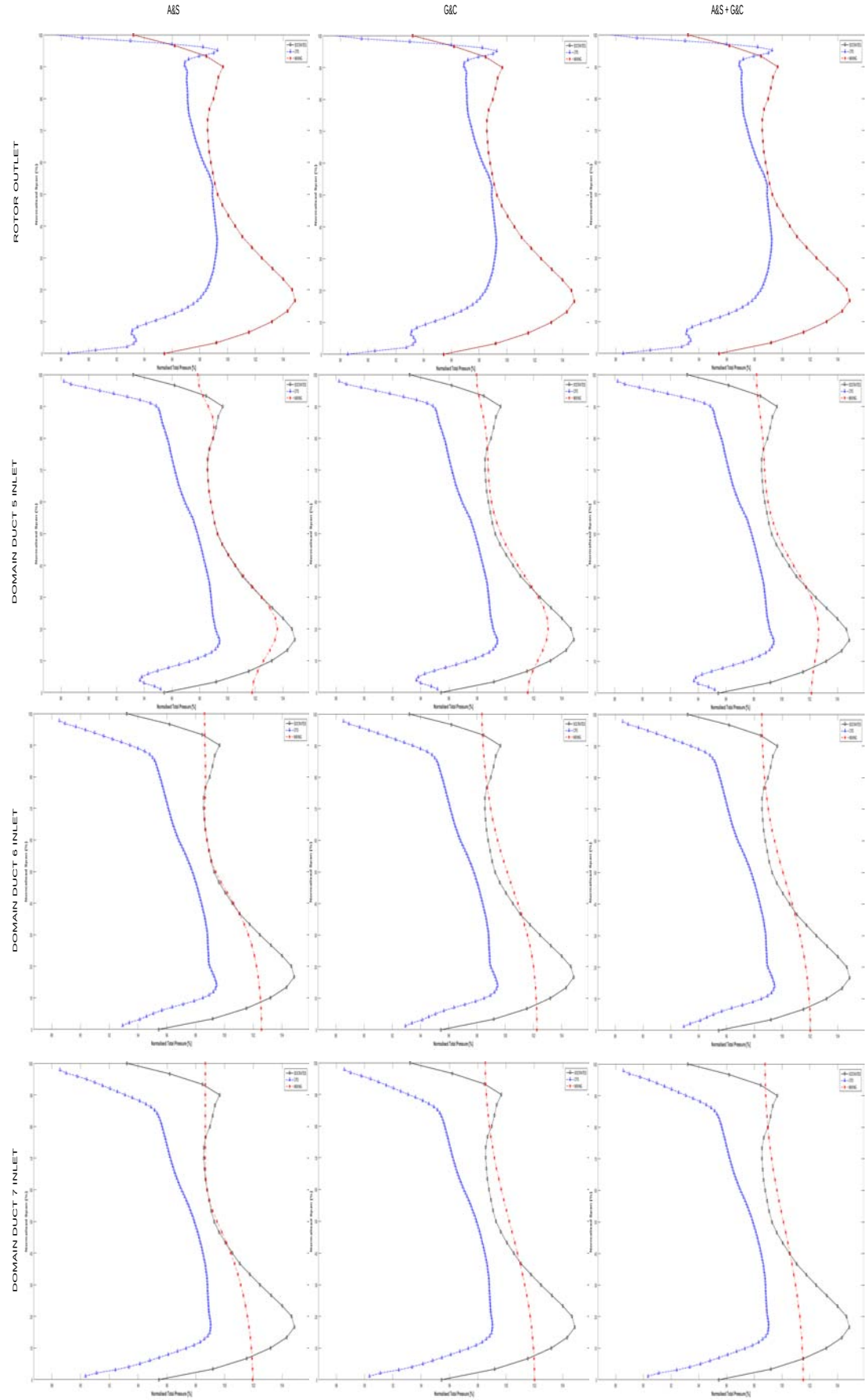

Figure 4.16: S-M-C near peak efficiency analysis results: total pressure. SOCRATES average value at rotor outlet is 158487 Pa. Solid black line with circles is SOCRATES, dotted blue line with triangles is CFD, dashed red line with stars is MIXING.

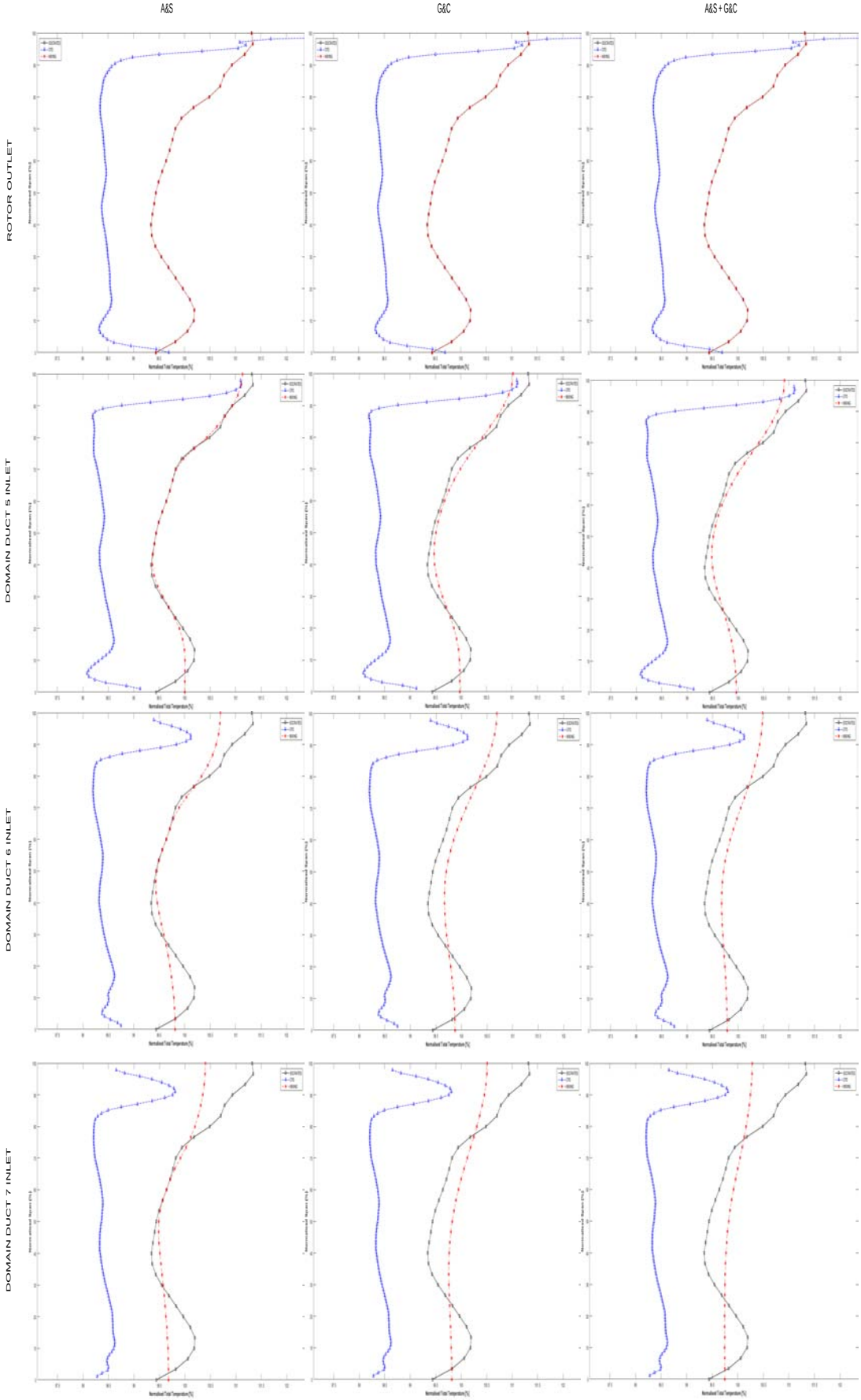

Figure 4.17: S-M-C near peak efficiency analysis results: total temperature. SOCRATES average value at rotor outlet is 332,3 K. Solid black line with circles is SOCRATES, dotted blue line with triangles is CFD, dashed red line with stars is MIXING.

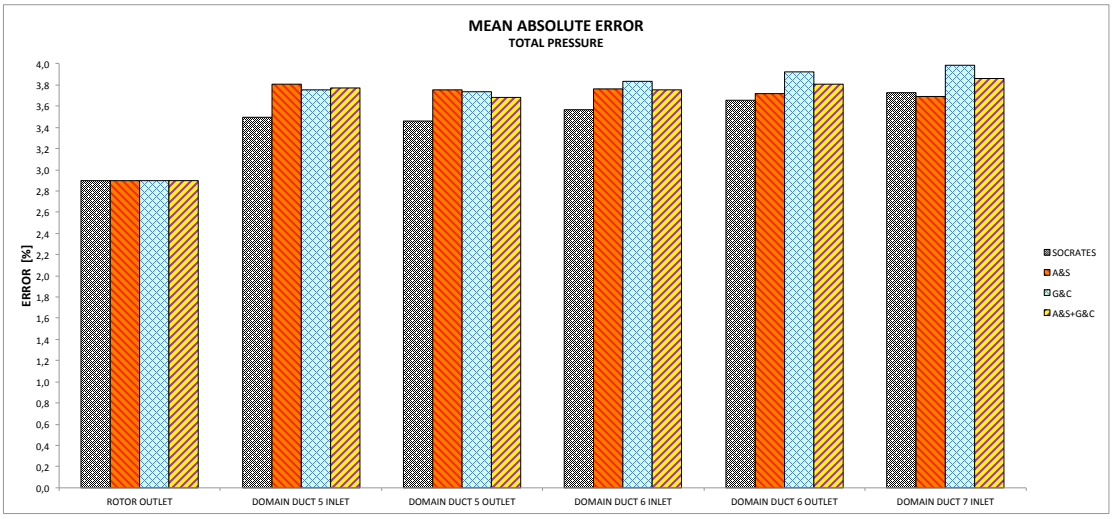

Figure 4.18: S-M-C near peak efficiency analysis mean absolute error: total pressure. Dotted black and white pattern is SOCRATES, orange pattern with descending red lines is MIXING A&S, green pattern with blue net is MIXING G&C, yellow pattern with ascending purple lines is MIXING A&S+G&C.

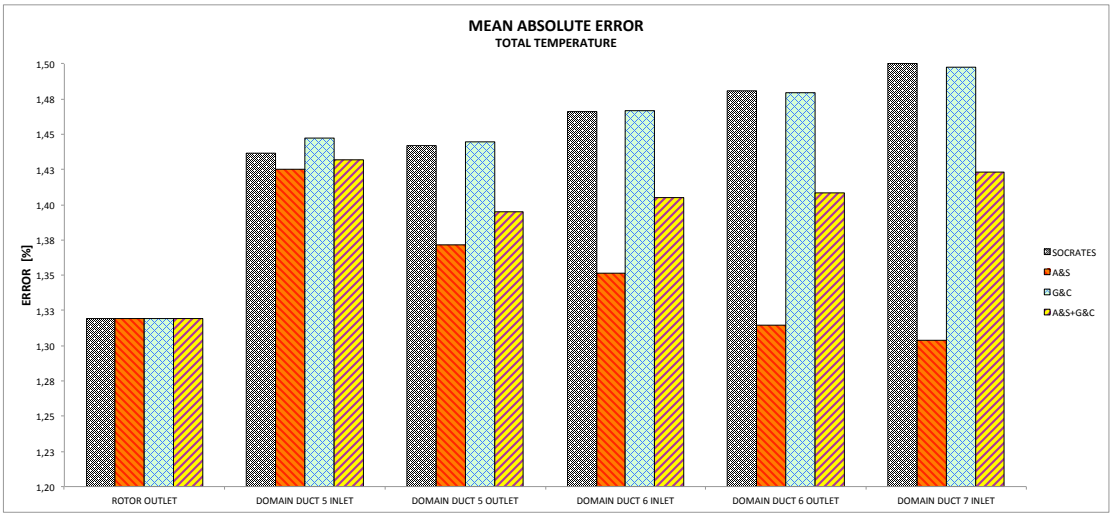

Figure 4.19: S-M-C near peak efficiency analysis mean absolute error: total temperature. Dotted black and white pattern is SOCRATES, orange pattern with descending red lines is MIXING A&S, green pattern with blue net is MIXING G&C, yellow pattern with ascending purple lines is MIXING A&S+G&C.

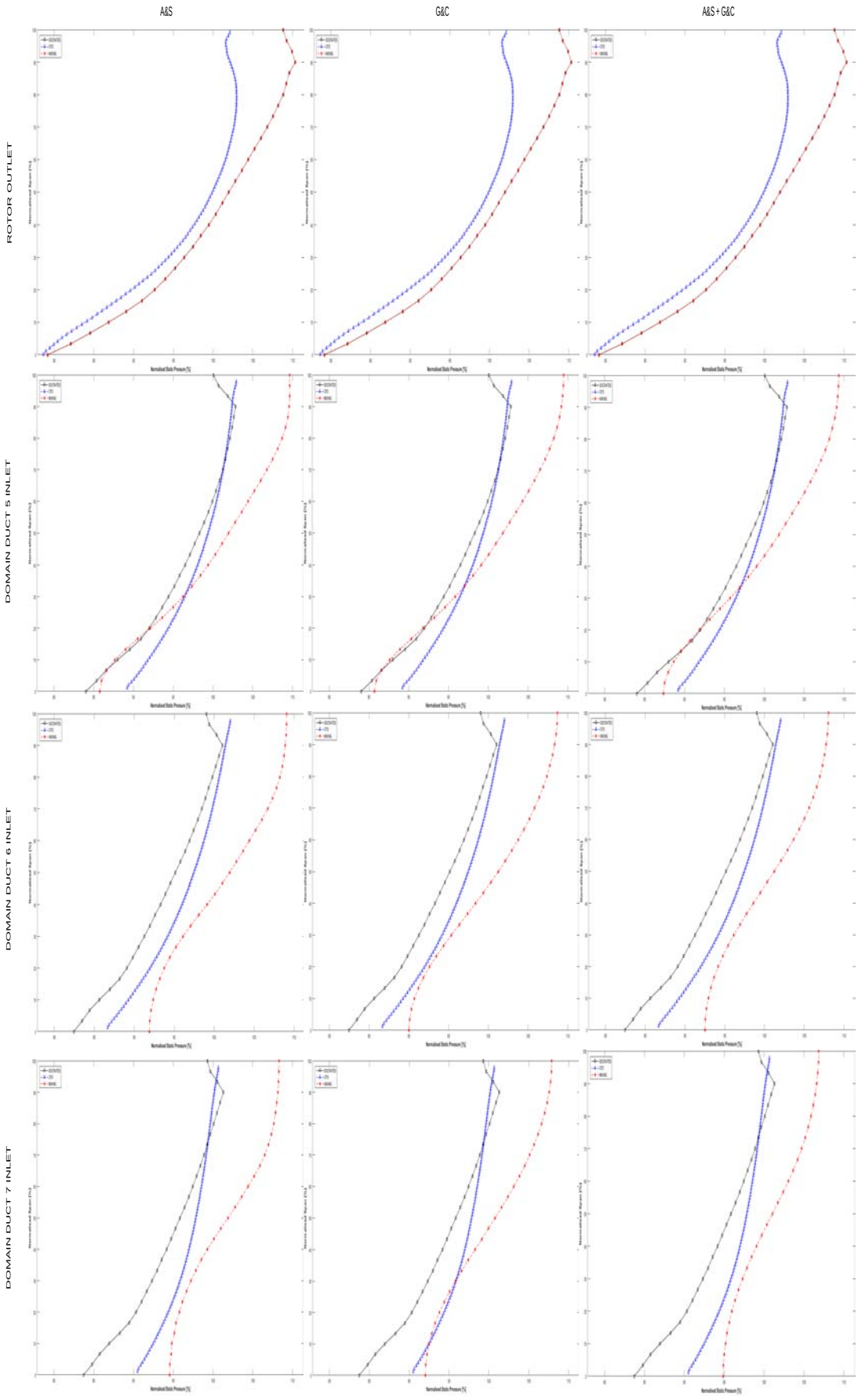

Figure 4.20: S-M-C near peak efficiency analysis results: static pressure. SOCRATES average value at rotor outlet is 112732 Pa. Solid black line with circles is SOCRATES, dotted blue line with triangles is CFD, dashed red line with stars is MIXING.

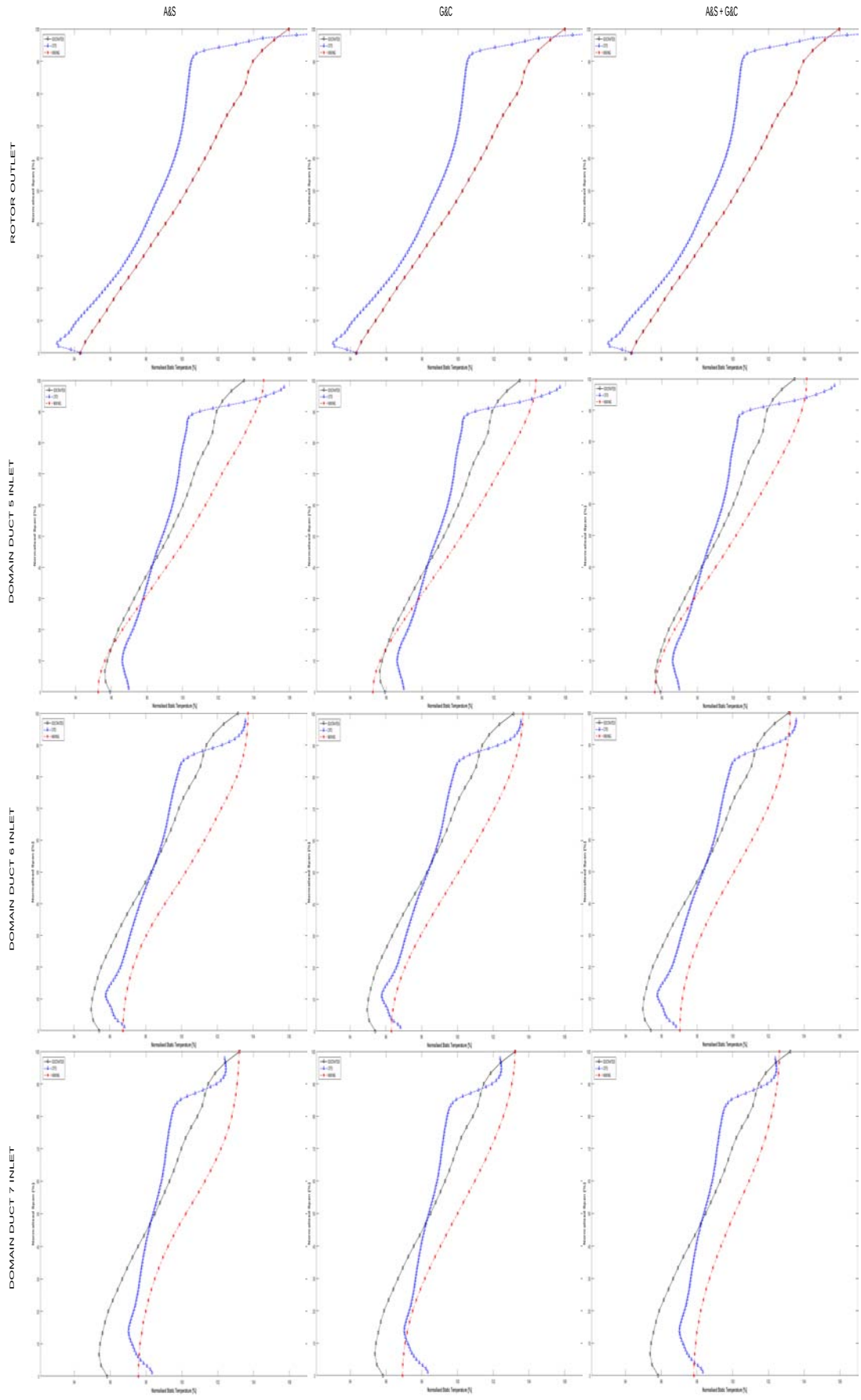

Figure 4.21: S-M-C near peak efficiency analysis results: static temperature. SOCRATES average value at rotor outlet is 301,2 K. Solid black line with circles is SOCRATES, dotted blue line with triangles is CFD, dashed red line with stars is MIXING.

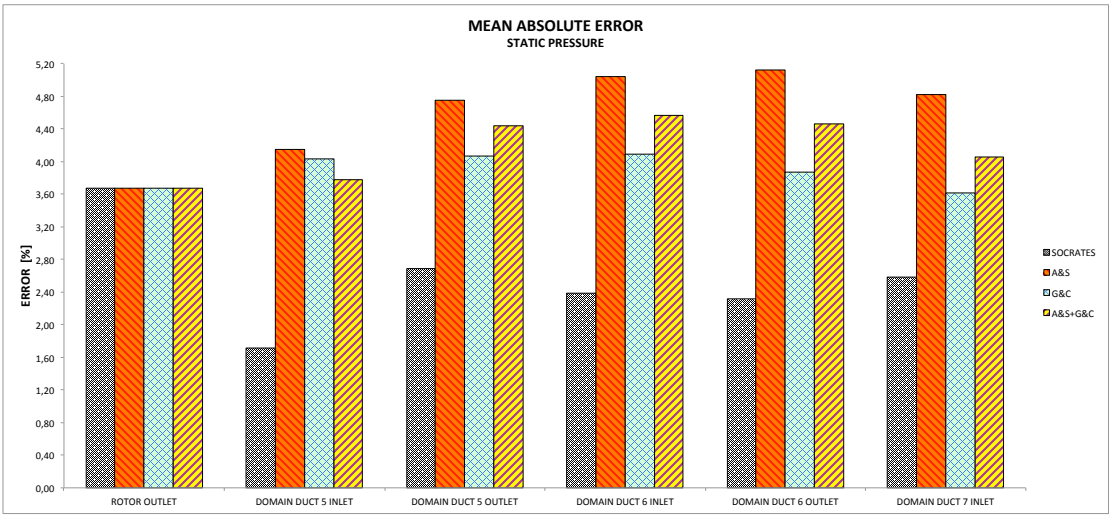

Figure 4.22: S-M-C near peak efficiency analysis mean absolute error: static pressure. Dotted black and white pattern is SOCRATES, orange pattern with descending red lines is MIXING A&S, green pattern with blue net is MIXING G&C, yellow pattern with ascending purple lines is MIXING A&S+G&C.

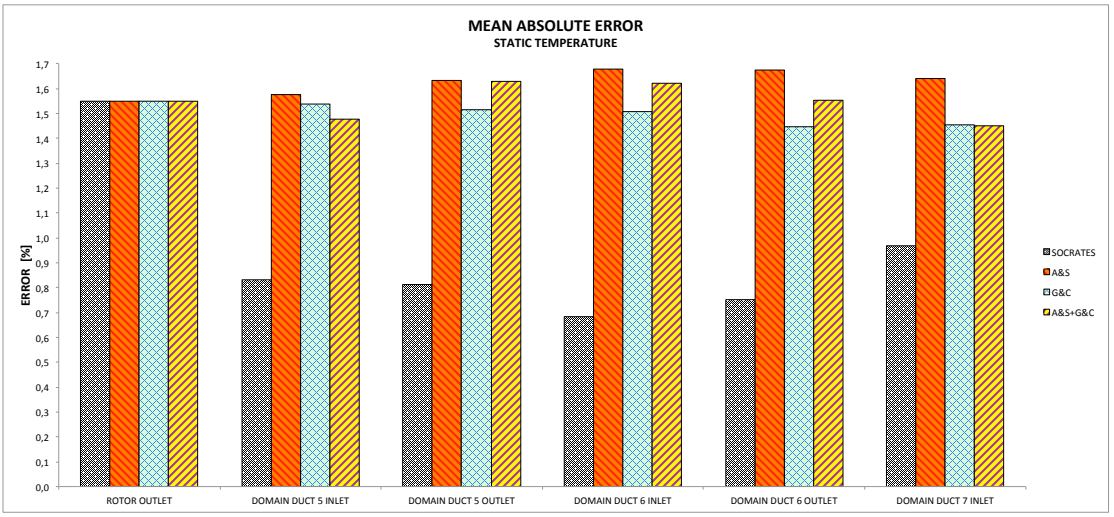

Figure 4.23: S-M-C near peak efficiency analysis mean absolute error: static temperature. Dotted black and white pattern is SOCRATES, orange pattern with descending red lines is MIXING A&S, green pattern with blue net is MIXING G&C, yellow pattern with ascending purple lines is MIXING A&S+G&C.

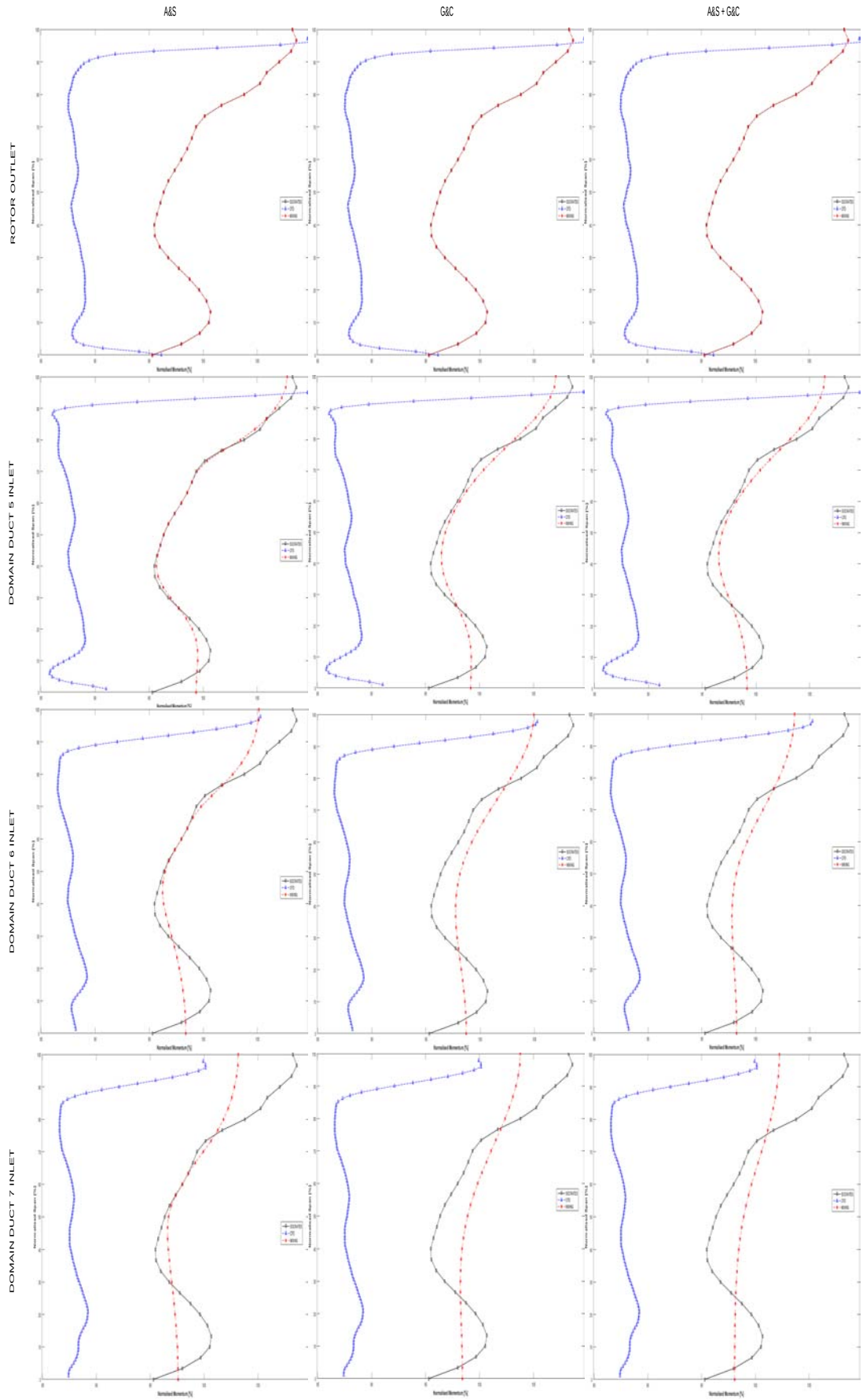

Figure 4.24: S-M-C near peak efficiency analysis results: angular momentum. SOCRATES average value at rotor outlet is 26.3 m^2/s. Solid black line with circles is SOCRATES, dotted blue line with triangles is CFD, dashed red line with stars is MIXING.

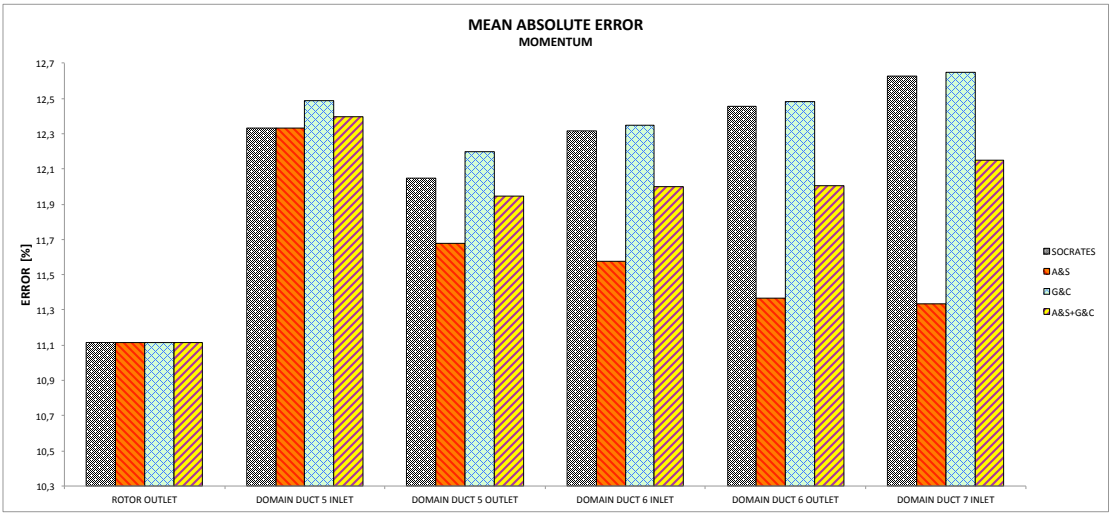

Figure 4.25: S-M-C near peak efficiency analysis mean absolute error: angular momentum. Dotted black and white pattern is SOCRATES, orange pattern with descending red lines is MIXING A&S, green pattern with blue net is MIXING G&C, yellow pattern with ascending purple lines is MIXING A&S+G&C.

4.3 M-C analysis

As it has already been mentioned in the introduction opening this chapter, M-C analysis objective is to investigate the capability of mixing model implemented to represent the flow actual behaviour, studying its applicability in the frame of throughflow calculations in axial-flow compressors.

In M-C analyses, MIXING propagates flow properties distributions through the whole duct region, solving the transport equation for total pressure, total temperature, static pressure, static temperature, and angular momentum, taking as input information provided by CFD solution for the calculation of the mixing coefficient and the initial flow property distribution at rotor blade trailing edge.

Differently from S-M-C analyses, M-C initial conditions are represented now by flow properties profiles at rotor blade trailing edge obtained from CFD: in this way, at rotor blade row exit CFD and MIXING have the very same values of quantities, as can be seen in the following figures illustrating the comparison between MIXING, and CFD at the inlet and outlet of each domain duct. For simplicity, these figures again report results only at rotor outlet, domain duct 5 inlet, domain duct 6 inlet and domain duct 7 inlet.

The results obtained from the mixing analysis are compared, using different mixing coefficient formulations, to those from the viscous CFD analysis, which contains itself the action of in the Navier-Stokes equations. CFD results are considered as representative of the actual behaviour of the flow in NASA Rotor 67.

As for S-M-C analysis discussion, the results of M-C analyses for two different operating points, namely near peak efficiency and near choke operating points, are presented in the following figures, which are composed of three columns referring to

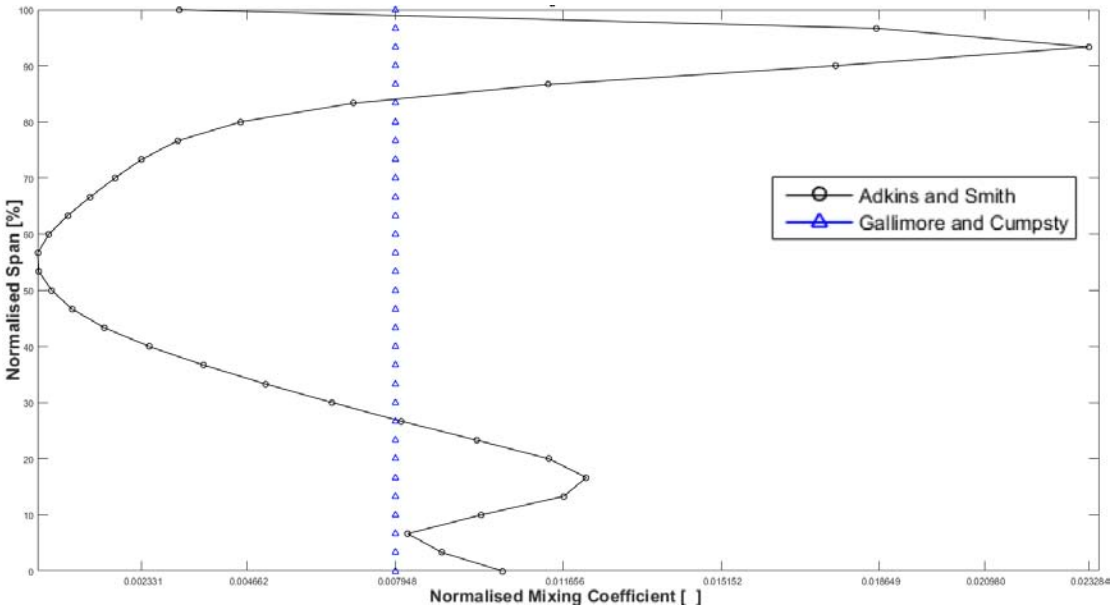

Figure 4.26: M-C near choke analysis normalised mixing coefficient. Solid black line with circles is Adkins and Smith formulation, solid blue line with triangles is Gallimore and Cumpsty formulation.

MIXING calculations each involving a specific mixing coefficient formulation. In particular, the first column refers to the Adkins and Smith mixing coefficient (A&S), the second column refers to that by Gallimore and Cumpsty (G&C), and the third represent mixing calculations including both the previous mixing coefficient definitions (A&S+G&C).

In addition to this, the analysis of the error is carried out below. The flow properties distributions at each domain duct are reported in percentage with respect to CFD average value at rotor blade trailing edge. Histograms dealing with the mean absolute error are presented in percentage to local CFD average value. Since MIXING and CFD have the same flow property profiles at rotor blade trailing edge, the error, as well as the mean absolute error, is zero at rotor blade trailing edge. Therefore, mean absolute error histograms can now be looked at as representative of the evolution of the average error committed by MIXING in its development in the duct region.

4.3.1 Near choke operating point

Fig 4.26 shows the distribution of the normalised mixing coefficient for the near choke analysis. First of all, it can be noticed that, the Adkins and Smith mixing coefficient distribution exhibit the same trend in the core region as for that calculated in S-M-C analysis in Fig 4.4, with a minimum of the mixing coefficient at midspan, but the behaviour at the endwalls is very different. Near the endwalls A&S mixing coefficient presents two peak points, while in correspondence to the endwalls it assumes values that are much lower than the relative peak ones. This peculiarity influences significantly MIXING results, as can be seen in the figures reported below.

Dealing with the comparison between the mixing coefficient computed in S-M-C and M-C analyses, it is interesting that G&C normalised mixing coefficient computed from SOCRATES in S-M-C analysis is equal to 1.8078×10^{-2}, while that computed from CFD in M-C analysis is equal to 7.9480×10^{-3}, that is about the half. On the other hand, A&S normalised mixing coefficients computed from both SOCRATES in S-M-C analysis and CFD in M-C analysis reach maximum values that are almost equal, specifically of 2.6617×10^{-2} and 2.3284×10^{-2} respectively.

Mixing coefficient distribution trends are in excellent agreement with the analysis reported by Dring in [26]. The values present a difference of about an order of magnitude, but this can be explained by the fact that in Dring's analysis the considered compressors were subsonic, while in the present dissertation a transonic compressor has been considered: transonic compressors, as it has been fully described in Chapter 2, may exhibit significant secondary flows, and their environment is highly influenced from turbulence.

Fig 4.27 reports MIXING stagnation pressure resulting distributions. All the total pressure profiles have an inflection point due to the zero-gradient endwall boundary condition. It appears somewhat surprising that all the calculations, involving different mixing coefficients, exhibit the same trend and provide total pressure profiles that are barely different. In the region near the hub the three computations reach fast a uniform mixed out condition, and therefore total pressure remains almost constant in the region 0 - 40% span already at domain duct 6 inlet. Near the casing, MIXING calculations shows some minor differences due to the particular distribution of the mixing coefficient described above. In particular, in G&C mixing analysis, the effect of mixing near the casing is weaker than A&S counterpart, and this permits to the total pressure profile computed with G&C mixing coefficient to stay closer to CFD distribution.

As it is apparent in Fig 4.27, there are several intersections of MIXING predicted profiles and those from CFD. This is representative of the fact that the implemented mixing model operates properly starting from CFD data.

These considerations find confirm also in the error analysis. Fig 4.29, reporting the histogram of the mean absolute error, highlight the good agreement of G&C mixing calculation with CFD, with a mean absolute error lower than 3% compared to a CFD maximum-minimum initial variation of about 30%.

Fig 4.28 illustrate stagnation temperature distributions obtained from the mixing analysis, and the relative mean absolute error histogram is depicted in Fig 4.30. It is immediately evident that total temperature profile is already practically constant at rotor blade trailing edge, where CFD maximum-minimum variation is about 3%. Evolving from rotor outlet to domain duct 7 inlet, CFD total temperature profile changes slightly, and therefore, MIXING is capable of predict the final distribution with an excellent, even if approximate, result.

Again, the mixing action prescribed by the transport equation is carried out in the core region, and not in the endwalls, where the boundary condition influences the solution. For the case of total temperature, G&C mixing calculation reaches the best agreement with CFD. This can be explained focusing attention on the error $\delta T_{0,G\&C}$: in Fig 4.28, G&C mixing analysis profile intersects the CFD one several times, differently

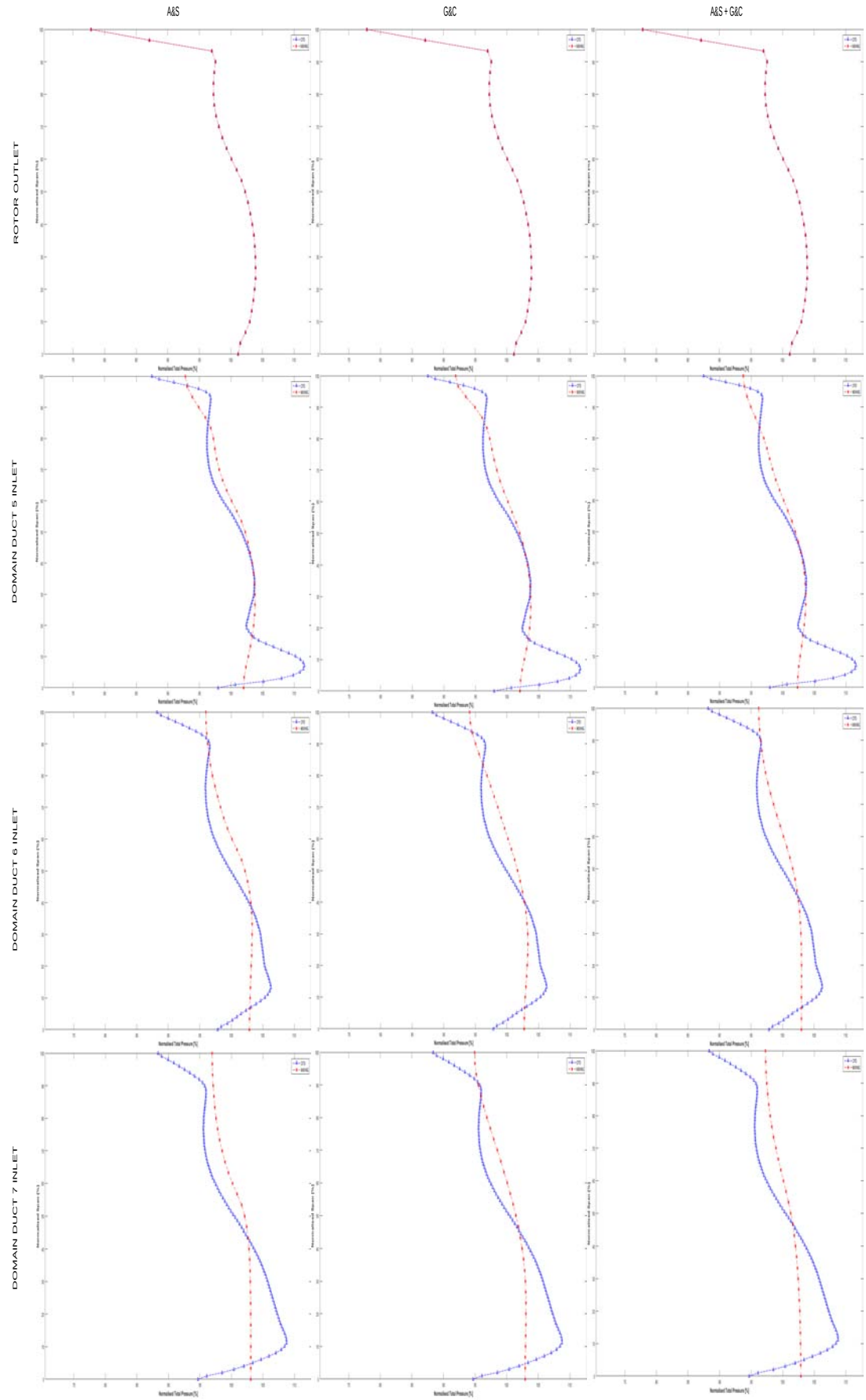

Figure 4.27: M-C near choke analysis results: total pressure. CFD average value at rotor outlet is 147936 Pa. Dotted blue line with triangles is CFD, dashed red line with stars is MIXING.

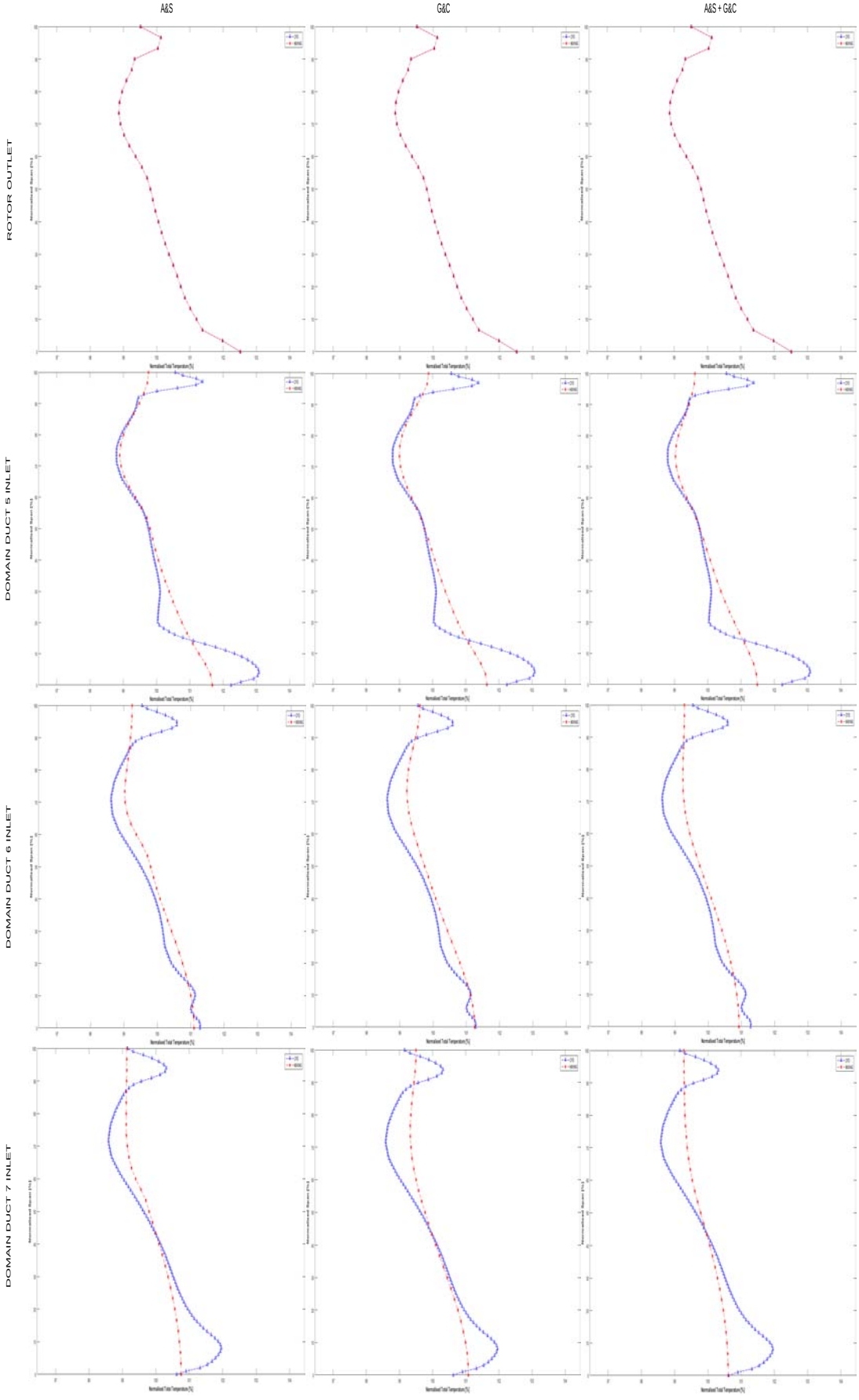

Figure 4.28: M-C near choke analysis results: total temperature. CFD average value at rotor outlet is 327.2 K. Dotted blue line with triangles is CFD, dashed red line with stars is MIXING.

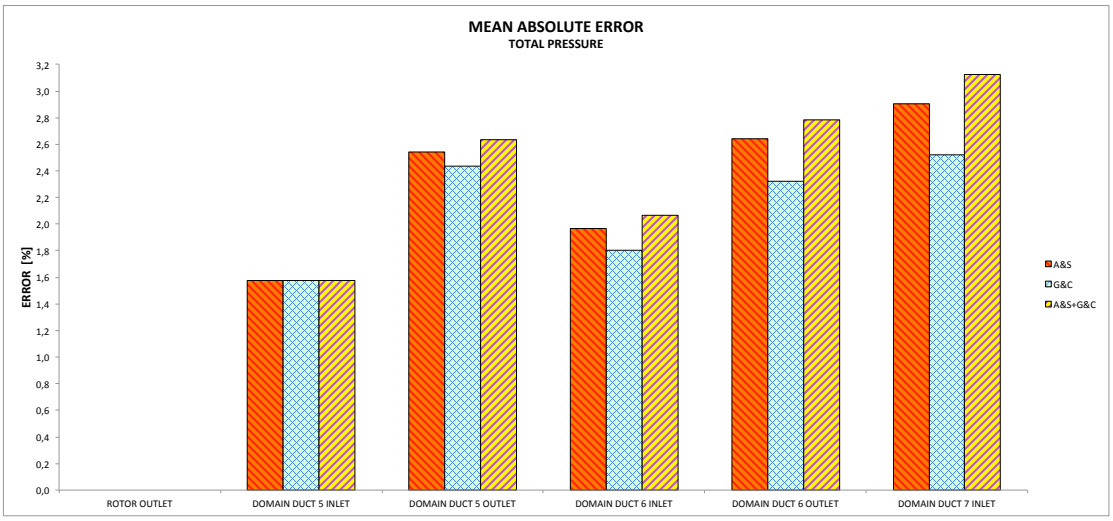

Figure 4.29: M-C near choke analysis mean absolute error: total pressure. Orange pattern with descending red lines is MIXING A&S, green pattern with blue net is MIXING G&C, yellow pattern with ascending purple lines is MIXING A&S+G&C.

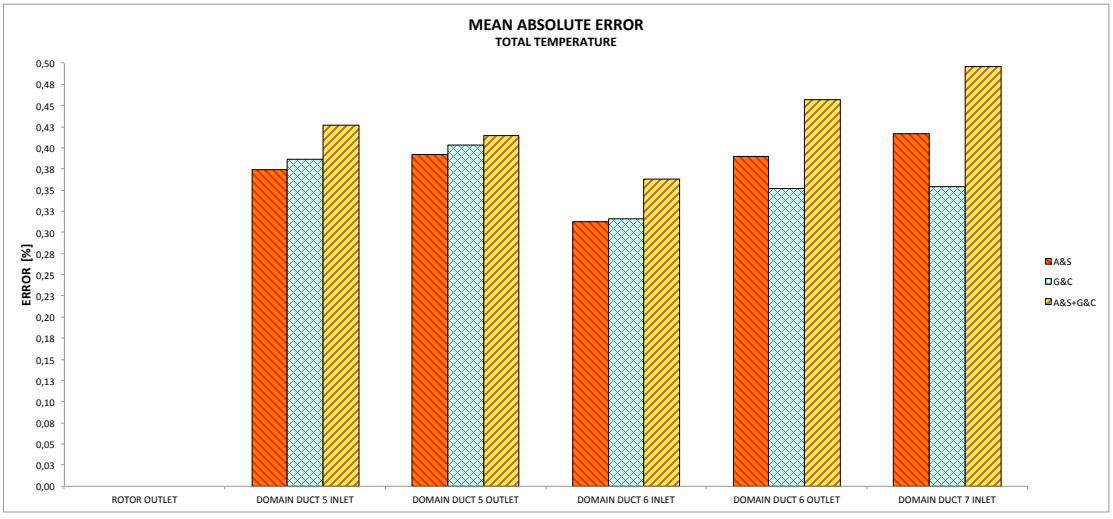

Figure 4.30: M-C near choke analysis mean absolute error: total temperature. Orange pattern with descending red lines is MIXING A&S, green pattern with blue net is MIXING G&C, yellow pattern with ascending purple lines is MIXING A&S+G&C.

from the other mixing calculations. In each case, the mean absolute error is lower than 0.5%.

Concerning with static quantities, Figs 4.31 and 4.32 illustrate respectively static pressure and static temperature distributions obtained from MIXING. For static pressure, CFD profile at domain duct 7 inlet appears almost as a straight, even if not vertical, line, with an initial maximum-minimum variation of about 25% with respect to CFD average value at rotor blade trailing edge. For static temperature, CFD profile is almost straight in the core region, with peak values at the endwalls, and presents an initial maximum-minimum variation of about 8%.

MIXING profiles, which always exhibit an inflection point, are capable of matching this behaviour only in function of the prescribed mixing coefficient distribution. This explains why the A&S+G&C mixing analysis, involving the combined effects of secondary flow and turbulence mixing coefficient formulations, can achieve the best agreement with CFD, as it is evident also in Figs 4.33 and 4.34 reporting the mean absolute error for static pressure and static temperature respectively. In both cases, A&S+G&C mean absolute error is very low, specifically it is lower than 2.8% for static pressure and lower than 1% for static temperature.

Finally, angular momentum results from MIXING are showed in Fig 4.35. Angular momentum CFD distribution is more complicated than those of static pressure and temperature, and the reliability of the mixing analysis stands on the confidence of the mixing coefficient formulation used. Although MIXING predicts well angular momentum behaviour at midspan, it presents major discrepancies moving toward the endwalls. This can be addicted to the boundary condition used: the zero-gradient boundary condition is very simple and can be acceptable for approximate results, but it is not always representative of flow actual evolution. Another possible explanation is the fact that angular momentum profiles are not smoothing proceeding in the streamwise direction, and seem not subjected to a mixing process as that predicted by MIXING.

Nevertheless, the errors are not enormous, as can be seen in Fig 4.36. G&C mixing calculation matches closer CFD results, with a mean absolute error lower than 3%.

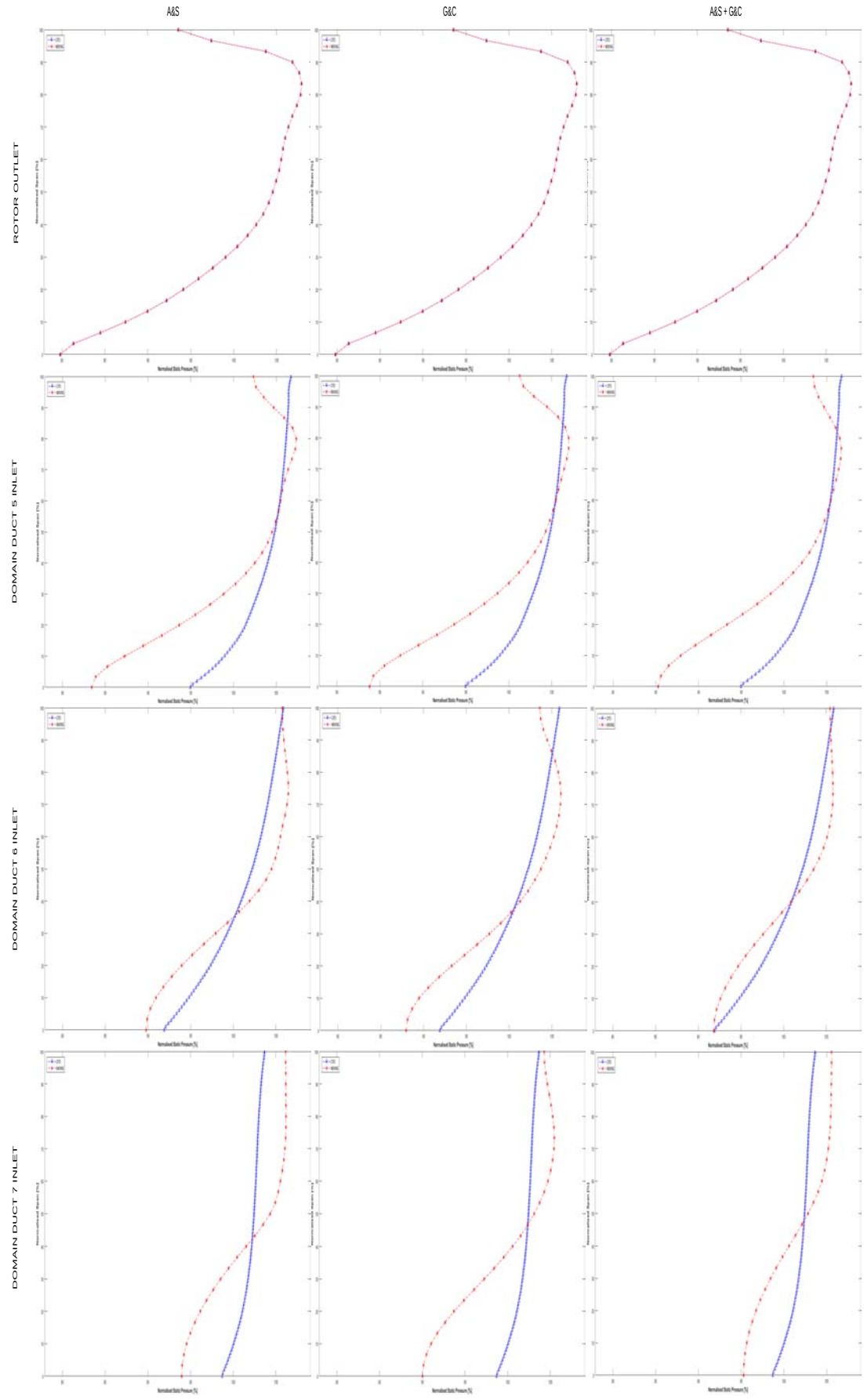

Figure 4.31: M-C near choke analysis results: static pressure. CFD average value at rotor outlet is 101876 Pa. Dotted blue line with triangles is CFD, dashed red line with stars is MIXING.

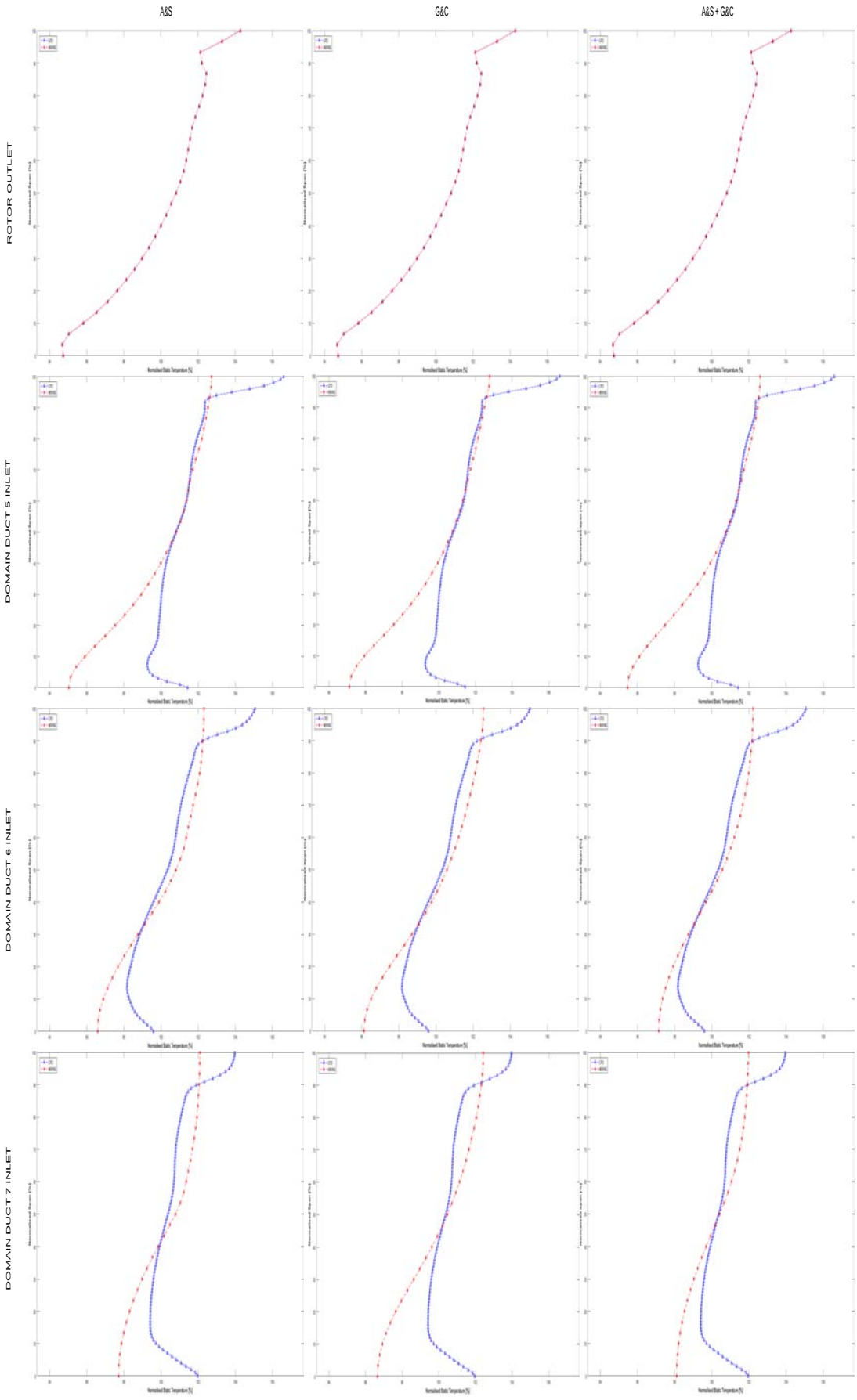

Figure 4.32: M-C near choke analysis results: static temperature. CFD average value at rotor outlet is 293,6 K. Dotted blue line with triangles is CFD, dashed red line with stars is MIXING.

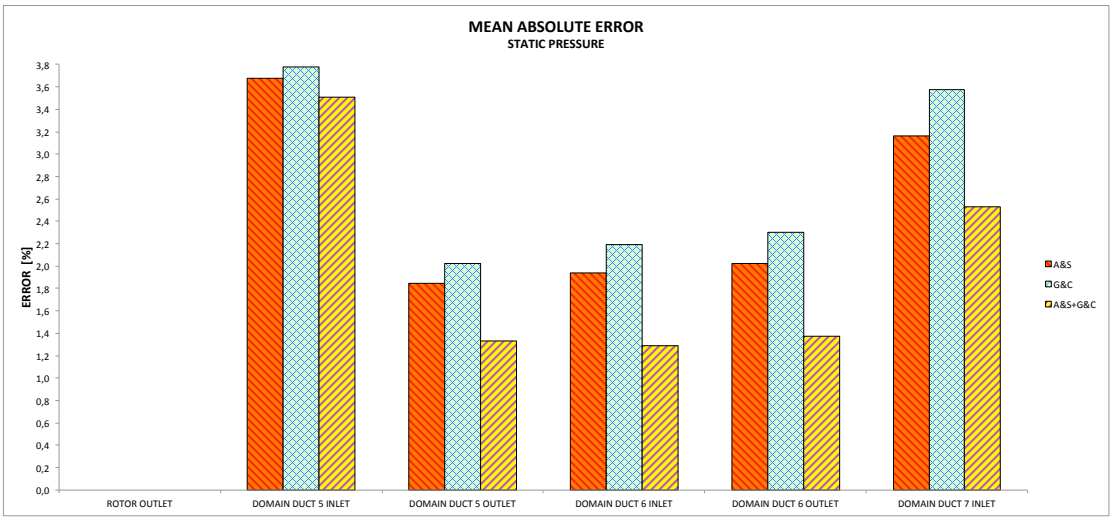

Figure 4.33: M-C near choke analysis mean absolute error: static pressure. Orange pattern with descending red lines is MIXING A&S, green pattern with blue net is MIXING G&C, yellow pattern with ascending purple lines is MIXING A&S+G&C.

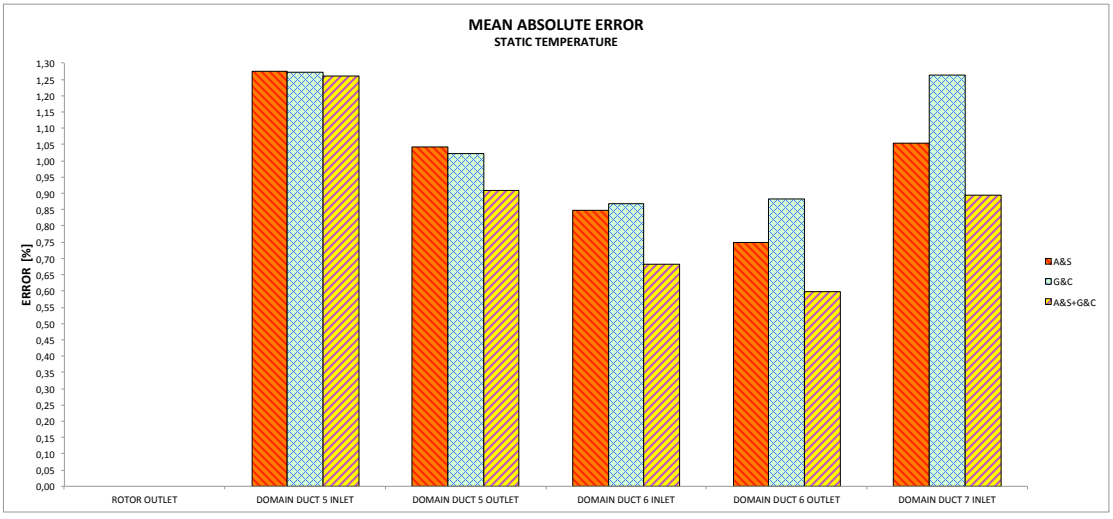

Figure 4.34: M-C near choke analysis mean absolute error: static temperature. Orange pattern with descending red lines is MIXING A&S, green pattern with blue net is MIXING G&C, yellow pattern with ascending purple lines is MIXING A&S+G&C.

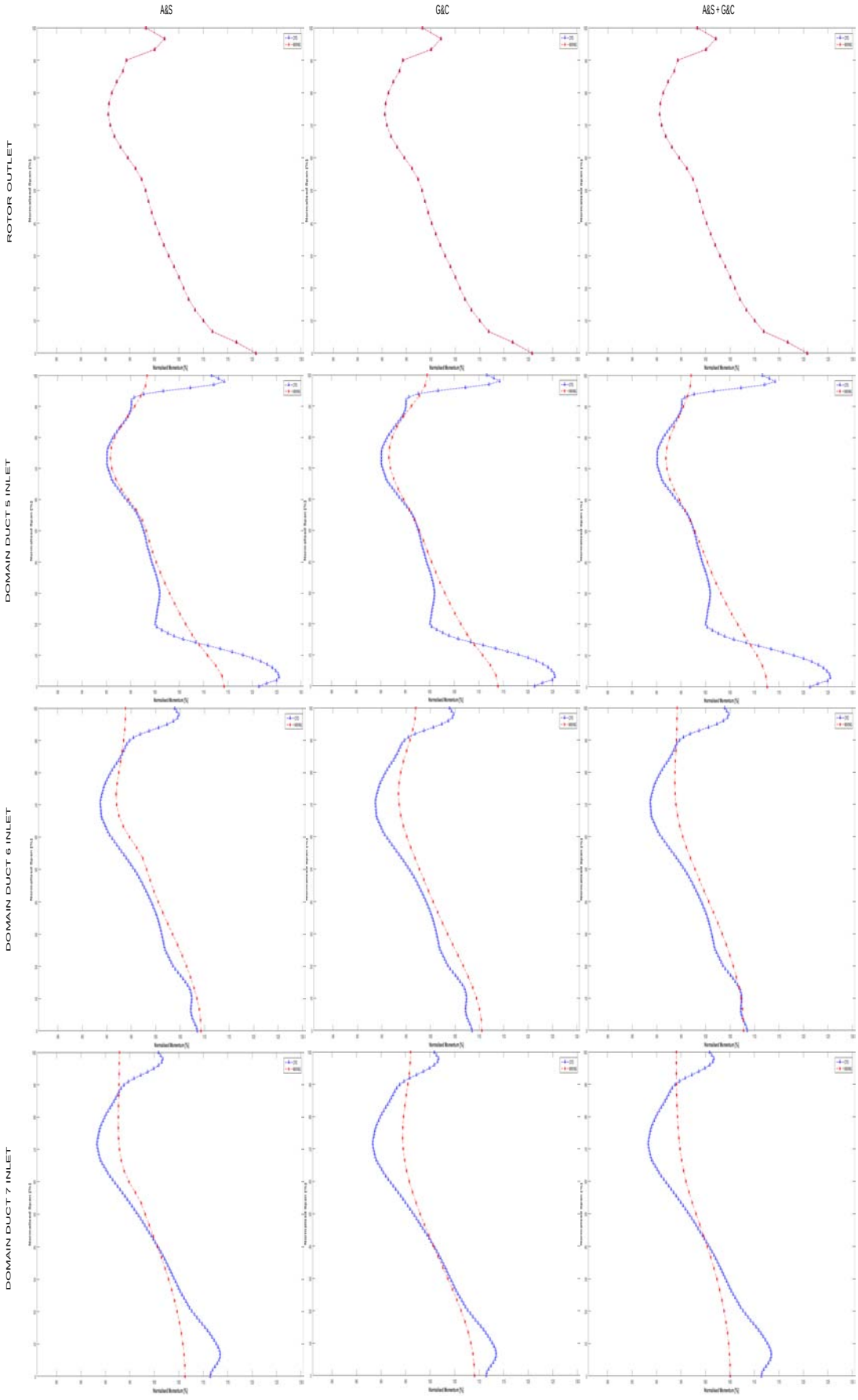

Figure 4.35: M-C near choke analysis results: angular momentum. CFD average value at rotor outlet is 23,3 m^2/s. Dotted blue line with triangles is CFD, dashed red line with stars is MIXING.

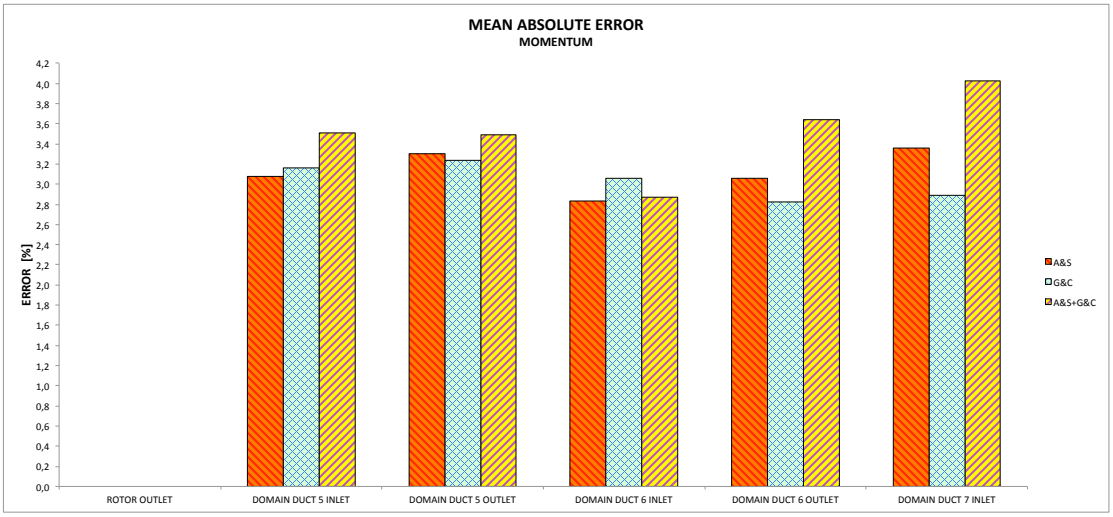

Figure 4.36: M-C near choke analysis mean absolute error: static pressure. Orange pattern with descending red lines is MIXING A&S, green pattern with blue net is MIXING G&C, yellow pattern with ascending purple lines is MIXING A&S+G&C.

4.3.2 Near peak efficiency operating point

In this section the results of M-C analysis for near peak efficiency operating point of NASA Rotor 67 are reported and discussed.

Fig 4.15 reports the distributions of the Adkins and Smith, and Gallimore and Cumpsty mixing coefficient. At the near peak efficiency operating point considered, G&C normalised mixing coefficient is slightly increased to 8.4260×10^{-3} with respect to its value at near choke, due to the changed shock configuration. A&S normalised mixing coefficient distribution at NPE shows a trend which is dual with respect to its counterpart at near choke condition, having a peak in the hub region equal to 2.3543×10^{-2}. The mixing profile influence in mixing analysis distribution behaviour can be seen in the following figures reporting MIXING results.

For instance, considering Fig 4.38 dealing with total pressure, it is apparent that stagnation pressure A&S profile is smoothed faster in the region near the hub, where the mixing coefficient is higher, while, very near the casing, the mixing solution is influenced mainly by the boundary condition rather than the transport equation. This is also evident in Fig 4.39 in which total temperature profiles reach a full mixed condition near the hub since domain duct 5 inlet.

Similarly to S-M-C analyses, M-C near peak efficiency mixing analysis features resemble those encountered in near choke analysis. In particular, for stagnation pressure, stagnation temperature, and angular momentum, the G&C mixing analysis matches better CFD data, with a very small mean absolute error. This corroborates the consideration that the spanwise mixing model implemented can effectively represent the flow behaviour in a transonic compressor environment.

Regarding static quantities, it is clear from the error analysis that the A&S+G&C gives a better result, taking into account the combined effect of both secondary flows,

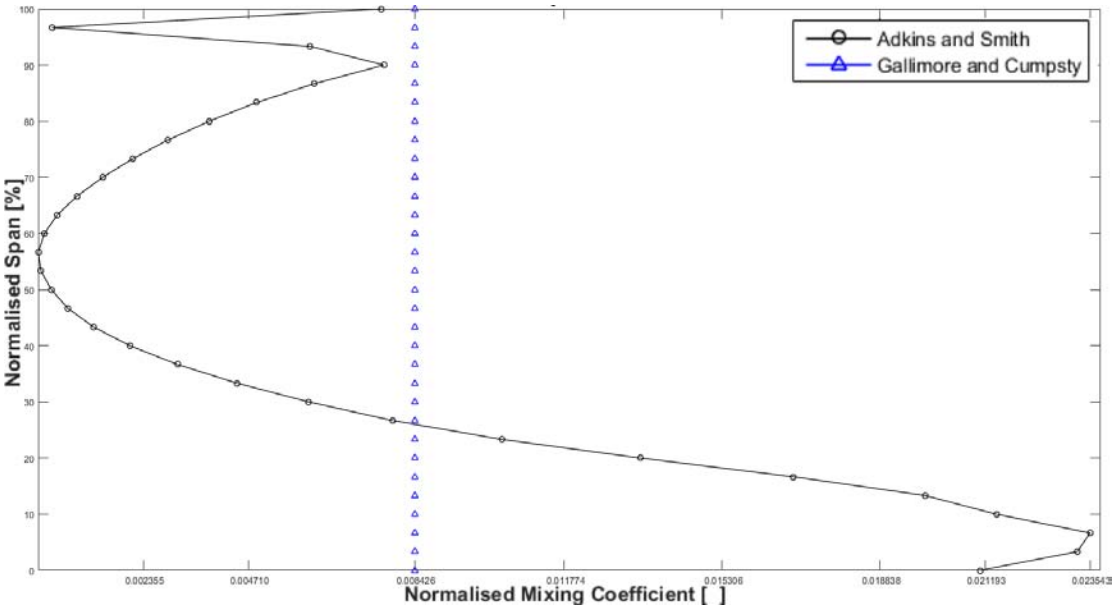

Figure 4.37: M-C near peak efficiency analysis normalised mixing coefficient. Solid black line with circles is Adkins and Smith formulation, solid blue line with triangles is Gallimore and Cumpsty formulation.

interacting principally in the endwall regions, and turbulence, whose effect influences the flow in the whole span, in particular in the core region.

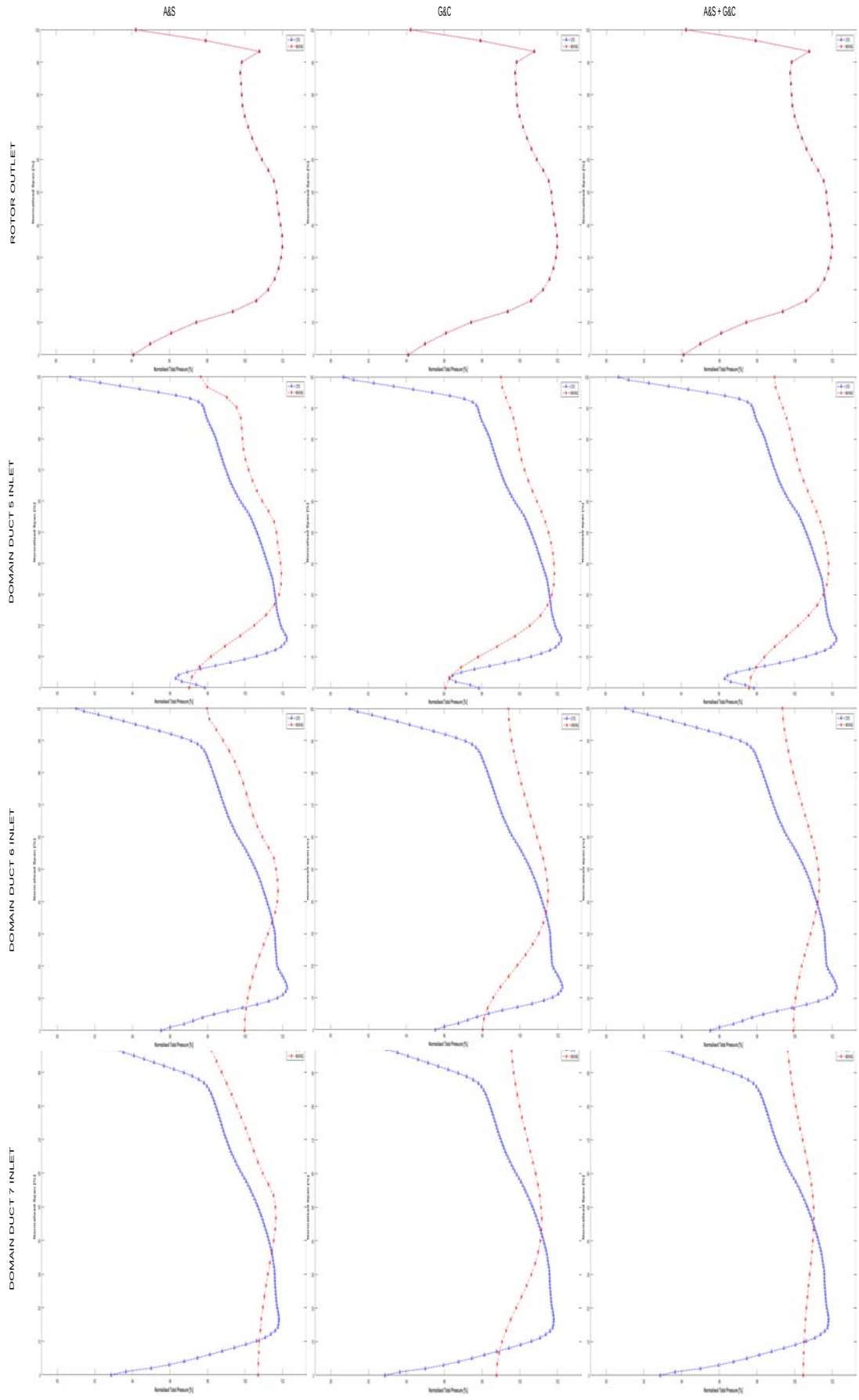

Figure 4.38: M-C near peak efficiency analysis results: total pressure. CFD average value at rotor outlet is 158639 Pa. Dotted blue line with triangles is CFD, dashed red line with stars is MIXING.

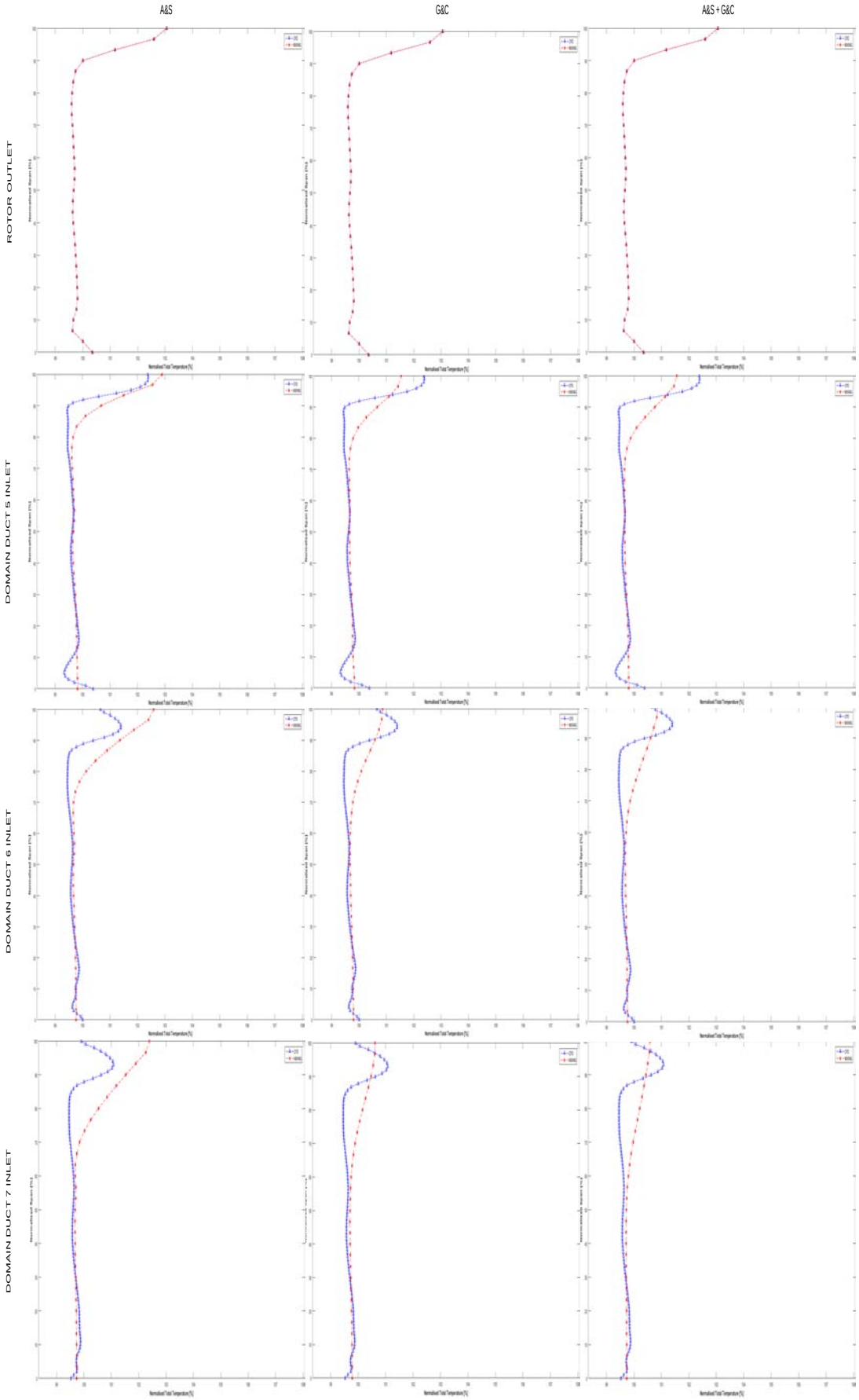

Figure 4.39: M-C near peak efficiency analysis results: total temperature. CFD average value at rotor outlet is 332.3 K. Dotted blue line with triangles is CFD, dashed red line with stars is MIXING.

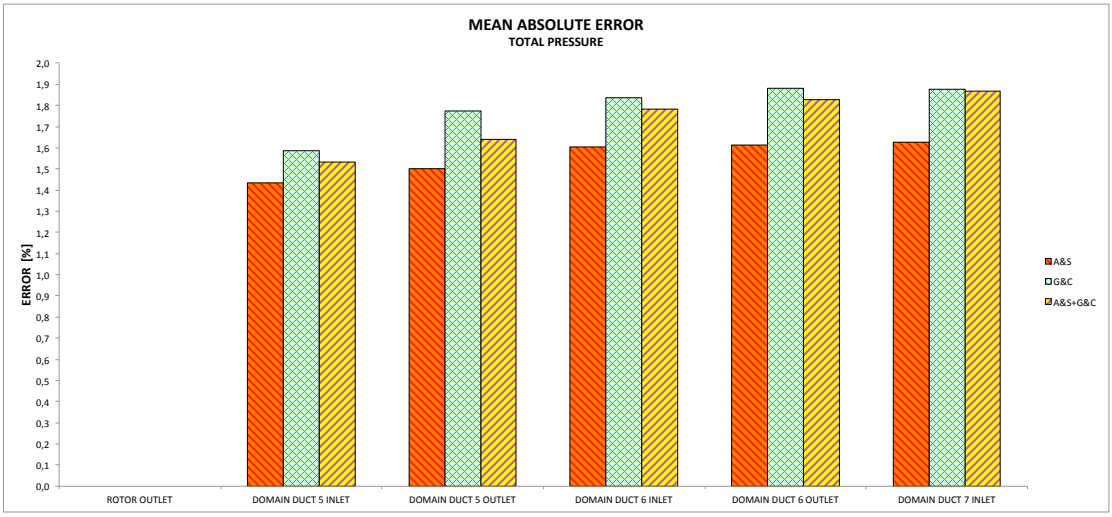

Figure 4.40: M-C near peak efficiency analysis mean absolute error: total pressure. Orange pattern with descending red lines is MIXING A&S, green pattern with blue net is MIXING G&C, yellow pattern with ascending purple lines is MIXING A&S+G&C.

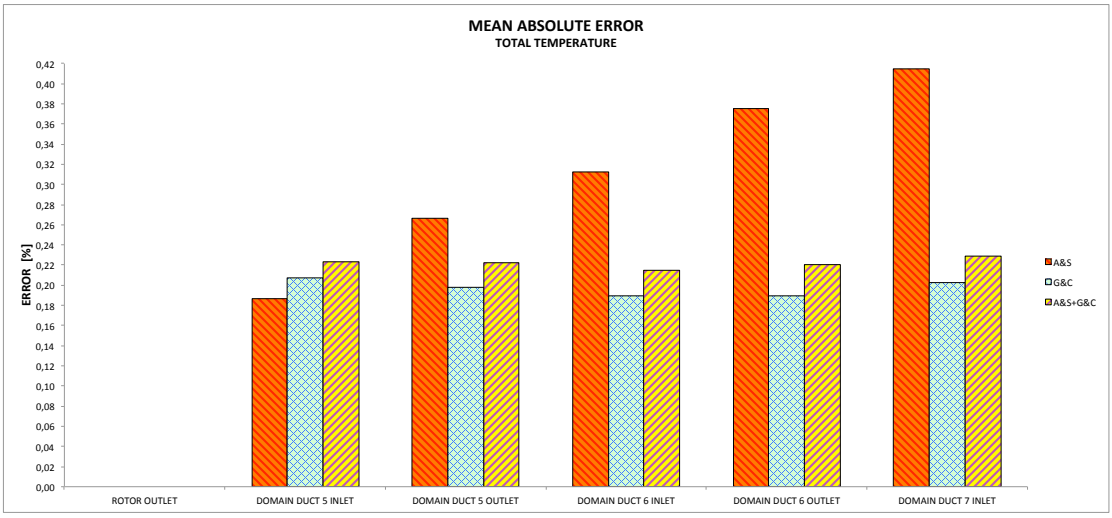

Figure 4.41: M-C near peak efficiency analysis mean absolute error: total temperature. Orange pattern with descending red lines is MIXING A&S, green pattern with blue net is MIXING G&C, yellow pattern with ascending purple lines is MIXING A&S+G&C.

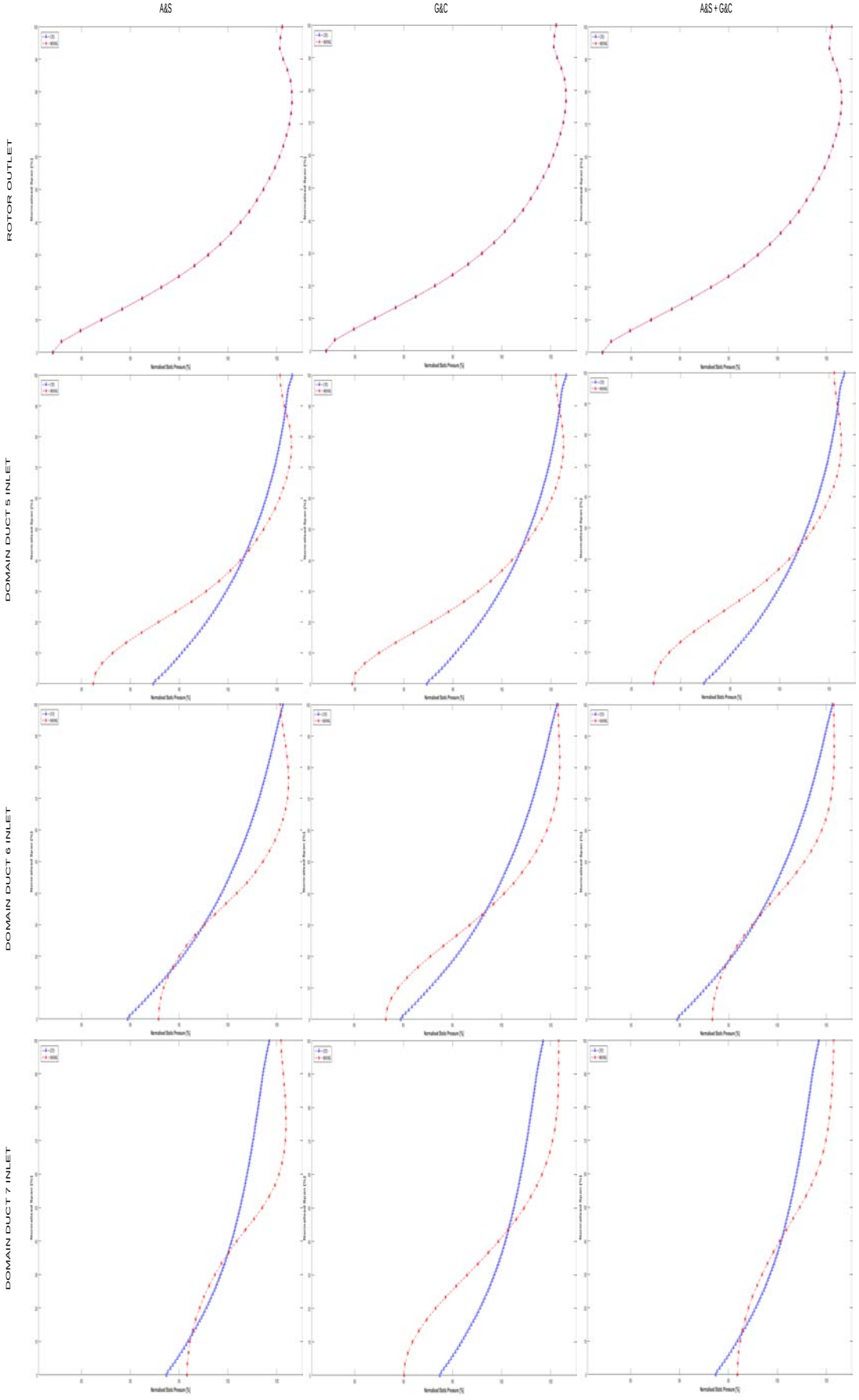

Figure 4.42: M-C near peak efficiency analysis results: static pressure. CFD average value at rotor outlet is 112884 Pa. Dotted blue line with triangles is CFD, dashed red line with stars is MIXING.

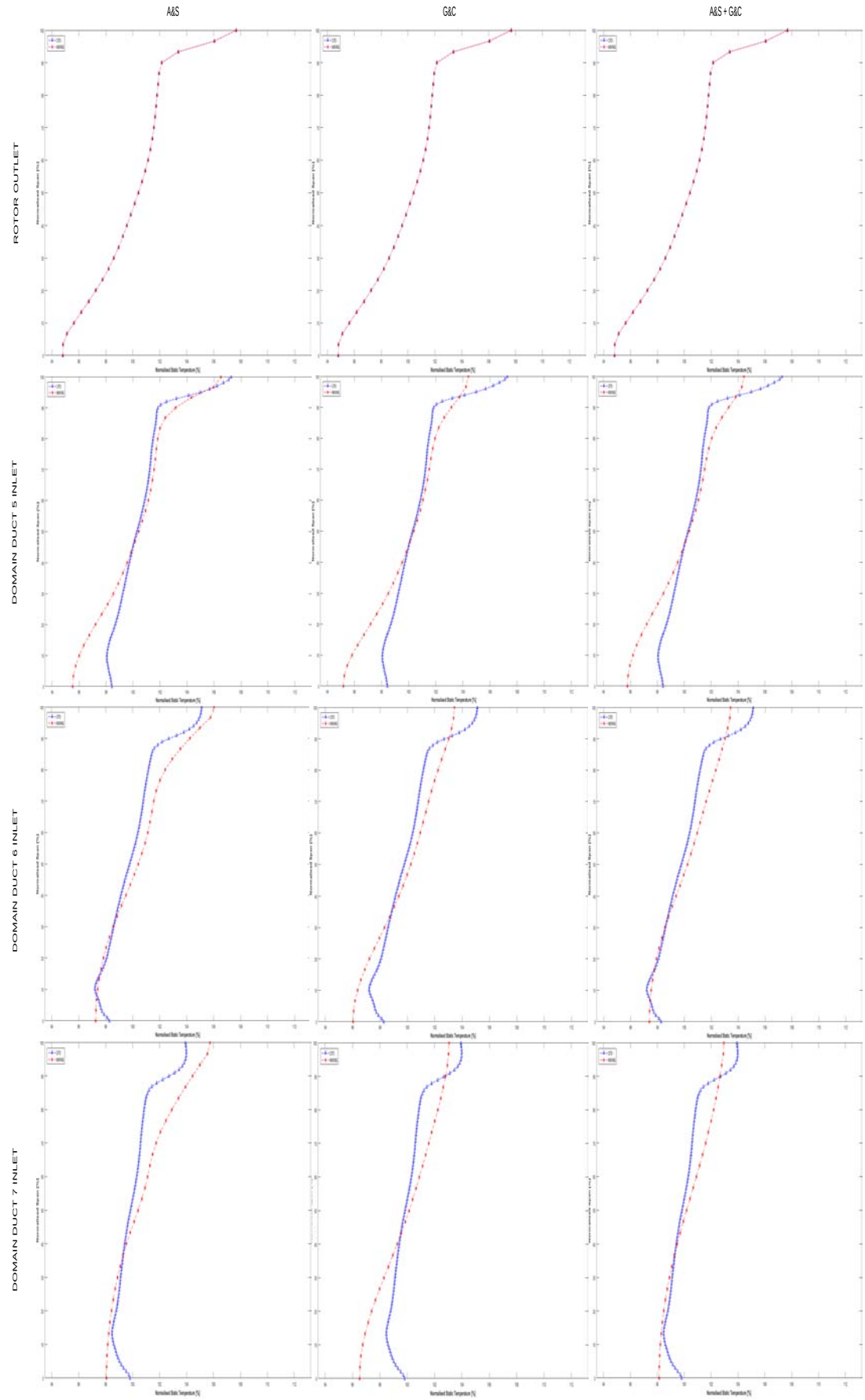

Figure 4.43: M-C near peak efficiency analysis results: static temperature. CFD average value at rotor outlet is 301.3 K. Dotted blue line with triangles is CFD, dashed red line with stars is MIXING.

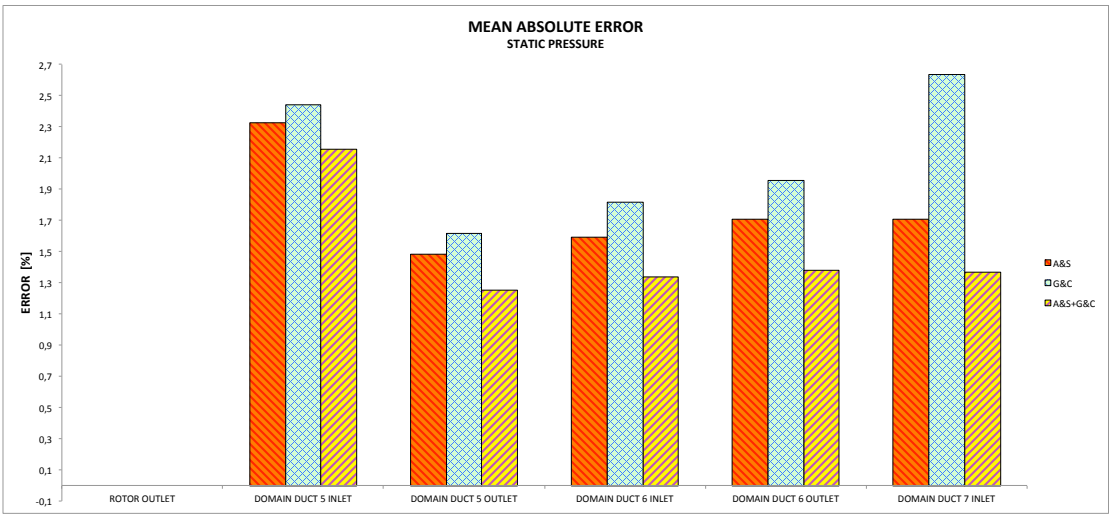

Figure 4.44: M-C near peak efficiency analysis mean absolute error: static pressure. Orange pattern with descending red lines is MIXING A&S, green pattern with blue net is MIXING G&C, yellow pattern with ascending purple lines is MIXING A&S+G&C.

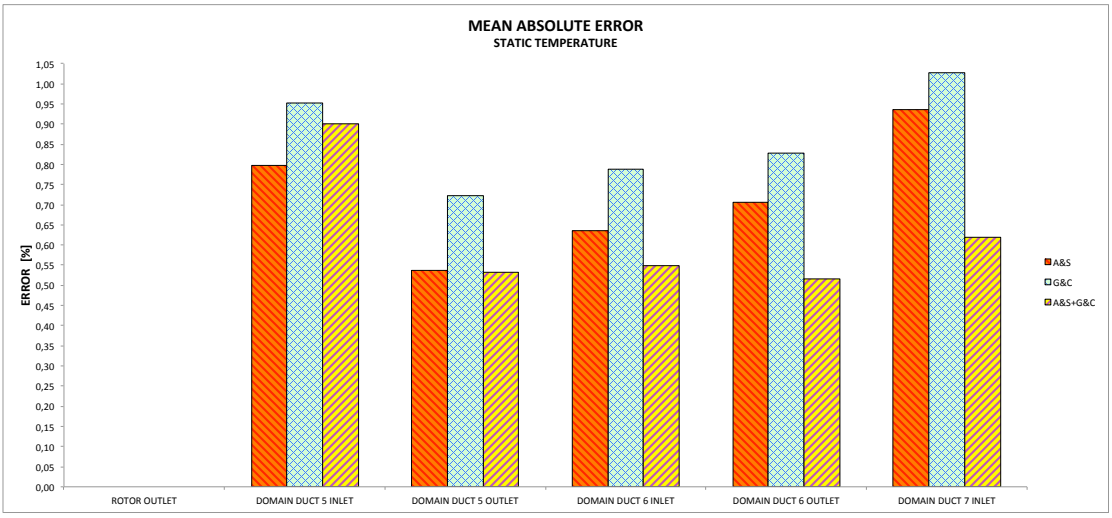

Figure 4.45: M-C near peak efficiency analysis mean absolute error: static temperature. Orange pattern with descending red lines is MIXING A&S, green pattern with blue net is MIXING G&C, yellow pattern with ascending purple lines is MIXING A&S+G&C.

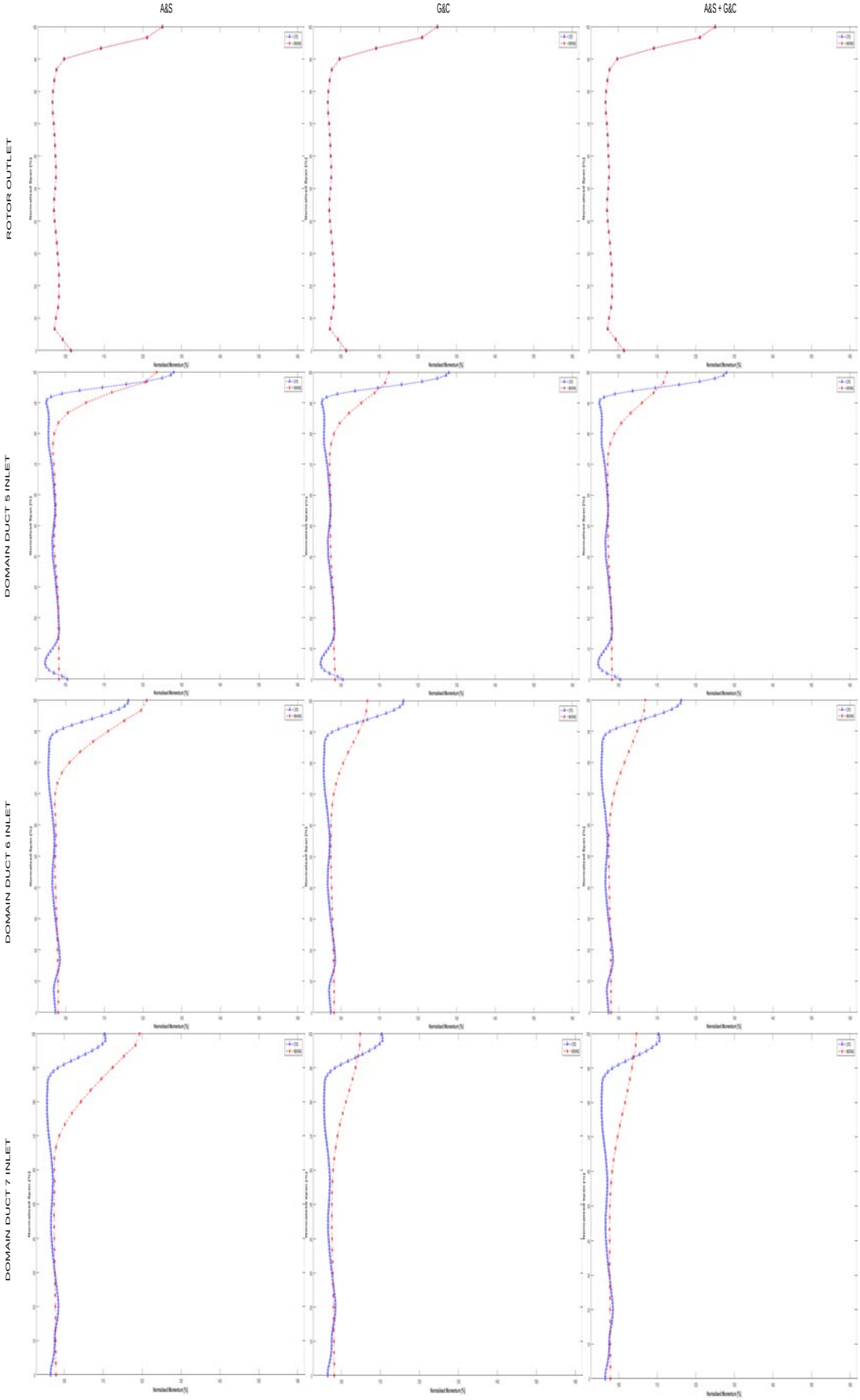

Figure 4.46: M-C near peak efficiency analysis results: angular momentum. CFD average value at rotor outlet is 26.4 m^2/s. Dotted blue line with triangles is CFD, dashed red line with stars is MIXING.

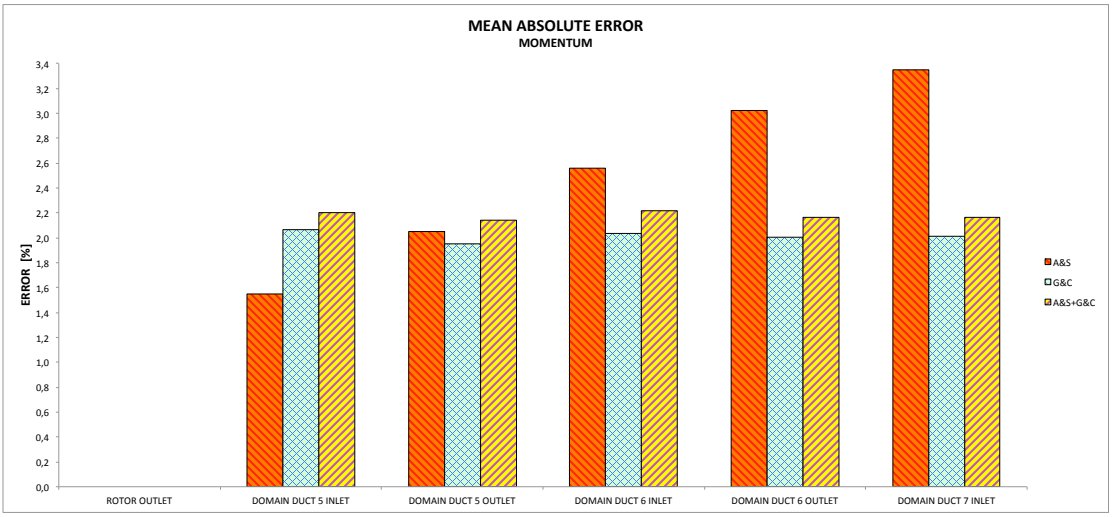

Figure 4.47: M-C near peak efficiency analysis mean absolute error: angular momentum. Orange pattern with descending red lines is MIXING A&S, green pattern with blue net is MIXING G&C, yellow pattern with ascending purple lines is MIXING A&S+G&C.

CHAPTER 5

Conclusions

The objective of the present study is to verify the applicability of a spanwise mixing model for throughflow calculations in axial-flow compressors, and to investigate its congruity with the actual physical behaviour of the flow in such environment. The spanwise mixing model implemented is that proposed by Adkins and Smith in their mixing analysis [4], and the test case chosen for the relative investigations is NASA Rotor 67 transonic compressor. Two kinds of analysis for two operating points, namely near choke and near peak efficiency operating points, were performed:

- S-M-C analysis,
- M-C analysis.

The spanwise mixing calculations considered three different formulations of the mixing coefficient involved in the transport equation solved by the spanwise mixing model. In particular, the mixing process was studied using the Adkins and Smith [4] mixing coefficient, based on the velocities of secondary flows, the Gallimore and Cumpsty [31] mixing coefficient, based on turbulence effects, and the mixing coefficient resulting by the sum of the former mixing coefficients, in order to take into account both aspects of the spanwise mixing phenomenon.

In order to provide a complete analysis of spanwise mixing model applicability, the effect of mixing was studied for stagnation pressure, stagnation temperature, static pressure, static temperature, and angular momentum.

In S-M-C analysis, the spanwise mixing model implemented, which has been referred to as MIXING, compares its predictions to those obtained from a 2-D streamline curvature throughflow program developed in Cranfield University, UK, by Pachidis et al. [63], known as SOCRATES, and to a well-validated CFD model described in [1]. A comparison of the flow property distributions obtained from SOCRATES, MIXING,

and CFD calculations, along with an analysis of errors, allowed to study the applicability of the implemented spanwise mixing model as a useful tool for improving throughflow inviscid solutions, and to highlight the limits of the approach.

It was found that propagating SOCRATES flow property distributions in a direct way, without any corrections from validation against physical principles such as conservation of mass, conservation of momentum, and conservation of energy, gives predictions that have uncertain physical reliability, since their confidence derive from the initial solution provided by SOCRATES.

It is thought that an integration of SOCRATES and MIXING, operating iteratively so that the spanwise mixing model is verified in a prediction-correction process against continuity and radial equilibrium, already included in SOCRATES, would give improved predictions toward a better agreement with experiments. Moreover, a further step in this trend would be represented by the implementation of a mixing model to each streamtube on the meridional plane: in this way, the initial inviscid axisymmetric computation would allow exchange of mass, momentum, and energy within and between each streamtube.

Since no further experimental or numerical data was available, a second type of analysis was performed. In M-C analysis, the spanwise mixing model implemented propagates flow property distributions directly obtained from CFD computations, which already take into account mixing effects by means of Navier-Stokes equations. MIXING relevance was investigated to verify its congruity with flow actual behaviour in axial-flow compressors.

It was found that the errors in the flow quantity distributions predicted by MIXING with CFD input data were not comparatively significant, especially for the final purpose of the considered kind of throughflow models including spanwise mixing, that is compressor design preliminary phases. In this context, the spanwise mixing model analysed is appropriate for the design of stator blades at certain distance from rotor blades, whose predictions are then verified in detail by 3-D numerical calculations. Furthermore, since throughflow analyses are inherently inviscid, the applicability field of the mixing model is restricted to near design conditions in regions away from the endwalls.

M-C analysis results suggest that for total pressure, total temperature, and angular momentum, the spanwise mixing model implemented including the Gallimore and Cumpsty mixing coefficient is in excellent agreement with CFD predictions. For static pressure and static temperature, however, the spanwise mixing model considering both the Adkins and Smith, and the Gallimore and Cumpsty mixing coefficients gives reliable predictions.

In conclusion, the applicability of a spanwise mixing model and its congruity with flow actual behaviour was investigated. Further improvements of the present analysis can be represented by the integration of the studied spanwise mixing model into a throughflow model that reach a solution considering the effect of mixing iteratively for each streamtube involved in the calculation.

Bibliography

[1] Abate G. (2012) *Aerodynamic Optimization of a Transonic Axial Compressor Rotor*, Università degli Studi di Padova, Padova, MSc Thesis in Aerospace Engineering.

[2] Adamczyk J. J. (1984) *Model Equation for Simulating Flows in Multistage Turbomachinery*, NASA-TM-86869.

[3] Adamczyk J. J. (1999) *Numerical Simulation of Multi-Stage Turbomachinery Flows*, Design Principles and Methods for Aircraft Gas Turbine Engines, RTO-MP-8 (21), 1-25.

[4] Adkins G. G. & Smith L. H. (1982) *Spanwise Mixing in Axial-Flow Turbomachines*, J. Eng. Power 104(1), 97-110.

[5] AGARD-CP-571 (1996) *Loss Mechanisms and Unsteady Flows in Turbomachines*.

[6] Aungier R. H. (2003) *Axial flow compressors: A strategy for aerodynamic design and analysis*, 1st Ed. ASME Press and Professional Engineering Publishing, New York, pp. 361.

[7] Benini E. (2005) *Propulsione Aerea*, CLEUP.

[8] Biollo R. & Benini E. (2011) *State-of-Art of Transonic Axial Compressors*, Advances in Gas Turbine Technology, InTech.

[9] Biollo R. and Benini E. (2013) *Recent advances in transonic axial compressor aerodynamics*, Progress in Aerospace Sciences, 56 (1), pp. 1-28.

[10] Benini E. (2014) Dispense del Corso di *Macchine a Fluido*, Ingegneria Aerospaziale, DII, Università degli Studi di Padova.

[11] Boyer K. M. (2001) *An Improved Streamline Curvature Approach for Off-Design Analysis of Transonic Compression Systems*, Ph.D. thesis, Virginia Polytechnic Institute and State University, Blacksburg, Virginia.

[12] Boyer K. M. & O?Brien W. F. (2003) *An improved streamline curvature approach for off-design analysis of transonic axial compression systems*, Trans. ASME J. Turbomachinery 125 (3), pp. 475- 481.

[13] Calvert W. J. & Ginder R. B. (1999) *Transonic fan and compressor design*, Proceedings IMechE, Part C, J. Mechanical Engineering Science 213 (5), pp. 419-436.

[14] Came P. M. (1975) *Streamline Curvature Throughflow analysis*, VDI-BER. 1185. Pp. 1-291.

[15] Carter A. D. S. (1949) *The low speed performance of related aerofoils in cascades*, Aeronautical Research Council Current Papers, National Gas Turbine Establishment, London, No. R.55, pp. 1-20.

[16] Casey M. & Robinson C. (2010) *A New Streamline Curvature Throughflow Method for Radial Turbomachinery*, J. Turbomachinery 132(3), 031021.

[17] Çetin M., Üçer A. S., Hirsch C. and Serovy G. K. (1987) *Application of Modified Loss and Deviation Correlations to Transonic Axial Compressors*, AGARD-R-745.

[18] Creveling H. F. & Carmody R. H. (1968) *Axial flow compressor computer program for calculating off-design performance (Program IV)*, NASA Technical Report, Lewis Researcher Center, Cleveland, Ohio, NASA CR-72427, pp. 1-257.

[19] Cumpsty N. A. (1989) *Compressor Aerodynamics*, Longman.

[20] Cunnan W.S., Stevens W., and Urasek D.C. (1978) *Design and Performance of a 427-Meter-per-Second-Tip-Speed Two-Stage Fan Having a 2.40 Pressure Ratio*, NASA TP-1314.

[21] Denton J. D. (1978) *Throughflow Calculations for Transonic Axial Flow Turbines*, J. Eng. Power 100(2), 212-218.

[22] Denton J. D. (2009) *The Evolution of Turbomachinery Design (Methods)*, lecture slides, PCA 20th Anniversary celebration.

[23] Denton J. D. & Dawes W. N. (1999) *Computational Fluid Dynamics for Turbomachinery Design*, Developments in Turbomachinery Design, Professional Engineering Publishing.

[24] De Ruyck J., Hirsch Ch. and Segaert P., (1988) *Secondary Flows and Radial Mixing in Axial Compressors*, AGARD-CP-469 Secondary Flows in Turbomachines.

[25] Doulgeris G., Khaleghi H., Pilidis P., and Kalfas A. (2011) *Development of a method for enhanced fan representation in gas turbine modeling*, Int. J. Rotating Machinery, 2011, ID 182906, pp. 1-8.

[26] Dring R. P. (1993) *Radial Transport and Momentum Exchange in an Axial Compressor*, J. Turbomachinery 115(3), 477-486.

[27] Dring R. P. (1996) *Radial Mixing in an Axial Turbine*, J. Turbomachinery 118(2), 262-267.

[28] Dunham J. (1992) *Analysis of High Speed Multistage Compressor Throughflow Using Spanwise Mixing*, ASME 1992 International Gas Turbine and Aeroengine Congress and Exposition, Paper No. 92-GT-013, pp. V001T01A006.

[29] Dunham J. (1997) *Modelling of Spanwise Mixing in Compressor Through-Flow Computations*, Proceedings of the Institution of Mechanical Engineers 211.3 (1997): 243.

[30] Frost D. H. (1970) *A Streamline CurvatureThrough-Flow Computer Program for Analysing the Flow through Axial-Flow Turbomachines*, National Gas Turbine Establishment.

[31] Gallimore S. J. & Cumpsty N. A. (1986) *Spanwise Mixing in Multistage Axial Flow Compressors: Part I - Experimental Investigation*, J. Turbomachinery 108(1), 2-9.

[32] Gallimore S. J. (1986) *Spanwise Mixing in Multistage Axial Flow Compressors: Part II - Throughflow Calculations Including Mixing*, J. Turbomachinery 108(1), 10-16.

[33] Gallimore S. J. (1997) *Viscous Throughflow Modeling of Axial Compressor Blade Rows using a Tangential Blade Force Hypothesis*, ASME Paper No. 97-GT-415.

[34] Gallimore S. J. (1999) *Axial Flow Compressor Design*, Proceedings IMechE, Part C, J. Mechanical Engineering Science, 213(5), pp. 437-449.

[35] Griepentrog H. R. (1970) *Secondary flow losses in transonic compressors*, AGARD Report, AGARD LS 39.

[36] Hah C. (1997) *Turbomachinery Fluid Dynamics and Heat Transfer*, CRC Press, Mechanical Engineering.

[37] Hah C. & Reid L. (1991) *A Viscous Flow Study of Shock-Boundary Layer Interaction, Radial Transport, and Wake Development in a Transonic Compressor*, ASME 1991 International Gas Turbine and Aeroengine Congress and Exposition, Paper No. 91-GT-069, pp. V001T01A022.

[38] Hale A. & O'Brien W. (1998) *A Three-Dimensional Turbine Engine Analysis Compressor Code (TEACC) for Steady-State Inlet Distortion*, Transactions of the ASME, J. of Turbomachinery, Vol. 120, pp. 422-430.

[39] Hirsch C. & Denton J. D. (1982) *Through Flow Calculations in Axial Turbomachines*, Propulsion and Energetics Panel Working Group 12, AGARD, Advisory Report No. 175.

[40] Hirsch C. & Warzee G. (1979) *An integrated quasi-3-D finite element calculation program for turbomachinery flows*, J. Eng. Power 101, 141-148.

[41] Horlock J. H. & Denton J. D. (2005) *A review of Some Early Design Practice Using Computational Fluid Dynamics and a Current Perspective*, J. of Turbomachinery, 127, 5-13.

[42] Horlock J. H. & Marsh H. (1971) *Flow Models for Turbomachines*, J. Mech. Eng. Sci., Vol 13, p. 358.

[43] Howard M. A. & Gallimore S. J. (1993) *Viscous Throughflow Modeling for Multistage Compressor Design*, J. Turbomachinery 115(2), 296-304.

[44] Howell A. R. (1945) *Fluid dynamics of axial compressors*, Proceedings IMechE, 153, pp. 441-452.

[45] Hu J. F., Ou-Yang H., Zhu X. Ch., Qiang X. Q., and Du Zh. H. (2011) *An improved streamline curvature approach for transonic axial compressor performance prediction*, Proceedings IMechE Part G: J. Aerospace Engineering 225 (5), pp. 575-584.

[46] Jansen W. & Moffatt W. C. (1967) *The off-design analysis of axial-flow compressors*, Trans. ASME J. Engineering for Power, 89 (4), pp. 453-462.

[47] Jennions I. K. (1994) *Elements of a Modern Turbomachinery Design System*, AGARD-LS-195, Turbomachinery Design Using CFD, pp. (2)1-22.

[48] Jennions I. K. & Stow P. (1985) *The quasi-three-dimensional turbomachinery blade design system, Part I: Through-flow analysis*, Trans. ASME J. Engineering for Gas Turbines and Power 107 (2), pp. 308-314.

[49] Kaldellis J., Douvikas D., Falchetti F. and Papailiou K. D., (1990) *A Secondary Flow Calculation Method for Single-Stage Axial Transonic Flow Compressors, Including Shock-Secondary Flow Interaction*, J. Turbomachinery 112(4), 652-668.

[50] Korpela S. A. (2011) *Principles of Turbomachinery*, John Wiley & Sons, Inc.

[51] Lakshminarayana B. & Horlock J. H. (1965) *Leakage and Secondary Flows in Compressor Cascades* ARC, R&M No. 3483.

[52] Li B., Gu C. W., Li X.T., Liu T. Q., and Xiao Y. B. (2015) *Development and Application of a Throughflow Method for High-Loaded Axial Flow Compressors*, Science China Technological Sciences, Volume 59, Issue 1, pp 93-108.

[53] Lewis K. L. (1994) *Spanwise Transport in Axial-Flow Turbines: Part 1 - The Multistage Environment*, J. Turbomachinery 116(2), 179-186.

[54] Lewis K. L. (1994) *Spanwise Transport in Axial-Flow Turbines: Part 2 - Throughflow Calculations Including Spanwise Transport*, J. Turbomachinery 116(2), 187-193.

[55] Leylek J. H. & Wisler D. C. (1991) *Mixing in Axial-Flow Compressors: Conclusions Drawn From Three-Dimensional Navier-Stokes Analyses and Experiments*, J. Turbomachinery 113(2), 139-156.

[56] Li Y. S. & Cumpsty N. A. (1991) *Mixing in Axial Flow Compressors: Part I - Test Facilities and Measurements in a Four-Stage Compressor*, J. Turbomachinery 113(2), 161-165.

[57] Li Y. S. & Cumpsty N. A. (1991) *Mixing in Axial Flow Compressors: Part II - Measurements in a Single-Stage Compressor and a Duct*, J. Turbomachinery 113(2), 166-172.

[58] Lieblein S. (1960) *Incidence and deviation-angle correlations for compressor cascades*, Trans. ASME J. Basic Engineering 82 (3), pp. 575-584.

[59] Lieblein, S. (1965) *Aerodynamic design of axial-flow compressors*, Special Publication, NASA, Washington, D.C. NASA SP-36, Chapter IV, pp.183.

[60] Marsh H. (1968) *A Digital Computer Program for the Through-flow Fluid Mechanics in an Arbitrary Turbomachine using a Matrix Method*, Aeronautical Research Council Reports and Memoranda.

[61] Menter R. F. (1994) *Two-Equation Eddy-Viscosity Turbulence Models for Engineering Applications*, AIAA Journal, vol. 32, no. 8, pp. 1598-1605.

[62] Novak R. A. & Hearsey R. M. (1977) *A Nearly Three-Dimensional Intrablade Computing System for Turbomachinery*, J. Fluids Engineering 99(1), 154-166.

[63] Pachidis V. (2006) *Gas turbine advanced performance simulation*, PhD Thesis, School of Engineering, Cranfield University, pp. 1-384.

[64] Pachidis V., Pilidis V., Texeira J., and Templalexis I. (2006) *A comparsion of component zooming simulation strategies using streamline curvature*, Proceedings IMechE Part G: J. Aerospace Engineering 221 (5), pp. 1-15.

[65] Pachidis V., Pilidis P., Marinai L., and Templalexis I. (2007) *Towards a Full Two Dimensional Gas Turbine Performance Simulation*, Proceedings of the RASoc, The Aeronautical Journal, AJ-3127.

[66] Pachidis V., Pilidis P., Templalexis I, Kotsiopoulos P., and Korakianitis T. (2007) *Prediction of engine performance under compressor inlet flow distortion using streamline curvature*, Trans. ASME J. Engineering for Gas Turbines and Power 129 (1), pp. 97-103.

[67] Pachidis V., Pilidis P., Templalexis I., and Marinai L. (2008) *An iterative method for blade profile loss model adaptation using streamline curvature*, J. Engineering for Gas Turbines and Power 130 (1), pp. 1-8.

[68] Pachidis V., Templalexis I, Pilidis P., and Kotsiopoulos P. (2010) *A dynamic convergence control scheme for the solution of the radial equilibrium equation in through-flow analyses*, Proceedings IMechE Part G: J. Aerospace Engineering 224 (G7), pp. 803-815.

[69] Petrovic M. V. & Riess W. (1997) *Off-Design Flow Analysis and Performance Prediction of Axial Turbines*, ASME 1997 International Gas Turbine and Aeroengine Congress and Exhibition, Paper No. 97-GT-055, pp. V001T03A013.

[70] Petrovic M. V., Wiedermann A., and Banjac M. B. (2010) *Development and Validation of a New Universal Through Fow Method for Axial Compressors*, Proceedings of the Institution of Mechanical Engineers, Part A, Journal of Power and Energy 1(A6):1-12.

[71] Petrovic M. V. & Wiedermann A. (2013) *Through-Flow Analysis of Air-Cooled Gas Turbines*, J. Turbomachinery 135(6), 061019.

[72] Schwenk F. C., Lewis G. W., and Hartman M. J. (1957) *A preliminary analysis of the magnitude of shock losses in transonic compressors*, NACA Research Memorandum, Lewis Flight Propulsion Laboratory, Cleveland, Ohio, NACA RM E57A30, pp. 1-49.

[73] Shan P. (2008) *A mass addition approach to the bypass turbomachine through flow inverse design problem*, J. Mechanical Science and Technology, 22 (10), pp. 1921-1925.

[74] Simon J. F. (2007) *Contribution to Throughflow Modelling for Axial Flow Turbomachines*, Ph.D. thesis, University of Liège, Liège, Belgium.

[75] Spurr A. (1980) *The Prediction of 3D Transonic Flow in Turbomachinery Using a Combined Throughflow and Blade-to-Blade Time Marching Method*, Int. J. Heat and Fluid Flow, 2(4), 189-199.

[76] Strazisar A. J., Wood J. R., Hathaway M. D., and Suder K. L. (1989) *Laser Anemometer Measurements in a Transonic Axial-Flow Fan Rotor*, NASA, Technical Paper 2879.

[77] Suryavamshi N. & Lakshminarayana B. (1992) *Numerical Prediction of Wakes in Cascades and Compressor Rotors Including the Effects of Mixing: Part I - Cascade Wakes Including the Effects of Incidence and Free-Stream Turbulence*, J. Turbomachinery 114(3), 607-616.

[78] Suryavamshi N. & Lakshminarayana B. (1992) *Numerical Prediction of Wakes in Cascades and Compressor Rotors Including the Effects of Mixing: Part II - Rotor Passage Flow and Wakes Including the Effects of Spanwise Mixing*, ASME 1991 International Gas Turbine and Aeroengine Congress and Exposition, Paper No. 91-GT-222, pp. V001T01A079.

[79] Swan W. C. (1961) *A practical method of predicting transonic-compressor performance*, Trans. ASME J. Power, 83 (3), pp. 322-330.

[80] Templalexis I., Pachidis V., Pilidis P., and Kotsiopoulos P. (2008) *The Effect of Blade Lean on the Solution of the Radial Equilibrium Equation*, GT2008-50259, ASME Turbo Expo, Power For Land, Sea and Air, Berlin, Germany.

[81] Templalexis I., Pachidis V., Pilidis P., and Kotsiopoulos P. (2011). *Development of a two-dimensional streamline curvature code*, J. Turbomachinery 133 (1), pp. 1-7.

[82] Templalexis I. (2014) *The importance of force terms modelling within the streamline curvature through-flow method*, Proceedings IMechE Part A: J. Power and Energy 228 (7), 825-835.

[83] Tiwari P., Stein A., and Lin Y. L. (2013) *Dual-solution and choked flow treatment in a streamline curvature througflow solver*, Trans. ASME J. Turbomachinery, 135 (4), pp. 1-8.

[84] Üçer A. S. & Erkilet M. (1990) *A Study on Secondary Flow and Spanwise Mixing*, AGARD PEP Specialist Meeting Proceedings on Secondary Flows in Turbomachines.

[85] Üçer A. S. & Shreeve R. P. (1992) *A Viscous Axisymmetric Throughflow Prediction Method for Multistage Compressors*, ASME Paper No 92-GT-293.

[86] Urasek D.C., Gorrell W.T., and Cunnan W.S. (1979) *Performance of Two-Stage Fan Having Low-Aspect-Ratio*, TP-1493.

[87] Wennerstrom A. J. (1991) *A Review of Predictive Efforts for Transport Phenomena in Axial Flow Compressors*, J. Turbomachinery 113(2), 175-179.

[88] Wilkinson D. H. (1970) *Stability, convergence, and accuracy of two-dimensional streamline curvature methods using quasi-orthogonals*, I.Mech.E. Convention, Glasgow, paper 35.

[89] Wisler D. C., Bauer R. C., and Okiishi T. H. (1987) *Secondary Flow, Turbulent Diffusion, and Mixing in Axial-Flow Compressors*, J. Turbomachinery 109(4), 455-469.

[90] Wu C. H. (1952) *A general theory of three-dimensional flow in subsonic and supersonic turbomachines of axial-, radial-, and mixed-flow types*, NACA-TN-2604.